Federal Agency and Organization: DOE BER
Funding Opportunity Announcement Number: DE-PSO2-07ER07-18
Science element: Novel Measurement and Monitoring Concepts
DOE/Office of Science Program Office: Environmental Remediation Science Division

Recipient Organization: Colorado school of Mines
DUNS Number: 010628170
Recipient Address: Department of Geophysics
1500 Illinois St.
Golden, Colorado 80401

Award Number: BER, DE-FG02-08ER64659

Project Title: Advanced Self-Potential Inversion: Development and Use for Investigating Natural Recharge Processes at the ORNL IFC

Principal Investigator: André Revil
Professor
arevil@mines.edu
720 536 8500

Date of Report Submission: January 15, 2013

Project Partners:

Institution	**Key Researchers**
Colorado School of Mines	A. Revil (PI)
Lawrence Berkeley Laboratory	S. Hubbard (collaborator)
Oak Ridge National Laboratory	D. Watson (collaborator)

DOE Contracting Officer: David Lesmes

Contents

1. Introduction and Importance

Understanding the influence of coupled biological, chemical, and hydrological processes on subsurface contaminant behavior at multiple scales is a prerequisite for developing effective remedial approaches, whether they are active remediation or natural attenuation strategies. To develop this understanding, methods are needed that can measure critical components of the natural system in real time. The Self-Potential (SP) method corresponds to the passive measurement of the distribution of the electrical potential at the surface of the Earth or in boreholes. Once filtered from anthropic and telluric signals, the residual self-potential signals can be directly related to polarization phenomena that occur in the subsurface. While most geophysical methods are sensitive to the architecture of a geological system or to the saturation of the various fluid phases that are present in porous or fractured subsurface environments, the self-potential signals repond to ground water flow and geochemical concentration gradients. By some aspects, the SP method, which is also one of the oldest of all the geophysical techniques, is similar to medical imaging electroencaphalography, which tracks the electroactivity (or source of epilepsy) of the brain in real time.

Here, we propose to develop an SP inversion framework for subsurface characterization, to couple the inversion framework with the LBNL-developed TOUGHREACT simulator, and to apply the approach to time-lapse SP datasets collected to monitor groundwater responses to recharge events at the Oak Ridge National Laboratory Integrated Field Challenge (ORNL IFC) Site in Tennessee, which is described at http://www.esd.ornl.gov/nabirfrc/. The SP method is attractive for monitoring of subsurface transformations because it is a passive method that is cheap to implement and that can be used across a variety of spatial-temporal scales, and because the SP signals respond to both groundwater flux and concentration gradients. In recent years, the project PI has advanced SP inversion approaches for exploring responses to hydrological fluxes and geochemical variations. However, these processes have been explored in isolation from each other and only under fairly ideal conditions. In natural systems, precipitation events will lead to infiltration fluxes, which in turn can alter groundwater geochemistry. This disruption in geochemical equilibrium brought about by a hydrological flux is not well understood at the plume scale as it is difficult to extract this information from sparse wellbore information alone. These coupled natural hydrological and geochemical processes may play an important role when considering remedial strategies such as natural attenuation. This is especially true in sites dominated by large episodic and seasonal precipitation pulses, such as occur at the ORNL IFC site.

Contaminants in the groundwater plume at the ORNL IFC include uranium (U), technetium-99 (Tc), nitrate, thorium, and volatile organic compounds such as acetone, methylene chloride, toluene, and tetrachloroethylene. The groundwater pH, which can range from 3.2 in regions close to the continant source to over 7.0 in wells farther down gradient, is postulated to have a tremendous impact on subsurface processes and contaminant fate and transport. Recharge at the ORNL site is not only the hydraulic driver of contaminant plume migration, but is also expected to be a significant source of dilution, DO, and DOC.

2. Results by Tasks

In this study, we proposed to use theoretical, numerical, and experimental approaches to evaluate the potential of obtaining quantitative information from electrical measurements that can be used to elucidate system transformations associated with recharge and natural attenuation at the ORNL IFC. In particular, we propose we have tested the following hypotheses:

- *Advanced inversion approaches can be used with the easy-to-deploy, low-cost electrical methods (resistivity, induced polarization and especially self-potential) to distinguish between and provide quantitative information about both hydrological and geochemical variations.*

- *The developed approaches are useful at the ORNL IFC Site for investigating coupled hydrological-geochemical transformations that occur in response to natural recharge events over scales that are important for assessing natural attenuation strategies. We have shown for the first the geometry of the contaminant plumes at the site and we have developed a new characterization of the saprolitic material.*

In the following we describe task by Task what have been the results obtained during the course of this research project.

- **Task 1:** The goal of this task was to develop a framework for inverting borehole and surface-based self-potential datasets in terms of both hydrological and geochemical variables.

Results: We have developed a complete theoretical framework to understand self-potential signals in the subsurface associated with ground water flow and gradient in the ionic strength of the pore water. This work was published in Water Resources Research (Revil et al., 2011). In parallel, we have developed a complete modeling of the self-potential response associated with biogeobatteries and we have elucidated the role of biotic and abiotic conductors in the process (Revil et al., 2010). One of the most important contribution has been the modeling of the role of bacteria in the biogebattery process, which has been very controversial in the last decade. This is illustrated in Figures 1 and 2. This implies in turn that the long-range transport of electrons through bacteria biofilms is possible as advocated 10 years ago by Revil and colleagues (e.g., Naudet et al., 2003, 2004). The biogeobattery model was validated through laboratory experiment in Risgaard-Petersen et al. (2012).

In parallel to the modeling of the self-potential, we have done and published several papers on the modeling of induced polarization in porous media with a special attention to the saprolite from Oak Ridge (Revil et al., 2013a). The work we have performed on the modeling of the induced polarization response of porous rocks can be found in Revil and Florsch (2010), Skold et al. (2011) and Revil (2012). In karaoulis et al. (2011), we have developed a 3D time-lapse code to image change in spectral or time-domain induced polarisation of the subsurafce of the Earth.

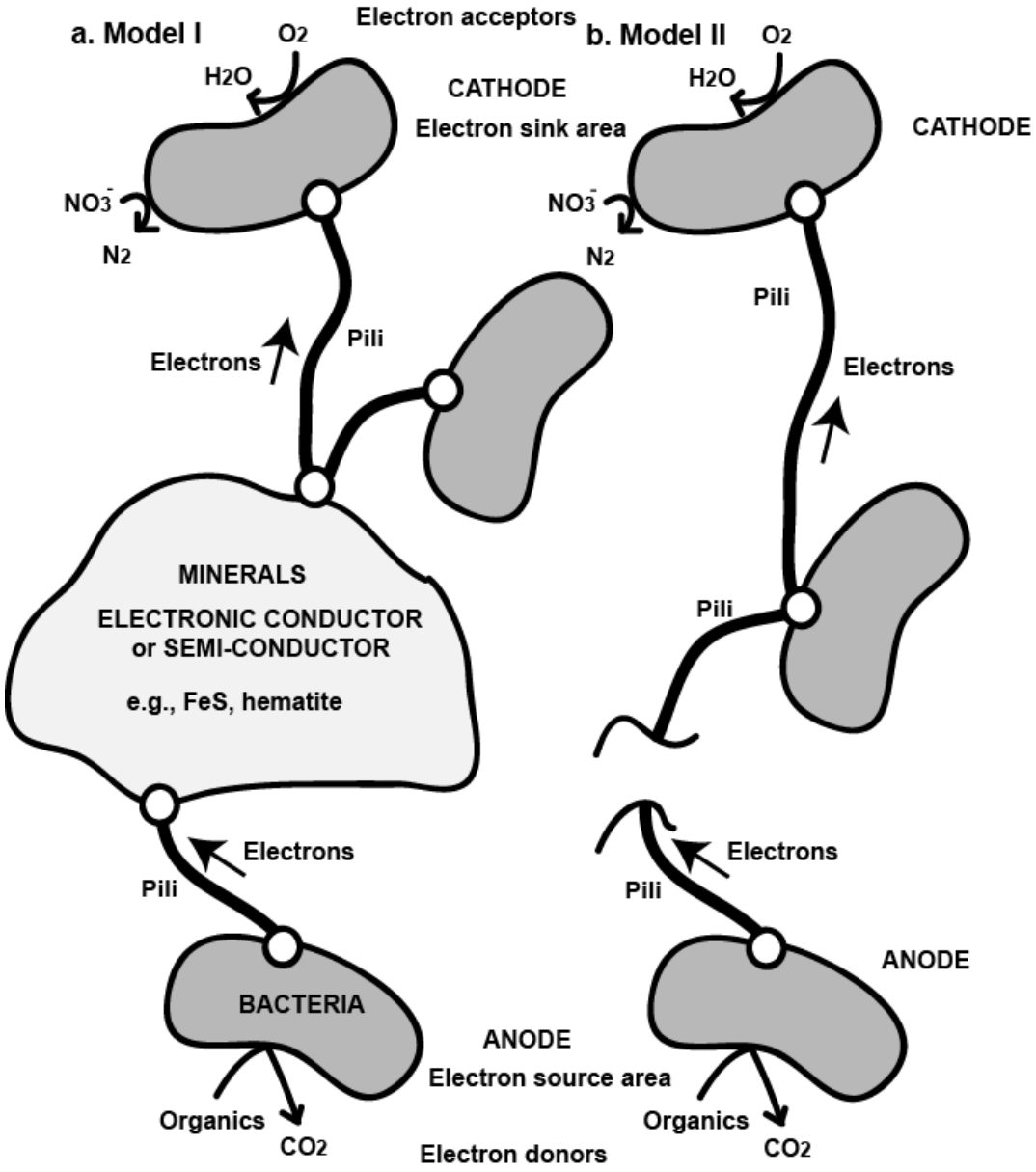

Figure 1. Sketch of two possible electron transfer mechanisms in a contaminant plume. **a.** In Model I, the presence of minerals facilitates electronic conduction. **b.** In Model II, only bacteria populations are connected by conductive pili. At the "bacterial anode" electrons are gained through the oxidation of the organic matter, iron oxides, or Fe-bearing phyllosilicates. The electrons are conveyed to the "bacterial cathode" through a network of conductive pili. At the "bacterial cathode", the reduction of oxygen and the nitrate prevails as electron acceptors. In this system, bacteria act as catalysts. The transport of electrons through the anode to the cathode of the microbattery may involve different bacterial communities and different electron transfer mechanisms including external electron shuttles (from Revil et al., 2010).

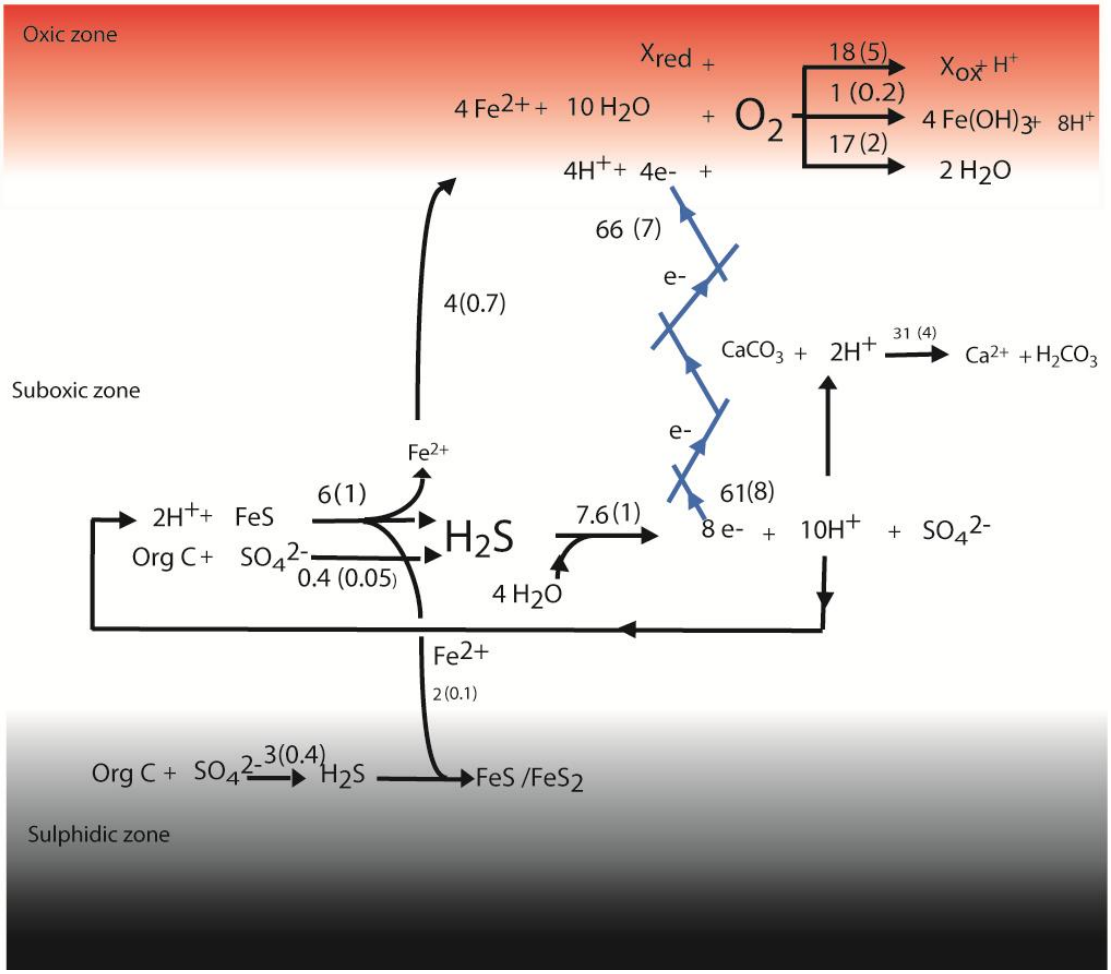

Figure 2. Long distance electron transmission couples anodic sulphide oxidation and cathodic oxygen reduction. Electrons are passed from the reduced sulphur to oxygen through a native conductor, the composition of which is presently unknown. Numbers beside arrows represent quantitative estimates of process rates and fluxes and are presented as the mean ± s.e.m. (n = 3–4). The units are mmol m^{-2} d^{-1}. Note that the rate of FeS dissolution is calculated from the Fe^{2+} profile; while the rate of sulphide oxidation is calculated from the SO_4^{2-} profile and the rate of sulphate reduction (from Risgaard-Petersen et al., 2012).

- **Task 2:** Explicitly couple self-potential and transport phenomena within a transport simulator.

We have developed some modules to determine the self-potential signals associated with salt tracer tests, heat tracer tests, and two phase flow conditions. For instance we have developed the complete forward and inverse modeling of self-potential signals associated with a salt tracer test in four

papers: Martínez-Pagán et al. (2010), Revil and Jardani (2010), Ikard et al. (2012), and Jardani et al. (2012). Figures 3 is showing the modeling of the self-potential response associated with a salt injection a sandbox experiment in presence of a preferential pathway characterized by a high hydraulic conductivity. This was the first time that transport modeling and time-lapse modeling of the self-potential method was bridged.

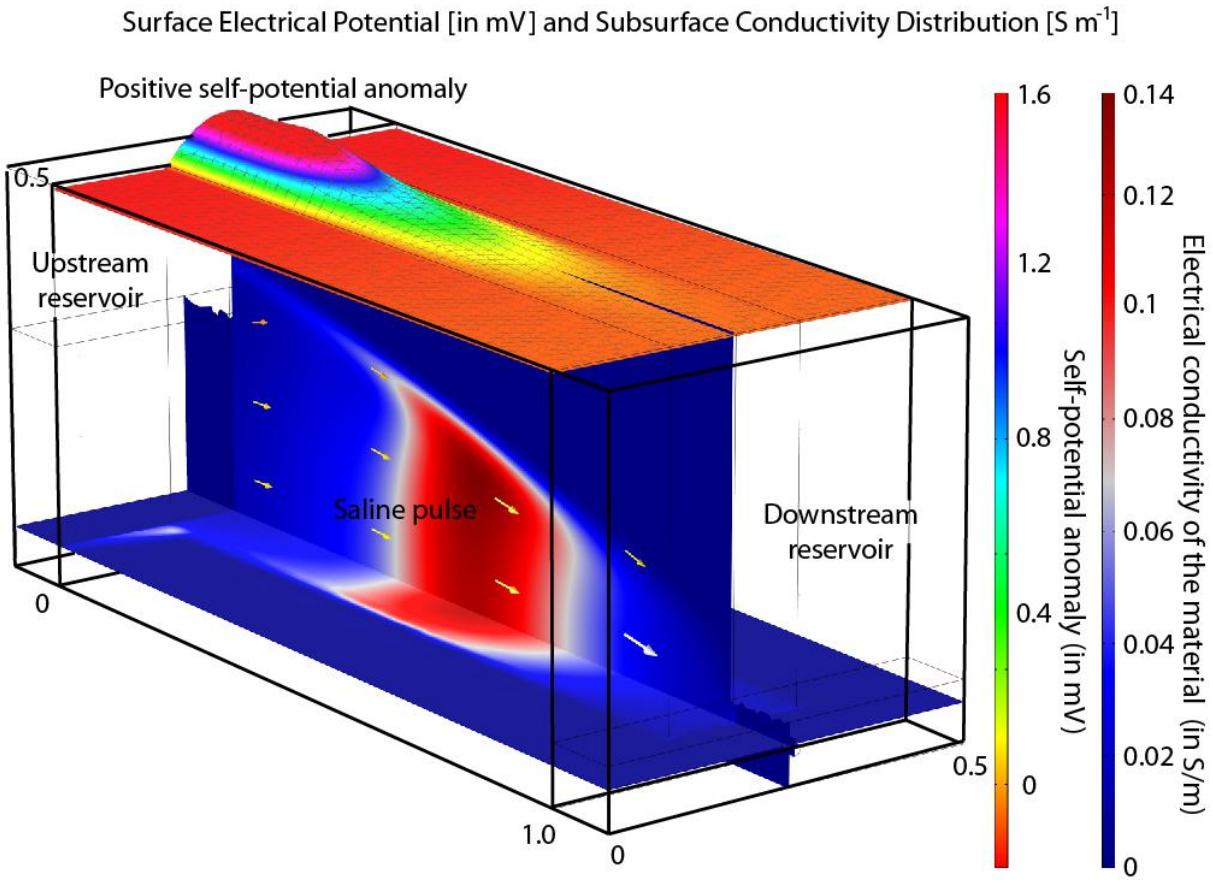

Figure 4. Snapshot (120 s after the salt injection, see Figure 4) of the 3D distribution of the resistivity and map of the self-potential anomaly at the top surface of the tank during the saline pulse experiment. The arrows correspond to the direction of the Darcy velocity (their lengths are proportional to the intensity of the flow density vector **u**). From Ikard et al. (2012).

- **Task 3:** Test developed inversion and modeling framework under controlled laboratory conditions

We have developed several well-controlled sandbox experiments to test the theoretical framework developed in Task 1 and the numerical modeling framework developed in Task 2. For instance in Ikard et al. (2012), a method is proposed to localize preferential fluid flow pathways in porous media based on time-lapse self-potential measurements associated with a salt tracer injection. This method ws first tested using a sandbox experiment as shown in Figure 5. A network of non-

polarizing electrodes located is connected to a highly sensitive voltmeter used to record the resulting electrical field fluctuations occurring over time at the surface of the tank.

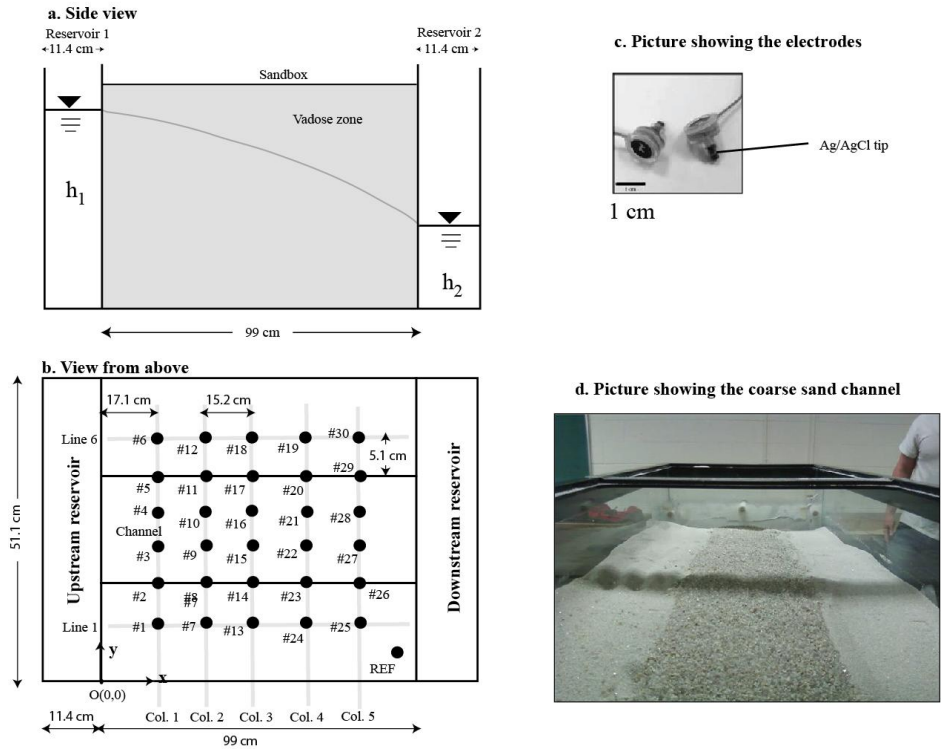

Figure 5. Sketch of the experimental setup showing the position of the channel and the positions of the non-polarizable electrodes (small filled circles, the true size of the electrodes being much smaller than the size of the filled circles, see Figure 5b) located at the top surface of the sand. The hydraulic gradient is defined by the difference between the heads h_1 and h_2 in the two reservoirs located 99 cm apart. The width of the tank is 51.1 cm. REF denotes the position of the reference electrode. **a.** Side view. **b.** Top view (not to scale). **c.** Picture showing the size of the Ag/AgCl electrodes with the amplifiers. **d.** Picture of the tank showing the coarse sand channel between fine-grained banks. From Ikard et al. (2012).

Figure 6 shows the development of the self-potential signals over time. The self-potential disturbance shows very clearly the position of the preferential flow pathway. The transport of the conductive salt plume through the permeable porous materials changes the localized streaming potential coupling coefficient associated with the advective drag of the excess of charge of the pore water and is also responsible for a diffusion current associated with the salinity gradient. Monitoring of the electrical potential distribution at the ground surface can be used to localize the pulse of saline water over time, and to determine its velocity. This method applies in real time and can be used to track highly localized flow pathways characterized by high permeability. The type of sandbox experiment developed in Ikard et al. (2012) demonstrates the applicability of this new method under well-controlled conditions with a coarse sand channel embedded between fine-sand banks. A finite element model allows to reproduce the time-lapse electrical potential distribution over the channel (Figure 7). Finally, we performed a numerical simulation for a synthetic case study inspired by a recently published field case study. A Markov-chain Monte Carlo (McMC) sampler is used to

determine the permeability and the porosity of the preferential fluid flow pathway. We called this method the SMART test.

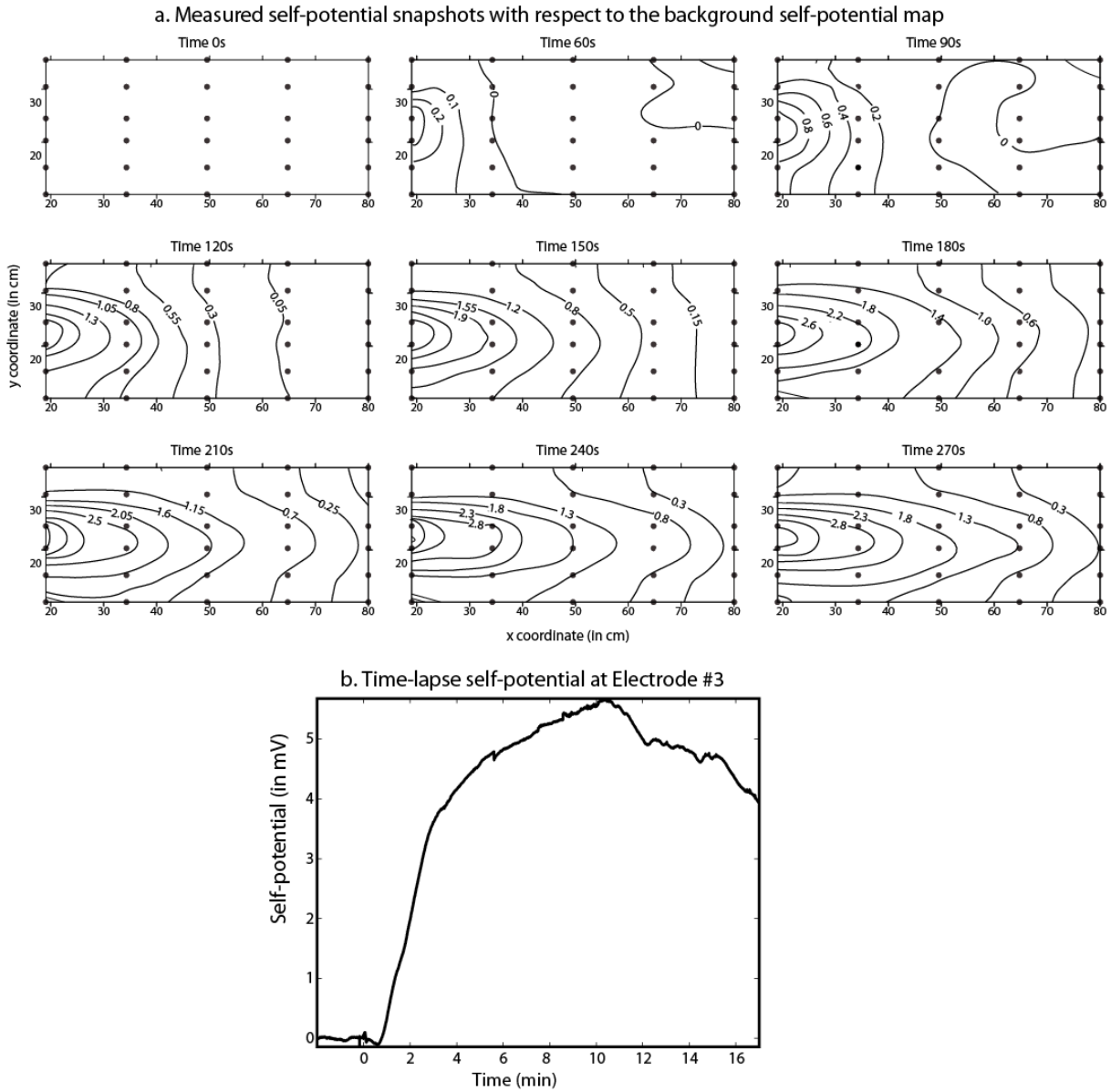

Figure 5. Observed self-potential anomalies. **a.** Kriged measured self-potential anomaly contours (expressed in mV) at different elapsed times (t = 0 corresponds to the infiltration of the salt in the upstream reservoir). The background potential measured prior to salt injection has been removed. This explains that at t = 0 s, there is no self-potential anomaly. Constant flow conditions are maintained for the duration of the experiment. **b.** Self-potential (mV) versus time at electrode #3. From Ikard et al. (2012)

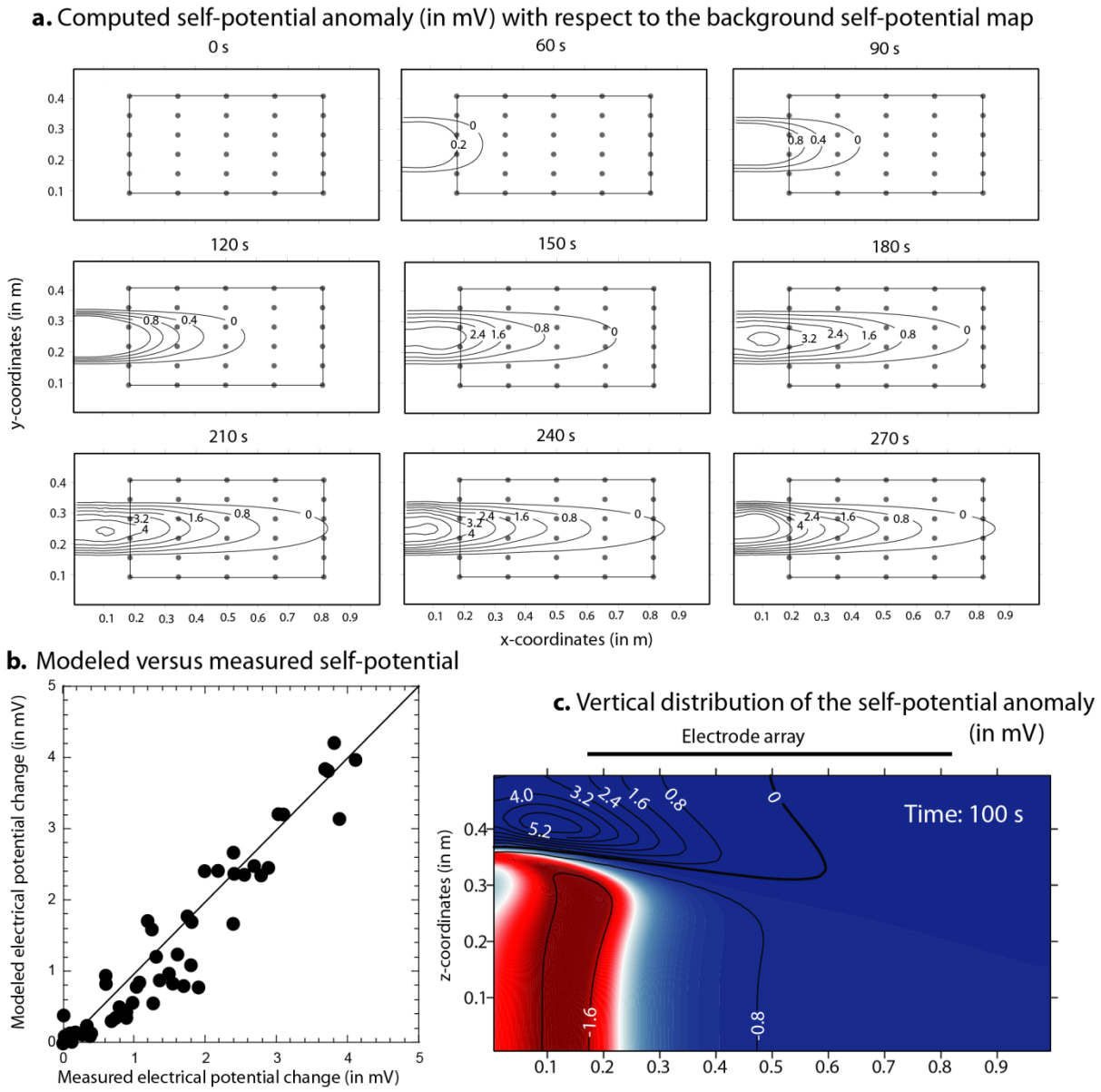

Figure 6. Computed self-potential anomaly contours at different elapsed times (t = 0 corresponds to the injection of the salt in the upstream reservoir). **a.** Result of the model. The outer rectangle corresponds to the dimension of the tank while the inner rectangle corresponds to the area covered by the electrodes. Constant flow conditions are maintained during the numerical experiment and insulating boundary conditions are applied at the top, sides, and bottom of the tank. **b.** Comparison between the prediction of the model and the measured data for the two lines of electrodes just above the channel (R = 0.95). **c.** Vertical distribution of self-potential. The colors corresponds to the conductivity. From Ikard et al. (2012).

Other experiments were also performed to test how the self-potential data can be used to invert the permeability and dispersivity of the subsurface. For instance we performed a sandbox experiment in which we monitor a salt tracer plume (Martínez-Pagán et al., 2010). This dataset was

used by Revil and Jardani (2010) to show that a stochastic approach can be used to invert the permeability and the two dispersion coefficients of a sand in a sandbox.

- **Task 4 to 7: Field data. Task 4:** Development and/or installation of self-potential arrays and real-time logging system at two key areas within the ORNL Bear Creek Watershed. **Task 5:** Acquisition of field datasets over 1.5 year timeframe. **Task 6:** Apply developed framework to collected ORNL field datasets. **Task 7:** Synthesize the inversion-modeling approach in terms of hydrological and geochemical properties associated with natural recharge.

At the Oak Ridge Integrated Field Research Challenge (IFRC) site, near Oak Ridge, Tennessee, contaminants from the former S-3 ponds have infiltrated a shallow saprolitic aquifer for over 60 years. The position of the problem is explianed in Figure 7. We have performed time lapse resistivity survey over several years at the Oak Ridge Integrated Field Research Challenge (IFRC) site in the vicinity of the former S-3 ponds. We found that the site was too noisy for time-lapse self-potential surveys because of the presence of two grounded generators on the site. Nevertheless, we performed various surveys including DC resistivity, time domain induced polarization, and self-potential mapping. We present the main results below (see also Appendix A to D).

DC-resistivity tomography was used to find the number and location of the main contaminant plumes around the former S-3 ponds. We identified a total of 5 main plumes (termed CP1 to CP5 in our nomenclature). Plume CP2 corresponds to the main plume in terms of nitrate concentration (~50,000 mg L^{-1}). These contaminant plumes have typically an electrical resistivity in the range 2 to 20 ohm m while the background saprolite resistivity is in the range 60 to 120 ohm m, so the difference of resistivity was easily mapped using DC-resistivity tomography to locate the contaminant pathways and to infer the nitrate concentration (Figures 8 and 9). We develop indeed a relationship to derive the in situ nitrate concentrations from the 3D resistivity tomograms (see validation in Figure 8). The footprint of the contamination upon the resistivity is found to be much stronger than the local variations associated with changes in the porosity and the clay content. This study points out the importance of accounting for surface conductivity. Self-potential data shows the existence of a strong bipolar anomaly (about 400 mV peak to peak) possibly associated with the presence of a gradient of the redox potential in the saprolitic aquifer due to a biostimulation experiment. The inverted source current density points responsible for the observed self-potential anomaly is located at a depth between 4 to 8 m, just at the top of the contaminant plumes where the strongest gradient in the redox potential is expected.

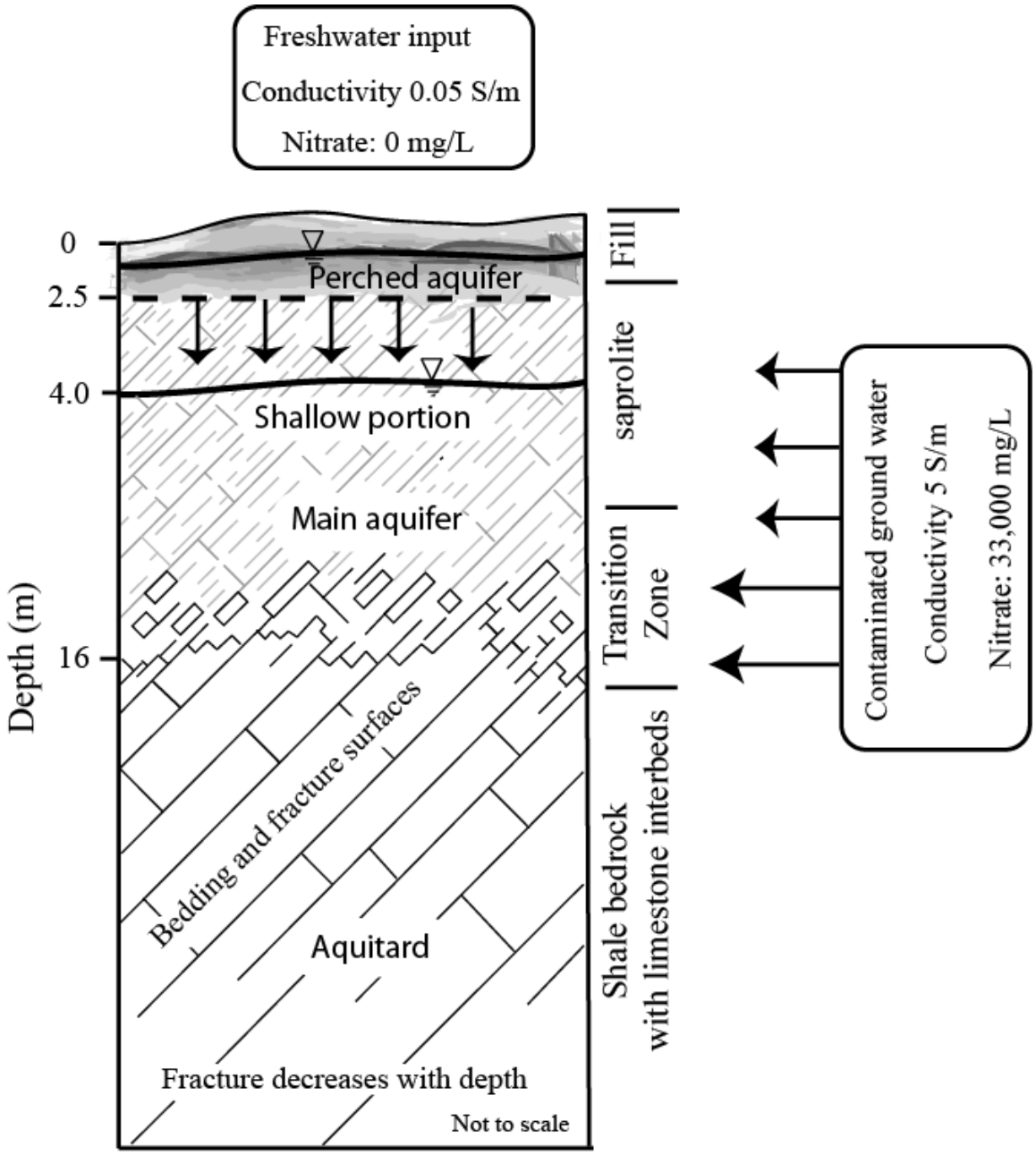

Figure 7. Position of the problem. Typical section of saprolite and parent rock at the Oak Ridge Integrated Field Research Challenge (IFRC) site. The transition zone at the bottom of the saprolitic aquifer is an area of higher permeability than the upper portion of the aquifer. Water infiltration can come either from the perched aquifer or from a ditch located in the vicinity of the S-3 pond. The shallow portion of the aquifer (sampled by the shallow Well F116) is influenced by the pervasive infiltration from the shallow aquifer.

The study made by Revil et al. (2013a) allowed to rech the following conclusions: Hydrogeophysical investigations performed around the former S-3 settling basins at the Oak Ridge Integrated Field Research Challenge site, Tennessee have revealed the following features: 1. Five

main plumes have been detected by 2.5D/3D resistivity tomography, three plumes on the Western part of the S-3 Ponds (CP1, CP2, and CP3), 1 main plume (CP4) in the southern part of the S-3 ponds, and potentially another small plume further north to the CP3 plume named CP5.

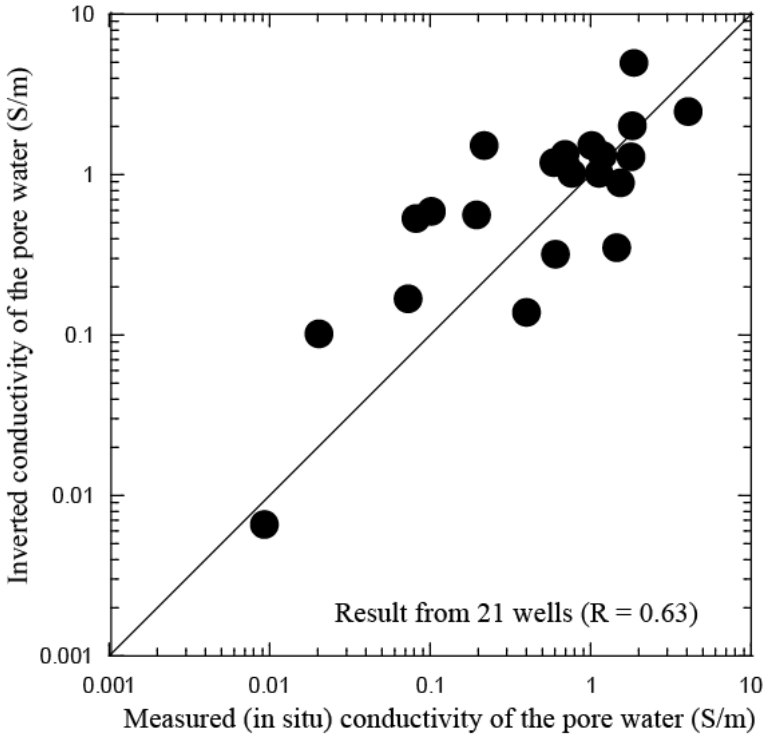

Figure 8. Comparison between the conductivity of the pore water determined from the tomograms and the in situ sampling of the pore water conductivity in 21 wells located around the former S-3 basins (see Figure 3).

2. A methodology has been developed to use the resistivity tomograms and compute the nitrate concentration in the plumes around the S-3 ponds. This methodology is based on a conductivity model accounting for both the formation factor and the surface conductivity. This is in contrast with previous works in which surface conductivity was considered negligible despite the presence of 20% (weigth) clay fraction and clays characterized by a high CEC. This conductivity model has been validated in a previous laboratory work (Revil et al., 2012). The pore water conductivity is related to the nitrate concentration through a linear equation accounting for the vanishingly small nitrate concentration in the background pore water and validated through well data. Future works could include larger scale resistivity tomography (at the scale of the valley) to reveal deeper flow paths used by the contaminants to move downstream. The approach developed in this paper can be applied to different sites but the values of the surface conductivity and formation factor need to carefully estimated for different formations and rock types. 3. The self-potential show a dipolar anomaly with an amplitude of four hundred millivolts centered on a biostimulated area of the CP1 plume. This could open the door to the use of time-lapse self-potential data to monitor non-intrusively bioremediation in the saprolitic aquifer.

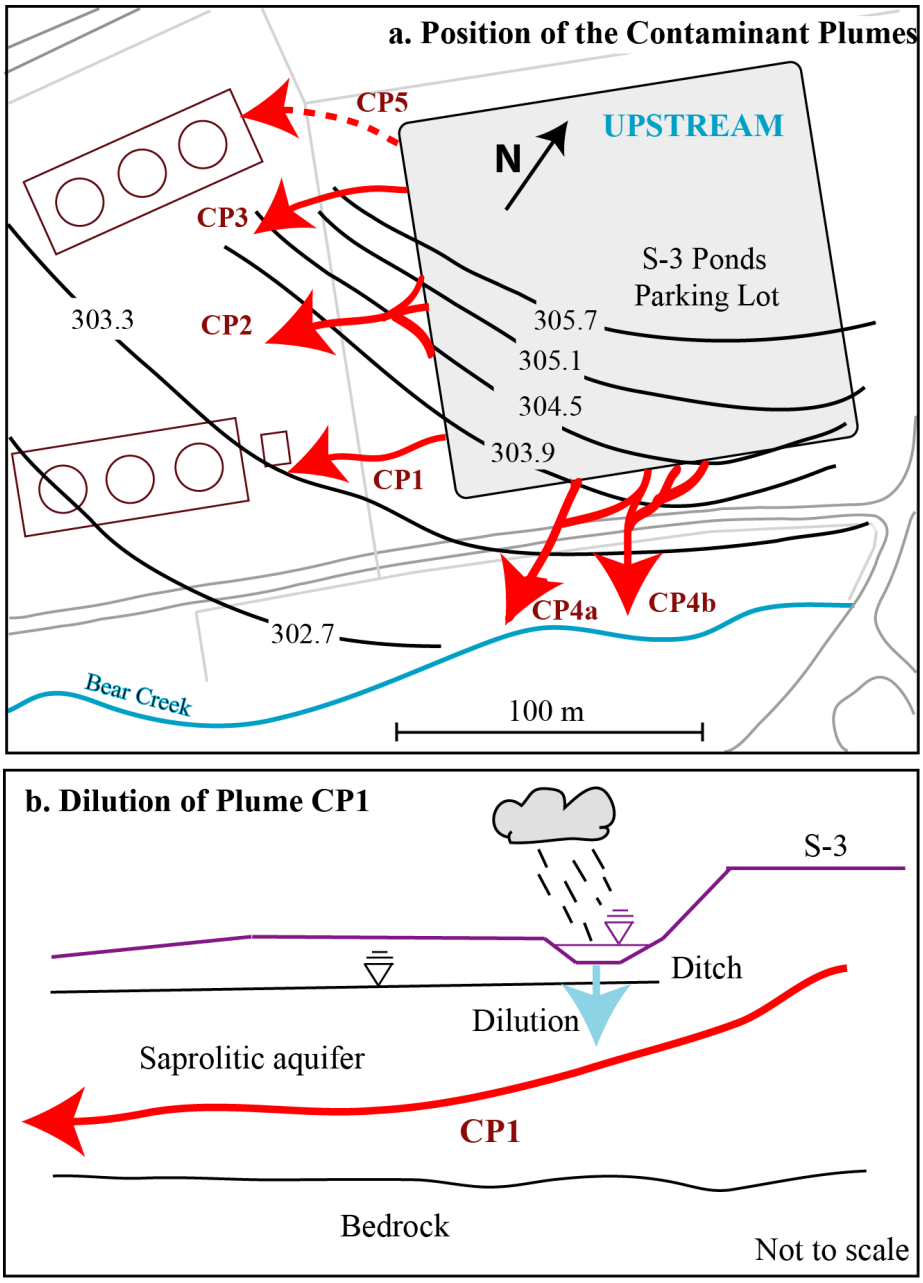

Figure 9. Geometry of the contaminant plumes. **a.** Horizontal position of the contaminant plumes downstream the S-3 pond. **b.** Contaminant plume CP2 breaks into two plumes, one descending along a fault zone into the bedrock. The ditch is also recharging the saprolitic aquifer and influence the nitrate concentration of the contaminant plume CP1.

We also applied our model to time-lapse resistivity data collected downstream, south of the former S-3 disposal pond during the period 11/06/2008 to 01/31/2009 (see position Figure 10a and Kowalsky et al., 2011, and Gasperikova et al., 2012 for further details). The direction of the two contaminants plumes CP1 and CP2 (intersecting the resistivity profile) is south west because of the strong anisotropy of the formation and

the topography of the aquifer-substratum interface while the head gradient is from north to south. Fall 2008 was characterized by strong rain events (Figure 10b). As the result, the ditch surrounding the S-3 pond was partially filled with water in its southern portion and meteoritic water infiltrated the perched aquifer (see Figure 7). In this section, we analyze the time-lapse resistivity data collected during this period using a recently developed method, the Active Time Constrained approach (ATC,, Karoulis et al., 2011a, b). This time-lapse inversion is used to see how the infiltration event of fresh water was recorded in the resistivity time-series and how the model described in Section 3 and validated in Section 4 above can be used to interpret these data.

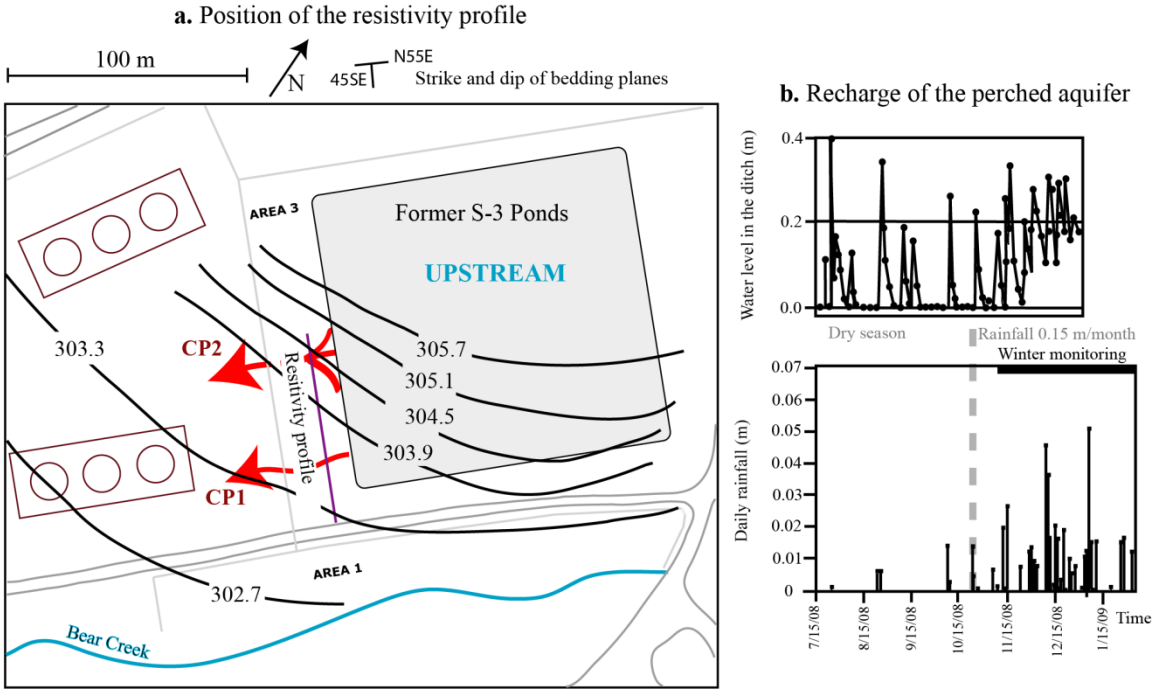

Figure 10. Position of the resistivity profile downstream the former S-3 disposal ponds. **a.** Sketch showing the position of the former disposal ponds, the piezometric lever in the saprolitic aquifer (in meters above sea level), and the position of the plumes CP1 and CP2. **b.** Water level in the ditch surround the former S-3 basins and daily rainfalls showing the recharge of the perched aquifer at the end of 2008. Note that the flow direction is controlled by the fractures along the bedding planes. So the flow is parallel to the bedding planes or strike.

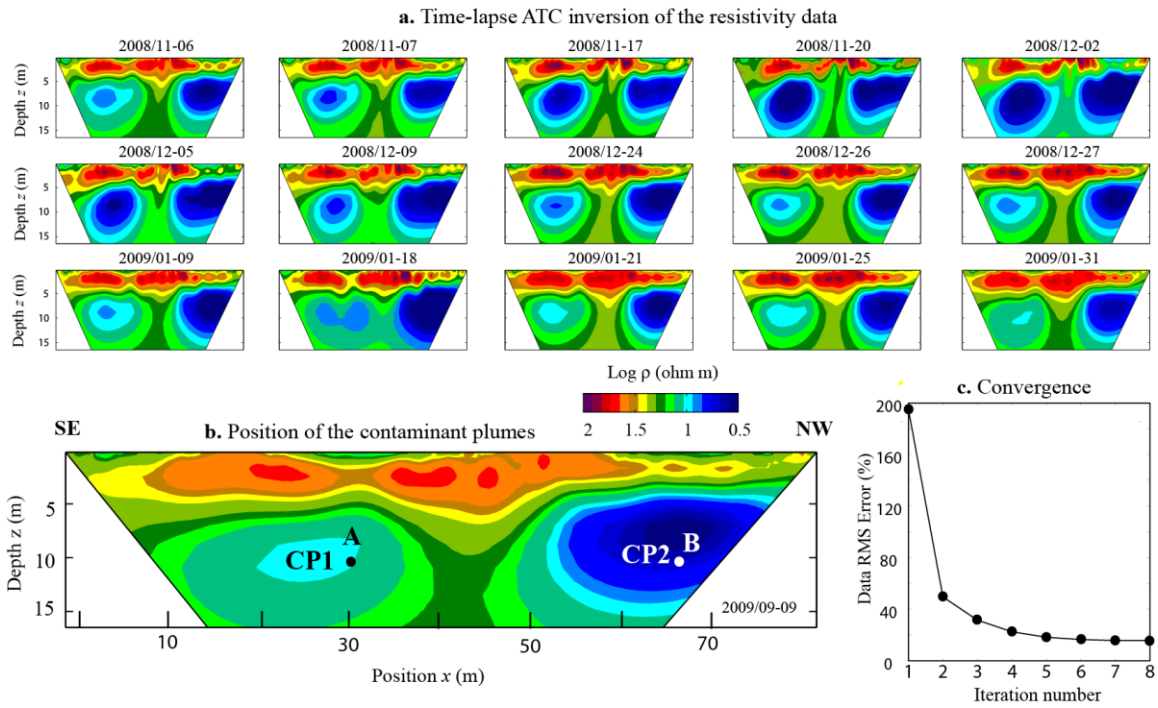

Figure 11. Time lapse tomography based on the Active Time Constrain (ATC) approach. **a.** Results of the time lapse inversion for a profile located in Area 3 (see Figure 1c). **b.** Analysis of a tomogram showing the position of the plumes CP1 and CP2. **c.** Data RMS Error versus the number of iterations (convergence is reached after 7 iterations).

A total of 15 snapshots of dipole dipole resistivity data were obtained donwstream the former S-3 Ponds on a portion of Profile P1. Each snapshot comprises 2568 measurements. The inversion of the data was performed by using the code developed by Karaoulis et al. (2011a, b). The results of the inversion are shown in Figure 11a. Inversion converged after 7 iterations with a data RMS misfit of 15% (Figure 11b). The inverted tomograms show the position of both the CP1 plume (characterized by low nitrate and high uranium concentrations) and the CP2 plume (characterized by high nitrate and low uranium concentrations).

In Figure 12, we show the time series for points A and B located in plumes CP1 and CP2, respectively (see Figure 11a). According to the time lapse resistivity tomograms, the main change in resistivity occurs in the plume CP1, which means that the mixing between the infiltrated water and the original water from the CP1 plume occurs upstream (with respect to the position of the resistivity profile) between the source (the former S-3 disposal ponds) and the position of the resistivity profile. The time-lapse resistivity variations shown in Figure 17a seem to exclude a direct infiltration from the perched aquifer into the deeper portion of the saprolite (the transition zone). Indeed, a gradual infiltration should show a gradual change in the resistivity from the top to the deeper portions of the saprolite over time. Instead we see only changes in the plume CP1 at the depth of the transition zone. This may therefore indicates that the mixing between the fresh water and the contaminated water occurs upstream with respect to the position of the resistivity profile.

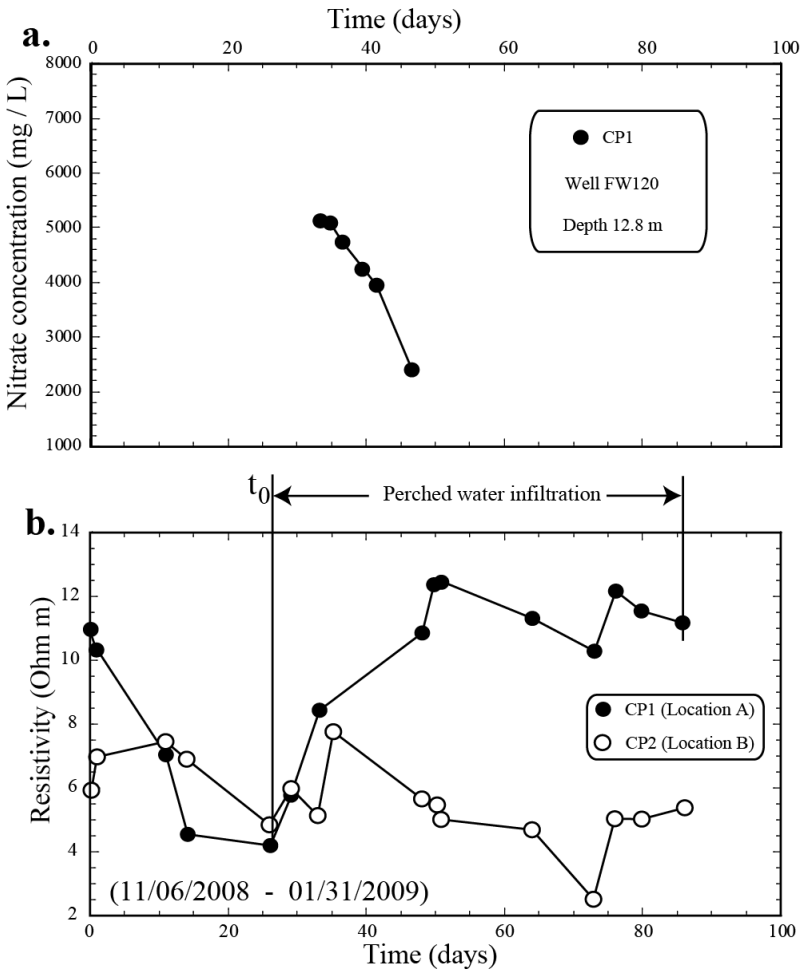

Figure 12. Change of the nitrate concentration and resistivity versus time. **a.** Change of nitrate concentration in Well FW120 at a depth of 13.2 m. **b.** Field data: Change of resistivity at points A and B (plumes CP1 and CP2) over time. In plume CP1, we see a consistent increase of the resistivity after Day 26 and corresponding therefore to a dilution of the CP1 plume by the infiltration of fresh water from the perched aquifer. Locations A and B are shown in Figure 11.

Before discussing a conceptual model of mixing of the fresh and contaminated waters, we point out that the results displayed by the resistivity tomograms agree with some available and limited in situ observations during this time period. Indeed, Figure 12a shows the dilution of the nitrate plume in Well FW120 during this period. Figure 13 shows that the dilution of the contaminant plume followed an exponential relationship as observed in our column experiment (see Revil et al., 2013b).

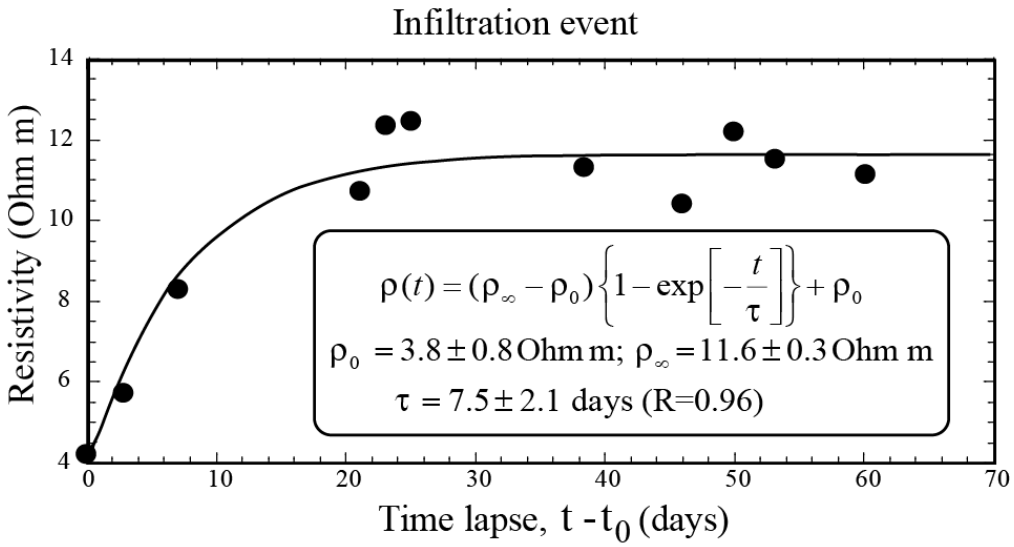

Figure 13. Field data: fit of an exponential relationship to the in situ resistivity data after Day 26. The relaxation time associated with the resistivity change is 7.5 days. This can be compared with a relaxation time of 19.4 days for the laboratory experiment, indicating that the timing of the laboratory column experiment is on the same magnitude as field changes.

As mentioned above our model indicates that the mixing between the fresh and contaminated water occurs in between the position of the resistivity profile and the position of the former S-3 ponds. As shown in Figure 14, this area is the setting of the ditch surrounding the former S-3 basins. We think therefore that the ditch plays a major role in the infiltration of the meteoric water and its mixing with the CP1 plume. Indeed, as explained above, the south corner of the ditch surrounding the S-3 basins has the lowest altitudes and therefore is an area where water accumulates preferentially after storms and rainfalls. This may explain why there is some infiltration and mixing for the CP1 plume and not for the CP2 plume. The conceptual model sketched in Figure 14 implies that the fresh water and the contaminated water mixed just below the ditch. The next question to address is how much fresh water mixed with the contaminated water.

In Revil et al. (2013b), we determined how much fresh water mixes with contaminated water in plume CP1. According to our resistivity model (transforming the resistivity into nitrate concentration using a correction for the surface conductivity), the nitrate concentration of the CP1 plume is 33,000 mg L^{-1} in absence of mixing with the fresh water and 11,500 mg L^{-1} during steady state infiltration of the fresh water. The concentration of nitrate in the fresh aquifer is 0 mg L^{-1}. We can therefore compute how much water from the perched aquifer mixes with the contaminated water from the source of the CP1 plume. During mixing, the nitrate concentration in the mixed pore water $C(\mathrm{NO_3}, \mathrm{mix})$ is given by $C(\mathrm{NO_3}, \mathrm{mix}) = \chi C(\mathrm{NO_3}, \mathrm{CP1})$ where $C(\mathrm{NO_3}, \mathrm{CP1})$ denotes the concentration in the CP1 plume in absence of infiltration from the ditch or the perched aquifer (33,000 mg L^{-1}). It follows, $\chi \approx C(\mathrm{NO_3}, \mathrm{mix}) / C(\mathrm{NO_3}, \mathrm{CP1}) \approx 0.35$. Therefore during the steady state infiltration into the CP1 plume, the pore water is a mix of one third of the original pore water from the heavily contaminated sediment located beneath the former S-3 pond and two thirds of fresh water possibly infiltrating the aquifer from the ditch. With the conceptual model proposed in Figure 14 and the amount of mixing allowed by the infiltration of the fresh water and contaminated water, we can test our model with respect to the resistivity data to see if it is compatible with the properties of the aquifer. We use therefore exactly the type of 1D model used for the column experiment. Initially, contaminated water flows in the CP1

plume. At a certain time, this water is replaced by a mix of one third of the original pore water from the S-3 pond and two thirds of fresh water infiltrating from the ditch. We use a conductivity equation developed in Revil et al. (2013b) to fit the time-lapse resistivity data in the plume CP1 (located in the transition zone) using the velocity of the pore water determined from the head gradient in the aquifer (0.02) and the permeability of the aquifer . The data are fitted with a Peclet number of 2.3 (Figure 15a) pretty close to the one determined in the flow through experiment (Pe=3.5).

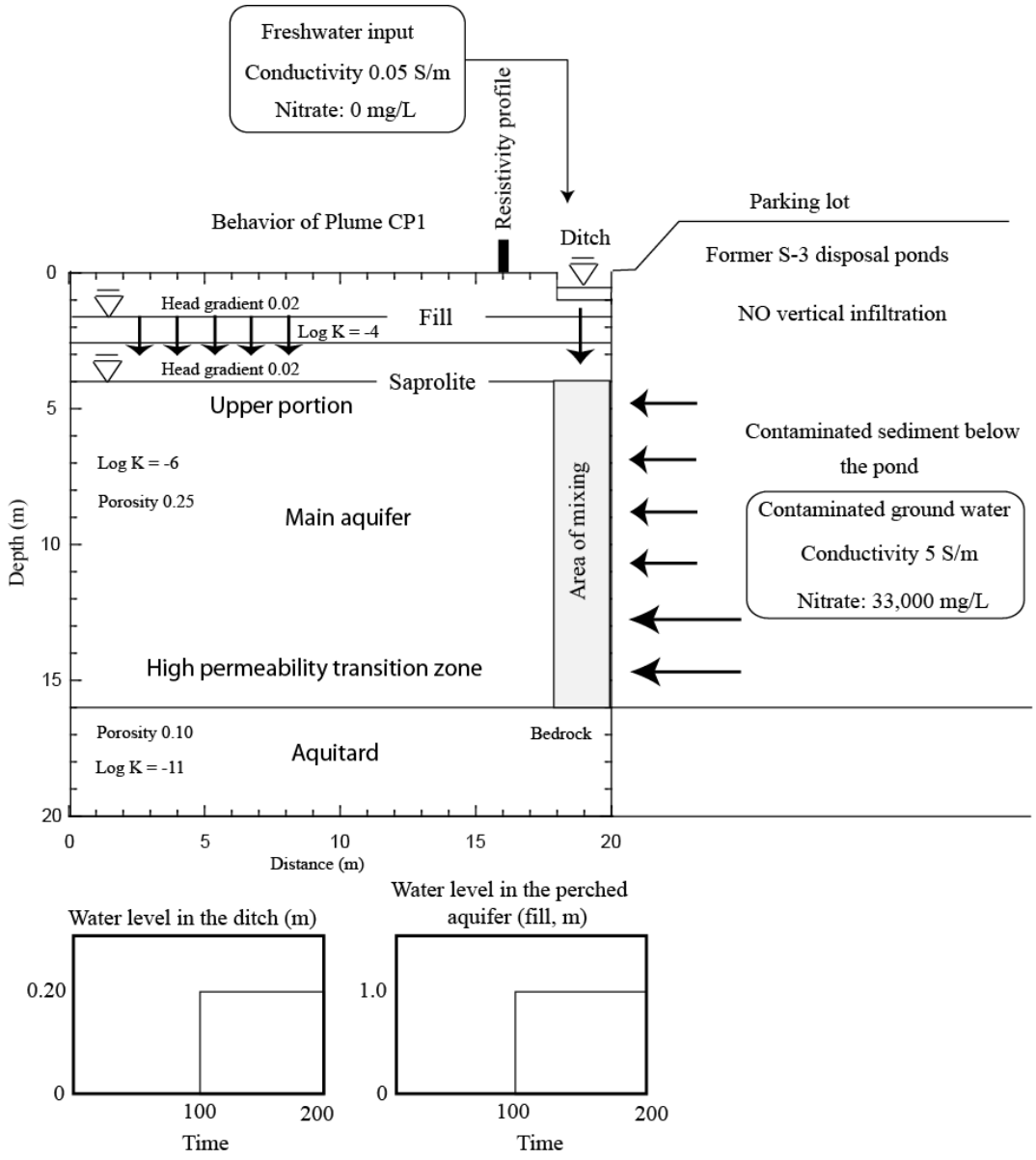

Figure 14. Conceptual model of infiltration in the plume CP1. The ponds are capped with a multilayer cap so there is minimal leaching from above. There is a huge reservoir of contaminants in the saprolite and rock matrix beneath the former disposal ponds and resulting from contamination between 1951 and 1983. The flow of groundwater through the underlying contaminated materials is responsible for the plumes found downstream in the strike direction. Possibly there is a mixing of this contaminated water with fresh water infiltrating the saprolite from the southern portion of the ditch.

In Figure 15b, we predict the variation of the nitrate concentration versus time in plume CP1 showing the transition from 33,000 mg L^{-1} to about 11,000 mg L^{-1}. The addition of complex conductivity data (through frequency-domain or time-domain induced polarization measurements) could be used to assess also the variation of the pH of the pore water versus time during such an infiltration event.

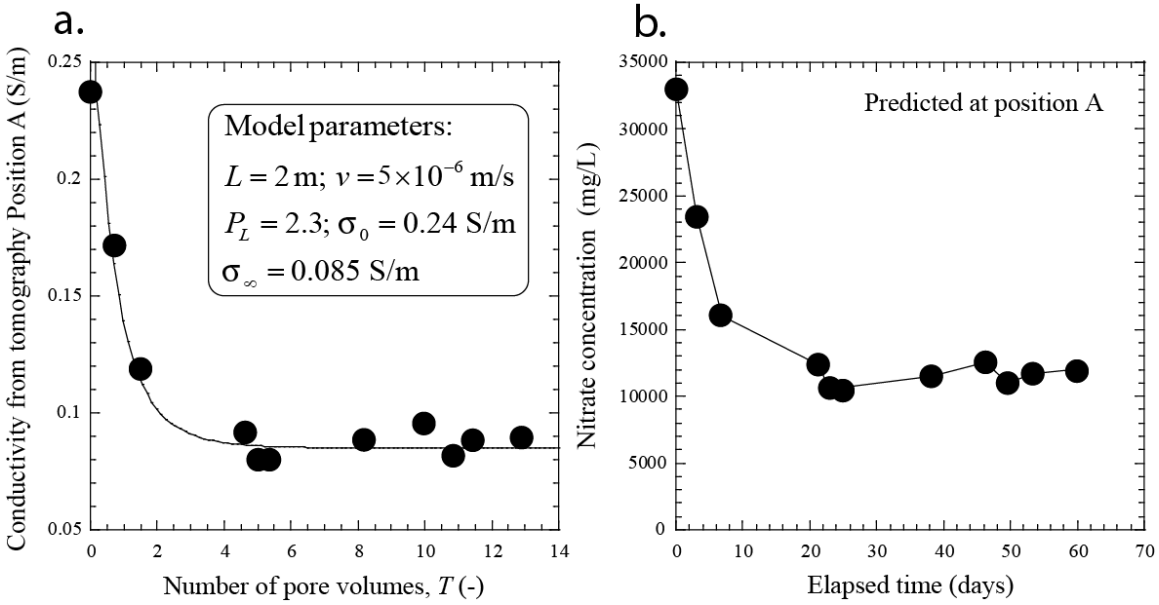

Figure 15. Analysis of the field data. **a.** Modeling of the conductivity data in terms of Peclet number, mean pore water velocity at a depth of 10 m (plume CP1, position A, see Figures 10 and 11). The conductivities σ_0 and σ_∞ denote the conductivity of the aquifer at the beginning and end of the infiltration event. We analysis is performed according to the conceptual model shown in Figure 14. **b.** Predicted evolution of the nitrate concentration during the infiltration event.

3. Conclusions

Our proposed project brought together a multidisciplinary research team that was needed to perform this project. This included some expertise in inversion methodologies of electrical methods (time-lapse resistivity, self-potential, and induced polarization data), reactive transport modeling, and geophysical investigations at the ORNL IFC. The project has focused on exploring the utility of geophysical methods for remotely tracking biogeochemical transformations associated with active biostimulation treatments (e.g., Kowalsky et al., 2011; Gasperikova et al., 2012). Through advancing our understanding of the responses of geoelectrical approach to datasets collected at the ORNL IFC, this

project also complemented the existing geophysical monitoring being performed as part of the funded DOE ORNL IFC project.

We have developed a unified theory of self-potential signals including all the components: streaming current, diffusion current, thermoelectric effect, and the biogeobettery effect. In parallel, we have developed a good understand of low-frequency induced polarization phenomena is non-metallic porous media. These models have been validated though laboratory experiments, including with samples of saprolite from the Oak Ridge IFRC site. All these data have been published in the peer-reviewed literature. We have also performed a flow-though experiment to understand the effect of the recharge with fresh water on the evolution of the contamination of a core sampled from one of the contamination plume of the Oak Ridge IFRC site.

We have developed new algorithms to perform time-lapse inversion of geophysical data. These algorithms fall into two categories: deterministic algorithms based on Tikhonov regularization and stochastic algorithm based on the use of Markov Chain Monte Carlo samplers. In the first case, we have developed new algorithms for the time lapse problem including an active time constrain approach that proved to be superior to the sequential inversion traditionally used in geophysics. In the second case, we have combined the Adaptative Metropolis Algorithm to the Pilot Point Method to perform fully coupled inversion of geophysical and in situ measurements. This approach is very powerful in determining the properties of aquifers (for instance mapping the permeability and therefore the preferential flow pathways).

Regarding the Oak Ridge IFRC site itself, we have developed both laboratory and field measurements to determine the physical properties of the saprolites and to map the position of the diffeernt contaminant plumes and to understand their dynamics associated with the infiltration of meteoritic water in the saprolitic aquifer. The laboratory measurements have included both measurements on clean core samples from the background site and a flow through experiment on a saprolitic column from one of the main contaminant plume associated with the former S-3 settling basins. The field measurements have included self-potential data, 3D resistivity tomography, and 2D time-domain induced polarization spectra. In addition, we have analyzed 2D time-lapse resistivity tomography performed in the framework of the DOE ORNL IFC project. These data have allow to understand the geometry of the various contaminant plumes and their dynamics in terms of rain water infiltration.

4. Published papers with their abstracts

This section list all the papers published in the course of this project and submitted with their abstracts. Project DOE; BER, DE-FG02-08ER646559. The papers that are not yet published are reproduced in the appendices at the end of the report (Appendix A to D).

[1] **Revil A**., C.A. Mendonça, E. Atekwana, B. Kulessa, **S.S. Hubbard**, and K. Bolhen, Understanding biogeobatteries: where geophysics meets microbiology, Journal of Geophysical Research, 115, G00G02, doi:10.1029/2009JG001065, 2010. Abstract. Although recent research suggests that contaminant plumes behave as geobatteries that produce an electrical current in the ground, no associated model exists that honors both geophysical and biogeochemical constraints. Here, we develop such a model to explain the two main electrochemical contributions to self-potential signals in contaminated areas. Both contributions are associated with the gradient of the activity of two types of charge carriers, ions and electrons. In the case of electrons, bacteria act as catalysts for reducing the activation energy needed to exchange the electrons between electron donor and electron acceptor. Possible mechanisms that facilitate electron migration include iron oxides, clays, and conductive biological materials, such as bacterial conductive pili or other conductive extracellular polymeric substances. Because we explicitly consider the role of biotic processes in the geobattery model, we coined the term "biogeobattery". After theoretical development of the biogeobattery model, we compare model predictions with self-potential responses associated with laboratory and field-scale experiments conducted in contaminated environments. We demonstrate that the amplitude and polarity of large (>100 mV) self-potential signatures require the presence of an electronic conductor to serve as a bridge between electron donors and acceptors. Small self-potential anomalies imply that electron donors and electron acceptors are not directly interconnected, but instead result simply from the gradient of the activity of the ionic species that are present in the system.

[2] **Revil A.**, and N. Florsch, Determination of permeability from spectral induced polarization data in granular media, Geophysical Journal International, 181, 1480-1498, doi: 10.1111/j.1365-246X.2010.04573.x, 2010. Abstract. Surface conductivity of porous rocks has two contributions: the first is associated with the diffuse layer coating the grains and is frequency independent as long as the diffuse layer is above a percolation threshold. The second contribution is associated with the Stern layer of weakly sorbed counterions on the mineral surface and is frequency dependent if the Stern layer is discontinuous at the scale of the representative elementary volume. In the frequency range 1 mHz-100 Hz, this second contribution is also associated with the main polarization mechanism observed by the spectral induced polarization method in granular media (neglecting the contribution of other polarization processes like those associated with redox processes and membrane polarization). At the macroscale, we connect the Stern layer contribution to the complex conductivity to the expectation of the probability distribution of the inverse of the grain size. This is done by performing a convolution between the probability distribution of the inverse of the grain size and the surface conductivity response obtained when all the grains have the same size. Surface conductivity at the macroscopic scale is also connected to an effective pore size used to characterize permeability. From these relationships, a new equation is derived connecting this effective pore size, the electrical formation factor, and the expected value of the probability distribution for the inverse of the grain size, which is in turn related to the distribution of the relaxation times. These new

relationships are consistent with various formula derived in the literature in the limit where the grain size distribution is given by the delta function or a log normal distribution and agree fairly well with various experimental data showing also some limitations of the induced polarization method to infer permeability. One of them is the difficulty to detect the polarization in the phase associated with the smaller grains as this polarization may be hidden by the Maxwell-Wagner polarization at relatively high frequencies (>100 Hz). Also cemented aggregates of grains can behave as coarser grains.

[3] **Revil, A.,** and A. Jardani, Stochastic inversion of permeability and dispersivities from time lapse self-potential measurements: A controlled sandbox study, Geophys. Res. Lett., 37, L11404, doi:10.1029/2010GL043257, 2010. Abstract. We test the ability of the self-potential method to provide information that can be used to invert the permeability and the dispersivities of a porous material.We first formulate the semi-coupled system of equations describing the occurrence of self-potential signals associated with the transport of salt in a porous material like sand. Two contributions in the source current density arise from the electrokinetic coupling associated with the flow of the pore water and the diffusion potential due to the gradient in the activity of the salt. A controlled laboratory sandbox experiment is performed to show that time-lapse self-potential measurements can be used to invert, in a Bayesian framework, the permeability and dispersivities.

[4] Martínez-Pagán P., A. Jardani, **A. Revil**, and A. Haas, Self-potential monitoring of a salt plume, Geophysics, 75(4), WA17–WA25, doi: 10.1190/1.3475533, 2010. Abstract: Monitoring non-intrusively the spread of contaminants in real time with a geophysical method is an important task in hydrogeophysics. We have developed a sandbox experiment showing that the self-potential method is able to locate both the source of leakage and the front of a contaminant plume. We monitored the leakage of a plume of salty water from a hole at the bottom of a small tank located at the top of a main sandbox. The sand was initially saturated by tap water. At a given time, a hole was open at the bottom of the tank allowing the salty water to migrate by diffusion and buoyancy-driven flow in the main sandbox. The bottom of the sandbox contained a network of 32 non-polarizing silver-silver chloride electrodes with amplifiers and connected to a multichannel voltmeter. The self-potential response associated with the migration of the salt plume in the sandbox was recorded over time. A self-potential anomaly was observed with an amplitude varying from few millivolts at the start of the leak to few tens of millivolts after few minutes. The self-potential data were inverted using a time-lapse tomographic algorithm in order to reconstruct the position of the volumetric source current density over time. A positive volumetric source current density was associated with the position of the leak at the bottom of the leaking tank while a negative volumetric source current density was associated with the salinity front moving down inside the sandbox. These poles were well reproduced by performing a finite element simulation of the problem. Using this information, we estimated the speed of the salt plume sinking inside the sandbox. Therefore the self-potential method can be used to track, in real time, the position of the front of a contaminant plume in a porous material.

[5] **Revil A.**, and M. Skold, Salinity dependence of spectral induced polarization in sands and sandstones, Geophysical Journal International, **187,** 813–824, doi: 10.1111/j.1365-246X.2011.05181.x, 2011. Abstract: In electrolyte-saturated sands, the reversible storage of electrical charges is responsible for a phase lag between the current (injected and retrieved by two current electrodes) and the electrical field recorded by two voltage electrodes. This phenomenon is called "spectral induced polarization" (SIP) in geophysics and can potentially be used to monitor salt

tracer tests in shallow aquifers in order to infer their permeability and dispersivity tensors. We demonstrate analytically that the polarization of the inner part of the electrical triple layer coating the surface of the grains (named the Stern layer in electrochemistry) is consistent with available data. We also perform new experiments using silica sands saturated by NaCl and $CaCl_2$ pore water solutions. The salinity dependence of quadrature conductivity can be modelled using an analytical solution of the triple layer model, which offers a simple way to interpret laboratory and field data. This analytical solution depends on the total site density of the mineral surface, the pH value, and the sorption coefficient of the cation in the Stern layer. This model shows that both the specific surface conductivity of the Stern layer and the quadrature conductivity of the porous material depend on the conductivity of the pore water. The quadrature conductivity is becoming independent of the salinity above 1 S m^{-1}. The parameters entering the analytical model are consistent with independent estimates from titration data and zeta potential measurements, which are two classical methods to characterize the electrical triple layer at the pore water mineral interface.

[6] **Revil, A.,** W.F. Woodruff, and N. Lu, Constitutive equations for coupled flows in clay materials, Water Resources Research, 47, W05548, doi:10.1029/2010WR010002, 2011. Abstract. We first upscale the local transport (Stokes and Nernst-Planck) equations to the scale of a single capillary saturated by a binary 1:1 electrolyte. These equations are then upscaled to the scale of a network of tortuous capillaries embedded in a homogeneous and continuous mineral matrix, including the influence of the distribution of pore sizes but excluding the effect of connectivity between the pores. One of the features of our theory is to account for transport along the mineral surface in the so-called Stern layer, because of recent evidences for this mechanism to be effective in describing frequency-dependent electrical conductivity. Real clay materials are however not described by a set of capillaries so we have to modify the model to include the effect of transversal dispersivity for instance. We found no evidence for transport in the Stern layer because of the discontinuity of the solid phase at the scale of a representative elementary volume in clay materials. The effect of the diffuse layer is accounted for through the use of a Donnan equilibrium approach to determine the effective concentrations of the ions in the pore space, which are different from the ionic concentrations of an ionic reservoir in local equilibrium with the porous material. We found that the diffuse layer controls various transport properties, including, for instance, the DC-electrical conductivity, the osmotic efficiency coefficient, the streaming potential coupling coefficient, and the macroscopic Hittorf numbers. Comparison to a large dataset of experimental data, mainly on clay materials, confirms the validity of the derived relationships used to describe the material properties entering into the constitutive equations.

[7] Karaoulis M., **A. Revil**, D.D. Werkema, B. Minsley, W.F. Woodruff, and A. Kemna, Time-lapse 3D inversion of complex conductivity data using an active time constrained (ATC) approach, Geophysical Journal International, 187, 237–251, doi: 10.1111/j.1365-246X.2011.05156.x, 2011. Abstract. Induced polarization (more precisely the magnitude and the phase of the impedance of the subsurface) is measured using a network of electrodes located at the ground surface or in boreholes. This method yields important information related to the distribution of permeability and contaminants in the shallow subsurface. We propose a new time-lapse 3D modeling and inversion algorithm to image the evolution of complex conductivity over time. We discretize the subsurface using hexahedronal cells. Each cell is assigned a complex resistivity or conductivity value. Using the finite-element approach, we model the in-phase and out-of-phase (quadrature) electrical potentials on the 3D grid, which are then transformed into apparent complex resistivity. Inhomogeneous Dirichlet

boundary conditions are used at the boundary of the domain. The calculation of the Jacobian matrix is based on the principles of reciprocity. The goal of time-lapse inversion is to determine the change in the complex resistivity of each cell of the spatial grid as a function of time. Each model along the time axis is called a "reference space model". This approach can be simplified into an inverse problem looking for the optimum of several reference space models using the approximation that the material properties vary linearly in time between two subsequent reference models. Regularizations in both space domain and time domain reduce inversion artifacts and improve the stability of the inversion problem. In addition, the use of the time-lapse equations allows the simultaneous inversion of data obtained at different times in just one inversion step (4D inversion). The advantages of this new inversion algorithm are demonstrated on synthetic time-lapse data resulting from the simulation of a salt tracer test in an heterogeneous random material described by an anisotropic semi-variogram.

[8] **Revil, A.,** Spectral induced polarization of shaly sands: Influence of the electrical double layer, Water Resour. Res., 48, W02517, doi:10.1029/2011WR011260, 2012. **Abstract.** I develop a new model named POLARIS describing the complex conductivity of (pyrite-free) shaly poorly-sorted sands. This model is based on the solution given by the effective medium theory for grains coated by an electrical double layer and immersed in a background electrolyte. The electrical double layer comprises the Stern layer and the diffuse layer. Both layers play very distinct roles in the in-phase and quadrature conductivities. The polarization of the shaly sands is mainly controlled by the polarization of the Stern layer (except at very high salinities) with a very small mobility of the counterions contained in this layer. The in-phase component of the conductivity is controlled by the conductivity of the pore water with a contribution associated with the diffuse layer (the contribution of the Stern layer seems negligible). The fraction of counterions in the Stern layer is computed from a simple sorption isotherm and is used to infer the quadrature conductivity. The quadrature conductivity is assumed to be frequency-independent, which is a reasonable approximation in clayey sands and sandstones in agreement with observations. The polarization model is also based on the assumption that the Stern layer is discontinuous between grains, an assumption that is consistent with recent models of ionic transport in clayey sands. POLARIS explains the dependence of the quadrature conductivity on the salinity, cation exchange capacity, specific surface area (or specific surface per unit pore volume), and temperature. It can be used to predict the saturation and the permeability (inside one order of magnitude).

[9] Ikard, S. J., **A. Revil**, A. Jardani, W. F. Woodruff, M. Parekh, and M. Mooney, Saline pulse test monitoring with the self-potential method to nonintrusively determine the velocity of the pore water in leaking areas of earth dams and embankments, Water Resour. Res., 48, W04201, doi:10.1029/2010WR010247, 2012. Abstract**.** A method is proposed to localize preferential fluid flow pathways in porous media based on time-lapse self-potential measurements associated with salt tracer injection upstream. This method is first tested using laboratory data. A network of non-polarizing electrodes located is connected to a highly sensitive voltmeter used to record the resulting electrical field fluctuations occurring over time at the surface of the tank. The transport of the conductive salt plume through the permeable porous materials changes the localized streaming potential coupling coefficient associated with the advective drag of the excess of charge of the pore water and is also responsible for a diffusion current associated with the salinity gradient. Monitoring of the electrical potential distribution at the ground surface can be used to localize the pulse of saline water over time, and to determine its velocity. This method applies in real time and can be used to track highly localized flow pathways characterized by high permeability. Our sandbox experiment

demonstrates the applicability of this new method under well-controlled conditions with a coarse sand channel embedded between fine-sand banks. A finite element model allows to reproduce the time-lapse electrical potential distribution over the channel, but some discrepancies were observed on the banks. Finally, we performed a numerical simulation for a synthetic case study inspired by a recently published field case study. A Markov-chain Monte Carlo (McMC) sampler is used to determine the permeability and the porosity of the preferential fluid flow pathway of this synthetic case study.

[10] Risgaard-Petersen N., **A. Revil**, P. Meister, and L.P. Nielsen, Sulfur, iron-, and calcium cycling associated with natural electric currents running through marine sediment, Geochimica et Cosmochimica Acta 92, 1–13, 2012. Abstract. Anaerobic oxidation of organic matter in marine sediment is traditionally considered to be coupled to oxygen reduction via a cascade of redox processes and transport of intermittent electron donors and acceptors. Long distance electron transmission (LDET) has recently been shown to shortcut this cascade and directly couple oxygen reduction at the surface to sulphide oxidation in deeper anoxic layers. Here we show that spatial separation of oxidation and reduction processes in marine sediment causes non-conventional sulphur, iron, and calcium cycling. Reduced sediment was incubated with overlying oxic water and the vertical distribution of solutes and solids analysed 45 days later. As much as 44% of sediment oxygen consumption proved to be mediated by LDET, and electrogenic oxidation of sulphide to sulphate resulted in significant dissolution of iron sulphides and calcium carbonates in the anoxic layers of the sediment. Most of the mobilised iron diffused to the oxic zone where it formed oxidised iron minerals. Calcium precipitated out in the oxic zone as magnesium-calcite. In marine sediment, LDET thus generates unique chemical conditions whereby key minerals are mobilised and relocated, probably along with trace elements and nutrients. We suggest that LDET flourishes in marine sediments after transient oxygen depletion, leaving distinct signatures of such events in the geological record.

[11] **A. Revil**, **Skold M**., **S. S. Hubbard, Y. Wu, D. B. Watson**, and M. Karaoulis, Petrophysical properties of saprolite from the Oak Ridge Integrated Field Research Challenge site, Tennessee, in press in Geophysics, 2013a. **Abstract.** At the Oak Ridge National Laboratory, weathering of shales and limestones has produced saprolite, which composes the shallow aquifer. This aquifer is contaminated by nitric acid, uranium and metals originating from the former S3 settling ponds. In order to interpret low frequency geophysical methods used to image contaminant plumes, we have characterized the petrophysical properties of 3 saprolite core samples. The hydraulic conductivity of the core samples ranges from 10^{-7} to 10^{-6} m s^{-1} in agreement with field data. We have performed complex conductivity measurements in the frequency range 1 mHz-45kHz with NaCl solutions as pore water with electrical conductivities in the range 5×10^{-3} S m^{-1} to 2.35 S m^{-1}. The electrical conductivity data are well reproduced using a simple linear conductivity model between the saprolite conductivity and the pore water conductivity. The conductivity plots were used to estimate the formation factor (hence with porosity the cementation exponent, m = 1.6±0.1) and the surface conductivity (in the range 0.007- 0.030 S m^{-1}). The magnitude of the surface conductivity depends on the degree of weathering and therefore on the amount of smectite and mixed layer (illite-smectite) clays. The chargeability of one of the core samples is in the range 20-800 mV V^{-1} and is strongly dependent on the salinity. We also performed streaming potential measurements with the same pore fluid composition than used for the complex conductivity measurements. We found an excess of moveable electrical charges on the order of 100 to 500 C m^{-3} in agreement with previous

investigations connecting the moveable charge density to permeability. The zeta potential is in the range -10 to -20 mV independent of the NaCl concentration. The electrical measurements are consistent with an average CEC of 10.5 cmol kg^{-1} and a specific surface area on the order of 30 m^2 g^{-1}.

[12] **Revil A.**, M. Skold, M. Karaoulis, M. Schmutz, **S. S. Hubbard**, T.L. Mehlhorn, and **D. B. Watson**, Hydrogeophysical investigations of the S-3 ponds contaminant plumes, Oak Ridge Integrated Field Research Challenge site, Tennessee, accepted with revision in Geophysics, 2013b. Abstract. At the Oak Ridge Integrated Field Research Challenge (IFRC) site, near Oak Ridge, Tennessee, contaminants (including nitrate, uranium, technetium, strontium, mercury and cadmium) from the former S-3 ponds have infiltrated a shallow saprolitic aquifer for over 60 years aquifer and pose a threat to the local ecosystem. DC-resistivity survey is used to find the number and location of the main contaminant plumes. We identified a total of 5 main plumes (CP1 to CP5). The plume CP2 corresponds to the main plume in terms of nitrate concentration (~50,000 mg L^{-1}). These contaminant plumes have typically an electrical resistivity in the range 2 to 20 ohm m while the background saprolite resistivity is in the range 60 to 120 ohm m, so the difference of resistivity can be easily mapped using DC-resistivity tomography to locate the contaminant pathways. The flow paths associated with these plumes are controlled not only by the local head gradient but also by the geometry of the bedrock / saprolitic aquifer. We develop relationships to derive the in situ nitrate concentrations from the 3D resistivity tomograms. For the contaminant plumes CP1 and CP2, we use a recently developed time-lapse resistivity approach, the Active Time Constrained (CPA) approach, to investigate the variation of resistivity over time of plumes CP1 and CP2. Self-potential data shows the existence of a strong bipolar anomaly (about 400 mV peak to peak) possibly associated the presence of a gradient of the redox potential in the saprolitic aquifer.

[13] **Revil A**., Y. Wu, M. Karaoulis, **S. S. Hubbard**, and **D. B. Watson**, Geochemical and geophysical responses during shallow perched water infiltration into contaminated saprolite from the Oak Ridge Integrated Field Research Challenge site, Tennessee, submitted to Water Resources Research. Abstract. At the Oak Ridge Integrated Field Research Challenge (IFRC) site, near Oak Ridge, Tennessee, the saprolitic aquifer is contaminated by leakages from the former S-3 settling ponds. The chemistry of the contaminant plume is episodically impacted by fresh meteoritic water infiltrating from a shallow perched aquifer. We performed a column experiment to understand the geochemical and complex conductivity signatures associated with such events. The changes in the pH and pore water conductivity are responsible for measurable changes in both the in-phase and quadrature conductivities of the saprolite. The pore water conductivity can be related to the nitrate concentration (the dominating ionic species in the plume) and the release of uranium is strongly controlled by the pH. We developed a simple model to determine the pore water conductivity and pH from the recorded complex conductivity. This model is applied to time-lapse resistivity data at the IFRC site. Time-lapse inversion of resistivity data shows clearly an infiltration event during the winter of 2008-2009 with a dilution of the pore water chemistry and an increase of the pH.

[14] **Revil A.,** J.D. Eppehimer, **M. Skold**, M. Karaoulis, L. Godinez, and M. Prasad, Low-frequency complex conductivity of sandy and clayey materials, in press in Journal of Colloid Interface Science, 2013d. Abstract: Low-frequency polarization of sands and sandstones seem to be dominated by the polarization of the Stern layer, the inner part of the electrical double layer coating the surface of the silica grains and clay particles. We investigate a simple model of Stern layer polarization combined

with a simple complexation model of the surface of the grains immersed in a 1:1 electrolyte like NaCl. In isothermal conditions, the resulting model can be used to predict the complex conductivity of clayey materials as a function of the porosity, the cation exchange capacity of the clay fraction (alternatively the specific surface area of the material), and the salinity of the pore water. A new set of experimental data is presented. This dataset comprises low-frequency (1 mHz-45 kHz) complex conductivity measurements of saprolites and sandstones that are well-characterized in terms of their petrophysical properties (porosity, permeability, specific surface area or CEC, and pore size). This dataset, together with incorporating additional data from the literature, is used to test the Stern layer polarization model. We find an excellent agreement between the predictions of this model and this experimental dataset indicating that the new model can be used to predict the complex conductivity of natural clayey materials and clay-free silica sands.

[15] Jardani, A., **A. Revil**, and J.P. Dupont, Stochastic joint inversion of hydrogeophysical data for salt tracer test monitoring and hydraulic conductivity imaging, Advances in Water Resources, 52, 62-77, 2012. Asbtract: The assessment of hydraulic conductivity of heterogeneous aquifers is a difficult task using traditional hydrogeological methods (e.g., steady state or transient pumping tests) due to their low spatial resolution. Geophysical measurements performed at the ground surface and in boreholes provide additional information for increasing the resolution and accuracy of the inverted hydraulic conductivity field. We used a stochastic joint inversion of Direct Current (DC) resistivity and Self-Potential (SP) data plus *in situ* measurement of the salinity in a downstream well during a synthetic salt tracer experiment to reconstruct the hydraulic conductivity field between two wells. The pilot point parameterization was used to avoid over-parameterization of the inverse problem. Bounds on the model parameters were used to promote a consistent Markov chain Monte Carlo sampling of the model parameters. To evaluate the effectiveness of the joint inversion process, we compared 8 cases in which the geophysical data are coupled or not to the *in situ* sampling of the salinity to map the hydraulic conductivity. We first tested the effectiveness of the inversion of each type of data alone (concentration sampling, self-potential, and DC resistivity), and then we combined the data two by two. We finally combined all the data together to show the value of each type of geophysical data in the joint inversion process because of their different sensitivity map. We also investigated a case in which the data were contaminated with noise and the variogram unknown and inverted stochastically. The results of the inversion revealed that incorporating the self-potential data improves the estimate of hydraulic conductivity field especially when the self-potential data were combined to the salt concentration measurement in the second well or to the time-lapse cross-well electrical resistivity data. Various tests were also performed to quantify the uncertainty in the inverted hydraulic conductivity field.

5. Cited References

Gasperikova E., S. S. Hubbard, D. B. Watson, G. S. Baker, J. E., Peterson, M. B. Kowalsky, M. Smith, and S. Brooks, 2012. Long-term electrical resistivity monitoring of recharge-induced contaminant plume behavior: in press in Contaminant Hydrogeology, 2012.

Ikard, S. J., A. Revil, A. Jardani, W. F. Woodruff, M. Parekh, and M. Mooney, Saline pulse test monitoring with the self-potential method to nonintrusively determine the velocity of the pore water in leaking areas of earth dams and embankments, Water Resour. Res., 48, W04201, doi:10.1029/2010WR010247, 2012.

Jardani, A., A. Revil, and J.P. Dupont, Stochastic joint inversion of hydrogeophysical data for salt tracer test monitoring and hydraulic conductivity imaging, Advances in Water Resources, 52, 62-77, 2012.

Karaoulis M., A. Revil, D.D. Werkema, B. Minsley, W.F. Woodruff, and A. Kemna, Time-lapse 3D inversion of complex conductivity data using an active time constrained (ATC) approach, Geophysical Journal International, 187, 237–251, doi: 10.1111/j.1365-246X.2011.05156.x, 2011.

Kowalsky, M. B., E. Gasperikova, S. Finsterle, D. Watson, G. Baker, and S. S. Hubbard, 2011, Coupled modeling of hydrogeochemical and electrical resistivity data for exploring the impact of recharge on subsurface contamination: Water Resources Research, 47, W02509.

Martínez-Pagán P., A. Jardani, A. Revil, and A. Haas, Self-potential monitoring of a salt plume, Geophysics, 75(4), WA17–WA25, doi: 10.1190/1.3475533, 2010.

Naudet, V., A. Revil, J.-Y. Bottero, and P. Bégassat, Relationship between self-potential (SP) signals and redox conditions in contaminated groundwater, *Geophys. Res. Lett*., *30*(21), 2091, doi: 10.1029/2003GL018096, 2003.

Naudet, V., A. Revil, E. Rizzo, J.-Y. Bottero, et P. Bégassat, Groundwater redox conditions and conductivity in a contaminant plume from geoelectrical investigations, *Hydrology and Earth System Sciences (HESS)*, 8(1), 8-22, 2004.

Revil A., C.A. Mendonça, E. Atekwana, B. Kulessa, S.S. Hubbard, and K. Bolhen, Understanding biogeobatteries: where geophysics meets microbiology, Journal of Geophysical Research, 115, G00G02, doi:10.1029/2009JG001065, 2010.

Revil A., and N. Florsch, Determination of permeability from spectral induced polarization data in granular media, Geophysical Journal International, 181, 1480-1498, doi: 10.1111/j.1365-246X.2010.04573.x, 2010.

Revil, A., and A. Jardani, Stochastic inversion of permeability and dispersivities from time lapse self-potential measurements: A controlled sandbox study, Geophys. Res. Lett., 37, L11404, doi:10.1029/2010GL043257, 2010.

Revil A., and M. Skold, Salinity dependence of spectral induced polarization in sands and sandstones, Geophysical Journal International, 187, 813–824, doi: 10.1111/j.1365-246X.2011.05181.x, 2011.

Revil, A., W.F. Woodruff, and N. Lu, Constitutive equations for coupled flows in clay materials, Water Resources Research, 47, W05548, doi:10.1029/2010WR010002, 2011.

Revil, A., Spectral induced polarization of shaly sands: Influence of the electrical double layer, Water Resour. Res., 48, W02517, doi:10.1029/2011WR011260, 2012.

Revil A., Skold M., S. S. Hubbard, Y. Wu, D. B. Watson, and M. Karaoulis, Petrophysical properties of saprolite from the Oak Ridge Integrated Field Research Challenge site, Tennessee, in press in Geophysics, 2013a.

Revil A., M. Skold, M. Karaoulis, M. Schmutz, S. S. Hubbard, T.L. Mehlhorn, and D. B. Watson, Hydrogeophysical investigations of the S-3 ponds contaminant plumes, Oak Ridge Integrated Field Research Challenge site, Tennessee, accepted with revision in Geophysics, 2013b.

Revil A., Y. Wu, M. Karaoulis, S. S. Hubbard, and D. B. Watson, Geochemical and geophysical responses during shallow perched water infiltration into contaminated saprolite from the Oak Ridge Integrated Field Research Challenge site, Tennessee, submitted to Water Resources Research, 2013c.

Revil A., J.D. Eppehimer, M. Skold, M. Karaoulis, L. Godinez, and M. Prasad, Low-frequency complex conductivity of sandy and clayey materials, in press in Journal of Colloid Interface Science, 2013d.

Risgaard-Petersen N., A. Revil, P. Meister, and L.P. Nielsen, Sulfur, iron-, and calcium cycling associated with natural electric currents running through marine sediment, Geochimica et Cosmochimica Acta 92, 1–13, 2012.

Appendix A

Petrophysical properties of saprolites from the Oak Ridge Integrated Field Research Challenge site, Tennessee

Running Head: Electrical properties of saprolites

A. Revil (1, 2), M. Skold (1), S. S. Hubbard (3), Y. Wu (3),

D. B. Watson (4), and M. Karaoulis (1)

(1) Colorado School of Mines, Department of Geophysics, Golden, 80401, CO, USA

(2) ISTerre, CNRS, UMR CNRS 5275, Université de Savoie, 73376 cedex, Le Bourget du Lac, France

(3) Lawrence Berkeley National Laboratory, 1 Cyclotron Road, MS 90R1116, Berkeley, 94720, CA.

(4) Oak Ridge National Laboratory, 1 Bethel Valley Road, MS 6038, Oak Ridge, 37831-6038, TN

Corresponding author: A. Revil (arevil@mines.edu)

Emails: arevil@mines.edu; sshubbard@lbl.gov; watsondb@ornl.gov; mskold@mines.edu;

marios.karaoulis@gmail.com; ywu3@lbl.gov

Accepted for publication in Geophysics

Abstract. At the Oak Ridge Integrated Field Research Challenge (IFRC) site, near Oak Ridge, Tennessee, the shallow saprolitic aquifer is contaminated by nitric acid, uranium, and metals originating from the former S3 settling ponds. In order to interpret low frequency geophysical methods used to image contaminant plumes, we have characterized the petrophysical properties of 3 representative saprolite core samples. Their hydraulic conductivity ranges from 10^{-7} to 10^{-6} m s^{-1} in agreement with field data. Complex conductivity measurements, in the frequency range 1 mHz-45 kHz, were performed with NaCl solutions with electrical conductivities in the range 5×10^{-3} S m^{-1} to 2.35 S m^{-1}, a range representative of field conditions. The electrical conductivity data are well reproduced with a simple linear conductivity model between the saprolite conductivity and the pore water conductivity. The conductivity plots were used to estimate the formation factor (the cementation exponent is about 2.2±0.3) and the surface conductivity (0.007- 0.040 S m^{-1}). The magnitude of the surface conductivity depends on the degree of weathering and therefore on the amount of smectite and mixed layer (illite-smectite) clays present in the saprolite. The chargeability of the core samples is in the range 20-800 mV V^{-1} and is strongly dependent on the salinity. We also performed streaming potential measurements with the same pore fluid composition than used for the complex conductivity measurements. We found an excess of moveable electrical charges on the order of 100 to 500 C m^{-3} in agreement with previous investigations connecting the moveable excess charge density to permeability. The zeta potential is in the range -10 to -20 mV independent on the salinity. The electrical measurements are consistent with an average CEC in the range 1.4 to 11 cmol kg^{-1} and a specific surface area on the order of 4,000 to about 30,000 m^2 kg^{-1}.

Keywords: Electrical properties; Hydrogeophysics; Permeability and porosity.

Introduction

Various geophysical methods have been used to locate contaminant migration at the Oak Ridge Integrated Field Research Challenge (IFRC) site, near Oak Ridge, Tennessee (USA) (Watson et al., 2005; Chen et al., 2006, 2010; Kowalsky et al., 2011; Gasperikova et al., 2012). The IFRC was established as a part of the U.S. Department of Energy (DOE) Subsurface Biogeochemistry Research (SBR) program to evaluate different remediation technologies. The S3 settling basins are located in the Bear Creek valley at the Western edge of the Y-12 plant belonging to the Oak Ridge Reservation of the U.S. Department of Energy (DOE). These basins consisted of four ponds built in 1951. For the following 32 years, they received a yearly volume of 7.6 millions of liter of acidic (pH <2) liquid wastes consisting of nitric acid, uranium, technetium, cadmium, mercury, chlorinated solvents, and strontium among other harmful species (Gu et al. 2003). The contaminants from the S3 basins have infiltrated the shallow saprolitic aquifer resulting in plumes extending up to 5 kilometers down gradient from the basins location. Many of the geophysical studies performed at the IFRC relied on site-specific empirical relationships. To improve the quantitative interpretation of low-frequency geoelectrical data (DC resistivity, induced polarization, and self-potential), there is a need to understand at a more fundamental level the petrophysical properties of the saprolite.

The present work concerns the development of database of various petrophysical measurements of saprolitic core samples from the uncontaminated IFRC background location. These samples were collected from the same geological formation as the former S3 ponds and share the same characteristics of the saprolite as the contaminated area. In this paper, we present a comparison between recently derived petrophysical models and this new set of petrophysical measurements including permeability, complex conductivity, and streaming potential data on saprolite cores samples.

Material and Methods

Saprolitic Materials

Both the contaminated and uncontaminated areas are situated near the Y-12 National Security Complex in Bear Creek Valley in Oak Ridge, Tennessee (Figure 1). The shallow subsurface consists of saprolites, which results from the weathering of Middle Cambrian interbedded shale, siltstone, and limestone forming the parent rock material (Figure 1c, Driese et al., 2001; Watson et al., 2004). It overlies the calcite-rich Nolichucky shale formation, which is part of the Cambrian Conasauga Group, located in Bear Creek Valley.

A number of publications describe the mineralogy of the saprolite and some of their properties at the IFRC (e.g., Jardine et al., 1993a, b). Despite the fact that there are some variations in the clay content with depth, the sand and silt fractions (in weight) are grossly 50% and 31%, respectively, and the clay fraction is about 19% (Jardine et al., 1988, 1993a, b). The cation exchange capacity of saprolite soil samples collected at 1 m depth is typically 10.5 cmol kg^{-1} (0.105 meq g^{-1}, see Kim et al., 2009). Jardine et al. (1993a) reported a CEC in the range 7 to 16 cmol kg^{-1} (0.07-0.16 meq g^{-1}). Waxman and Smits (1968) developed the following relationship between the CEC and the specific area $S_{Sp} = N\,e\,\mathrm{CEC}/(Q_S)$ where Q_S = 0.32 C m^{-2} (Revil et al., 1998, and Woodruff and Revil, 2011) denotes the charge per unit surface area for clays and the CEC expressed in C kg^{-1}. Taking 10.5 cmol kg^{-1} is therefore consistent with a specific surface area of about 30,000 m^2 kg^{-1}. This value is itself pretty consistent with the reactive surface area of the saprolite from Oak Ridge measured by Kooner et al. (1995), 40,000 m^2 kg^{-1}, and, as shown below, it agrees with our own estimates.

According to Kim et al. (2009), quartz, illite, and microcline (K-feldspar) make up 95% of the total mineral composition. The main component of the minor fraction (remaining 5%) is vermiculite, a 2:1 clay mineral. Taking 5% weight fraction of vermiculite with a CEC of 1 meq g^{-1} (1 mol kg^{-1}) implies that the weight fraction of illite, with a CEC of 0.20 meq g^{-1} (20 cmol kg^{-1}), is 28% on average (see CEC values in Lipsicas, 1984 and Zundel and Siffert, 1985). The percentage of vermiculite increases with weathering and therefore with depth. The grain density is assumed to be equal to 2650 kg m^{-3} and the porosity decreases with depth from ~0.50 close to the ground surface to ~0.25 at a depth of 5 m (Driese, 2002).

Several saprolite core samples from the background (upgradient) location, near the Oak Ridge National Laboratory (Figure 1b), were collected by augering and a split spoon sampler. The background site is located within the same geological formation as the former S3 ponds and the collected samples are representative of the contaminated saprolite (same mineralogy and petrophysical properties). Continuous sediment samples were collected in five feet long plastic sleeves from just below the ground surface to a depth of approximately 8.2 m. At the background site, the depth of the water table oscillates between 2 to 4 m and the pH of the aquifer is between 4.8 and 6.0. The samples were stored in capped plastic sleeves until use in the laboratory experiments. Groundwater was sampled from monitoring well FW-300 located in the background location. The shallow uncontaminated groundwater at the background site is typically a Ca-HCO_3 / MgCa-HCO_3 type groundwater due to the dissolution of calcite and dolomite (Saunders and Toran, 1994). The composition of the ground water at the background site is given in Table 1 and its electrical conductivity in the range 0.0047 - 0.0081 S m^{-1} at 25°C.

Three saprolite core samples were collected from 2.7 m, 4.9 m, and 6.7 m below the ground surface (Samples S9, S16, and S22, respectively, the number denotes the depth of the sample in feet). The core samples were cut from the original plastic sleeves and homogenized in a ball mill for 5 min at 20°C. We check that this process did not crush the grains. Then they were packed into 5 cm long portion of 4.4 cm diameter acrylic columns. These samples were chosen to represent the saprolitic material at different depths above the parent rocks. The end caps of the columns were slotted to distribute the flow evenly across the samples. At mid height of the samples, four Ag(s)/AgCl electrodes were installed circumferentially at 60 degrees angle for complex conductivity measurements (Figure 2) and two additional Ag(s)/AgCl close to the end-faces of the core samples were used to measure the streaming potential. The experimental setup served as a constant head permeameter and was used for all petrophysical measurements. The samples were saturated from the bottom up with background groundwater under vacuum for three days. The porosity of the packed samples was approximately 47% (measured after the experiments by drying the core samples).

The samples were initially flushed with 42-124 pore volumes of background groundwater to establish equilibrium conditions (the volume injected through the samples was accurately measured and the pore volume estimated from the porosity and the volume of the core samples). Once the electrical conductivity of the influent and effluent solutions was within 20×10^{-4} S m^{-1} of each other and the pH differed less than approximately 0.5 pH units, the hydraulic conductivity, streaming potential coupling coefficient, and complex conductivity were measured. The samples were subsequently flushed with 3, 10, 30, 100, and 300 mM NaCl solutions and a pH near to pH 5.7 and with 10 mM NaCl solutions with pH adjusted to various pH values comprised between 3 and 6 as discussed further below. We found that ~100 pore volumes were flushed through each core sample before equilibrium was reached (the differences of conductivity and pH between the influent and effluent solutions were vanishingly small). The experiments reported in this paper took therefore several months to be completed.

Mineralogical analyses were performed on three background saprolite samples from the same cores and at nearly the same depths as the samples used for petrophysical measurements. The samples were collected from 3.0 m , 5.1 m, and 6.9 m below the ground surface (Samples S10, S17, and S23, respectively; the number denotes the depth of the sample in feet). The mineralogical composition of these whole rock samples were analyzed using X-ray diffraction (XRD, Figure 2). The remainder of the samples was disaggregated in deionized water (DI) and the clay-sized fraction was separated by centrifugation. The fraction <0.3 μm was air dried, reacted with ethylene glycol for one hour, and subsequently heated to 375°C to evaporate the ethylene glycol and collapse the expanded spaces between the smectite clay layers. After each treatment XRD analyses were performed on samples with the clay layers oriented parallel to the surface of the mounting plate.

Quartz, potassium feldspar, plagioclase and clay minerals were identified by XRD analyses of the whole rock samples. The XRD analyses did not allow for quantitative analysis of mineral content. However, the intensity of the reflections of the clay minerals increased with depth while the intensity of the quartz reflection decreased. The intensity of the clay reflections normalized to the intensity of the quartz reflection were approximately 50% greater in the sample S17 compared to the Sample S10. The quartz-normalized intensity of the clay reflections of the deepest sample was approximately one order of magnitude greater compared to sample S10. The clay fractions of all three samples were dominated by illite and mixed clays consisting of 80-90% illite and 10-20% smectite (Figure 2). A trace amount of chlorite may be present in sample S23 but kaolinite or vermiculite were not identified in any sample.

We performed also specific surface area measurements using the BET approach (Brunauer et al., 1938) at the Colorado School of Mines. For Samples S7, S15, and S21 (at 7, 15, and 21 feet depth), we obtained the following (measured) specific surface areas: 21,670±30 m^2 kg^{-1}, 14,980±20 m^2 kg^{-1}, and 23,110±30 m^2 kg^{-1}.

Petrophysical Measurements

Darcy's law is a constitutive equation connecting the volumetric flux of water through a porous material **u** (the Darcy velocity) to the gradient of the pore fluid pressure or hydraulic head. In saturated conditions, Darcy's law is written as (Darcy, 1856),

$$\boldsymbol{u} = -\frac{k}{\eta_f}\nabla p = -K\nabla h\,, \tag{1}$$

where k denotes the permeability (in m^2), K the hydraulic conductivity (in m s^{-1}), p the pore fluid pressure (in Pa), h the hydraulic head (in m), and η_f the dynamic viscosity of the pore water ($\eta_f = 10^{-3}$ Pa s at 25°C). From previous studies (e.g., Salomon et al., 1992, McKay et al., 2005), the permeability of the saprolite is expected to be low but higher than 1 mD (10^{-15} m^2). We can use therefore the constant head permeameter shown in Figure 3 to determine the permeability for a broad range of NaCl solutions (from 3 mM to 300 mM). The fluxes were measured for different heads and Darcy's law was used to estimate the permeability.

We performed frequency-domain measurements of the impedance Z^* (in Ω) of the core samples in the frequency range 1 mHz - 45 kHz (see Vinegar and Waxman, 1984, Slater and Lesmes, 2002, Slater and Glaser, 2003 for an in-depth description of some laboratory procedures). The impedance Z^* (in Ω) is given by $Z^*(\omega) = |Z^*(\omega)| e^{i\phi(\omega)} = U / I$ where U is the voltage between the potential electrodes M and N (Figure 3), I the magnitude of the current injected between the current electrodes A and B (Figure 3), and $|Z^*(\omega)|$ and $\varphi(\omega)$ denote the amplitude and the phase of the impedance, respectively. The complex resistivity ρ^* is related to Z^* by a geometrical factor G (in m) by: $\rho^*(\omega) = GZ^*(\omega)$. The geometrical factor takes into account the position of the electrodes on the sample, its size and shape, and the boundary conditions for the potential. The complex resistivity ρ^* can be recasted into the complex conductivity ($\sigma^* = 1/\rho^*$) described in the previous section. The measurements were done with the sample holder shown in Figure 3 during the permeability measurements thus maintaining the same packing.

The measurements were performed with the high precision impedance meter described in Zimmerman et al. (2008). The accuracy of the instrument is ~0.1-0.3 mrad at frequencies below 1 kHz (see Zimmerman et al., 2008 and Revil and Skold, 2011 for various benchmark tests). The geometric factor was determined numerically using Comsol Multiphysics 4.1 solving the Laplace equation for the electrical potential and using the geometry of the sample holder shown in Figure 3 (see Jougnot et al., 2010 for details). This estimate was consistent with an estimate of the geometric factor obtained by having a solution of known conductivity in the sample holder and performing a measurement of the resistance for the same electrode configuration.

The setup for the measurement of the streaming potential coupling coefficient is the same that used to measure the permeability (Figure 3). To measure the streaming potential coupling coefficient, we use the following protocol. A given hydraulic head is imposed on the cylindrical sample inside the tube by adding water to the water column in the tube in such a way that the hydraulic head is maintained constant. The gradient of the fluid pressure is controlled by the hydraulic head in the tube and the length of the porous pack (typically between 1 to 60 centimeters). In both cases, the brine is flowing through the porous sample. The resulting electrical potential is measured with two non-polarizable $Ag/AgCl_2$ electrodes (Ref321/XR300, Radiometer Analytical) located in the vicinity of the end faces of the sample. The difference of the electrical potential

measured between the end faces of the porous pack divided by the length of the sample is the streaming electrical field associated with the flow of the solution through the porous sample. The voltages are measured with a data logger (Easy Log, internal impedance of 10 Mohm, sensitivity of 0.1 mV) or with a voltmeter (Metrix MX-20, internal impedance 100 Mohm, sensitivity of 0.1 mV). Both provided consistent measurements.

Permeability

The permeability data are shown in Figure 5. The hydraulic conductivities of our core samples range from 10^{-6} m s^{-1} to 10^{-7} m s^{-1} and the corresponding permeabilities are in the range 10^{-13} to 10^{-14} m^2 (100 to 10 mD). For the least concentrated NaCl solution used in our investigations (3 mM NaCl, 1200 μm cm^{-1}, 25°C), the permeability of the core sample range from 7 to 16 mD (Table 2). The measured hydraulic conductivities for the different salinities are reported in Tables 3 to 5 and Figure 5. These permeabilities are comparable to the in situ measurements of the hydraulic conductivity of the saprolite reported by McKay et al. (2005), which range from 10^{-6} m s^{-1} to 10^{-9} m s^{-1}. We also performed experiments at different pH values in the range 3-6 (Figure 5). The hydraulic conductivity of the 3 core samples does not seem to be dependent on the pH value but there is a noticeable jump in the hydraulic conductivity above pH 5.6. We have no explanation for this jump.

Electrical Conductivity

When the displacement and conduction current densities are taken together, the combined total current density is (Vinegar and Waxman, 1984),

$$\mathbf{J}_t = \left(\sigma^* + i\omega\varepsilon_\infty\right)\mathbf{E}, \tag{2}$$

where **E** is the electrical field (in V m^{-1}), σ^* is the complex conductivity associated with charge electromigration and accumulation, ω is the angular frequency, and ε_∞ is the high frequency dielectric constant of the porous material (in F m^{-1}). In the following, we will neglect the high frequency dielectric term and focus on the frequency range 1 mHz - 10 kHz. The complex conductivity is related to the measured conductivity amplitude $|\sigma|$ and the measured phase lag φ by (Seigel, 1959),

$$\sigma^* = |\sigma| \cdot \exp(i\varphi) = \sigma' + i\sigma'', \tag{3}$$

where the amplitude is given by $|\sigma| = \sqrt{\sigma'^2 + \sigma''^2}$ and the phase angle by $\varphi = \text{atan}(\sigma''/\sigma') \approx \sigma''/\sigma' (< 0)$ (the approximation holds for phase angle smaller than 100 mrad), i denotes the pure imaginary number, σ' and σ'' denote the in-phase (real) and quadrature (imaginary)

components of the complex conductivity, respectively. The in-phase conductivity represents the ability of the porous material to transmit electrical current while the quadrature conductivity describes the ability of the porous material to store reversibly electrical charges.

The physics of induced polarization is however not completely clear as several mechanisms of charge storage compete at low frequencies (Olhoeft, 1985; Schwarz, 1962; Revil and Florsch, 2010; Revil, 2012). In absence of metallic particles like pyrite or magnetite, the main mechanisms of polarization is possibly related to the polarization of the inner part of the electrical double layer called the Stern layer (Stern, 1924; Schwarz, 1962, Leroy et al., 2008, Revil and Florsch, 2010, Vaudelet et al., 2011a, b). That said, other polarization mechanisms, like the membrane polarization, could contribute to the measured response (Marshall and Madden, 1959). The electrical double layer comprises: (i) the Stern layer including mobile weakly sorbed counterions that are able to move tangentially along the mineral surface (outer-sphere complex in the terminology used in electrochemistry, the inner-sphere complexes are not mobile because they are strongly sorbed onto the mineral surface) and (ii) the diffuse layer of counterions and coions located further in the pore water but still in the vicinity of the mineral/water interface (Figure 4). When an electrical field is applied to a single grain, the cations within the electrical double layer move in the direction of the electric field and accumulate at the edge of the grain; when the electrical field is removed, the chemical gradient causes the cations to diffuse back to equilibrium (e.g., Revil and Florsch, 2010).

Low-frequency induced polarization is usually described in terms of a Cole-Cole distribution given by (e.g., Cole and Cole, 1941; Seigel, 1959; Pelton et al., 1978),

$$\sigma^* = \sigma_\infty \left[1 - \frac{M}{1 + \left(i\omega\tau_{CC} \right)^\alpha} \right], \tag{4}$$

$$M = \frac{\sigma_\infty - \sigma_0}{\sigma_\infty}, \tag{5}$$

where M ($0 \leq M \leq 1$) denotes the chargeability (and is usually expressed in mV/V), σ_0 denotes the DC (Direct Current) electrical conductivity ($\omega=0$), σ_∞ is the high frequency electrical conductivity ($\omega >> 1/\tau_{CC}$), τ_{CC} denotes the Cole-Cole time constant (in s), α denotes the unitless Cole-Cole exponent, which describes the broadness of the relaxation times distribution. The normalized chargeability is defined as $M_n = M\sigma_\infty = \sigma_\infty - \sigma_0$. The angular frequency of the phase peak (expressed in rad) is given by (Seigel, 1959)

$$\omega_{\text{peak}} = \left(\frac{\sigma_\infty}{\sigma_0} \right)^{1/2\alpha} \frac{1}{\tau_{CC}} = \left(\frac{1}{1-M} \right)^{1/2\alpha} \frac{1}{\tau_{CC}}. \tag{6}$$

If the chargeability *M* is very small (<<1), then $\omega_{\text{peak}} \approx 1/\tau_{CC}$ and

$$f_{\text{peak}} \approx 1/(2\pi\tau_{CC}) . \tag{7}$$

The recent model of Revil et al. (2012) yields an explicit function for the DC (σ_0) and high frequency (σ_∞) conductivities and for the chargeability

$$\sigma_0 = \frac{1}{F}\sigma_w + \sigma_S^0 , \tag{8}$$

$$\sigma_\infty = \frac{1}{F}\sigma_w + \sigma_S^\infty . \tag{9}$$

Combining equations 5, 7, and 9, we obtain the following expression of the chargeability

$$M = \frac{F(\sigma_S^\infty - \sigma_S^0)}{\sigma_w + F\sigma_S^\infty} , \tag{10}$$

In these equations σ_w denotes the pore water conductivity, and σ_S^0 and σ_S^∞ denote the low and high frequency conductivities of the porous media. Equations 8 and 9 predicts a linear relationship between the conductivity of the material and the conductivity of the pore water like in the Waxman and Smits (1968) model. The formation factor *F* is related to the connected porosity ϕ by,

$$F = \phi^{-m} , \tag{11}$$

with *m* denoting the cementation exponent (Archie, 1942).

The complex conductivity spectra of Samples S8, S16, and S22 are displayed in Figure 6. The in-phase conductivity generally increases with the frequency and with the electrical conductivity of the pore water. The in-phase and quadrature conductivity data used for the analysis are reported in Table 6. We use the following relationship to fit the data at a given frequency:

$$\sigma' = \frac{1}{F}\sigma_w + \sigma_S . \tag{12}$$

Equation 12 is able to fit the (in phase) conductivity data at 1 Hz very well (*R* = 0.97 to 0.99 for the three samples, see Figure 7a and 7b) and it is used to determine the formation factor *F* and the surface conductivity σ_S at 1 Hertz by fitting the conductivity data with a linear least-square method. The fitted values of the (intrinsic) formation factor and surface conductivity (see fit in Figures 7a, b) are reported in Table 2.

The value of the formation factor ranges from 4 to 6 in agreement with the value determined from field data from Watson et al. (2005) (see Figure 7d). In Table 2, the cementation exponent is therefore estimated from the porosity and the formation factor using $m = -\ln F / \ln \phi$. Using the formation factors and porosities given in Table 2, we obtain m = 2.2±0.3.

The surface conductivity σ_S is found to be in the range 0.004 to 0.038 S m^{-1}. The highest surface conductivity value is associated with Sample S22, which has the highest clay content and probably a relatively high CEC value. This is consistent with the fact that the CEC of smectite is very high (around 1 meq g^{-1}, ~1 mol kg^{-1}). This high CEC is therefore responsible for a very high surface conductivity (see Vinegar and Waxman, 1984; Revil et al., 1998, Revil, 2012). To understand at a more fundamental level these values of the surface conductivity, we need a model connecting the surface conductivity to the CEC. Surface conductivity can be given by the following first-order approximation of the model developed by Revil (2012) for high porosity materials:

$$\sigma_S = \frac{1}{F} \beta_{(+)} (1 - f) Q_V , \tag{13}$$

$$Q_V = \rho_g \left(\frac{1-\phi}{\phi} \right) \text{CEC} , \tag{14}$$

where f is the fraction of counterions in the Stern layer (also called the partition coefficient by Revil and Florsch, 2010) and ρ_g the grain density. Equation (13) means that the surface conductivity is controlled by the diffuse layer with a fraction of counterions (1-f) (see Figure 3) and a mobility of the counterions $\beta_{(+)}$ equal to the mobility of the counterions in the bulk pore water. In average for illite and smectite, we have f = 0.90 (see Revil, 2012). Equation 14 is from Waxman and Smits (1968) and is used to determine the total (Stern plus diffuse layers) volumetric charge density per unit pore volume This equation is used to compute the volumetric charge density using CEC = 10.5 cmol kg^{-1} and ρ_g = 2650 kg m^{-3} as discussed above and ϕ = 0.46 (see Table 2), we obtain Q_V = 3.1×10^7 C m^{-3}. Using equation 13 with $f \approx 0.90$, $\beta_{(+)}$ (Na$^+$, 25°C) = 5.2×10^{-8} m^{2}s^{-1}V^{-1} (the value of the mobility for sodium in the pore water), F = 5 (Table 2), we obtain a surface conductivity σ_S = 0.033 S m^{-1}, in good agreement with the value of surface conductivity for sample S22 (0.038 S m^{-1}). Smaller values for the two other samples imply smaller values of the CEC on the order of 1 cmol kg^{-1}.

From Figures 7a and 7b, we observe that at low pore water electrical conductivities, the electrical conductivity of the saprolite is higher than that of the pore water. The data show therefore a critical pore water conductivity at which the conductivity of the porous material is equal to the conductivity of the pore water. This point is called the isoconductivity point in electrochemistry. The three core samples exhibit an isoconductivity point (see Figures 7a, b). This means that the conductivity of a porous saprolite can be higher than the conductivity of its pore water. This type of observations has strong implications in the interpretation of resistivity tomograms in fresh-water environments, a point often missed by hydrogeophycists.

The Dukhin number is defined as the ratio of surface to pore water electrical conductivity (Dukhin and Shilov, 2002). It can be used to normalize the conductivity data by plotting the electrical conductivity of the porous material normalized by the electrical conductivity of the pore water versus the Dukhin number. In this case, all the data for various samples with the same formation factor collapse on the same trend. This trend is well-reproduced by Equation 12 (see Figure 7c). The electrical conductivity of the background ground water at 25°C is 0.0047 - 0.0081 S m^{-1}, which means that for all the samples, we are below the isoconductivity point for the ground water conductivity and therefore the in situ conductivity of the saprolite is higher than the conductivity of the pore water. This shows the limit of neglecting surface conductivity to interpret resistivity tomogram in the field.

The quadrature conductivity data are shown in Figure 6 as a function of the frequency for different pore water conductivities and the values at 1 Hertz are given in Table 6. The absolute value of the quadrature conductivity increases with the pore water conductivity (Figures 8a and 8b) as predicted by the model of Revil (2012). The quadrature conductivity increases by one order of magnitude when the pore water conductivity increases from 5×10^{-3} S m^{-1} to 2.35 S m^{-1} (NaCl).

Sample S16 is the only sample exhibiting a clear relaxation peak for the quadrature conductivity (sample S9 seems to show two small peaks). The peak frequency is around 10 Hertz and seems independent of the salinity as reported before in the literature for sands (Revil and Skold, 2011, Weller et al., 2011). The magnitude of the quadrature conductivities increase with the salinity (Figures 8a, b). For these samples, the Cole-Cole parameters were inverted using a simulated annealing approach (see for two examples, Figures 8c, d). We used the strategy called threshold acceptance (Dueck and Scheuer 1990) and its implementation in Mathematica (function NMinimize). The Cole Cole parameters were used to determine the chargeabilities for each salinity and pH. The inverted chargeability values are shown as a function of the pore water conductivity in Figure 8e . Equation 9 provides a very good fit to the data. In Figure 8f, we show that the Cole-Cole relaxation time is independent on the pore water conductivity, which is consistent with Equation 10.

Following Revil (2012), the quadrature conductivity can be expressed as,

$$\sigma'' = -\frac{1}{F}\beta_{(+)}^{S} f\, Q_V . \tag{15}$$

This means that the polarization is controlled by the Stern layer with a fraction of counterions f (see Figure 3) and a mobility for these counterions $\beta_{(+)}^{S}$. At high porosities, the formation factor can be approximated by the following equation (Revil and Florsch, 2010)

$$F = 1 + \frac{3}{2}\left(\frac{1-\phi}{\phi}\right) \approx \frac{3}{2}\left(\frac{1-\phi}{\phi}\right). \tag{16}$$

The approximation used in equation 16 corresponds to $F >> 1$ and therefore $F\text{-}1 \approx F$. Combining Equations 14 to 16 yields the following expression between the quadrature conductivity and the CEC (see Revil, 2012),

$$\sigma'' \approx -\frac{2}{3}\beta_{(+)}^{S} f \rho_g \mathrm{CEC}\,. \tag{17}$$

Taking $\beta_{(+)}^{S}$ (25°C, Na^+) = 1.5 × 10^{-10} $m^2s^{-1}V^{-1}$, f = 0.90, and ρ_g = 2650 kg m^{-3}, we obtain $\sigma'' \approx -a\mathrm{CEC}$ with $a \approx (2/3)\beta_{(+)}^{S} f \rho_g$ = 2.4×10^{-7} S kg $C^{-1}m^{-1}$. Starting with Equation 17 and using the relationship between the CEC and the specific surface area given above, Revil (2012) developed also the following relationship between the quadrature conductivity and the specific surface area (in kg m^{-2}) of the porous material:

$$\sigma'' \approx -\frac{2}{3}\beta_{(+)}^{S} f \rho_g Q_S S_{Sp}\,, \tag{18}$$

where Q_S denotes the mean surface charge per unit surface area of the clay minerals (in C m^{-2}) and S_{Sp} denotes the specific surface area (surface area per unit mass of the solid grains). Taking $\beta_{(+)}^{S}$ (25°C, Na^+) = 1.5 × 10^{-10} $m^2s^{-1}V^{-1}$, f = 0.90, Q_S = 0.32 C m^{-2} (Revil, 2012), ρ_g = 2650 kg m^{-3}, we have $\sigma'' \approx -a S_{Sp}$ with a = 7.6×10^{-8} S kg m^{-3}. This trend is shown in Figure 9 for clayey materials. In Figure 9, we have also reported the values of the quadrature conductivity for the saprolite core samples as a function of the specific surface area determined in Table 2 from the surface conductivity. The quadrature / specific surface area data are consistent with the clayey sand linear trend of the POLARIS induced polarization model developed recently by Revil (2012).

Using equations 12, 13, and 15, the expression of the phase and it critical value at low salinities (see Revil, 2012) are given by

$$\varphi = -\frac{\beta_{(+)}^{S} f\, Q_V}{\sigma_w + \beta_{(+)}(1-f)Q_V}\,, \tag{19}$$

$$\lim_{\mathrm{Du}>>1} \varphi = -\frac{\beta_{(+)}^{S} f}{\beta_{(+)}(1-f)}\,. \tag{20}$$

This critical phase value is independent of the texture of the clayey material and is observed to be on the order of -30 mrad (see Vinegar and Waxman, 1984; Revil, 2012). This value of -30 mrad is consistent with taking $\beta_{(+)}^{S}$ (Na^+) = 1.5 × 10^{-10} $m^2s^{-1}V^{-1}$, $\beta_{(+)}$ (Na^+)=5.2×10^{-8} $m^2s^{-1}V^{-1}$, and f = 0.91 in Eq. (20). In Figure 10, we plotted the phase lag data for the three samples and we determined the mean value of f and the mean value of Q_V. We obtained f = 0.924±0.004 and Q_V = (5.7±0.9)×10^7 C m^{-3}. The value of f is fairly consistent with the default value given by Revil (2012) for clayey

materials (f = 0.90). The value of Q_V is consistent with the value given above (3.1×10^{7} C m^{-3}, determined using the CEC value of Kim et al., 2009, and the value of the porosity, see discussion above). The value f = 0.92 is used in turn in Table 2 with the formation factor and surface conductivity data to determine the value of the CEC for each sample. Note that the CEC estimates determined in Table 2 from the surface conductivity data (in the range 1.4 to 12 cmol kg^{-1}) are grossly consistent with the CEC measurement of Kim et al. (2009, 10.5 cmol kg^{-1}).

We can also use the model developed by Revil (2012) to investigate the salinity dependence of the quadrature conductivity. In this model, the salinity dependence of the quadrature conductivity is coming from the salinity dependence of the partition coefficient f, which is given by,

$$f = f_{\mathrm{M}}\left[\frac{\left(\frac{K_{\mathrm{Na}}}{10^{-\mathrm{pH}}(1-f_M)}\right)C_f}{1+\left(\frac{K_{\mathrm{Na}}}{10^{-\mathrm{pH}}(1-f_M)}\right)C_f}\right], \tag{21}$$

where f_M denotes the maximum value of the partition coefficient reached at high salinity, the value of the equilibrium constant for the sorption of sodium is approximately K_{Na} = (3.0 ± 0.4) $\times10^{-4}$ (Revil, 2012), and the pH is typically 6. Using the proportionality between the concentration and the electrical conductivity, we have.

$$f = \frac{f_{\mathrm{M}}\sigma_w}{\frac{10^{3}eN\left(\beta_{(+)}+\beta_{(-)}\right)10^{-\mathrm{pH}}(1-f_M)}{K_{\mathrm{Na}}}+\sigma_w}, \tag{22}$$

where e represents the elementary charge (1.6×10^{-19} C) and N the Avogadro number (6.02×10^{23} Mol^{-1}). Combining equation 22 with equation 15 and adding an additional contribution due to mobile protons along the mineral surface, σ''_H (Skold and Revil, 2011) yields,

$$\sigma'' = -\frac{a\,\sigma_w}{b+\sigma_w}+c\,. \tag{23}$$

where the two constants a and b are given by,

$$a = \frac{1}{F}\beta^{S}_{(+)}\,Q_V\,f_{\mathrm{M}}\,, \tag{24}$$

$$b = \frac{10^{3}eN\left(\beta_{(+)}+\beta_{(-)}\right)10^{-\mathrm{pH}}(1-f_M)}{K_{\mathrm{Na}}}, \tag{25}$$

$$c = \sigma''_H . \tag{26}$$

A fit of equation 23 to the data of samples S9 and S22 is shown in Figure 11. For Sample S9, we obtain $a = (1.1\pm0.1)\times10^{-3}$, $b = (8.0\pm3.3)\times10^{-2}$ S m^{-1}, and $c = (1.06\pm0.30)\times10^{-4}$ S m^{-1}. For Sample S16, we obtain $a = (2.0\pm0.2)\times10^{-3}$, $b = (18.7\pm4.8)\times10^{-2}$ S m^{-1}, and $c = (0.82\pm0.17)\times10^{-4}$ S m^{-1}. The values of a and b can be compared with the predictions from equations 24 and 25. For Sample S9, taking f_M =0.92 and $Q_V = 5.7\times10^{7}$ C m^{-3} (both from Figure 10), $\beta^S_{(+)}(Na^+) = 1.5 \times 10^{-10}$ m^{2}s^{-1}V^{-1}, and $F = 3.95$ (Table 2), yields $a = 2.0\times10^{-3}$, which compares quite well with $a = (1.1\pm0.1)\times10^{-3}$ determined from the measurements. Taking the same values for Sample S16 but with $F = 5.9$ (Table 2), we obtain $a = (1.3\pm0.1)\times10^{-3}$, which compare well with $a = (2.0\pm0.2)\times10^{-3}$ determined from the measurements. For b, taking $K_{Na} = 3.0\times10^{-4}$ and pH = 4.5 in equation 25, we obtain $b = 10\times10^{-2}$ S m^{-1} in fair agreement with the value given above (for S9, $b = 8.0\pm3.3)\times10^{-2}$ S m^{-1} and for S16, $b = (18.7\pm4.8)\times10^{-2}$ S m^{-1}). The quadrature conductivity associated with the protons seems quite constant and equal to 1.0×10^{-4} S m^{-1} for the two samples.

Streaming Potential Coupling Coefficient

Streaming potential data from a typical experiment are shown at Figure 12. The differences of the electrical potential measured in the vicinity of the end-faces of the core sample are proportional to the imposed hydraulic heads, indicating good measurements. The slope of the linear trend of streaming potential vs. head corresponds to the streaming potential coupling coefficient (see equation 29).

The streaming current represents the quasi-static source current density associated with the drag of the excess of electrical charges in the electrical diffuse layer in porous material by the flow of the pore water. The streaming potential can be used in the field to characterize preferential groundwater flow paths (Wilt and Corwin, 1989; Wilt and Butler, 1990; Panthulu et al., 2001). The total (electromigration) current density is given for quasi-static conditions by (Revil et al., 2011)

$$\mathbf{J} = \sigma_0 \mathbf{E} + \hat{Q}_V \mathbf{u}, \tag{27}$$

where $\hat{Q}_V$ represent the effective (excess) charge of the diffuse layer that can be dragged by the pore water flow, **E** denotes the electrical field (V m-1) and σ_0 the DC conductivity. The last term of Eq. (27) can be obtained easily by volume averaging the local current density in the pore space $\mathbf{j}_S = \rho\mathbf{v}$ where ρ denotes the local charge density and **v** the local velocity. The (volumetric) charge density $\hat{Q}_V$ is expected to be only a fraction of the diffuse layer volumetric charge density given by,

$$\bar{Q}_V = (1-f)Q_V, \tag{28}$$

(Revil and Florsch, 2010; Jougnot et al., 2012). Using Q_V = 4.0×10^7 C m^{-3} and f = 0.9 yields $\bar{Q}_V$ = 4×10^6 C m^{-3}. Therefore $\hat{Q}_V$ represents only a very small fraction of this value.

We use Darcy's law, equation 1, to express in equation 27 the Darcy velocity **u** as a function of the hydraulic head *h*.. This yields the following expression for the total current density,

$$\mathbf{J} = -\sigma_0 \nabla \psi - K\hat{Q}_V \nabla h, \tag{29}$$

where h denotes the hydraulic head (in m), σ_0 the DC conductivity (in S m^{-1}), and ψ the streaming potential (in V). The streaming potential coupling coefficient is defined by (see Helmholtz, 1879)

$$C \equiv \left(\frac{\partial \psi}{\partial h} \right)_{\mathbf{J}=0}, \tag{30}$$

where we have used the hydraulic head instead of the fluid pressure in the classical definition found in the literature. This coupling coefficient characterizes the sensitivity of the electrical potential, in this case called the streaming potential, to the hydraulic head. It can be determine directly from the streaming potential data reported versus the hydraulic heads (so it corresponds to the slope of the trends shown in Figure 12). From equations 29 and 30, this coefficient is given by (Bolève et al., 2007a, b; Revil et al., 2010)

$$C = -\frac{K\hat{Q}_V}{\sigma_0}. \tag{31}$$

Equation 31 is used to determine the effective volumetric charge density $\hat{Q}_V$ from the measurements of the streaming potential coupling coefficient C, hydraulic conductivity, and DC electrical conductivity. Using equations 8 and 31, the coupling coefficient is related to the pore water conductivity as,

$$C = -\frac{FK\hat{Q}_V}{\sigma_w + F\sigma_S}. \tag{32}$$

The streaming potential coupling coefficient is the fundamental petrophysical parameter characterizing the magnitude of streaming potentials in the field. This equation can be used to see if we can predict the coupling coefficient.

An alternative approach to describe the streaming potential coupling coefficient is to use the zeta potential ζ (Merkler et al., 1989; Pengra et al., 1999; Leroy et al., 2004; Leroy and Revil, 2009). In this case the expression for the streaming potential coupling coefficient becomes:

$$C = -\frac{\varepsilon_w \rho_w g \zeta}{\eta_w \left(\sigma_w + F\sigma_S\right)}. \tag{33}$$

where ρ_w denotes the mass density of the pore water, g is the gravitational acceleration (9.81 m s^{-2}), and ε_w denotes the dielectric constant of the pore water ($81\times8.84\times10^{-12}$ F m^{-1}). Equation 33 is a variant of the so-called Helmholz-Smoluchowski equation (Helmholz, 1879), which is usually given without the surface conductivity term ($C_{HS} = -\varepsilon_w \rho_w g \zeta / \eta_w \sigma_w$ or $C_{HS} = -\varepsilon_w \zeta / \eta_w \sigma_w$ if the head is expressed in pore fluid pressure, see Bolève et al., 2007b).

The streaming potential coupling coefficient was determined for the three samples at NaCl concentrations ranging from 3 mM to 300 mM. In Figure 13, we report the value of the streaming potential coupling coefficient as a function of the conductivity of the pore water. We fit a function of the form,

$$C = -\frac{a}{\sigma_w + b}. \tag{34}$$

and once a is determined, the value of the effective charge density is determined by $\hat{Q}_V = a / FK$. The results are reported in Table 2. The volumetric charge density $\hat{Q}_V$ is in the range 140-490 C m^{-3}, which represents therefore only a small fraction of the total charge density of the diffuse layer ($\bar{Q}_V$ = 4×10^6 C m^{-3}), which is consistent with the results reported recently by Jougnot et al. (2012). The estimates for the effective charge per unit pore volume are compared with other literature data in Figure 14. Like for other natural porous materials at near neutral pH values, the effective charge per unit pore volume $\hat{Q}_V$ is controlled by the value of the permeability of the material.

We use equation 33 to determine the values of the zeta potential for each core sample at the different pore water conductivities. We use the values of the surface conductivities and formation factors reported in Table 2. The results are shown in Figure 15. The zeta potential is in the range -10 to -20 mV and seems independent of the conductivity of the pore water.

Influence of the pH

The previous analysis was done with keeping the pH at relatively high values (in the range 5.5-7.0). Does these petrophysical properties representative of the saprolite near the S-3 ponds,

which has been bathed in acid for few decades? To partially reply to this question, we have also performed additional investigations to look at the effect of the pH (in the range 3 to 6) on these petrophysical properties.

The pH dependence of the hydraulic conductivity is shown in Figure 5. It seems that there is no pH dependence of the hydraulic conductivity with the pH, which may indicate that there is no dissolution during our experiments (over a two months period). The pH dependence of the streaming potential coupling coefficient is shown in Figure 13 and reported in Table 7. Samples S9 and S16 have an isoelectric point at a pH close to 3 (the isoelectric point corresponds to the value of the pH for which the zeta potential is equal to zero). We observe that Sample S22 shows a different behavior but the data are noisier.

We analyzed now the in-phase and quadrature conductivity data as a function of the pH. The spectra are shown in Figure 16 and the in-phase and quadrature conductivities are shown in Figure 17 versus the pH at 1 Hertz. We see that both the in-phase and quadrature conductivities are pH dependent but the correlation between the pH and the conductivities is not clear. The surface conductivity (see the grey area in the first column of Figure 17) is highly pH dependent and is nearly zero at the isoelectric points for Samples S9. This is consistent with the POLARIS model of Revil (2012) in which the surface conductivity is dominated by the diffuse layer and the quadrature conductivity by the Stern layer. A possibility is that the surface conductivity is therefore expected to be zero at the isoelectric point at which the diffuse layer disappears (Sample S9). We see that the quadrature conductivity is not going to zero for all the samples. This is consistent with the fact that there are still some counterions in the Stern layer at the isoelectric point which would explain why the quadrature. conductivity is not equal to zero at the isoelectric point.

For Samples S16 and S22, the streaming coupling coefficient shown in Figure 13c and d do not exhibit an isoelectric point and the surface conductivity remains high at low pH values. We know that smectite exhibits such type of behavior. Indeed, according to Kriaa et al. (2009), the layers of smectite haw a permanent negative charge associated with isomorphic substitutions in the crystalline framework (Figure 4). They have also a pH dependent charges on the edge of their crystals due to the presence of hydroxyl sites. The point of zero charge of these amphoteric edges sites is however in the range ∼7.5–9.3, so above the pH range investigated in the present work. The observed dependence of the zeta potential with the pH of the saprolite could be due to a mix influence of the surface properties of silica, illite, and smectite depending on the clay composition of the material. There is therefore an incentive to pursue this work using a broader database of core samples.

Conclusions

We have documented the permeability, the complex conductivity, and the streaming potential coupling coefficient of three saprolite samples collected from the IFRC background location at Oak

Ridge. Regarding the petrophysical data gathered in this study and their interpretation in terms of a physics-based model, the following conclusions have been reached:

(1) The hydraulic conductivity of the core samples ranges between 10^{-7} and 10^{-6} m s^{-1} in agreement with field observations.

(2) For electrical conductivity measurements, the cementation exponent is equal to 2.2±0.3 and the surface conductivity at 25°C ranges between 4×10^{-3} S m^{-1} (Sample S9) and 38×10^{-3} S m^{-1} (Sample S22) depending on the alteration of the material. The core samples show the existence of an isoconductivity point at low pore water conductivity (at this point, the conductivity of the saprolite is equal to the conductivity of the pore water). The surface conductivity is dominated by electromigration in the electrical diffuse layer coating the pore water / mineral interface.

(3) The streaming potential coupling coefficient is in agreement with recent models. At high salinities, the streaming potential coupling coefficient is inversely proportional to the pore water conductivity while at very low salinities, the streaming potential coupling coefficient is controlled by the surface conductivity and is therefore smaller for highly weathered samples containing mixed layer illite-smectite and smectite clays. The samples with the highest amount of smectite (S16 and S22) keep a high surface conductivity including at low pH values, possibly because of the high level of isomorphic substitutions in the crystalline framework.

(4) For all the samples, the quadrature conductivity is weakly pH dependent. This proves clearly that the quadrature conductivity (hence the polarization) is not controlled by the diffuse layer but more likely by the Stern layer. The quadrature conductivity / CEC data (the CEC being determined by the in-phase surface conductivity) implies a mobility of the counterions in the Stern layer two orders of magnitude smaller than in the diffuse layer.

The petrophysical properties determined from laboratory experiments presented in this work will be used in a subsequent study to interpret geophysical surveying (3D resistivity tomography, time lapse 2D DC resistivity, time-domain induced polarization data and self-potential measurements) performed around the former S-3 ponds. The geoelectrical data, interpreted using the petrophysical model tested here, is expected to be useful at this key DOE contaminated site for locating preferential fluid flow pathways and for investigating the 3D geometry of the contaminant plumes near the former S-3 ponds.

Acknowledgments. We thank the Environment Remediation Science Program (ERSP), U.S. Department of Energy (DOE), for funding (award DE-FG02-08ER646559), Richard Wendlandt for XRD analysis, and Manika Prasad for the specific surface area (BET) measurements. We thank Egon

Zimmerman for the quality of his impedance meter. We thank the Editor Evert Slob and three anonymous referees for their very constructive reviews.

References

Ahmad, M.U., 1969, A laboratory study of streaming potentials: Geophysical Prospecting, **12**, no. 1, 49-64.

Archie, G.E., 1942, The electrical resistivity log as an aid in determining some reservoir characteristics: Transactions of AIME**, 146,** 54–62.

Bolève, A., A. Revil, F. Janod, J.L. Mattiuzzo, and A. Jardani, 2007a, Forward modeling and validation of a new formulation to compute self-potential signals associated with ground water flow: Hydrology and Earth System Sciences, **11**, 1661–1671.

Bolève, A., A. Crespy, A. Revil, F. Janod, and J. L. Mattiuzzo, 2007b, Streaming potentials of granular media: Influence of the Dukhin and Reynolds numbers, Journal of Geophysical Research, **112**, B08204, doi:10.1029/2006JB004673.

Börner, F.D., 1992, Complex conductivity measurements of reservoir properties: Proceedings of the Third European Core Analysis Symposium, Paris, 359-386.

Brunauer, S., P. Emmett, and E. Teller, 1938, Adsorption of gases in multimolecular layers: Journal of American Chemical Society, **60**, 309–319.

Casagrande, L., 1983, Stabilization of soils by means of electro-osmosis: State of art: Journal of Boston Society of Civil Engineers, **69**, no 2, 255-302.

Chen, J., S.S. Hubbard, V. Korneev, D. Gaines, G. Baker, and D. Watson, 2010, Stochastic inversion of seismic refraction data for estimating watershed-scale aquifer geometry: development and application to a contaminated aquifer: Water Resources Research, **46**, W11539, doi:10.1029/2009WR008715.

Chen, J., S.S. Hubbard, J. Peterson, K. Williams, M. Fienen, P. Jardine, and D. Watson, 2006. Development of a joint hydrogeophysical inversion approach and application to a contaminated fractured aquifer: Water Resources Research, **42**, W06425, doi:10.1029/2005WR004694.

Cole, K.S. and R.H. Cole, 1941, Dispersion and absorption in dielectrics I. Alternating current characteristics: Journal of Chemical Physics, **9**, 341–351.

Darcy, H., 1856, Les Fontaines Publiques de la Ville de Dijon: Dalmont, Paris. 647 p.

Dueck, G. and T. Scheuer, 1990, Threshold Accepting: A General Purpose Optimization Algorithm Appearing Superior to Simulated Annealing: J. Comp. Phys., **90**, 161-175.

Driese, S.G., L.D. McKay, and C.P. Penfield, 2001, Lithologic and pedogenic influences on porosity distribution and groundwater flow in fractured sedimentary saprolite: a new application of environmental sedimentology: Journal of Sedimentary research, **71**, no. 5, 843–857.

Driese, S.G., 2002, Report on petropgraphic and geochemical characterization of Nolichucky shale saprolite, Cores FB300 and FB301, NABIR Field Site, Oak Ridge reservation: DOE report, 23 pp., http://public.ornl.gov/orifc/other/Petographicrpt.pdf.

Dukhin S.S., and V.N. Shilov, 2002, Non-equilibrium electrical surface phenomena and extended electrokinetic characterization of particles: In Delgado A.V. (ed.) Interfacial electrokinetics and electrophoresis, Surfactant Science Series: **106**, CRC, Boca Raton, FL, 55–85.

Friborg, J., 1996, Experimental and theoretical investigations into the streaming potential phenomenon with special reference to applications in glaciated terrain, Ph.D. thesis, Lulea University of Technology, Sweden.

Gasperikova E., S. S. Hubbard, D. B. Watson, G. S. Baker, J. E., Peterson, M. B. Kowalsky, M. Smith, and S. Brooks, 2012. Long-term electrical resistivity monitoring of recharge-induced contaminant plume behavior: in press in Contaminant Hydrogeology.

Gu B., S.C. Brooks, Y. Roh P.M. Jardine, 2003, Geochemical reaction and dynamics during titration of a contaminated groundwater with high uranium, aluminum, and calcium: Geochimica et Cosmochimica Acta, **67**, 2749–2761.

Hancock S., A. Revil, M. Skold, and M. Karaoulis, 2012, Frequency domain induced polarization of sandstones from a Uranium deposit, submitted to Geophysical Prospecting.

Helmholz H., 1879, Study concerning electrical boundary layers: Weidemann Annal Physik Chemie, **7**, 337–382, 3rd Ser.

Horikawa, Y., R.S. Murray, and J.P. Quirk, 1988, The effect of electrolyte concentration on the zeta potentials of homoionic montmorillonite and illite: Colloids and Surfaces, **32**, 181-195.

Jardani, A., A. Revil, A. Bolève, J.P. Dupont, W. Barrash, and B. Malama, 2007, Tomography of groundwater flow from self-potential (SP) data: Geophysical Research Letters: **34**, L24403.

Jardine, P. M., G. V. Wilson, and R. J. Luxmoore, 1988, Modeling the transport of inorganic ions through undisturbed soil columns from two contrasting watersheds: Soil Science Society of America Journal, **52**, 1252- 1259.

Jardine, P. M., G. K. Jacobs, and G. V. Wilson. 1993a, Unsaturated transport processes in undisturbed heterogeneous porous media. I. Inorganic Contaminants: Soil Science Society of America Journal, **57**, 945-953.

Jardine, P. M., G. K. Jacobs, and J. D. O'Dell, 1993b, Unsaturated transport processes in undisturbed heterogeneous porous media II. Co-Contaminants: Soil Science Society of America Journal, **57**, 954-962.

Jougnot D., A. Ghorbani, A. Revil, P. Leroy, and P. Cosenza, 2010, Spectral Induced Polarization of partially saturated clay-rocks: A mechanistic approach: Geophysical Journal International, **180**, no. 1, 210-224.

Jougnot D., N. Linde, A. Revil, and C. Doussan, 2012, Derivation of soil-specific streaming potential electrical parameters from hydrodynamic characteristics of partially saturated soils: Vadoze Zone Journal, **11**, no. 1, doi:10.2136/vzj2011.0086.

Kim Y.J., J.W. Moon Y. Roh, and S. C. Brooks, 2009, Mineralogical characterization of saprolite at the FRC background site in Oak Ridge, Tennessee: Environmental Geology, **58**, 1301–1307.

Koch, K., A. Kemna, J. Irving, and K. Holliger, 2011, Impact of changes in grain size and pore space on the hydraulic conductivity and spectral induced polarization response of sand: Hydrology and Earth System Sciences, **15**, 1785-1794, doi: 10.5194/hess-15-1785-2011.

Kooner, Z. S., P. M. Jardine, and S. Feldman, 1995, Competitive surface complexation reactions of SO_4^{2-} and natural organic carbon on soil: Journal of Environmental Quality, **24**, 656-662.

Kowalsky, M. B., E. Gasperikova, S. Finsterle, D. Watson, G. Baker, and S. S. Hubbard, 2011, Coupled modeling of hydrogeochemical and electrical resistivity data for exploring the impact of recharge on subsurface contamination: Water Resources Research, **47**, W02509.

Kriaa A., N. Hamdi and E. Srasra, 2009, Proton adsorption and acid-base properties of Tunisian illites in aqueous solution: Journal of Structural Chemistry, **50**, no. 2, 273-287.

Leroy, P. and A. Revil, 2004, A triple layer model of the surface electrochemical properties of clay minerals: Journal of Colloid and Interface Science, **270**(2), 371-380.

Leroy P. and A. Revil, 2009, Spectral induced polarization of clays and clay-rocks: Journal of Geophysical Research, **114**, B10202, doi:10.1029/2008JB006114.

Leroy P., A. Revil, A. Kemna, P. Cosenza, and A. Gorbani, 2008, Spectral induced polarization of water-saturated packs of glass beads: Journal of Colloid and Interface Science, **321**, 103-117.

Lipsicas, M., 1984, Molecular and surface interactions in clay intercalates, in *Physics and Chemistry of Porous Media*, edited by D. L. Johnson and P. N. Sen, pp. 191–202, American Institute of Physics, College Park, Md.

Merkler G.-P., H. Militzer, H. Hötzl, H. Armbruster, and J. Brauns, 1989, Detection of Subsurface Flow Phenomena. Lecture Notes in Earth Sciences, **27**, Springer, Berlin/Heidelberg, ISBN 978-3-540-51875-4, 514 pages.

McKay, L.D., W.E. Sanford, and J.M. Strong, 2000, Field scale migration of colloidal tracers in a fractured shale saprolite: Ground Water, **38**, no. 1, 139-147.

McKay L. D., S. G. Driese, K. H. Smith, and M. J. Vepraskas, 2005, Hydrogeology and pedology of saprolite formed from sedimentary rock, eastern Tennessee, USA, Geoderma, **126**, 27–45.

Olhoeft, G. R., 1985, Low-frequency electrical properties: Geophysics, **50**, 2492-2503.

Panthulu T.V., C. Krishnaiah, and J.M. Shirke, 2001, Detection of seepage paths in earth dams using self-potential and electrical resistivity methods: Engineering Geology, **59**, 281-295.

Pengra, D., S. X. Li, and P. Wong, 1999, Determination of rock properties by low-frequency AC electrokinetics: Journal of Geophysical Research, **104**, 485–508.

Pelton, W.H., Ward, S.H., Hallof, P.G., Sill, W.R. and Nelson, P.H. 1978. Mineral discrimination and removal of inductive coupling with multifrequency IP: Geophysics, **43** (3), 588-609.

Revil, A., Cathles, L.M., Losh, S., and Nunn, J.A., 1998, Electrical conductivity in shaly sands with geophysical applications: Journal of Geophysical Research, **103**, no. B10, 23,925-23,936.

Revil, A., P. Leroy, and K. Titov, 2005, Characterization of transport properties of argillaceous sediments. Application to the Callovo-Oxfordian argillite: Journal of Geophysical Research, **110,** B06202, doi:10.1029/2004JB003442.

Revil A., N. Linde, A. Cerepi, D. Jougnot, S. Matthai, and S. Finsterle, 2007, Electrokinetic coupling in unsaturated porous media: Journal of Colloid and Interface Science, **313**, 315-327.

Revil, A. and N. Florsch, 2010, Determination of permeability from spectral induced polarization in granular media: Geophysical Journal International, **181**, 1480-1498, doi: 10.1111/j.1365-246X.2010.04573.x.

Revil, A., W.F. Woodruff, and N. Lu, 2011, Constitutive equations for coupled flows in clay materials: Water Resources Research, **47**, W05548, doi:10.1029/2010WR010002.

Revil A., and M. Skold, 2011, Salinity dependence of spectral induced polarization in sands and sandstones: Geophysical Journal International, **187**, 813–824, doi: 10.1111/j.1365-246X.2011.05181.x.

Revil, A., 2012. Spectral induced polarization of shaly sands: Influence of the electrical double layer: Water Resources Research, **48**, W02517, doi:10.1029/2011WR011260.

Revil, A., K. Koch, and K. Holliger, 2012, Relating grain size distribution to permeability and spectral induced polarization relaxation times in sands: Water Resources Research, **48**, W05602, doi:10.1029/2011WR011561.

Salomon, D.K., G.K. Moore, L.E. Toran, and W.M. McMaster, 1992, A hydrologic framework for the Oak Ridge Reservation: ORNL/TM-12026. Oak Ridge, Tennessee: Dept. of Energy.

Saunders, J. A., and L. E. Toran, 1994, Evidence for dedolomitization and mixing in Paleozoic carbonates near Oak Ridge, Tennessee: Ground Water, **32**, 207-214.

Schreiber, M. E.. 1995. Spatial variability in groundwater chemistry in fractured rock: Nolichucky Shale, Oak Ridge, TN. Unpublished M. S. thesis, University of Wisconsin - Madison, Madison, WI, 248 p.

Schwarz, G., 1962, A theory of the low-frequency dielectric dispersion of colloidal particles in electrolyte solution: Journal of Physical Chemistry, **66**, 2636-2642.

Sheffer, M., 2007, Forward modeling and inversion of streaming potential for the interpretation of hydraulic conditions from self-potential data: PhD thesis, The University of British Columbia.

Seigel, H. O., 1959, Mathematical formulation and type curves for induced polarization: Geophysics, **24**, 547-565.

Skold M., and A. Revil, 2011, The pH dependence of spectral induced polarization of silica sands: Experiment and modeling: Geophysical Research Letters, **38**, L12304, doi:10.1029/2011GL047748.

Slater, L., and D.P. Lesmes, 2002, Electrical-hydraulic relationships observed for unconsolidated sediments: Water Resources Research, **38**, 1213-1225.

Slater, L., and D. Glaser, 2003, Controls on induced polarization in sandy unconsolidated sediments and application to aquifer characterization, Geophysics, **68**, no. 5, 1547-1558.

Stern, O., 1924, Zur theorie der electrolytischen Doppelschicht (The theory of the electrolytic double layer), Z. Elektrochemie, **30**, 508-516.

Vaudelet P., A. Revil, M. Schmutz, M. Franceschi, and P. Bégassat, 2011a, Induced polarization signature of the presence of copper in saturated sands: Water Resources Research, **47**, W02526, doi:10.1029/2010WR009310.

Vaudelet P., A. Revil, M. Schmutz, M. Franceschi, and P. Bégassat, 2011b, Changes in induced polarization associated with the sorption of sodium, lead, and zinc on silica sands: Journal of Colloid and Interface Science, **360**, 739-752, 2011.

Vinegar, H.J., and M.H. Waxman, 1984, Induced polarization of shaly sands: Geophysics, **49**, 1267-1287.

Watson, D.B., W.E. Doll, T.J. Gamey, J.R. Sheehan, and P. M. Jardine, 2005, Plume and lithologic profiling with surface resistivity and seismic tomography: Ground Water, **43**, no. 2, 169-177.

Watson, D.B., J.E. Kostka, M.W. Fields, and P.M. Jardine, 2004, The Oak Ridge Field Research Center Conceptual Model, NABIR FRC Technical Report: NABIR FRC. http://public.ornl.gov/orifc/FRC-conceptual-model.pdf.

Waxman, M. H., and L. J. M. Smits, 1968, Electrical conductivities in oilbearing shaly sands: Journal of the Society of Petroleum Engineers, **8**, 107–122.

Weller, A., K. Breede, L. Slater, and S. Nordsiek, 2011, Effect of changing water salinity on complex conductivity spectra of sandstones: Geophysics, **76**, no. 5, 315-327.

Wilt M.J., and R.F. Corwin, 1989, Numerical modeling of self-potential anomalies due to leaky dams: Model and field examples: In Lecture Notes in Earth Sciences, **27**, ed. Merkler G.P. et al., Detection of Subsurface Flow Phenomena, Springer-Verlag, Berlin Heidelberg, 73-89.

Wilt, M.J., and D.K. Butler, 1990, Geotechnical applications of the self-potential (SP) method; Report 4: Numerical modelling of SP anomalies: documentation of program SPPC and applications: Technical Report REMR-GT-6. U. S. Army Corps of Engineers, Waterways Experiment Station.

Woodruff, W. F., and A. Revil, 2011, CEC-normalized clay-water sorption isotherm: Water Resources Research, **47**, W11502, doi:10.1029/2011WR010919.

Zimmermann, E., A. Kemna, J. Berwix, W. Glaas, H.M. Münch, and J.A. Huisman, 2008, A high-accuracy impedance spectrometer for measuring sediments with low polarizability: Measurement Science and Technology, **19**, doi:10.1088/0957-0233/19/10/105603.

Zundel, J. P., and B. Siffert, 1985, Mécanisme de rétention de l'octylbenzene sulfonate de sodium sur les minéraux argileux: In Solid-Liquid Interactions in Porous Media, pp. 447– 462, Technip, Paris.

Table

Table 1. Background ground water composition and properties (from Schreiber 1995).

Element or property	Value
Ca (mg/L) GW	26 - 73
Mg (mg/L) GW	1.7 - 9.4
K (mg/L)	< 2.0 - 3.8
Na (mg/L)	2.7 - 120
HCO_3 (mg/L)	98 - 330
Cl (mg/L)	0.9 - 5.5
SO_4 (mg/L)	6.6 - 170
Alk. (mg/kg as $CaCO_3$)	80 - 270
pH	6.9 - 8.1
Eh (mV)	550 (1)
TDS (mg/L)	152 - 714
Conductivity σ_w (S/m)	0.0047 - 0.0081 (2)

(1) From Jardine et al. (1993b)

(2) This work

Table 2. Petrophysical properties of the three samples (S9, S16, and S22) investigated in this study. The reported porosities are the total connected porosity.

Property	S9	S16	S22
Connected porosity ϕ (-)	0.48	0.49	0.43
Formation factor F (-)	4.1±0.3	5.9±0.1	4.4±0.5
Surface conductivity σ_S (S m^{-1}) (1)	(39±6) ×10^{-4}	(95±2) ×10^{-4}	(376±34) ×10^{-4}
Cementation exponent m (-)	1.9	2.5	1.8
Permeability k (m^2) (2)	(16±3)×10^{-15}	(5.0±3)×10^{-15}	(7.7±0.7)×10^{-15}
Charge density $\hat{Q}_V$ (C m^{-3}) (7)	140	400	490
Excess of charge Q_V (C m^{-3}) (3)	3.9×10^6	1.4×10^7	4.2×10^7
CEC (cmol kg^{-1}) (4)	1.4	5.3	12
Specific surface area S_{Sp} (m^2 kg^{-1}) (5)	4,200	15.900	37,000
Specific surface area S_{Sp} (m^2 kg^{-1}) (6)	21,670±30	14,980±20	23,110±30

(1) At pH values in the range 5-6.

(2) 10 mM NaCl (1200 μm cm^{-1}, 25°C). Average of 7 measurements for each sample.

(3) Using surface conductivity data with $Q_V = F\sigma_S / [\beta_{(+)}(1-f)]$ with f = 0.924.

(4) Using $\mathrm{CEC} = \frac{Q_V}{\rho_g}\left(\frac{\phi}{1-\phi}\right)\left(\frac{100}{Ne}\right)$ with N = 6.02×10^{23} Mol^{-1}, e = 1.6×10^{-19} C, and with $Q_V = F\sigma_S / [\beta_{(+)}(1-f)]$ with f = 0.924, and the measured porosities.

(5) Using $\mathrm{S}_{Sp} = \frac{\mathrm{CEC}}{Q_S}\left(\frac{Ne}{100}\right)$ with Q_S = 0.32 C m^{-2}.

(6) BET measurements, Samples S7, S15, and S21.

(7) Obtained from the streaming potential data using equation 32.

Table 3. Streaming potential coupling coefficient *C* and hydraulic conductivity *K* for Sample S9. GW stands for the natural Ground Water.

Test	Influent σ_w (S m^{-1})	Influent pH	*C* (mV m^{-1})	Effluent σ_w (S m^{-1})	Effluent pH	*K* (m s^{-1})
FW-300 (GW)	0.00640	6.60±0.40	-1.65±0.11	0.00495	4.67	1.2000e-07
FW-300 (GW)	0.00723	6.96	-2.02±0.78	0.00495	5.59	7.5000e-07
3mM NaCl	0.0391	5.40	-1.21±0.29	0.0382	5.41	4.5000e-07
10 mM NaCl	0.1218	5.55	-0.50±0.06	0.121	5.76	5.4000e-07
30 mM NaCl	0.3230	5.69	-0.21±0.05	0.323	4.79	3.8000e-07
100 mM NaCl	0.9030	5.75	-0.09±0.02	0.873	4.69	2.7000e-07
300 mM NaCl	2.544	6.33	-0.05±0.02	2.33	4.61	-

Table 4. Streaming potential coupling coefficient *C* and hydraulic conductivity *K* for Sample S16. GW stands for the natural Ground Water.

Test	Influent σ_w (S m^{-1})	Influent pH	*C* (mV m^{-1})	Effluent σ_w (S m^{-1})	Effluent pH	*K* (m s^{-1})
FW-300 (GW)	0.00640	6.60±0.40	-1.43±0.05	0.00606	6.65	7.4000e-05
FW-300 (GW)	0.00723	6.96	-1.17±0.67	0.00580	6.57	1.8000e-07
3mM NaCl	0.0391	5.40	-1.17±0.09	0.0388	5.97	1.3000e-07
10 mM NaCl	0.1218	5.55	-0.63±0.02	0.121	5.82	3.2000e-07
30 mM NaCl	0.3230	5.69	-0.29±0.03	0.322	5.73	8.9000e-08
100 mM NaCl	0.9030	5.75	-0.13±0.01	0.883	5.81	1.3000e-07
300 mM NaCl	2.544	6.33	-0.040±0.02	2.35	5.72	-

Table 5. Streaming potential coupling coefficient and permeability for Sample S22. GW stands for the natural Ground Water.

Test	Influent σ_w (S m^{-1})	Influent pH	C (mV m^{-1})	Effluent σ_w (S m^{-1})	Effluent pH	K (m s^{-1})
FW-300 (GW)	0.00640	6.60±0.40	-	0.00953	7.15	1.6000e-08
FW-300 (GW)	0.00723	6.96	-	0.00709	7.03	2.7000e-07
3mM NaCl	0.0391	5.40	-0.22±0.11	0.0401	6.36	6.2000e-07
10 mM NaCl	0.1218	5.55	-0.18±0.08	0.122	6.80	1.0300e-06
30 mM NaCl	0.3230	5.69	-0.13±0.04	0.327	5.96	3.8000e-07
100 mM NaCl	0.9030	5.75	-0.10±0.02	0.879	6.23	4.6000e-07
300 mM NaCl	2.544	6.33	-0.05±0.02	2.34	6.03	-

Table 6. Conductivity and phase lag data at 1 Hz for different pore fluid salinities.

Sample	Effluent σ_w (S m^{-1})	Effluent pH	σ' (S m^{-1})	σ'' (S m^{-1})	φ (mrad)
S9	4.95e-3	4.67	3.98e-3	-1.51e-4	-37.9
S9	4.95e-3	5.59	6.45e-3	-1.81e-4	-28.1
S9	3.82e-2	5.41	1.47e-2	-5.10e-4	-34.7
S9	1.21e-1	5.76	3.63e-2	-6.61e-4	-18.2
S9	3.23e-1	4.79	8.66e-2	-8.10e-4	-9.4
S9	8.73e-1	4.69	2.20e-1	-1.1e-3	-4.8
S9	2.33	4.61	5.5e-1	-1.3e-3	-2.5
S16	4.95e-3	4.67	1.02e-2	-1.41e-4	-13.8 (1)
S16	5.80e-3	6.57	1.03e-2	-1.27e-4	-12.3 (1)
S16	3.88e-2	5.97	1.67e-2	-4.74e-4	-28.4
S16	1.21e-1	5.82	3.07e-2	-7.96e-4	-25.9
S16	3.22e-1	5.73	6.49e-2	-1.16e-3	-17.9
S16	8.83e-1	5.81	1.63e-1	-1.65e-3	-10.2
S16	2.35	5.72	3.9e-1	-2.1e-3	-5.6
S22	9.53e-3	7.15	4.94e-2	-3.04e-4	-6.2 (1)
S22	7.09e-3	7.03	3.34e-2	-3.56e-4	-10.6 (1)
S22	4.01e-2	6.36	4.15e-2	-1.32e-3	-31.8
S22	1.22e-1	6.8	6.73e-2	-1.63e-3	-24.2
S22	3.27e-1	5.96	1.18e-1	-1.59e-3	-13.5
S22	8.79e-1	6.23	2.55e-1	-1.55e-3	-6.1
S22	2.34	6.03	5.1e-1	-1.6e-3	-3.1

(1) Not considered for the fit shown in Figure 10.

Table 7. Influence of the pH upon the streaming potential coupling coefficient *C* (25°C, NaCl 10 mM).

pH	Sample	Effluent σ_w (S m^{-1})	*C* (mV/m)
5.8	S9	0.121	-0.50
5.3	S9	0.118	-0.15
4.5	S9	0.119	-0.24
3.6	S9	0.118	-0.17
3.0	S9	0.162	0.02
6.0	S16	0.120	-0.53
5.8	S16	0.121	-0.63
4.6	S16	0.120	-0.57
3.9	S16	0.116	-0.45
3.0	S16	0.145	-0.02
6.8	S22	0.122	-0.18
6.3	S22	0.119	-0.34
4.6	S22	0.120	-0.43
3.6	S22	0.120	-0.56
3.2	S22	0.152	-0.30

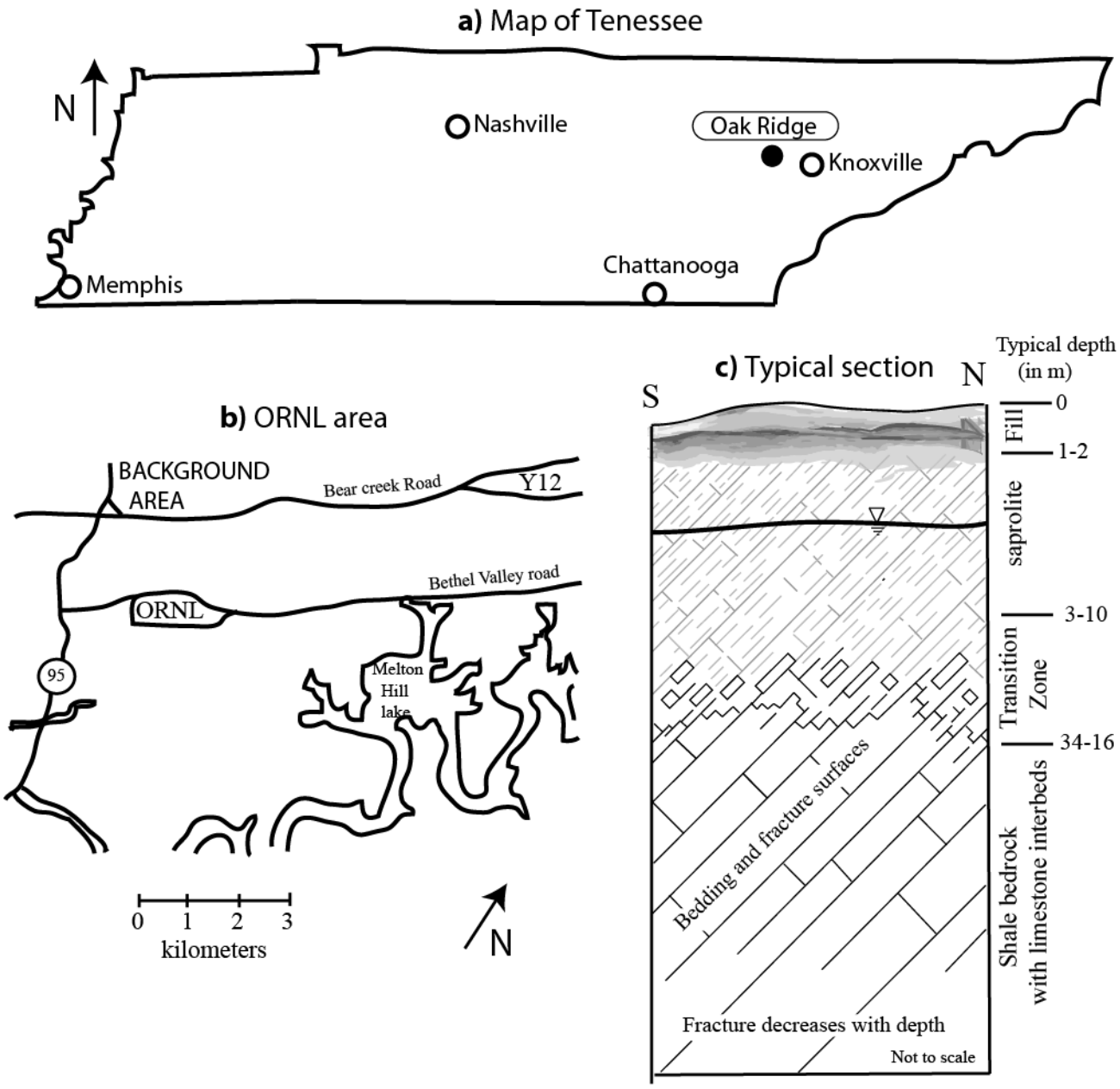

Figure 1. Position of the site where the samples have been extracted. **a.** Position of Oak Ridge in Tennessee. **b.** Position of the background site (ORNL: Oak Ridge National Laboratory). **c.** Typical section of saprolite and parent rock at the Oak Ridge Integrated Field Research Challenge (IFRC) site.

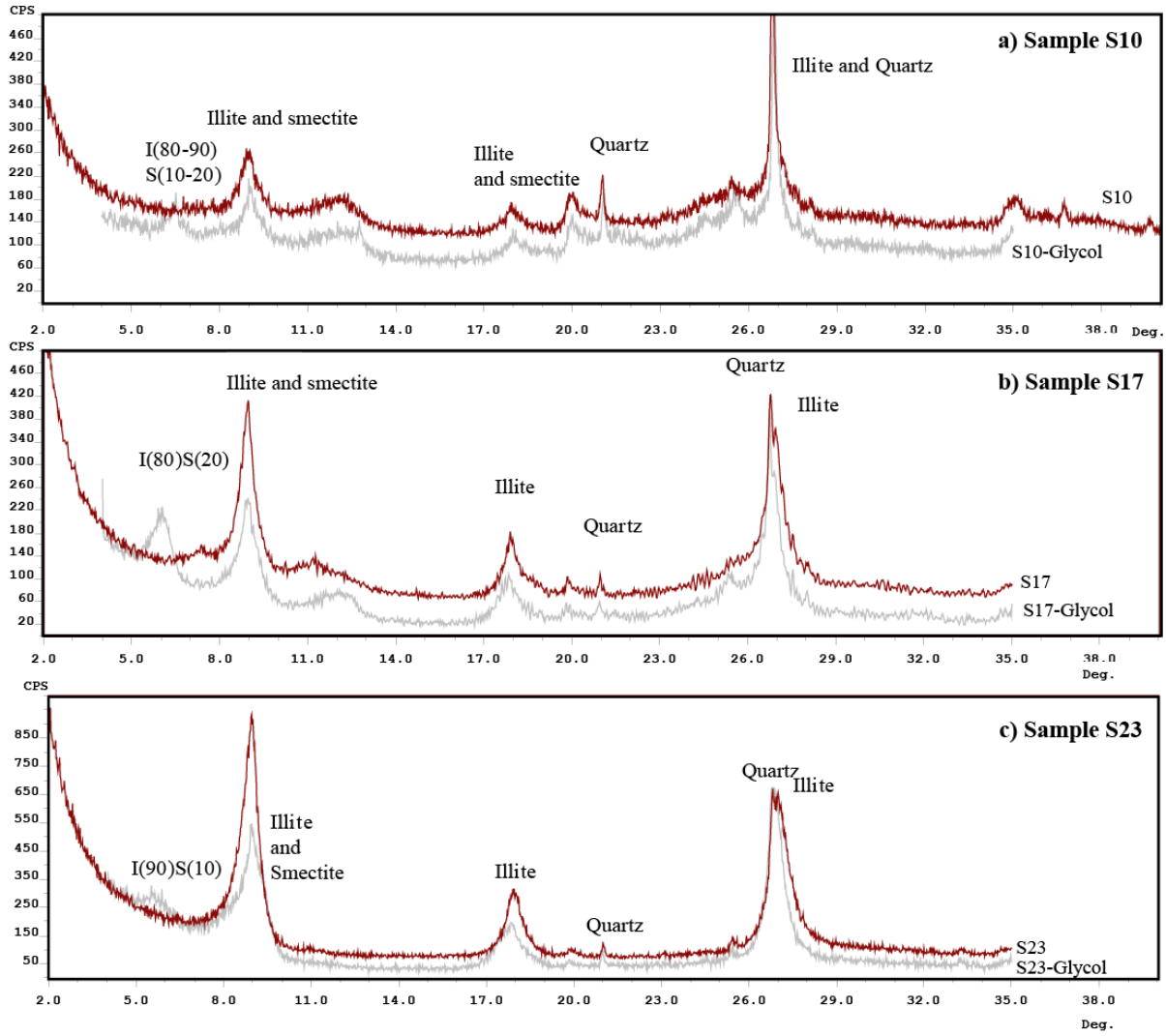

Figure 2. XRD analysis. **a.** Sample S10. **b.** Sample S17. **c.** Sample S23. Illite can be identified in all the three samples. Mixed layer $Illite_{80}Smectite_{20}$ is identified for Sample S17. For Sample S23, the peak shift indicates the presence of mixed layer clays ($Illite_{90}Smectite_{10}$). For Sample S23, note the lower intensity of the quartz reflection and the greater intensity of the clay reflections compared to the other two samples. This sample contains significantly more clay than the two other.

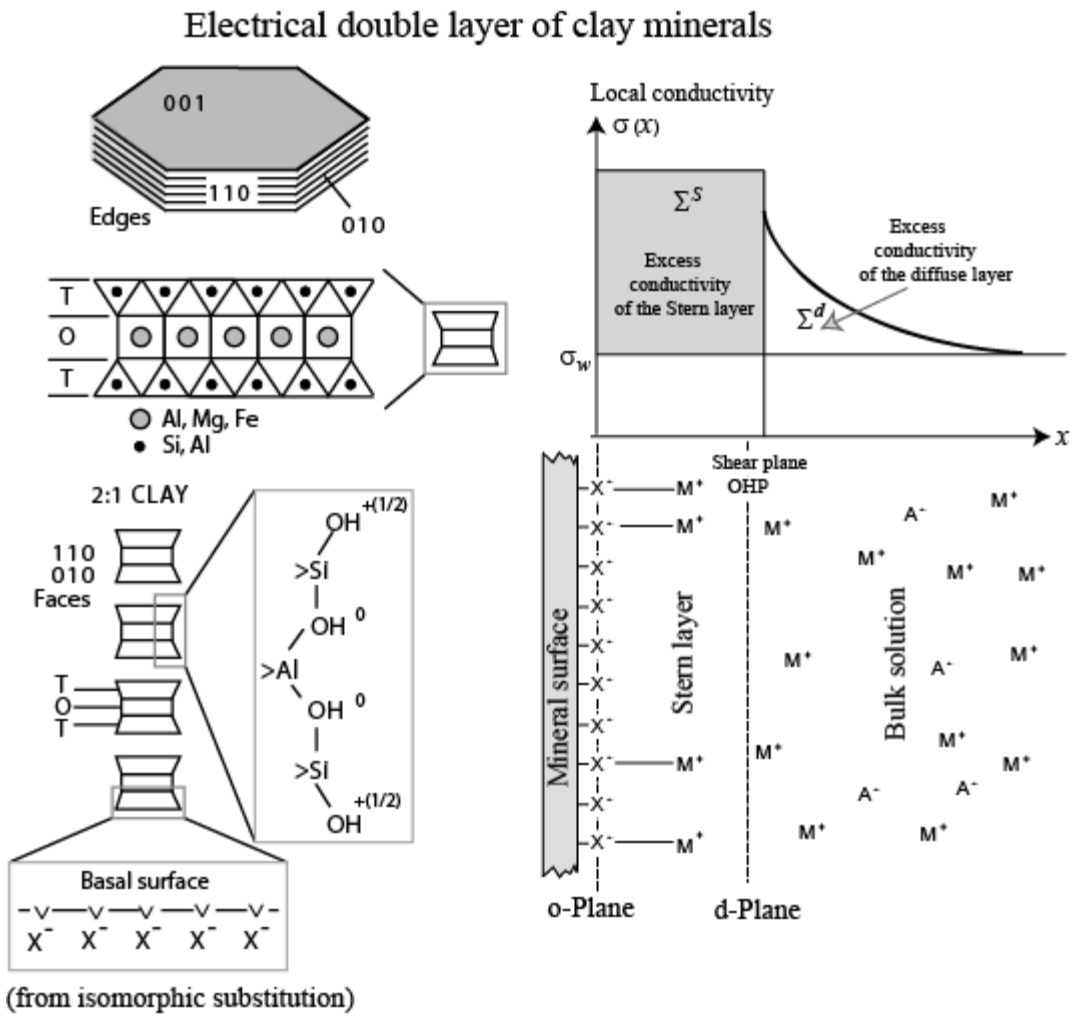

Figure 3. Electrical double layer at the surface of clay minerals. The surface charge of illite and smectite is heterogeneous with amphoteric sites located on the 110 and 010 crystalline planes and isomorphic substitutions in the crystalline framework associated with negative charges on the basal surfaces 001. The electrical double layer is formed of the Stern layer of sorbed counterions and the diffuse layer. The o-plane defines the mineral surface while the d-plane defined the interface between the Stern layer and the diffuse layer on the 110 and 010 crystalline planes. The specific surface conductivities Σ_S and Σ_d define the excess surface conductivity associated with the Stern and diffuse layers with respect to the conductivity of the pore water. The counterions are partitioned between the Stern layer and the diffuse layer and *f* denotes the partition coefficient (modified from Revil, 2012).

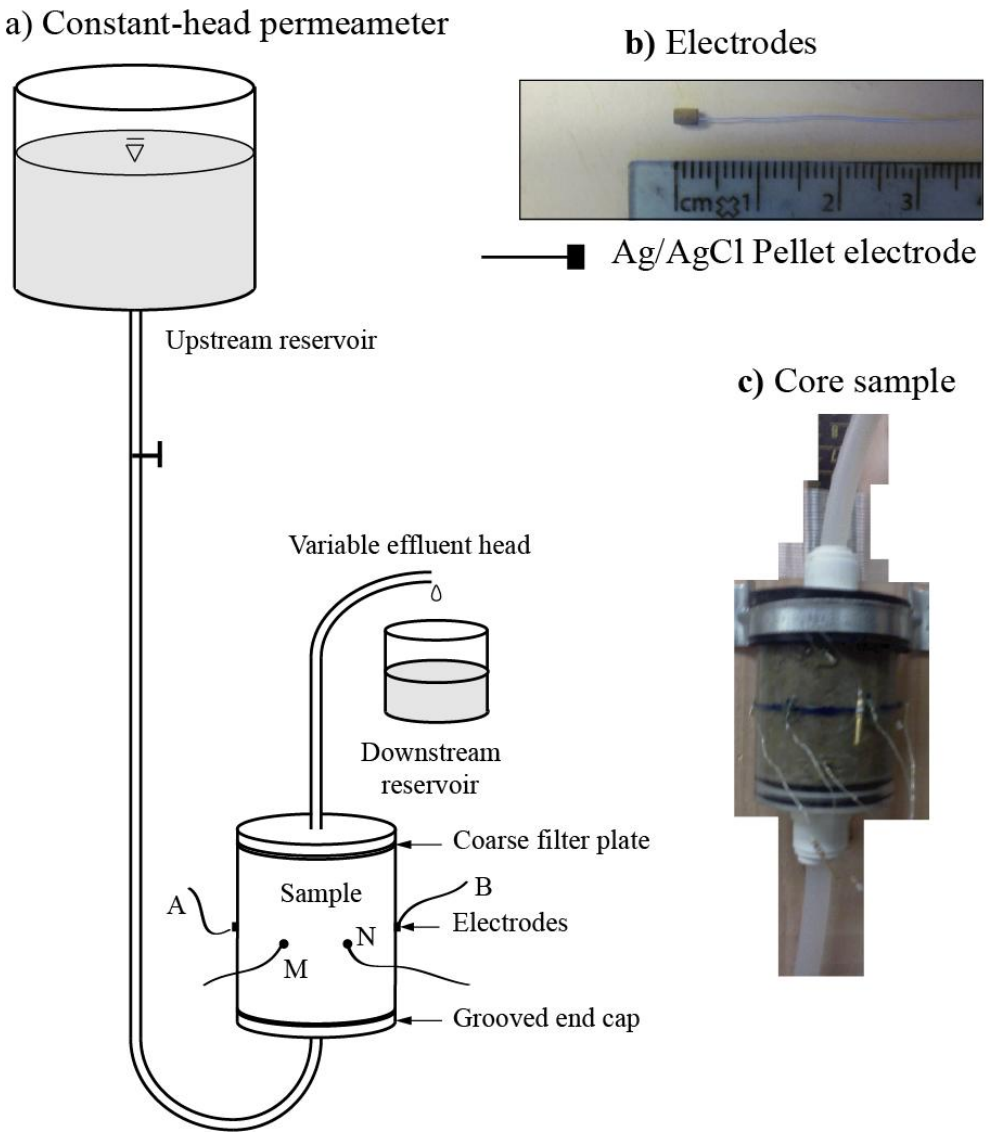

Figure 4. Sketch of the equipment used for the permeability and electrical measurements. **a.** Constant head permeameter. The non-polarizing Ag/AgCl electrodes for the measurement of the complex conductivity are organized in a Wenner array (A and B are the current electrodes, M and N are the potential electrodes). The electrodes ABMN are located in the middle of the sample holder. The geometrical factor for this array is modeled with Comsol Multiphysics 3.5a. The non-polarizing electrodes for the streaming potential measurements are placed at the two end-faces of the core sample (not shown here). **b.** Non-polarizing Ag/AgCl electrodes. **c.** Picture of the core sample.

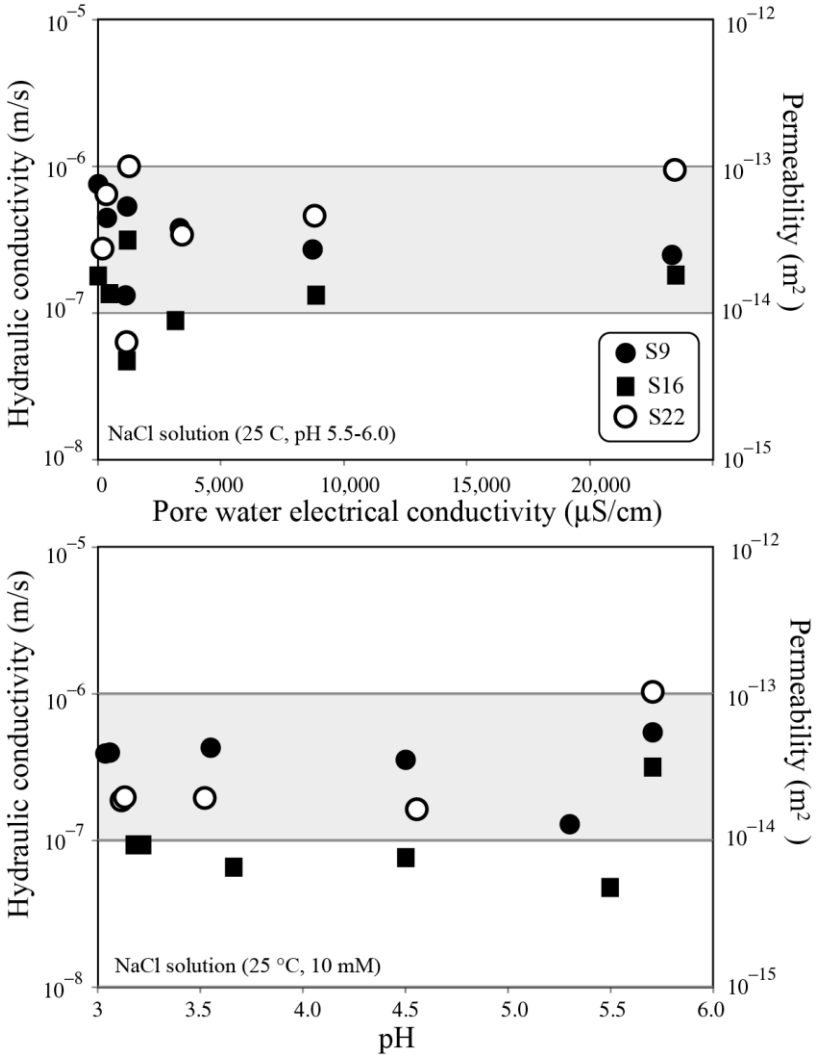

Figure 5. Measured saturated hydraulic conductivity or permeability versus the pore water conductivity and pH. Most of the measured values are between 10^{-7} and 10^{-6} m s^{-1}. These laboratory data are consistent with the in situ measurements of the saturated hydraulic conductivity by McKay et al. (2005, KS-1 pit). The gray area corresponds to the range 10^{-6} to 10^{-7} m s^{-1}.

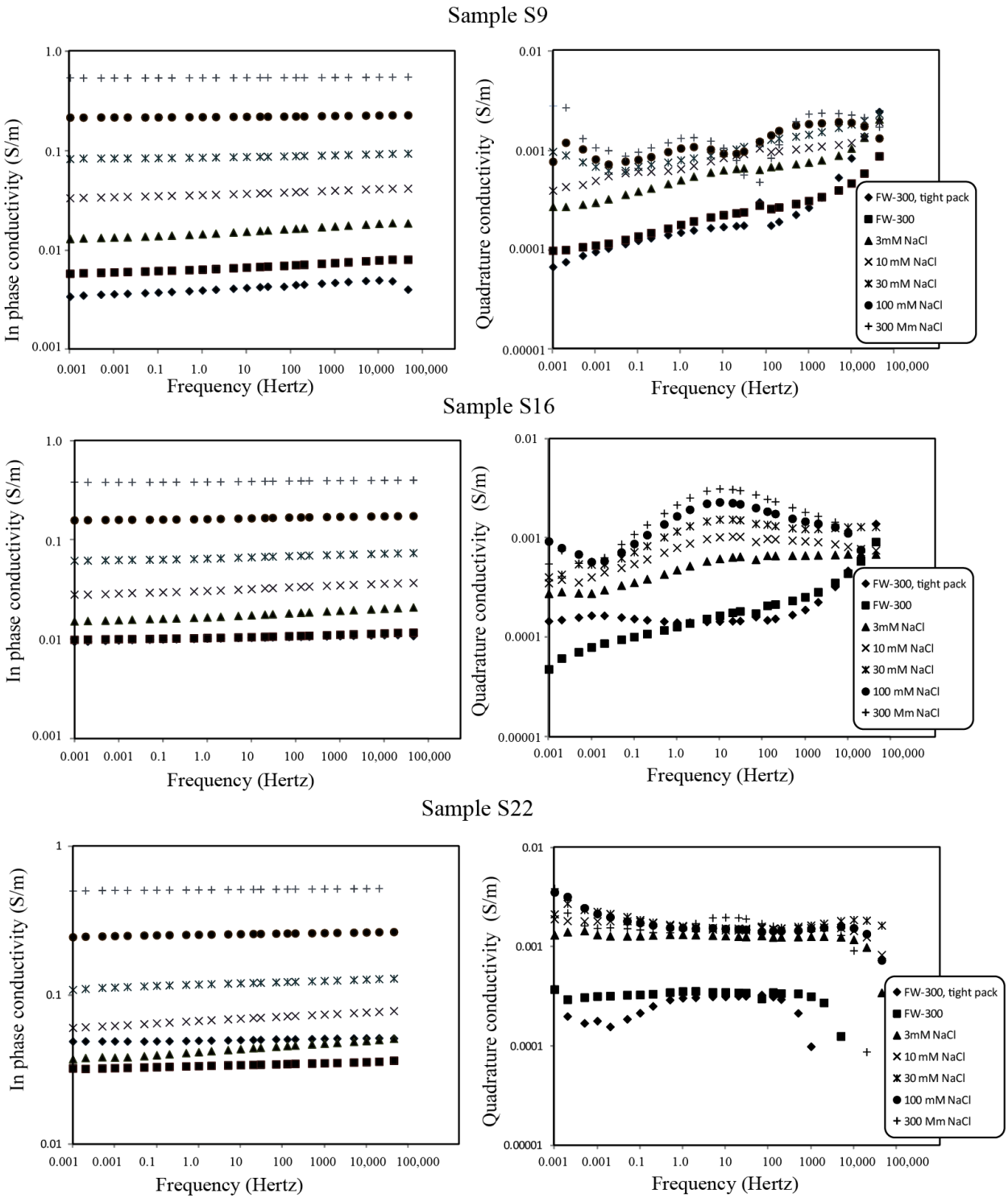

Figure 6. In-phase and quadrature conductivities at different pore water salinities. pH values in the range 5-6.

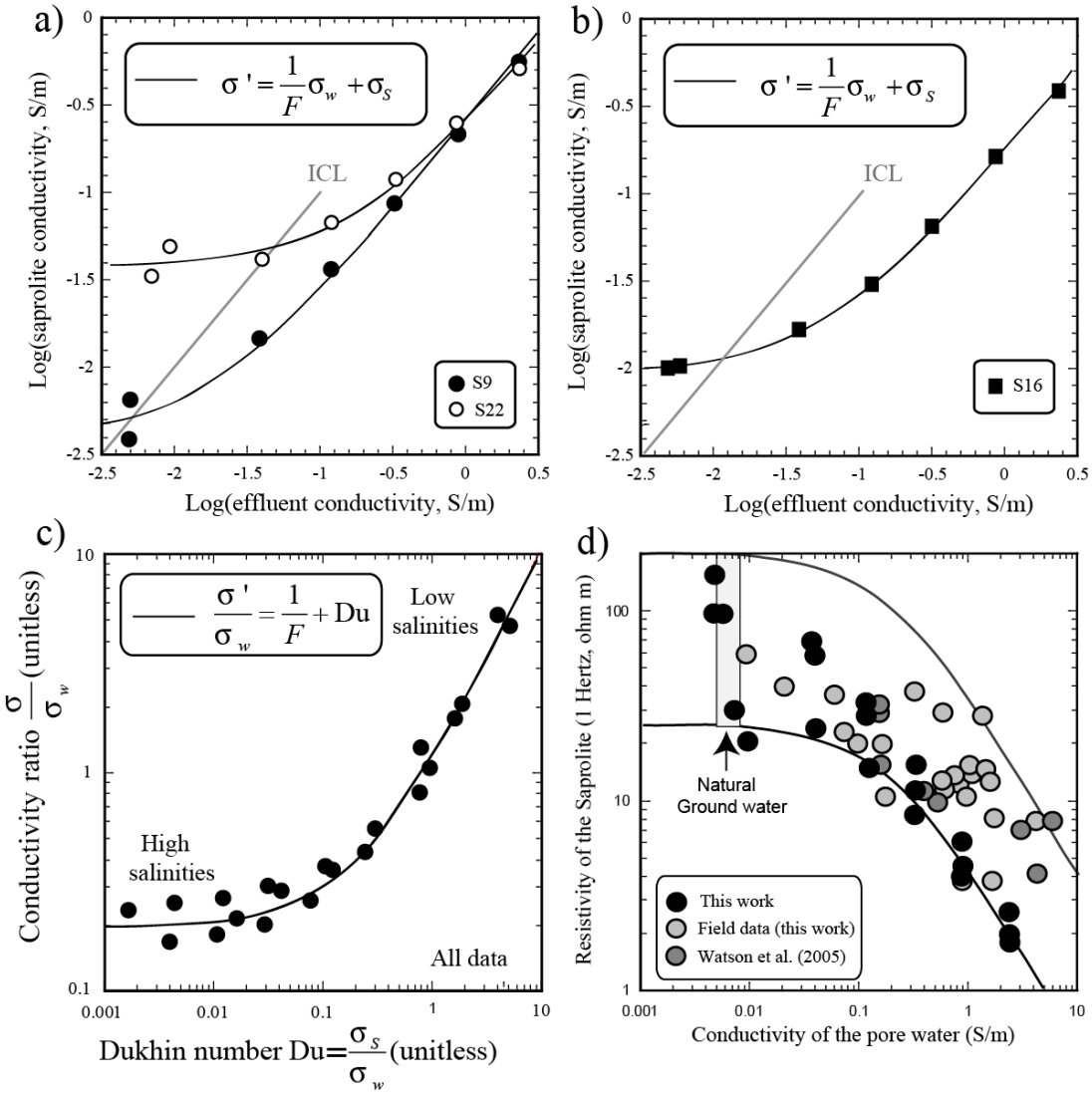

Figure 7. Analysis of the in-phase conductivity data. **a. b.** In-phase electrical conductivity of the saprolite versus the conductivity of the effluent taken as a proxy for the pore water conductivity (measurement at 1 Hertz). **c.** Normalization of the dataset. The ICL represents the Iso-Conductivity Line for which the conductivity of the core sample is equal to the pore water conductivity. Therefore the three core samples have an isoconductivity point. **d.** Field data from Watson et al. (2005) and Revil et al. (2012). The field data indicate a formation factor in the range 5-40 and the same magnitude for the surface conductivity shown by the laboratory data.

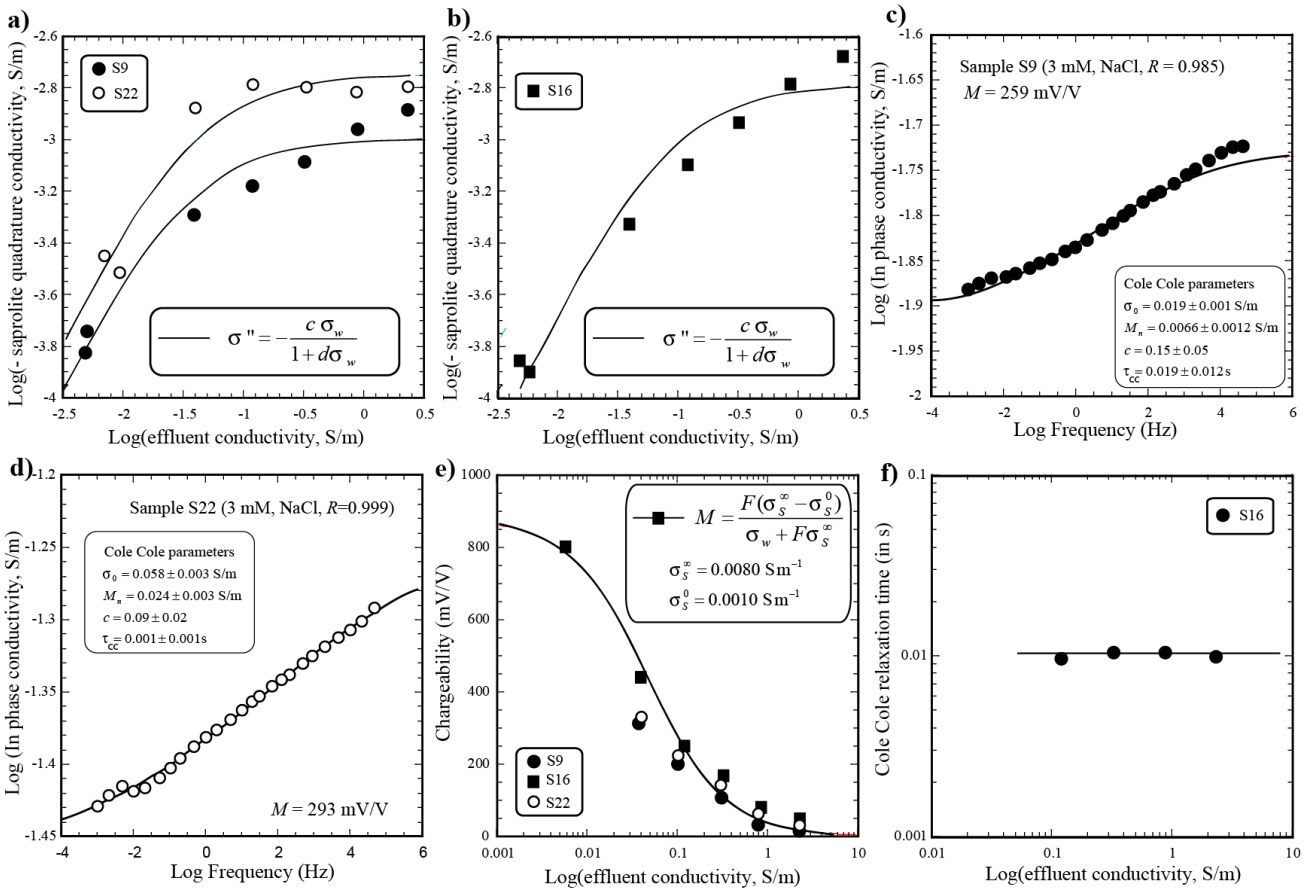

Figure 8. Induced polarization parameters. **a. b.** Quadrature electrical conductivity of the saprolite versus the conductivity of the effluent taken as a proxy for the pore water conductivity (measurement at 1 Hertz). **c. d.** Determination of the chargeability by fitting a Cole Cole model to the in-phase conductivity data. **e.** Chargeability versus pore water conductivity. **f.** Cole Cole relaxation time (in s) for conductivity versus the pore water conductivity (in S m^{-1}).

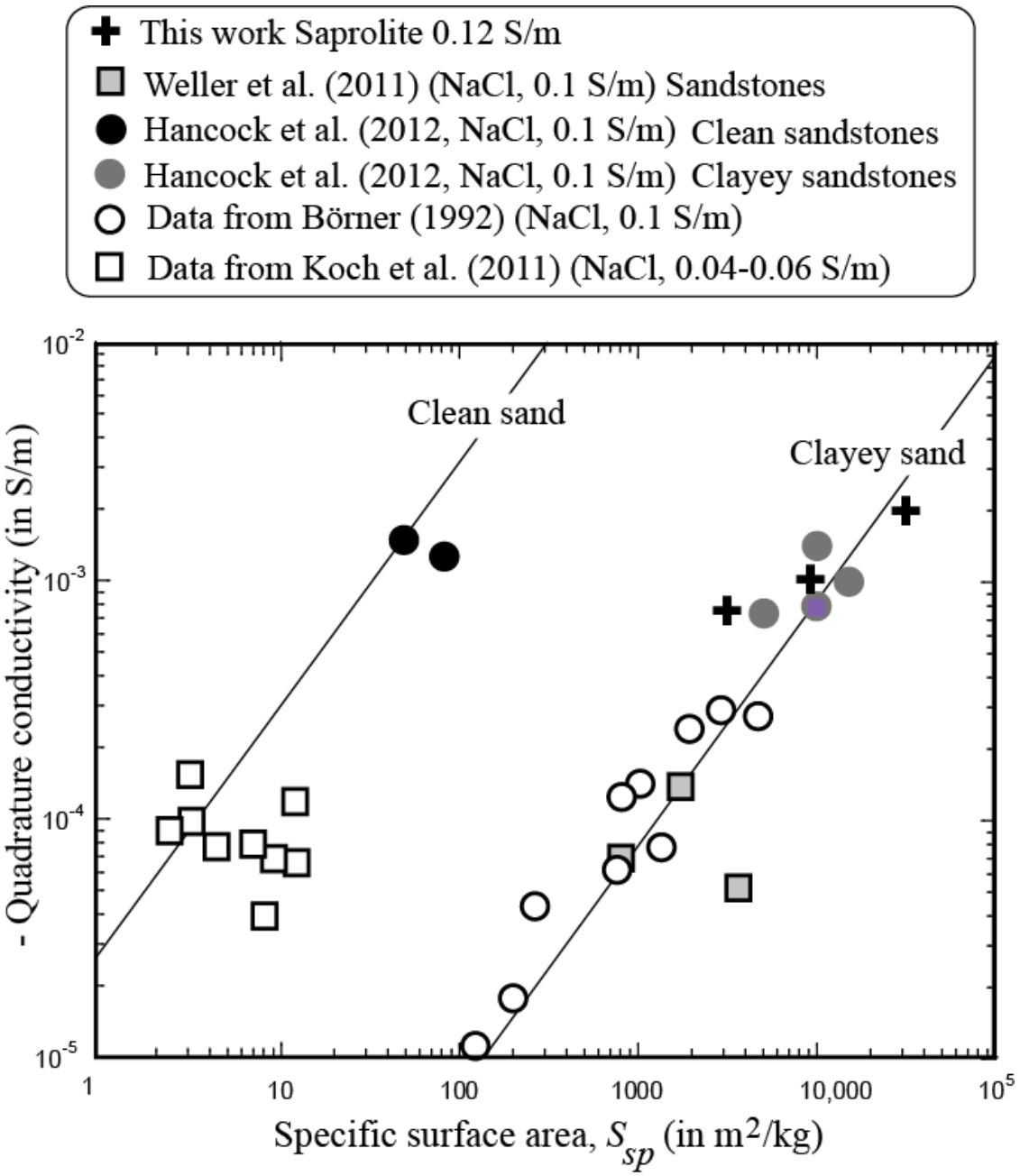

Figure 9. Influence of the specific surface area S_{Sp} upon the quadrature conductivity. We observe that the saprolite samples are characterized by relatively high specific surface areas and high quadrature conductivities in agreement with the trend determined for clayey sands by Revil (2012). Data from Weller et al. (2011), Hancock et al. (2012), Börner (1992), and Koch et al. (2011). For the saprolite, the values are taken at 10 Hertz and the CEC are from Table 1 (from surface conductivity).

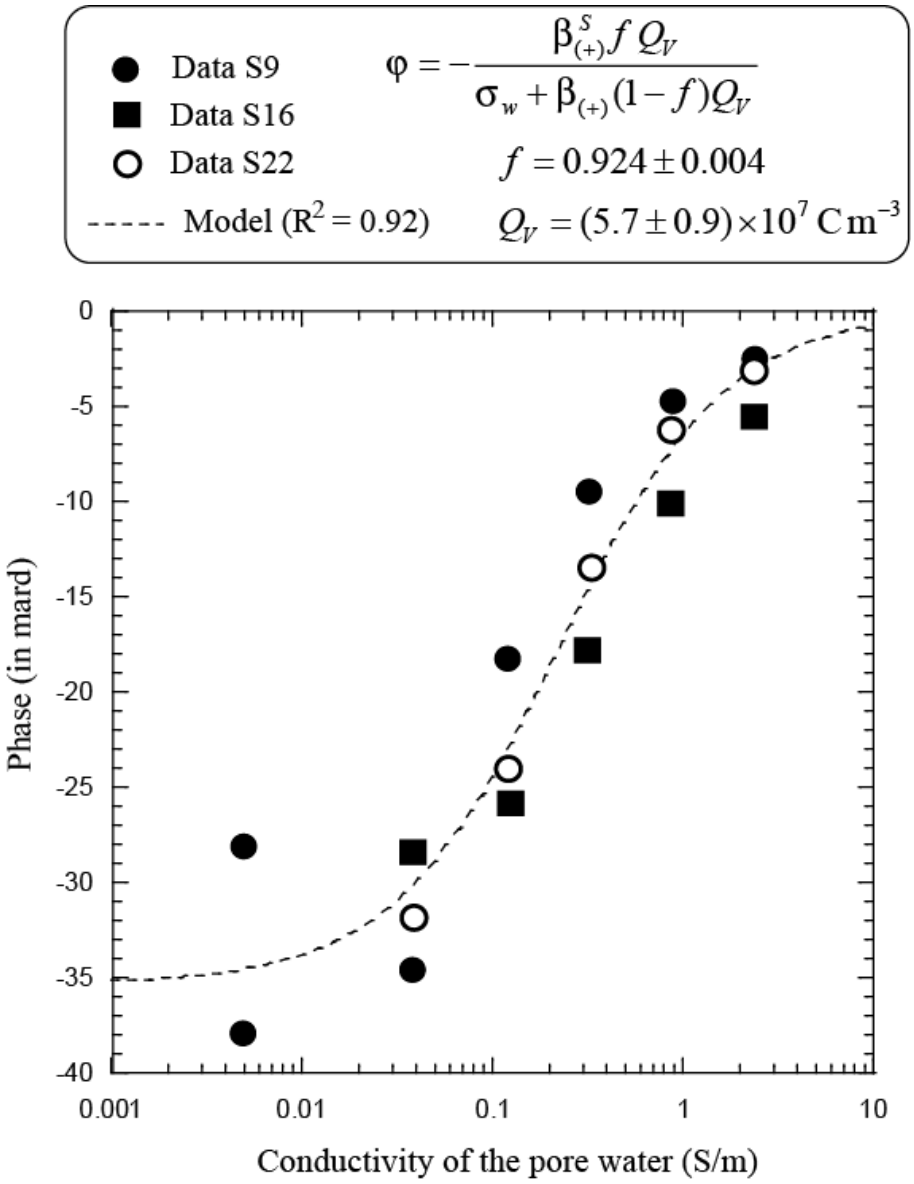

Figure 10. Determination of the partition coefficient *f* (fraction of the counterions in the Stern layer) and total volumetric charge density Q_V using the phase lag data plotted as a function of the conductivity of the pore water (at 1 Hertz, NaCl). The dash line corresponds to the best fit of the model.

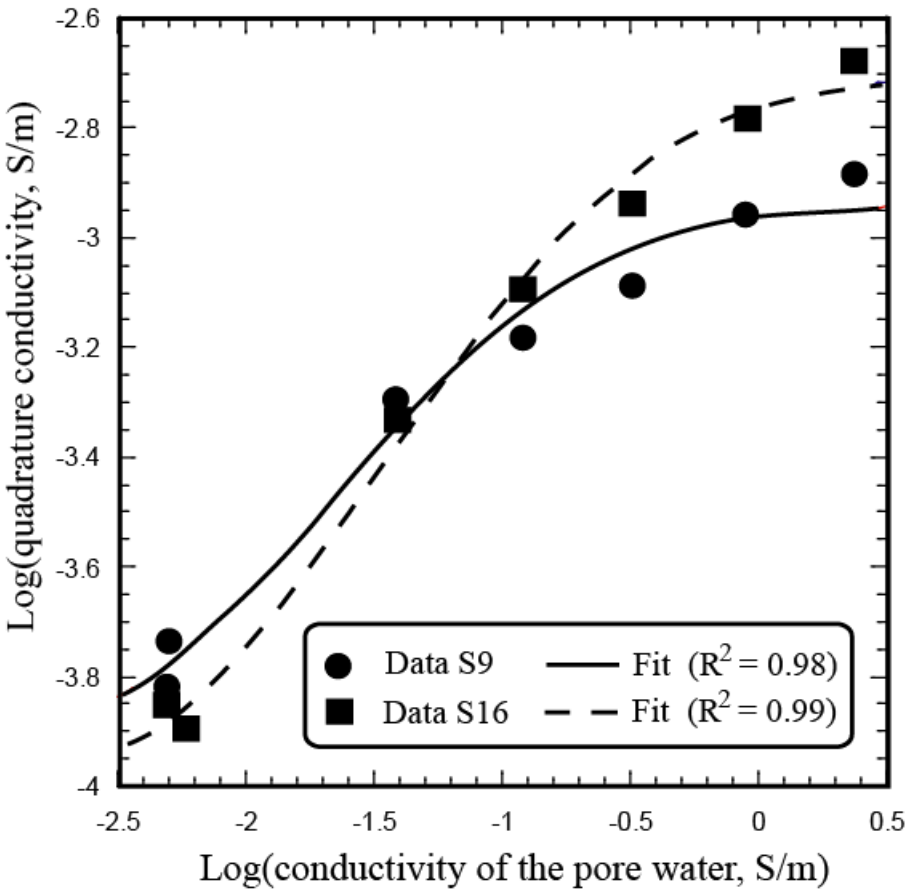

Figure 11. Quadrature conductivity versus pore water electrical conductivity. The plain and dashed lines correspond to the best least-square fit of equation 23 of the main text. Note the sigmoid shape of the trends indicating the existence of both a low-salinity asymptotic limit (associated with mobile protons) and a high salinity limit associated with the sorption of sodium on the mineral surface.

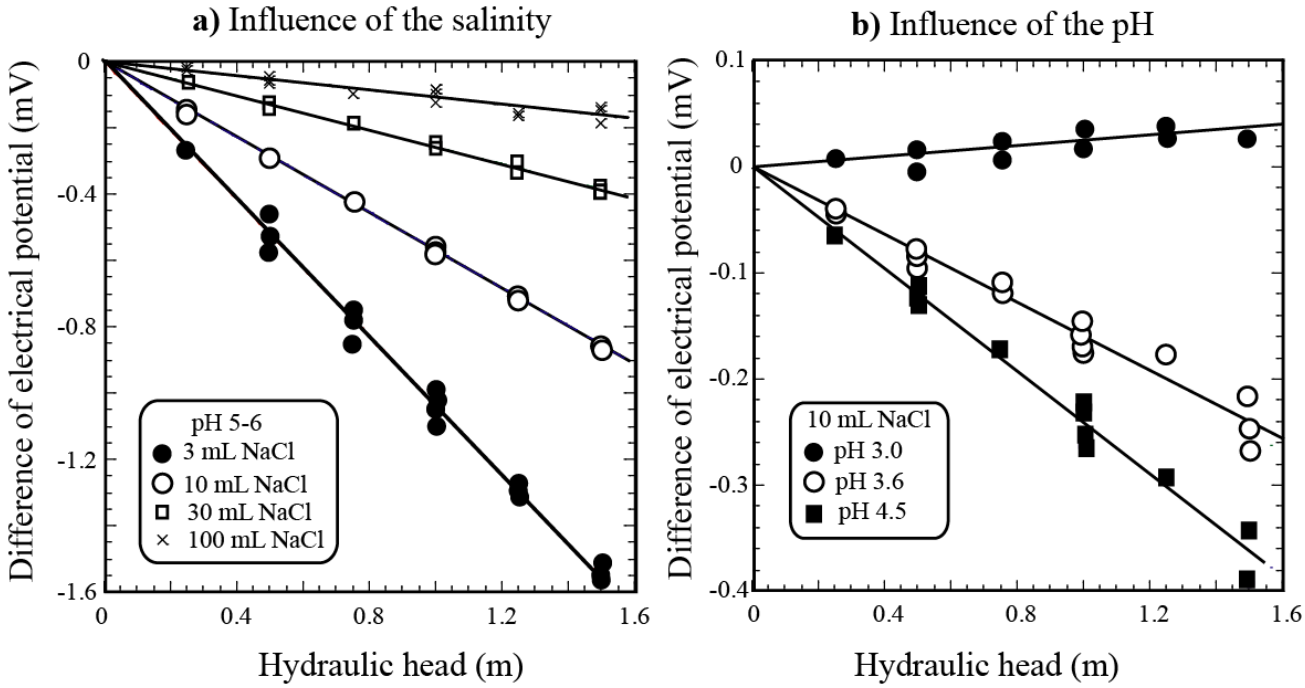

Figure 12. Example of the measurement of the streaming potential for various values of the hydraulic head **a.** Influence of the salinity various salinities (NaCl solutions, Sample S16). **b.** Influence of the pH (NaCl solution 10 mM, Sample S9). Note that at pH 3, the coupling coefficient is positive and hence the zeta potential is positive. This indicates that the isoelectric point is comprised between pH 3.6 and 3.0.

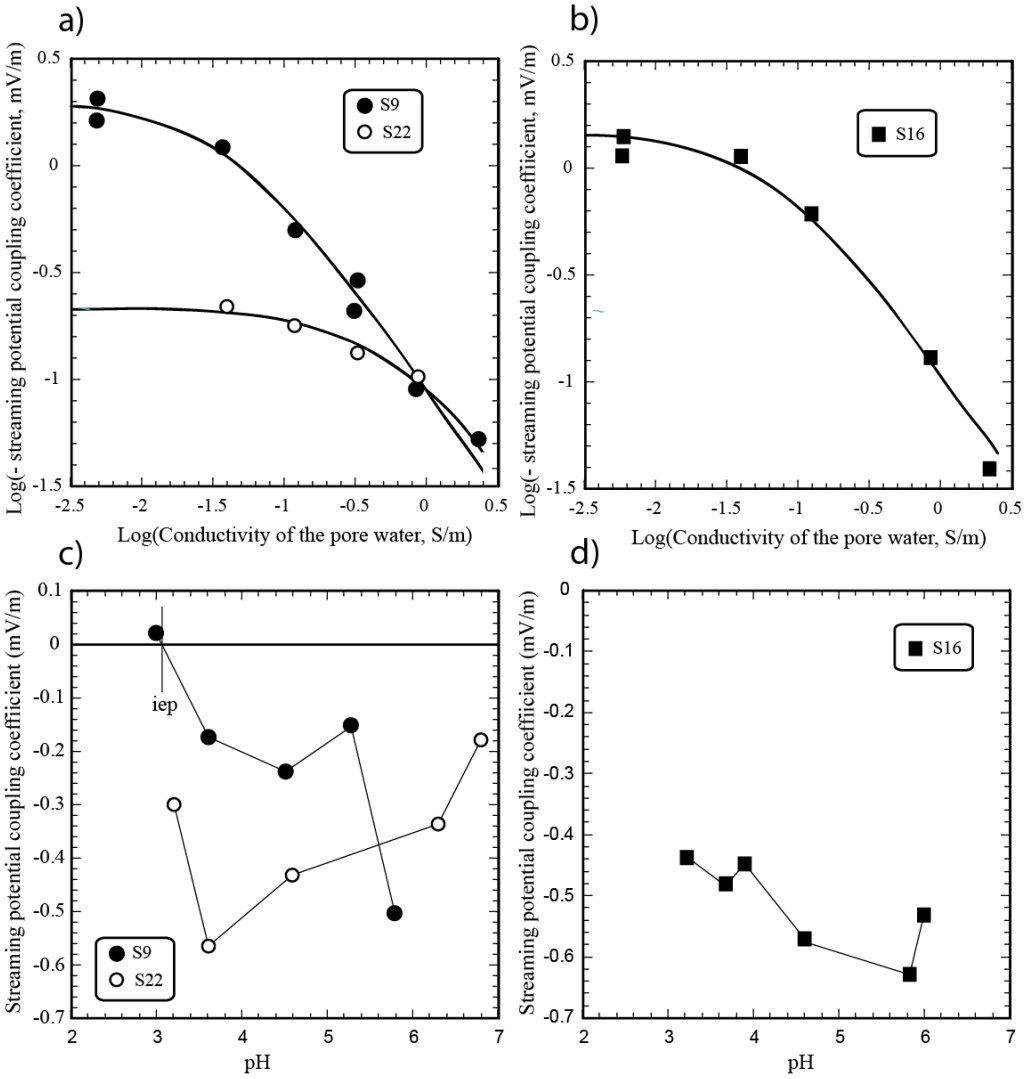

Figure 13. Streaming potential coupling coefficient. **a. b.** Value of the streaming potential coupling coefficient (negative) versus the pore water conductivity (NaCl solutions, pH ≈ 6). The plain lines correspond to the fit of the data with a function $C = a / (\sigma_f + b)$. Sample S22 is influenced by the presence of the smectite, which is generating a high surface conductivity and therefore a smaller value of the magnitude of the streaming potential coupling coefficient at low salinities. The term "iep" stands for isoelectric point. **c. d.** Value of the streaming potential coupling coefficient versus the pH (NaCl solutions, σ_w in the range 0.12-0.16 S m^{-1}).

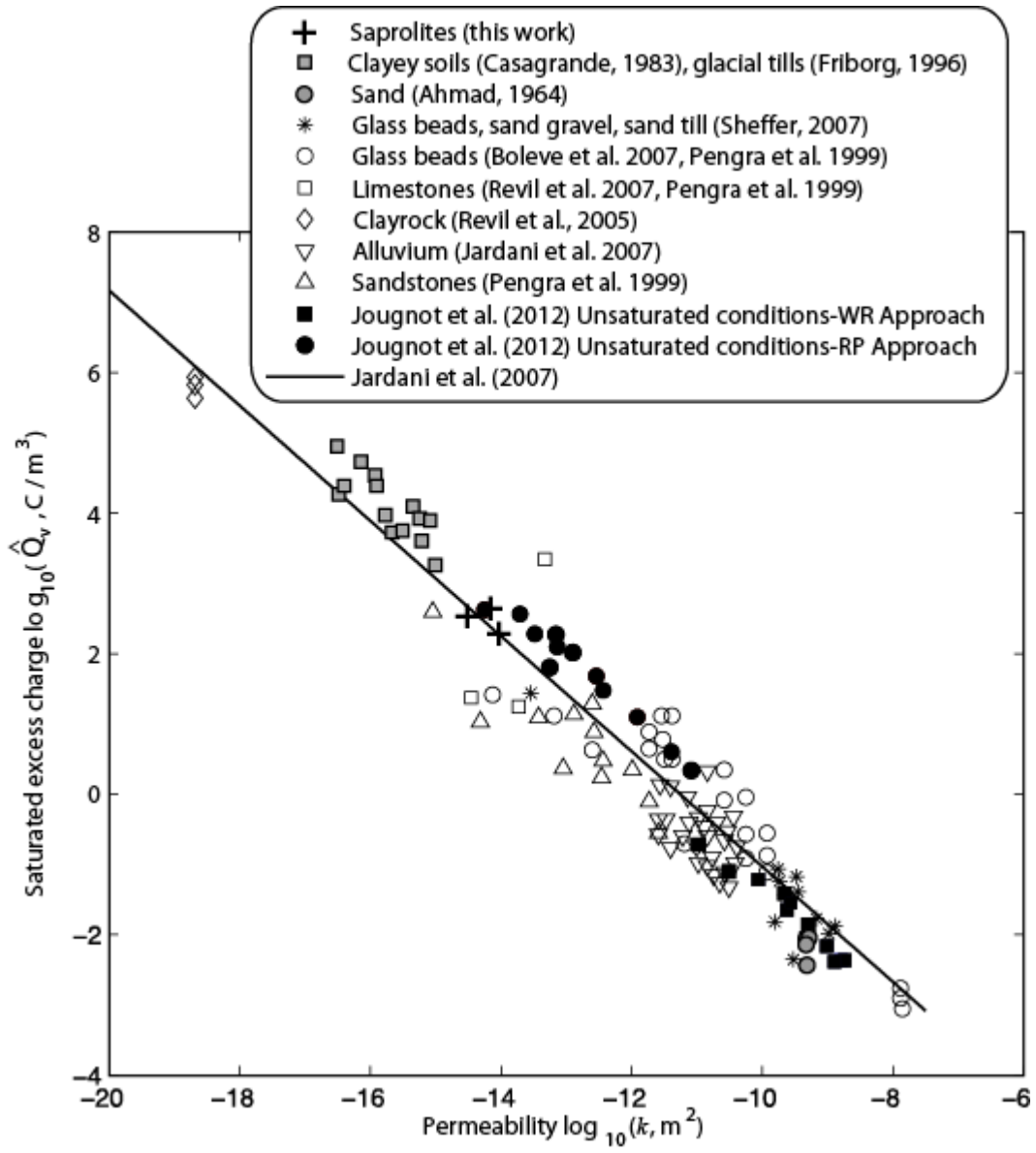

Figure 14. Effective excess of electrical charges moveable by the pore water flow versus permeability for a broad collection of core samples near neutral pH conditions (5 to 8). Data from Ahmad (1964), Bolève et al. (2007), Casagrande (1983), Friborg (1996), Jougnot et al. (2012), Jardani et al. (2007), Pendra et al. (1999), Revil et al. (2005, 2007), and Sheffer (2007).

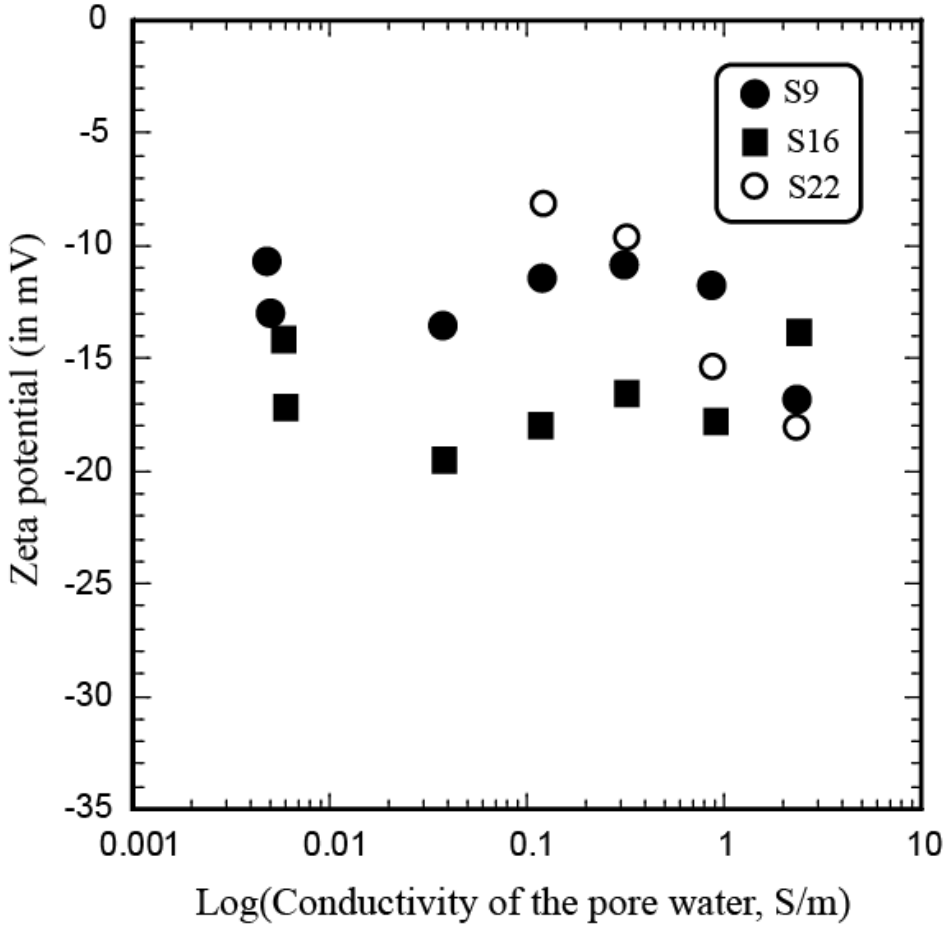

Figure 15. Estimation of the zeta potential of the three core samples. The zeta potential appears relatively independent of the pore water conductivity and suggest a constant zeta potential for the saprolite.

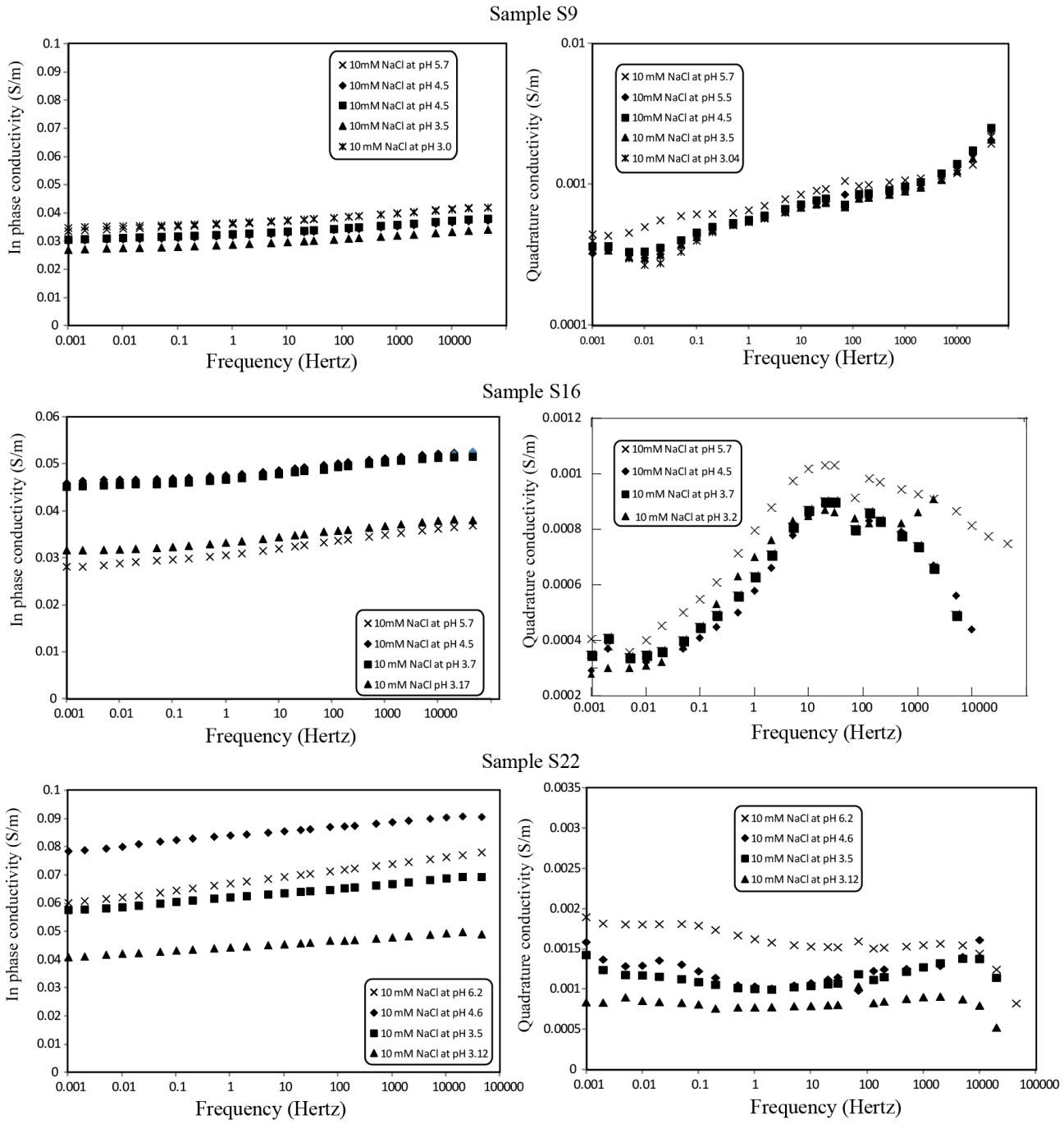

Figure 16. In-phase and quadrature conductivities at different pH value (NaCl, 10 mM). All the measurements are performed at equilibrium (pH of the effluent equal to the pH of the influent).

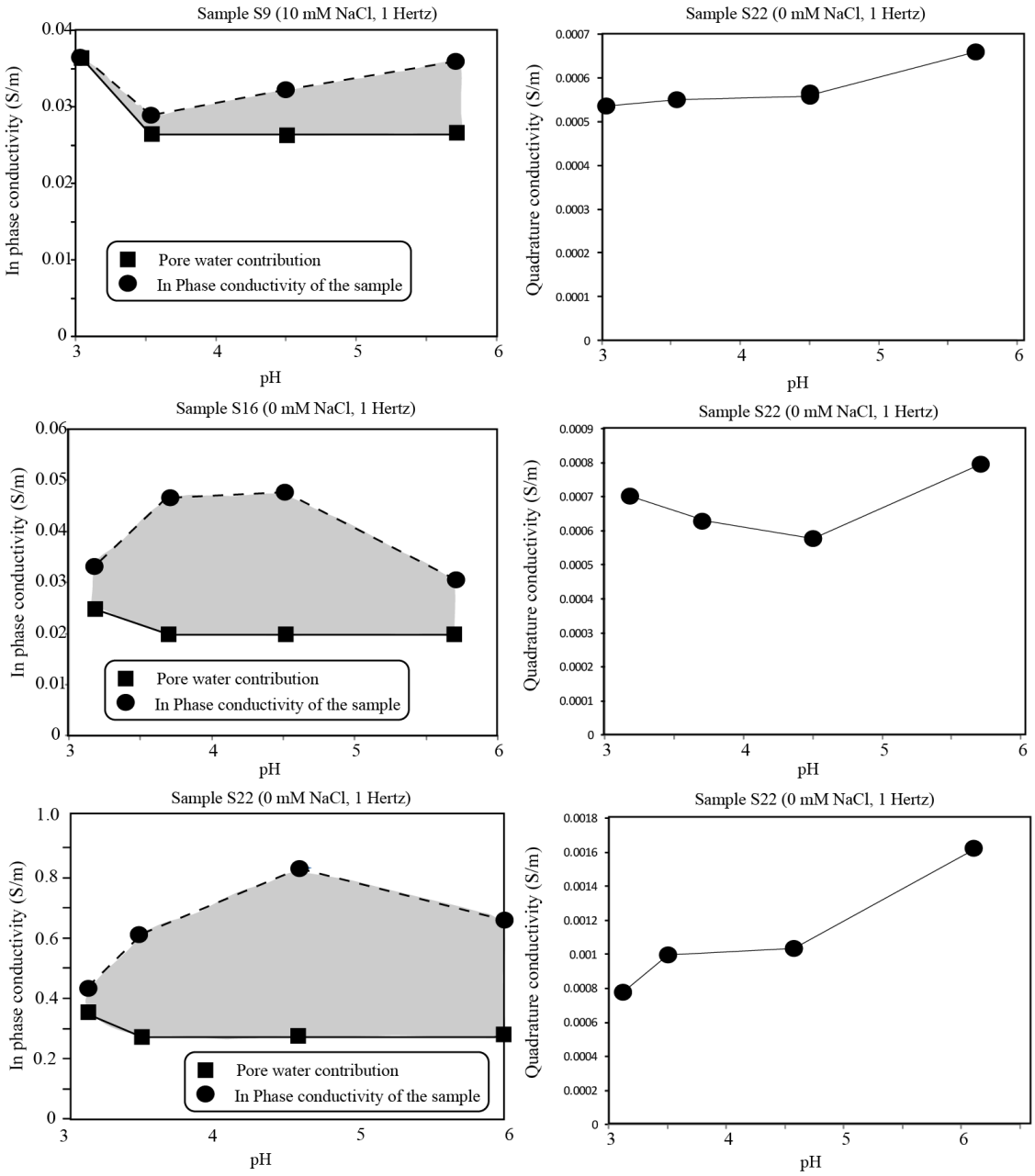

Figure 17. Influence of the pH upon the in-phase and quadrature conductivity components of the complex conductivity of the saprolite. The grey area corresponds to the surface conductivity determined from equation 12 and the data. The surface conductivity corresponds to the difference between the in-phase conductivity and the contribution of the pore water conductivity σ_w/F where σ_w denotes the measured pore water (effluent) conductivity and F is taken from Table 2 except for Sample S9 for which we use a slightly higher value, 4.5 instead of 4.1 to insure a positive surface conductivity).

Appendix B

Hydrogeophysical investigations of the S-3 ponds contaminant plumes, Oak Ridge Integrated Field Research Challenge site, Tennessee

A. Revil (1, 2), M. Skold (1), M. Karaoulis (1), M. Schmutz (3),

S. S. Hubbard (4), T.L. Mehlhorn (5) and D. B. Watson (5)

(1) Colorado School of Mines, Department of Geophysics, Golden, 80401, CO, USA

(2) ISTerre, CNRS, UMR CNRS 5275, Université de Savoie, 73376 cedex, Le Bourget du Lac, France

(3) EA 4592 – Institut Polytechnique de Bordeaux, 1 allée Daguin, 33607 Pessac - France

(4) Lawrence Berkeley National Laboratory, 1 Cyclotron Road, MS 90R1116, Berkeley, 94720, CA.

(5) Oak Ridge National Laboratory, 1 Bethel Valley Road, MS 6038, Oak Ridge, 37831-6038, TN

Running Head: Resistivity Imaging of Contaminant Plumes

Corresponding author: A. Revil (arevil@mines.edu)

Emails: arevil@mines.edu; sshubbard@lbl.gov; watsondb@ornl.gov; msold@mines.edu;

schmutz.myriam@gmail.com; marios.karaoulis@gmail.com; mehlhorntl@ornl.gov.

Keywords: Electrical properties; Hydrogeophysics; Permeability and porosity.

Intended for publication in Geophysics

Abstract. At the Oak Ridge Integrated Field Research Challenge (IFRC) site, near Oak Ridge, Tennessee, contaminants from the former S-3 ponds have infiltrated a shallow saprolitic aquifer for over 60 years. DC-resistivity tomography is used to find the number and location of the main contaminant plumes. We identified a total of 5 main plumes (termed CP1 to CP5). Plume CP2 corresponds to the main plume in terms of nitrate concentration (~50,000 mg L^{-1}). These contaminant plumes have typically an electrical resistivity in the range 2 to 20 ohm m while the background saprolite resistivity is in the range 60 to 120 ohm m, so the difference of resistivity can be easily mapped using DC-resistivity tomography to locate the contaminant pathways. We develop a relationship to derive the in situ nitrate concentrations from the 3D resistivity tomograms. The footprint of the contamination upon the resistivity is found to be much stronger than the local variations associated with changes in the porosity and the clay content. This study points out the importance of accounting for surface conductivity. We also used the recently developed active time constrained approach to perform time-lapse resistivity tomography over a section crossing the plumes CP1 and CP2. The sequence of tomograms is used to determine the changes in the nitrate concentrations associated with infiltration of fresh (meteoritic) water from a perched aquifer. Self-potential data shows the existence of a strong bipolar anomaly (about 400 mV peak to peak) possibly associated with the presence of a gradient of the redox potential in the saprolitic aquifer due to a biostimulation experiment. The inverted source current density points responsible for the observed self-potential anomaly is located at a depth between 4 to 8 m, just at the top of the contaminant plumes where the strongest gradient in the redox potential is expected.

Introduction

The Oak Ridge Integrated Field Research Challenge (IFRC, Oak Ridge, Tennessee) is a U.S. Department of Energy (DOE) test site developed to study the migration of various contaminants from the former S-3 basins. These basins are located in the Bear Creek valley, at the Western edge of the Y-12 plant belonging to the Oak Ridge Reservation of the DOE. The 5 m deep S-3 settling basins consisted of four ponds built in 1951 and covering a surface area of ~15,000 m^2. These ponds stored, for 32 years, a yearly volume of 7.6 millions liters of acidic (pH <2) liquid wastes consisting of nitric acid, uranium, technetium, cadmium, mercury, chlorinated solvents, and strontium among other harmful species (Geraghty and Miller, 1989; Shevenell et al., 1994). The concentration of nitrate in the ponds could have reach 70,000 mg L^{-1} (Shevenell et al., 1994). Drier et al. (1993) noted that the water level in the ponds was about 4.3 m above the water table resulting in downward infiltration of the contaminants in the saprolitic aquifer.

Shevenell et al. (1994) reported that the disposal of wastes to the S-3 ponds was reduced in 1976 and ended in early 1983. In June 1983, the water of the pond was neutralized by adding limestone, quicklime, and sodium hydroxide until a pH of ~9 was reached. This process was responsible for the precipitation of a 1 m-thick sludge formed of aluminium, calcium, and iron compounds. Biological denitrification of the water was performed from June 1983 to September 1984. The sludge was stabilized with coarse aggregates in 1988. Then the S-3 ponds were filled and sealed with a five-layer cap and an asphalt parking lot was built over them. Leakages of

contaminants have occurred since and a number of geochemical, biological, and geophysical studies have been devoted to the understanding of the plumes in the shallow saprolitic aquifer surrounding the ponds as well as in deeper aquifers in the bedrock. Shevenell et al. (1994) ended their paper by stating "Nitrate as nitrogen and all the other constituents of Bear Creek should meet drinkable water standards by 2012". A number of recent studies (Gu et al. 2003; Watson et al., 2004, 2005; Gasperikova et al., 2012) show that this is far from being the case as the aquifer is still heavily contaminated. Geophysical investigations are needed to (1) understand the geometry and dynamics of the contaminant plumes around the former S-3 ponds (Chen et al., 2006; Kowalsky et al., 2011), (ii) follow the natural attenuation of these plumes, and (3) to monitor the efficiency of long-term immobilization strategies.

In the present work, Direct Current (DC) resistivity and Self-Potential (SP) methods were used to investigate and locate the contaminant plumes next to the S-3 ponds. Electrical Resistivity Tomography (ERT) is an efficient active geophysical method to characterize the shallow subsurface and to monitor subsurface changes including pore water conductivity (Atekwana et al., 2004; Robert et al., 2012), water saturation (Legaz et al., 2009), and temperature (Hermans et al., 2012). Recently, time-lapse resistivity has been used successfully used to characterize salt tracer tests in shallow unconfined aquifers (Binley et al., 1996, 2002; Slater et al., 2000; Kemna et al., 2002; Singha and Gorelick, 2005; Vanderborght et al., 2005; Cassiani et al., 2006; Irving and Singha, 2010) or in sandbox experiments filled with heterogeneous materials (Pollock et al., 2012). In the present study, we are looking (1) to develop a new methodology to estimate the in situ nitrate concentration in saprolitic aquifers (previous works, with few exceptions, were not accounting for the effect of surface conductivity) and (2) use a recently developed methodology (the Active Time Constrained approach, ATC) to perform time-lapse tomography of two of these contaminant plumes to understand their dynamics. Such an approach, free of a lot of assumptions but considering carefully the petrophysics, can be considered as a first step to develop fully coupled inversion strategies at this site.

While the self-potential (SP) method has a long history in geophysics (De Witte, 1948; Sill, and Killpack, 1982), it has only emerged recently as a powerful passive electrical method to characterize dynamic processes occurring in the subsurface of the Earth. The occurrence of self-potential anomalies is always related to the existence of a gradient in the chemical potential of charge carriers resulting in a net source current density (Revil and Linde, 2006). The self-potential method has been used to map ground water preferential flow pathways (Ogilvy et al., 1969; Merkler et al., 1989; Rozycki 2009; Bolève et al., 2011; Ikard et al., 2012) and to locate redox fronts in shallow contaminated aquifers (Naudet et al., 2003; Linde and Revil, 2006; Revil et al., 2010). This is this last possibility that we are interested to pursue in our study. Indeed, a portion of the aquifer has been biostimulated and strong redox potential gradients have been observed since. We are interested to see if this biostimulated area is responsible for an observable self-potential anomaly.

Description of the Test Site

The IFRC is located 32 km West of Knoxville, Tennessee (Figure 1a). The position of the former S-3 settling ponds is shown in Figure 1b. Contaminants have infiltrated both the shallow saprolitic aquifer and the bedrock for 61 years and some of these plumes extend now ~5 kilometers downstream. A piezometric map of the shallow saprolitic aquifer around the S-3 ponds is shown in Figure 1b. The transport of the contaminant is controlled not only by the head gradient shown in Figure 1b but also by the hydraulic conductivity tensor. The hydraulic head gradient of the saprolitic aquifer is nearly from North to South with a mean head gradient of ~2.4 m per 100 m. The water table is located from few meters to 5 m below the ground surface. The shape of the hydraulic head equipotentials near Bear Creek indicates that the aquifer recharges the river all along the section shown in Figure 1b. The saprolitic aquifer resulting from the weathering of the parent bedrock, fractures can be found both in the bedrock and in the saprolite with a dip of 45SE and a strike of N55E (see Figure 2).

From the surface to 1 to 2 m deep, the top layer is made of a quite permeable fill (hydraulic conductivity of $\sim 5\times10^{-4}$ m s^{-1}, Kowalsky et al., 2011). After strong rain events, a perched aquifer is observed at the bottom of the fill. This perched aquifer lasts for most of the year except in the dry season (Kowalsky et al., 2011). The saprolitic aquifer itself is 15 to 30 m thick. There is a transition zone from the aquifer to the bedrock. This transition zone is often believe to be more permeable than the upper aquifer itself. The bedrock is made of interbedded limestones and shales and forms generally a very good aquitard. That said, the low pH of the some of the contaminant plumes (pH<4) can be responsible for local dissolution of the limestone generating local increase of the permeability. Also the permeability enhancement in the aquifer itself can increase the permeability of the preferential flow pathways, creating therefore a positive feedback reinforcing the localized character of the contaminant plumes (flow tube model).

The background (uncontaminated) pore water composition is reported in Table 1. The background pore water is a calcium bicarbonate solution with a slightly alkaline pH. The concentrations of the major constituents in the S-3 Ponds in 1978 are reported in Table 2. The background pore water and the pond water form the two-end members for the contamination around the S-3 Ponds. A relationship between the pore water conductivity and the nitrate concentration will be developed below in the next section (see Table 3 for some relevant concentrations and ground water characteristics around the S-3 ponds for the 2009-2012 period). The two extremes for the nitrates concentrations are 2.3 mg L^{-1} for the background pore water and 70,000 mg L^{-1} for the former nitrate concentration in the S-3 ponds. In situ pore water sampling is showing that, in the last decade, some of the contaminant plumes have a nitrate concentration higher than 49,000 mg L^{-1} (Watson et al., 2005). The hydrogeological properties of the different formations (see Figure 2) are reported in Table 4.

Electrical Resistivity Tomography Snapshots

Acquisitions and Inversion

A resistivity survey was performed in October 2011. There was no rain for the two weeks preceding the acquisition of the resistivity data. Seventeen DC resistivity profiles were performed around the S-3 ponds both upstream and downstream (see position in Figure 3). The total survey comprised a total of 978 electrodes and 6,889 quadripoles measurements. The measurements were performed with the ABEM SAS-4000 (4 channels). For each measurement, we performed stacking to get a standard deviation better than 5% with a maximum of 10 stacks used for each measurements (data with standard deviations higher than 10% were removed from the dataset). Data with standard deviations comprised between 5 to 10% were kept in the dataset. The data were both inverted in 2.5D and in 3D as discussed below (note that all the data were acquired along profiles, not in 3D). All the measurements were performed with the Wenner and Wenner Schlumberger arrays with 64 stainless steel electrodes per profile. With the exception of Profiles P6 and P9, the contact resistances were always smaller than 3 kOhm (better than 600 Ohm for 91% of the measurements). Profiles P6 and P9 were partly performed through asphalt and were characterized by contact resistances as high as 6 kOhm in some cases. The injected current was between 20 to 200 mA depending on the contact resistances.

The profiles were first inverted with the code of Karaoulis et al. (2011a, b). The approach is summarized in Appendix A. Topography was included in the inversion. Data quality (based on the standard deviation recorded by the impedance meter) was included in the inversion process. The noise was incorporated in a data covariance diagonal matrix and applied to the data misfit contribution of the cost function to minimize (Appendix A). The variance was determined from the repeats performed for each measurements. A subset of these profiles (P14 and P15) is shown in Figure 4a, b. In Figures 4c and d, we show the inversion of a synthetic case study with a resistive substratum, the saprolitic aquifer, and a more resistive vadose zone. A conductive plume is included in the aquifer. We used 48 electrodes on the ground surface (4 meter spacing), 5% random noise added to the data (typical of the field data) and the Wenner Schumberger array. The inversion converged in 5 iterations and the data RMS error was 1.8%. The inversion is showing that we can recover the position of the plume and get a fairly good idea of the position of the substratum.

The profiles were also inverted in 3D with the software ERTLab manufactured by Geostudi Astier (the algorithm is based on the work of Morelli and Labrecque., 1996, see also Santarato et al., 2011) using finite elements with tetrahedrons. Topography was included in the inversion. The inversion was done in 3 iterations leading to a data RMS error of 5 %. Anisotropy of the formations was not accounted for but expected to be much smaller than for permeability. The anisotropy ratio of permeability is on the order of 100 (the material is transversely isotropic material, see Shevenell et al., 1994). This strong anisotropy of permeability is due to the presence of cracks inherited from the parent bedrock (Figure 2). That said, the anisotropy ratio for resistivity is usually smaller than for permeability (Ghous et al., 2005). Note also that all our measurements are in the strike direction or perpendicular to it and therefore not accounting for resistivity anisotropy may be a reasonable choice in this case. The mesh grid size is equal to 1.25 m into x, y and z direction. The results of the 3D inversion with ERTLab is shown in Figure 5. An interpretation is discussed below.

Interpretation of the Resistivity Profiles

The profiles P8, P1, and P2 are located SouthWest of the S-3 ponds (Figure 3). From the 3D resistivity tomogram shown in Figure 5, three distinct plumes characterized by low resistivity anomalies (< 15 Ohm m) can be observed. They are typically located at a depth comprised between 4 to 12 m. CP2 is a plume recognized in previous surveys (Watson et al., 2005) has having a high nitrate concentration (>40,000 mg L^{-1}, see Table 3). CP1, further south, is characterized by the highest uranium concentration around the former S-3 ponds (Watson et al., 2005). The direction of the two plumes is nearly perpendicular to the edge of the S-3 basins.

Profiles P12, P11, P10, P14 and P15 are located SouthEast of the S-3 ponds. The 3D resistivity tomogram shows a main plume (termed CP4, see Figures 4a and 4b) localized between 5 to 15 m deep. Close to the S-3 ponds, this plume is nearly perpendicular to the edge of the ponds but move in the southern direction in the next profiles. The 3D resistivity tomogram (see Figure 5) displays a more resistive aquifer (in the range 50-80 Ohm m) along the north boundary of the S-3 ponds. This high resistivity is consistent with the absence of conductive contaminant plumes along this upstream boundary (Salomon et al., 1992). The tomograms suggest that the main plumes occur therefore downstream at the WestSouth and EastSouth sides of the S-3 ponds. This is showing clearly that the presence of the contaminants has a high impact upon the resistivity of the aquifer with local variations in the porosity and clay content playing a secondary role.

Connection to Petrophysics

The resistivity of the contaminant plumes is typically in the range 2 to 15 Ohm m while the resistivity of the uncontaminated bedrock is typically in the range 40 to 150 Ohm m. Figure 6 shows some saprolite resistivity data versus pore water conductivity data. This choice was made because we are interested to interpret the electrical resistivity tomograms in terms of pore water conductivity and then, as discussed further below, in terms of nitrate concentration. The in situ data are given in terms of water conductivity measured in a set of wells.. Figure 6 displays laboratory electrical conductivity measurements made by Revil et al. (2012) for three saprolitic samples from the background site of Oak Ridge, additional laboratory data on an intact core sample from the contaminanted portion of the aquifer (Revil et al., unpublished work), and some field data from Watson et al. (2005). These field data are based on the resistivity pixel associated with the wells at the position where the pore water sample used to measure the conductivity values was taken. The background site is an uncontaminated site localized few miles away, upgradient, in the same formations present at the IFRC. In the case of the data of Revil et al. (2012), the laboratory measurements were performed both with the background water and with NaCl solutions and are here reported at 1 Hz, which is the frequency used for the DC resistivity surveys. For the data reported by Revil et al. (unpublished work), the measurements were performed with in situ pore waters.

Figure 6 shows two end-members for the saprolite resistivity and pore water conductivity. With the background water (see Table 1), the resistivity of the saprolite is controlled by the surface conductivity along the mineral water interface and not by the formation factor. In these conditions,

the saprolite resistivity is in the range 20 to 150 ohm m (Revil et al., 2012). The other end-member is observed at high nitrate concentrations or NaCl salinity. In this case, the resistivity is controlled by the formation factor F which is in the range 4 to 6 according to the laboratory measurements.

In order to be more quantitative, the electrical conductivity of the saprolitic material σ (in S m^{-1}) can be explicitly written as a function of the formation factor F (dimensionless) and the surface conductivity σ_S (in S m^{-1}) by (Waxman and Smits, 1968; Revil et al., 2012),

$$\sigma = \frac{1}{F}\sigma_w + \sigma_S \, . \tag{1}$$

where σ_w denotes the pore water conductivity (in S m^{-1}). The DC-resistivity is given by $\rho = 1/\sigma$. According to Figure 6 (based on both laboratory and field data), a mean value of the formation factor is $F = 20 \pm 10$ and a mean value of the surface conductivity is $\sigma_S = (2 \pm 1) \times 10^{-2}$ S m^{-1} (at 25°C). The lower curve in Figure 6 corresponds to a formation factor of 5 and a mean value for the surface conductivity of 4×10^{-2} S m^{-1} while the upper line corresponds to a formation factor of 40 and a mean value for the surface conductivity of 0.5×10^{-2} S m^{-1}.

The second step of our analysis is to connect the ground water conductivity to the nitrate concentration. Indeed, knowing the nitrate concentration is of paramount importance to understand the chemistry of uranium (Wu et al., 2010, Gasperikova et al., 2012). This is because nitrates serve as an oxidant for uranium and transform immobile U(IV) to mobile U(VI). The conductivity of the pore water solution depends on all the ions that are present. Nitrate is however one of the major anion and therefore it is legitimate to look for a relationship between the ground water conductivity and the nitrate concentration. This relationship should honor the fact that there is nearly no nitrate in the background pore water (see Table 1). We propose therefore the following linear relationship between the conductivity of the pore water and the nitrate concentration (see Figure 7 and Kowalsky et al. 2011),

$$\sigma_w(25°\text{C}, C_N) = \sigma_w(25°\text{C}, \text{Background}) + 10^{-4} \times C_N(\text{mg/L}) \, , \tag{2}$$

where $C_N(\text{mg/L})$ denotes the concentration in nitrate expressed in mg L^{-1} while the conductivity of the pore water is expressed in S m^{-1}. The background conductivity of the pore water is reported in Table 1 for the background (upstream) site discussed by Revil et al. (2012). It is equal to 0.065 ± 0.020 S m^{-1} at 25°C (the nitrate concentration in the background water is < 0.1 - 2.3 mg L^{-1}, see Table 1, and therefore negligible). The factor 10^{-4} is from Kowalsky et al. (2011). However, the background value for the pore water conductivity used by Kowalsky et al. (2011) is much too high (0.363 S m^{-1} at 25°C) probably to compensate for surface conductivity, which is not accounted for in their work. The validity of Equation (2) can be also tested with the two highest concentration / pore water conductivities reported by Watson et al. (2005) for the contaminant plume CP2. These two highest concentrations are 44,248 and 49,800 mg L^{-1}. According to Eq. (2), this corresponds to pore water conductivities of 4.5 and 5.0 S m^{-1} (at 25°C), respectively. The measured values (corrected for

temperature at 25°C) are 4.2 and 5.3 S m^{-1}, respectively. Therefore there is a good agreement between the value predicted by equation (2) and those measured in the field including for extreme values of the nitrate concentrations (minimum and maximum cases).

The formation factor is related to the porosity by Archie's law,

$$F = \phi^{-m}. \tag{3}$$

where *m* is called the cementation exponent. A cementation exponent of 1.6 was observed for core sample measurements by Revil et al. (2012). A formation factor in the range 5 to 40 (see Figure 6) implies therefore a porosity of the aquifer in the range 0.10 to 0.37 with an average value of 0.23. This value is close to the porosity reported by Driese (2002) for the saprolitic aquifer (0.25 at 5 m depth). Kowalsky et al. (2011) found as a result of their inversion a cementation exponent in the range 0.8 to 1.3. A cementation exponent smaller than 1 is unphysical (Revil and Cathles, 1999) pointing out a problem in their procedure. A value of 1.3 seems also very low with respect to our laboratory measurements (m = 1.6±0.1, see Revil et al., 2012). Indeed, a formation factor of 20 with a cementation exponent of 1.3 yields a porosity of 10% for the transition zone, which is too low with respect to core sample measurements and in situ observations.

We can also check if the value of the surface conductivity determined from Figure 6 (mixing laboratory and field data) is reasonable or not with respect to the value of the cation exchange capacity reported for the saprolite. According to the recent model of Revil (2012), surface conductivity is mostly due to the cations present in the diffuse layer. The surface conductivity can be related to the cation exchange capacity CEC by (Revil, 2012; Revil et al., 2012),

$$\sigma_S = \frac{1}{F}\beta_{(+)}(1-f)Q_V, \tag{4}$$

$$Q_V = \rho_g\left(\frac{1-\phi}{\phi}\right)\mathrm{CEC}, \tag{5}$$

where *f* is the fraction of counterions in the Stern layer (also called the partition coefficient by Revil and Florsch, 2010, and Revil, 2012). Taking f = 0.92 (Revil et al., 2012, a very reasonable value for illite, see Revil, 2012) and $\beta_{(+)}(Na^+, 25°C) = 5.2\times10^{-8}$ $m^2s^{-1}V^{-1}$ (the value of the mobility for sodium in the pore water) yields $Q_V = 9.6\times10^7$ C m^{-3}. Using this value in Eq. (5) together with a mass density for the grains of ρ_g = 2650 kg m^{-3} (Revil et al., 2012) yields a CEC of 6.6 cmol kg^{-1}. This compares very well with the value of the CEC reported by Kim et al. (2009b), 10.5 cmol kg^{-1} for a saprolite from the IFRC collected at a depth of 1 m and using a chemical titration approach.

We have used the methodology discussed previously to compute the nitrate concentrations from the inversion of the resistivity profiles. We use the following two steps:

(1) Equation 1 is used to determine the pore water conductivity using a mean value for the formation factor of 20 and a mean value for the surface conductivity of 2×10^{-2} S m^{-1} (Figure 6).

(2) We use Equation 2 to determine the nitrate concentration using a background pore water conductivity of 0.065±0.020 S m^{-1} (Figure 7).

In Figure 8, 9, and 10, we see that the plumes follow some well defined flow tubes. The plumes located West to the former S-3 ponds follow the strike direction of the formations (see Figure 2). We found nitration concentrations typically comprised between about 0 and 50,000 mg L^{-1}, a result consistent with in situ measurements (e.g., Watson et al., 2005). The highest nitration concentrations are found in the plumes CP2 and CP4 (>40,000 mg L^{-1}) close to the boundaries of the S-3 Ponds. Plume CP1 is characterized by a nitrate concentration on the order of 10,000 mg L^{-1}. We will see however that the concentration of this plume changes over the year as reported by Kowalsky et al. (2011). Plume CP3 is characterized by a nitrate concentration on the order of 10,000 mg L^{-1} (see Figure 8). Plume CP5 is characterized by a nitrate concentration of about 10,000 (Figure 9).

We should however recognized that the present approach may be fraught with potential pitfalls like for instance mapping of regularization artifacts from the resistivity imaging into predictions of nitrate distributions. To check if this is the case, we looked at the prediction of our approach in terms of a comparison with in situ data.

Figure 11 provides a validation test of the accuracy of our approach. In this figure we plot the pore water conductivity inferred from the resistivity tomograms (using $\sigma_w = F(1/\rho - \sigma_S)$ and F = 20 and σ_S = 2×10^{-2} S m^{-1} as discussed above) versus in situ data based on water samples collected in 21 wells (see Figure 3). We see that our approach is validated by this test. The extreme changes in the ionic strength of the pore water due to the contamination overprint local effects associated with spatial change in the formation factor and surface conductivity. In other words, despite the fact that the petrophysical transforms is non-stationary, the biggest effects recorded in the resistivity tomograms comes from the contamination of the aquifer and not from local change in clay content, mineralogy, and porosity. We have performed an additional test without considering surface conductivity and we were unable to predict well the pore water conductivity. This shows that surface conductivity needs to be considered in the interpretation of the resistivity tomograms, a point that is however missed by most researchers in the hydrogeophysical community.

Geometry of the Contaminant Plumes

The interpretation of the 2.5D and 3D resistivity tomogram is summarized in Figure 12. Figure 12a is showing the flow direction of the 5 main plumes (CP1 to CP5) and the piezometric levels. The direction of the plumes CP1, CP2, CP3, and CP5 is likely due to the head gradient plus the effect of the strongly dipping heterogenity of the aquifer (Shevenell et al., 1994). Plumes CP4 move mostly in the direction of the head gradient because of the existence of some small valleys in

the saprolite / bedrock interface that are expected from the geology of the bedrock (Watson et al., 2004). The contaminant plumes are usually located in the transition zone between the saprolite and the bedrock (see Figure 3). This transition zone is usually considered to be more permeable than both the upper saprolitic aquifer and the bedrock (see Salomon et al., 1992 for in situ, ground-truth, investigations).

Time-Lapse Resistivity

In this section, we investigate the time-lapse behavior of the DC resistivity along a portion of profile P1 (see position in Figure 3) and focused on the monitoring of the contaminant plumes CP1 and CP2. As mentioned in the previous section, the plume CP1 is especially important because of its high concentration in uranium (see Table 3 and Watson et al., 2004, 2005).

Methodology

In time lapse resistivity tomography, one problem corresponds to the occurrence of artifacts in the resistivity tomograms resulting from noise present in the data. As a result, sequential inversion is not always adequate because the results can be strongly affected by the reference model used to start the sequential time-lapse inversion (see tests in Karaoulis et al., 2011a). Recently, a new time-lapse regularization tool has been developed for time-lapse resistivity tomography (Kim et al., 2009a; Karaoulis et al., 2011a, b). This method, called the Active Time Constrained (ATC) approach, incorporates a time-dependent term directly in the cost-function to minimize. This approach allows to improve time-lapse imaging especially when strong noise is present in the data as long as the noise is not correlated over time.

Dataset

A total 29 snapshots of dipole dipole apparent resistivity data have been obtained downstream the former S-3 Ponds on a portion of Profile P1 (see position Figure 3). The profile is 83 m long and comprises 112 stainless steel electrodes. Each snapshot include 2568 measurements with a combination of dipole-dipole, Wenner, and Wenner-Schlumberger arrays. The measurements were performed with AGI resistivity meter. The average contact resistance was 1 kOhm. A total of 74,472 total measurement were considered in our test and inverted altogether. Each resistivity dataset contained both repeated and reciprocal measurements to help identify and remove noisy data. Measurements that differed by more than 3% were removed from the data set prior the time lapse inversion. Less than 1% of the repeat and reciprocal measurements had an error > 3%, and less than 10% of the data were removed. The remaining data were averaged and the noise included in a covariance matrix to weight the data during the inversion process.

The result of the time-lapse inversion is shown in Figure 13a. The inversion converged after 7 iterations with a data RMS error of 15% (Figure 13c). This high RMS error is due to some relatively random noise in the data (filtering further the data prior the inversion reduced the data

RMS error to 5% without changing the structure of the tomogram). This is consistent with the results of Revil et al. (2008): adding random noise to the apparent resistivity data may increase significantly the data RMS error without changing the structure of the inverted model. The inverted tomograms show the position of both the CP1 plume (characterized by relatively low nitrate and high uranium concentrations) and the CP2 plume (characterized by high nitrate and low uranium concentrations) (see Figure 13b). A typical sensitivity map of the tomogram is shown in Figure 13d. This map provides credence that the changes in the plumes CP1 and CP2 are not artifacts of the inversion as discussed further below.

Results

We reported the evolution of the resistivity for two characteristic points (termed A and B) belonging to the plumes CP1 and CP2, respectively (see Figure 13c). These data are reported in Figure 14 for the set of snapshots corresponding to the winter time (Figure 14a) and for the snapshots corresponding to the summer time (Figure 14b). One characteristic event (Event #1 in Figure 14a) is the decrease, by a factor 3, of the resistivity of the plume CP1 located close to the main recharge of the aquifer through the South corner of the ditch surrounding the S-3 ponds.

This ditch may play an important role in the hydrogeology of the plumes. Indeed all the meteoritic water received by the parking lot built on the top of the former S-3 basins is collected by this ditch. The southern corner of the ditch is slightly lower in altitude than elsewhere and could serve as a preferential infiltration pathway to the aquifer. Note that the position of the profile P1 is located approximately 2 m from the center of this ditch.

The decrease of the resistivity of Plume CP1 by a factor 3 may therefore corresponds to a drying event (no recharge through the ditch) that occurred several months prior the record of the resistivity tomograms in summer 2008. The background resistivity of plume CP2 is 5 ohm m and remains nearly constant during the investigated period of time. Using equations 1 and 2, this corresponds to a nitrate concentration of 39,000 mg L^{-1} in plume CP2 at the time of the measurements The understanding of the dynamics of the plumes CP1 and CP2 will obviously require further modeling but could be due to infiltration from the ditch as shown in Figure 12b at the south corner of the former S-3 ponds.

Figure 15 shows the computation of the evolution of the nitrate concentration at point A of plume CP1 using the resistivity data extracted from the tomograms at this point (Figure 14a). We used the same transforms as above to analyze the static distribution of the resistivity in terms of pore water conductivity and nitrate concentration. Very few in situ measurements were performed at the same time (Winter 2008-2009) around plume CP1. That said, the end of Event 1 in Figure 14 is consistent with the variations recorded in well FW120 nearby where the nitrate concentration was observed to decrease from 5200 mg L^{-1} to 3300 mg L^{-1} (Kowalsky et al., 2011).

Self-potential

Measurements and Observation

A self-potential survey was performed in May, 2011 and includes 764 measurements (1 m spacing along 6 profiles). The position of the self-potential stations is shown in Figure 16. Unfortunately the raw data were dominated by a strong cultural source coming from a mise-à-la-masse at location A in Figure 3. Therefore before to be able to interpret the self-potential data, we had to remove the effect of this spurious cultural source. In agreement with the shape of the buried metallic body, we simulated a buried horizontal line source. This source current is described by its current amplitude and its position. The genetic algorithm from the MATLAB Global Optimization Toolbox was used for that purpose. The inversion of this source was performed by accounting for the 3D resistivity distribution shown in Figure 5. We obtained a source amplitude of 0.11 A/m, the current source starts at position (-48 m, 34 m, 0 m) and ends at position (-46 m, 70 m, 0 m) (see the plain line in Figure 16a). This position is consistent with the visual inspection of where the mise-à-la-masse is observed in the field. After estimating the distribution of the electrical voltage distribution due to this current source, we removed this distribution from the raw self-potential map to obtained a corrected (residual) self-potential map, which is shown in Figures 16b and 17.

The residual self-potential map exhibits a strong dipolar anomaly (150 mV to -200 mV). The position of this anomaly is grossly consistent with an area that was biostimulated in 2005 (Luo et al., 2006; Wu et al., 2006a, see the two rectangles in Figure 17). Bioremediation was stimulated by injecting ethanol as an electron donor (Luo et al., 2006; Wu et al., 2006a). Injection of ethanol over a period of 13 months resulted in U(VI) reduction and denitrification (Wu et al., 2006b). Sulfate reduction was also observed towards the end of the experiments. Aqueous sampling and analysis in February 2012 indicated that nitrate concentrations still remained lower in this area compared to the concentrations reported before the biostimulation experiment. Throughout 2011, the ground water pH was adjusted by addition of potassium hydroxide to clean water injected in this area.

Physics

Areas characterized by gradients in the redox potential and microbial activity (thanks to the presence of nutrient like ethanol) are usually characterized by strong self-potential anomalies (Revil et al., 2010; Fachin et al., 2012). It is therefore possible that the dipolar anomaly observed in the field is the result of the bioremediation experiment. The two half-reactions for the electron donor (ethanol) and electron acceptor (oxygen) are,

$$3H_2O + C_2H_5OH \Leftrightarrow 2CO_2 + 12H^+ + 12e^-, \quad (7)$$

$$3O_2 + 12H^+ + 12e^- \Leftrightarrow 6H_2O. \quad (8)$$

Wu et al. (2006b) have shown that the bacteria population is dominated by Rhodanobacter (a nitrate reducer bacteria) with a maximum density if 10^4 cells mL^{-1} in the acidic portion of the plume (10^{12}

cells m^{-3}). This pretty high density of cells may be responsible for the formation of biofilms. Therefore according to the model developed by Revil et al. (2010), all the ingredients that are required for a geobattery are present at this site. Two observations may confirm this idea: (i) the magnitude of the self-potential dipolar anomaly should be half of the difference of redox potential and (ii) the position of the source current density should be shallow at the upper fringe of the plume (4 to 8 m deep). We test now these two points.

The source current density in presence of a redox potential gradient and in presence of a pathway for the electrons, is given by,

$$\mathbf{j}_S = \frac{k_b T}{e} \sigma \nabla \ln\{e^-\} = -\sigma \nabla E_h , \tag{9}$$

where T is the absolute temperature in K, e is the elementary charge of the electron, k_b is the Boltzmann constant, $\{e^-\}$ denotes the activity of the electrons, and E_h the redox potential. The total current density is given by,

$$\mathbf{j} = -\sigma \nabla \psi - \sigma \nabla E_h , \tag{10}$$

If the total current density **j** is zero, the electrical potential is equal in magnitude and opposite in sign to the redox potential (Revil et al., 2010). The redox potential in the wells around the S-3 ponds is typically 200±100 mV (Watson et al., 2004). In the biostimulated area, the redox potential reaches -250 mV. This implies a difference of electrical redox potential of 450 mV with a positive pole in the biostimulated area. The observed difference of electrical potential is 400 mV, which is consistent with the conceptual model outlined above.

In order to localize the depth of the causative source responsible for the observed self-potential anomaly, we need to invert the self-potential data. We used below a gradient-based approach outlined in Appendix B. The continuity equation for the current is $\nabla \cdot \mathbf{j} = 0$, which yields the following Poisson equation for the electrical potential ψ,

$$\nabla \cdot (\sigma \nabla \psi) = \nabla \cdot \mathbf{j}_S . \tag{11}$$

In Appendix B, we describe the gradient-based algorithm used to invert the self-potential data in term of a source current density distribution in the subsurface. The inversion accounts for the 3D resistivity distribution shown in Figure 5. In our model the subsurface was discretized in 2000 cells, (size: x = 2.5m, y = 3.5 m, z = 4 m) covering the domain from x= -32 m to 15 m, y from 0 m to 70 m, and z from a depth of 4 m to 24 m. The result of the inversion is shown in Figure 18. The source current density responsible for the residual self-potential anomaly is located between 4 and 8 m, that is consistent with the upper boundary of the CP1 plume (Figure 13b). Therefore there is the

possibility that the self-potential data provide some information relative to the distribution of te redox potential of the plume, an idea that would deserve more attention in the future.

Conclusions

Hydrogeophysical investigations performed around the former S-3 settling basins at the Oak Ridge Integrated Field Research Challenge site, Tennessee have revealed the following features:

1. Five main plumes have been detected by 2.5D/3D resistivity tomography, three plumes on the Western part of the S-3 Ponds (CP1, CP2, and CP3), 1 main plume (CP4) in the southern part of the S-3 ponds, and potentially another small plume further north to the CP3 plume named CP5.

2. A methodology has been developed to use the resistivity tomograms and compute the nitrate concentration in the plumes around the S-3 ponds. This methodology is based on a conductivity model accounting for both the formation factor and the surface conductivity. This is in contrast with previous works in which surface conductivity was considered negligible despite the presence of 20% (weigth) clay fraction and clays characterized by a high CEC. This conductivity model has been validated in a previous laboratory work (Revil et al., 2012). The pore water conductivity is related to the nitrate concentration through a linear equation accounting for the vanishingly small nitrate concentration in the background pore water and validated through well data. Future works could include larger scale resistivity tomography (at the scale of the valley) to reveal deeper flow paths used by the contaminants to move downstream. The approach developed in this paper can be applied to different sites but the values of the surface conductivity and formation factor need to carefully estimated for different formations and rock types.

3. Time-lapse resistivity tomography reveals that plume CP1 (which has the highest Uranium concentration) is characterized by fluctuations over time in agreement with in situ observations. These higher concentrations are possibly associated with the drying of the ditch surrounding the S-3 basins during the summer time and the lack of infiltration of fresh water from the ditch into the saprolitic aquifer.

4. The self-potential show a dipolar anomaly with an amplitude of four hundred millivolts centered on a biostimulated area of the CP1 plume. This could open the door to the use of time-lapse self-potential data to monitor non-intrusively bioremediation in the saprolitic aquifer.

Acknowledgments. We thank the Environment Remediation Science Program (ERSP), U.S. Department of Energy (DOE, award DE-FG02-08ER64659) for funding. The authors appreciate the efforts of Davis Lesmes, the ERSP program manager. We thank Lee Slater, two anonymous referees, the two editors, Michael Asten and Evert Slob, for the time spent on our manuscript and their comments.

References

Archie, G.E., 1942, The electrical resistivity log as an aid in determining some reservoir characteristics: Transactions of AIME**, 146,** 54–62.

Atekwana E.A., E. A. Atekwana, R. S. Rowe, D. D. Werkema Jr., and F. D. Legall, 2004, The relationship of total dissolved solids measurements to bulk electrical conductivity in an aquifer contaminated with hydrocarbon: Journal of Applied Geophysics, **56**, 281– 294.

Binley, A., S. Henry-Poulter, and B. Shaw, 1996, Examination of solute transport in an undisturbed soil column using electrical resistance tomography: Water Resources Research, 32, no. 4, 763–769.

Binley, A., G. Cassiani, R. Middleton, and P. Winship, 2002, Vadose zone flow model parameterisation using cross-borehole radar and resistivity imaging: Journal of Hydrology, 267, no. 3–4, 147–159.

Bolève A., F. Janod, A. Revil, A. Lafon, and J.-J. Fry, 2011, Localization and quantification of leakages in dams using time-lapse self-potential measurements associated with salt tracer injection: Journal of Hydrology, **403**, no. 3-4, 242-252.

Cassiani, G., V. Bruno, A. Villa, N. Fusi, and A. M. Binley, 2006, A saline trace test monitored via time-lapse surface electrical resistivity tomography, Journal of Applied Geophysics, **59**, no. 3, 244–259.

Chen, J., S.S. Hubbard, J. Peterson, K. Williams, M. Fienen, P. Jardine, and D. Watson, 2006. Development of a joint hydrogeophysical inversion approach and application to a contaminated fractured aquifer: Water Resources Research, **42**, W06425, doi:10.1029/2005WR004694.

Cole, K.S., and R.H., Cole, 1941, Dispersion and absorption in dielectrics I. Alternating current characteristics: Journal of Chemical Physics, **9**, 341–351.

De Witte, L. (1948), A new method of interpretation of self-potential field data: Geophysics, **13**, no. 4, 600-608.

Dey, A., and H. F. Morrison, 1979, Resistivity modeling for arbitrary shaped two-dimensional structures: Geophysical Prospecting, **27**, 106-136.

Dreier, R.B., T.O. Early, and H.L. King, 1993, Results and interpretation of ground water data obtained from multiport-instrumented coreholes (GW-131 through GW-135), fiscal years 1990-1991, Oak Ridge Y-12 Plant Report, Y-TS-803.

Driese, S.G., L.D. McKay, and C.P. Penfield, 2001, Lithologic and pedogenic influences on porosity distribution and groundwater flow in fractured sedimentary saprolite: a new application of environmental sedimentology: Journal of Sedimentary Research, **71**, no. 5, 843–857.

Fachin, S.J.S., E.L. Abreu, C.A. Mendonça, A. Revil, G.C. Novaes, and S.S. Vasconcelos, 2012, Self-potential signals from an analog biogeobattery model: Geophysics, **77**, no.4, EN29-EN37, doi: 10.1190/GEO2011-0352.1.

Gasperikova E., S. S. Hubbard, D. B. Watson, G. S. Baker, J. E., Peterson, M. B. Kowalsky, M. Smith, and S. Brooks, 2012, Long-term electrical resistivity monitoring of recharge-induced contaminant plume behavior, submitted to Contaminant Hydrogeology.

Geraghty and Miller Inc, 1989, Groundwater quality assessment of the S-3 site, hazardous waste disposal unit at the Y-12 Plant, 1988, Oak Ridge Y-12 Plant report Y-SUB/89-00206C/7.

Ghous A., F. Bauget, C. H. Arns, A. Sakellariou, T.J. Senden, A. P. Sheppard, R. M. Sok, W. V. Pinczewski, R. G. Harris, G. F. Beck, and M.A. Knackstedt, 2005, Resistivity and permeability anisotropy measured in laminated sands via digital core analysis, SPWLA 46th Annual Logging Symposium, June 26-29, 2005, Paper VVV, 14 pp.

Gu B., S.C. Brooks, Y. Roh, and P.M. Jardine, 2003, Geochemical reaction and dynamics during titration of a contaminated groundwater with high uranium, aluminum, and calcium: Geochimica et Cosmochimica Acta, **67**, 2749–2761.

Hermans, T., A. Vandenbohede, L. Lebbe, and F. Nguyen, 2012, A shallow geothermal experiment in a sandy aquifer monitored using electric resistivity tomography: Geophysics, **77**, no. 1, B11.

Ikard S., W.F. Woodruff, A. Revil, M. Parekh, and M. Mooney, 2012, A saline pulse test method monitored by self-potential to determine non-intrusively the velocity of the pore water: Water Resources Research, **48**, W04201, doi:10.1029/2010WR010247.

Irving, J., and K. Singha, 2010, Stochastic inversion of tracer test and electrical geophysical data to estimate hydraulic conductivities: Water Resources Research, **46**, W11514, doi:10.1029/2009WR008340.

Jardani A., A. Revil, A. Bolève, and J.P. Dupont, 2008, 3D inversion of self-potential data used to constrain the pattern of ground water flow in geothermal fields: Journal of Geophysical Research, **113**, B09204, doi: 10.1029/2007JB005302.

Johnson T. C., R. J. Versteeg, A. Ward, F. D. Day-Lewis, and A. Revil, 2010, Improved hydrogeophysical characterization and monitoring through high performance electrical geophysical modeling and inversion: Geophysics, 75, no. 4, WA27-WA41.

Karaoulis, M.,. J.-H. Kim, and P.I. Tsourlos, 2011a, 4D Active Time Constrained Inversion: Journal of Applied Geophysics, **73**, no. 1, 25-34.

Karaoulis M., A. Revil, D.D. Werkema, B. Minsley, W.F. Woodruff, and A. Kemna, 2011b, Time-lapse 3D inversion of complex conductivity data using an active time constrained (ATC) approach: Geophysical Journal International, **187**, 237–251, doi: 10.1111/j.1365-246X.2011.05156.x.

Kemna, A., 2000, Tomographic inversion of complex resistivity-theory and application: Ph.D Dissertation, Ruhr-University of Bochum, Germany, 196 pp.

Kemna, A., J. Vanderborght, B. Kulessa, and H. Vereecken, 2002, Imaging and characterization of subsurface solute transport using electrical resistivity tomography (ERT) and equivalent transport models, Journal of Hydrology, **267**, no. 3–4, 125–146.

Kim J.-H., M.J. Yi, S.G. Park, and J.G. Kim, 2009a, 4-D inversion of DC resistivity monitoring data acquired over a dynamically changing earth model: Journal of Applied Geophysics, **68**, no. 4, 522-532.

Kim Y.J., J.W. Moon Y. Roh, and S. C. Brooks, 2009b, Mineralogical characterization of saprolite at the FRC background site in Oak Ridge, Tennessee: Environmental Geology, **58**, 1301–1307.

Kowalsky, M. B., E. Gasperikova, S. Finsterle, D. Watson, G. Baker, and **S. S. Hubbard**, 2011, Coupled modeling of hydrogeochemical and electrical resistivity data for exploring the impact of recharge on subsurface contamination, Water Resources Research, **47**, W02509.

Kruschwitz, S., A. Binley, D. Lesmes, and A. Elshenawy, 2010, Textural controls on low frequency electrical spectra of porous media: Geophysics, **75**, no. 4, WA113-WA123.

LaBrecque D.J., M., Miletto, W.D., Daily, A.L., Ramirez, and E. Owen, 1996, The effects of noise on Occam's inversion of resistivity tomography data: Geophysics, **61**, 538-548.

Legaz, A., J. Vandemeulebrouck, A. Revil, A. Kemna, A. W. Hurst, R. Reeves, and R. Papasin, 2009, A case study of resistivity and self-potential signatures of hydrothermal instabilities, Inferno Crater Lake, Waimangu, New Zealand: Geophysical Research Letters, **36**, L12306, doi:10.1029/2009GL037573.

Linde, N., and A. Revil, Inverting self-potential data for redox potentials of contaminant plumes: Geophysical Research Letters, **34**, L14302, doi:10.1029/2007GL030084, 2007.

Luo, J., W. Wu, M.N. Fienen, P.M., Jardine, T.L. Mehlhorn, D. B. Watson, O.A. Cirpka, C.S. Criddle, and P.K. Kitanidis, 2006, A nested-well approach for in situ remediation: Ground Water, **44**, 266-274.

Ogilvy A.A., M.A. Ayed, and V.A. Bogoslovsky, 1969, Geophysical studies of water leakage from reservoirs: Geophysical Prospecting, **22**, 36–62.

McKay L. D., S. G. Driese, K. H. Smith, and M. J. Vepraskas, 2005, Hydrogeology and pedology of saprolite formed from sedimentary rock, eastern Tennessee, USA: Geoderma, **126**, 27–45.

Merkler G.-P., H. Militzer, H. Hötzl, H. Armbruster, and J. Brauns, 1989, Detection of Subsurface Flow Phenomena. Lecture Notes in Earth Sciences: **27**, Springer, Berlin/Heidelberg, ISBN 978-3-540-51875-4, 514 pages.

Morelli, G., and D.J. LaBrecque, 1996, Advances in ERT inverse modelling: European Journal of Environmental and Engineering Geophysical Society, **1**, no. 2, 171–186.

Müller, K., J. Vanderborght, A. Englert, A. Kemna, J. A. Huisman, J. Rings, and H. Vereecken, 2010, Imaging and characterization of solute transport during two tracer tests in a shallow aquifer using electrical resistivity tomography and multilevel groundwater samplers: Water Resources Research, **46**, W03502, doi:10.1029/2008WR007595.

Naudet, V., A. Revil, J.-Y. Bottero, and P. Bégassat, 2003, Relationship between self-potential (SP) signals and redox conditions in contaminated groundwater: Geophysical Research Letters, **30**, no. 21, 2091, doi: 10.1029/2003GL018096.

Pollock, D., and O. A. Cirpka, 2012, Fully coupled hydrogeophysical inversion of a laboratory salt tracer experiment monitored by electrical resistivity tomography: Water Resources Research**, 48**, W01505, doi:10.1029/2011WR010779.

Revil, A., L.M. Cathles, S. Losh, and J.A. Nunn, 1998, Electrical conductivity in shaly sands with geophysical applications: Journal of Geophysical Research, **103**, no. B10, 23,925-23,936.

Revil, A., and L.M. Cathles, 1999, Permeability of shaly sands: Water Resources Research, **35**, no. 3, 651-662.

Revil, A., and N. Linde, 2006, Chemico-electromechanical coupling in microporous media, Journal of Colloid and Interface Science, **302**, 682-694.

Revil, A. and N. Florsch, 2010, Determination of permeability from spectral induced polarization in granular media: Geophysical Journal International, **181**, 1480-1498. doi: 10.1111/j.1365-246X.2010.04573.x.

Revil A., C.A. Mendonça, E. Atekwana, B. Kulessa, S.S. Hubbard, and K. Bolhen, 2010, Understanding biogeobatteries: where geophysics meets microbiology: Journal of Geophysical Research, **115**, G00G02, doi:10.1029/2009JG001065.

Revil, A., 2012, Spectral induced polarization of shaly sands: Influence of the electrical double layer: Water Resources Research, **48**, W02517, doi:10.1029/2011WR011260.

Revil A., Y. Wu, M. Karaoulis, S. S. Hubbard, and D. B. Watson, 2012, Geochemical and geophysical responses during shallow perched water infiltration into contaminated saprolite from the Oak Ridge Integrated Field Research Challenge site, Tennessee, in preparation for Water Resources Research.

Revil, A., M. Skold, A. Revil, S. S. Hubbard, Y. Wu, D. B. Watson, M. Karaoulis, 2012, Petrophysical properties of saprolite from the Oak Ridge Integrated Field Research Challenge site, Tennessee, submitted to Geophysics.

Robert, T., D. Caterina, J. Deceuster, O. Kaufmann, and F. Nguyen, 2012, A salt tracer test monitored with surface ERT to detect preferential flow and transport paths in fractured/karstified limestones: Geophysics, **77**, no. 2, B55-B67.

Rozycki A., 2009, Evaluation of the streaming potential effect of piping phenomena using a finite cylinder model: Engineering Geology, **104**, no. 1-2, 98-108.

Salomon, D.K., G.K. Moore, L.E. Toran, and W.M. McMaster, 1992, A hydrologic framework for the Oak Ridge Reservation: ORNL/TM-12026. Oak Ridge, Tennessee: Dept. of Energy.

Santarato, G., G. Ranieri, M. Occhi, G. Morelli, Fischanger, and D. Gualerzi, 2011, Three Dimensional Electrical resistivity tomography to control the injection of expanding resins for the treatment and stabilization of foundation soils: Engineering Geology, **119**, no. 1-2, 18-30.

Shevenell, L.A., G.K. Moore, and R.B. Dreier, 1994, Contaminant spread and flushing in fractured rocks near Oak Ridge, Tennessee, GWMR, 120-129.

Sill, W.R., and T.J. Killpack, 1982, SPXCPL: Two-dimensional modelling program of self-potential effects from cross-coupled fluid and heat flow (User's guide and documentation for version 1.0): Report DOE/ID/12079-60 ESL-74, Earth Sciences Laboratory, University of Utah.

Singha, K., and S. M. Gorelick, 2005, Saline tracer visualized with threedimensional electrical resistivity tomography: Field-scale spatial moment analysis: Water Resources Research, **41**, W05023, doi:10.1029/ 2004WR003460.

Slater, L., A. M. Binley, W. Daily, and R. Johnson, 2000, Cross-hole electrical imaging of a controlled saline tracer injection: Journal of Applied Geophysics, 44, no. 2–3, 85–102.

Vanderborght, J., A. Kemna, H. Hardelauf, and H. Vereecken, 2005, Potential of electrical resistivity tomography to infer aquifer transport characteristics from tracer studies: A synthetic case study: Water Resources Research, **41**, W06013, doi:10.1029/2004WR003774.

Watson D.B., J.E. Kostka, M.W. Fields, P.M. Jardine, 2004, The Oak Ridge Field Research Center conceptual model, NABIR Research Project Report, 55 pp.

Watson, D.B., W.E. Doll, T.J. Gamey, J.R. Sheehan, and P. M. Jardine, 2005, Plume and lithologic profiling with surface resistivity and seismic tomography: Ground Water, **43**, no. 2, 169-177.

Waxman, M. H., and L. J. M. Smits, 1968, Electrical conductivities in oilbearing shaly sands: J. Soc. Pet. Eng., **8**, 107–122.

Wu, W., J. Carley, M. Fienen, T. Mehlhorn, K. Lowe, J. Nyman, J. Luo, M.E. Gentile, R. Rajan, D. Wagner, R.F. Hickey, B. Gu, D. Watson, O.A. Cirpka, P.K. Kitanidis, P.M. Jardine, and C.S. Criddle, 2006. Pilot-scale in situ bioremediation of uranium in a highly contaminated Aquifer. 1. Conditioning of a treatment zone: Environmental Science and Technology, **40**, 3978-3985.

Wu, W., J. Carley, T. Gentry, M.A. Ginder-Vogel, M. Fienen, T. Mehlhorn, H. Yan, S. Caroll, M.N. Pace, J. Nyman, J. Luo, M.E. Gentile, M.W. Fields, R.F. Hickey, B. Gu, D. Watson, A.A. Cirpka, J. Zhou, S. Fendorf, P.M. Kitanidis, P.M. Jardine, and C.S. Criddle, 2006, Pilot-scale in situ bioremediation of uranium in a highly contaminated aquifer. 2. Reduction of U(VI) and geochemical control of U(VI) bioavailability: Environmental Science and Technology, **40**, 3986-3995.

Appendix A. 2.5D Resistivity Tomography

We briefly describe the approach used in Karakoulis et al. (2011a, b) to perform the 2.5. resistivity tomography. The electrical potential ψ (in V) is related to the conductivity distribution σ (in S m^{-1}) and the injected current *I* (in A)through the following Poisson equation,

$$-\nabla\cdot\left[\sigma(x,y,z)\nabla\psi(x,y,z)\right]=I\delta(x-x_S)\delta(y-y_S)\delta(z-z_S)\,, \tag{A1}$$

where $\delta(x-x_s)\delta(y-y_s)\delta(y-y_s)$ in non-zero only at the locations of the electrode (δ denotes the delta function and *S* denotes the position of the source). Equation A1 is solved using the following boundary conditions:

$$\psi = p \text{ on } \Omega_1\,, \tag{A2}$$

$$\sigma\frac{\partial\psi}{\partial n}+\gamma\psi = q \text{ on } \Omega_2\,, \tag{A3}$$

where $\Omega_1+\Omega_2=\Omega$, which corresponds to the boundary enclosing the area of interest, $\hat{\boldsymbol{n}}$ denotes the outward unit vector to this surface, and *p*, *γ*, and *q* are known parameters associated with the physical properties of the boundary. In the half-space model, we used *p*=0 on Ω_1 located far away from the current sources (Dirichlet boundary condition). At the air-surface boundary Ω_2, we used *γ*=0 and *q*=0 (Neumann boundary condition).

Dey and Morisson (1979) showed that Equation A1 can be efficiently solved in 2.5D using the Fourier and inverse Fourier cosine transforms:

$$\tilde{\psi}(x,k_y,z)=\int_0^\infty\psi(x,y,z)\cos(k_y y)dy\,, \tag{A4}$$

$$\psi(x,y,z)=\frac{2}{\pi}\int_0^\infty\tilde{\psi}(x,k_y,z)\cos(k_y y)dk_y\,, \tag{A5}$$

where k_y denotes the wave number. Applying the Fourier transform to Equation A1, the field equation for the potential in the Fourier domain is given by,

$$\nabla\cdot\left[\sigma(x,z)\nabla\tilde{\psi}(x,k_y,z)\right]+k_y{}^2\tilde{\psi}(x,k_y,z)=-\frac{I}{2}\delta(x-x_S)\delta(z-z_S)\,. \tag{A6}$$

The wavenumbers k_y are calculated according to the approach developed by LaBreque et al. (1996) and Kemna (2000). The inversion is performed by minimizing the following cost function S using the L_2-norm,

$$P_\lambda(\mathbf{m}) = \left\| \boldsymbol{W}_d (\boldsymbol{Km} - \boldsymbol{d}) \right\| + \lambda \left\| \boldsymbol{Cm} \right\|, \tag{A6}$$

where $\boldsymbol{m}$ denotes the model vector, $\boldsymbol{Km}$ represents the predicted response, $\boldsymbol{W}_d$ the covariance matrix (square diagonal $M \times M$ matrix, M denotes the number of measurements) on the data vector $\boldsymbol{d}$, λ denotes the regularization parameter, and $\boldsymbol{C}$ is a square $N \times N$ regularization matrix containing the second-order derivatives of the model (N denotes the number of cells used to discretize the subsurface). The first term of the objective functions, ensures the convergence of the recovered model with respect to the observed data. The second part of the objection function is introduced to stabilize the inversion and to produce smooth models. The minimization was performed with the Gauss-Newton algorithm (see for instance Kim et al., 2009a and Johnson et al., 2010 for further details).

Appendix B. Self-Potential Tomography

The self-potential problem obeys a Poisson equation, equation 11, where ψ is the electrical potential (in V), σ is the electrical conductivity and $\mathbf{j}_S$ denotes the source current density vector characterized by three components in a cartesian coordinate system. Equation B1 is solved numerically using the finite element method and Comsol Multiphysics. The conductivity distribution was provided by the resistivity tomography discussed in the main text (see also Appendix A). Before we proceed with the inversion, we need to calculate the kernel matrix, i.e. the contribution of each point current source in the measured potential. Equation B1 is written in a matrix form as $\boldsymbol{d} = \boldsymbol{K}\boldsymbol{m}$ where $\boldsymbol{d}$ denotes the self-potential observations N-vector (N = 764) and $\boldsymbol{K}$ denotes the kernel $M \times N$ matrix and $\boldsymbol{m}$ the vector of source current density M-vector (M = 2000×3). The number of cells used to discretize the subsurface is much higher than the number of self-potential stations N ($M>>N$). The kernel is computed according to the approach discussed in Jardani et al. (2008). To determine the solution, we minimize the following cost function,

$$P_\lambda(\mathbf{m}) = \left\| \boldsymbol{W}_d(\boldsymbol{K}\boldsymbol{m} - \boldsymbol{d}) \right\| + \lambda s(\boldsymbol{m}), \tag{B1}$$

where $\boldsymbol{d}$ denotes the data vector (M observations), $s(\boldsymbol{m})$ denotes the stabilizer, λ is a Lagrange operator, $\boldsymbol{W}_d$ the covariance matrix (square diagonal $N \times N$ matrix). In order to avoid solution located close to the electrodes, we introduce a depth weighting matrix using $\boldsymbol{m}^* = \boldsymbol{J}\boldsymbol{m}$.. That way, all points of the subsurface have equal weight during the inversion process. An efficient way to calculate the depth weighting matrix $\boldsymbol{J}$ is

$$\boldsymbol{J} = \mathrm{diag}\sqrt{\sum_{i=1}^{N} {K_{ij}}^2} \tag{B3}$$

The inversion is done with the Gauss Newton approach like for resistivity.

Table 1. Background ground water composition and properties (Schreiber, 1995).

Element or property	Value
Ca (mg/L)	26 - 73; 81 (1)
Mg (mg/L)	1.7 - 9.4, 15 (1)
K (mg/L)	< 2.0 - 3.8; 3.2 (1)
Na (mg/L)	2.7 - 120, 12 (1)
HCO_3 (mg/L)	98 - 330
Cl (mg/L)	0.9 - 5.5
SO_4 (mg/L)	6.6 - 170, 14 (1)
NO_3 (mg/L)	< 0.1 - 2.1, 2.3 (1)
PO_4 (mg/L)	< 0.5
Alk. (mg/kg as $CaCO_3$)	80 - 270, 195
U (mg/L)	<0.001 (1)
pH	6.9 - 8.1, 7.7 (1)
Eh (mV)	550 (2)
TDS (mg/L)	152 - 714
Conductivity σ_w (S/m)	0.080 (1), 0.047 - 0.081 (3)

(1) Shevenell et al. (1994).

(2) Jardine et al. (1993).

(3) Skold et al. (2012).

Table 2. Maximum concentrations of the major constituents of the S-3 Ponds in 1978 together with the pH and density of the pore water (from Shevenell et al., 1994).

Element	Value (mg L^{-1})
Aluminium	4860
Boron	30
Calcium	3050
Chromium	60
Copper	44
Iron	1210
Lithium	25
Magnesium	670
Manganese	24
Nickel	130
Phosphorus	100
Potassium	420
Silicon	95
Thorium	120
Uranium	320
Chloride	2330
Fluoride	31
Nitrogen	73,800
pH	0.8
Density	1070 kg m^{-3}

Table 3. Composition of the pore water of the different plumes. U stands for Uranium concentration.

Property	CP1 FW117	CP2 FW010	CP3 FW008	CP4a FW022	CP4b FW027
σ_w (S/m)	0.54	4.11	0.77	0.75	1.59
pH	3.39	3.46	5.50	5.51	5.39
U (mg L^{-1})	22.18	0.19	0.0034	0.0856	0.0276

Table 4. Properties of the sediments. The parameter ϕ denotes the porosity, K(m s^{-1}) denotes the hydraulic conductivity, and m denotes the cementation exponent.

Property	Fill	Saprolite Upper Section	Saprolite Transition Zone	Bedrock
ϕ	0.50	0.36 (1), 0.3-0.5 (3)	0.25 (1)	0.1-0.2 (3)
K(m s^{-1})	5×10^{-4} (1)	10^{-7}-10^{-6}	4×10^{-6}	10^{-11} (3)
m (-)	1.5	1.6-1.7 (1, 2)	1.3 (1), 1.6 (2)	1.7 (2)

(1) Kowalsky et al. (2011)

(2) Skold et al. (2012)

(3) Solomon et al. (1992)

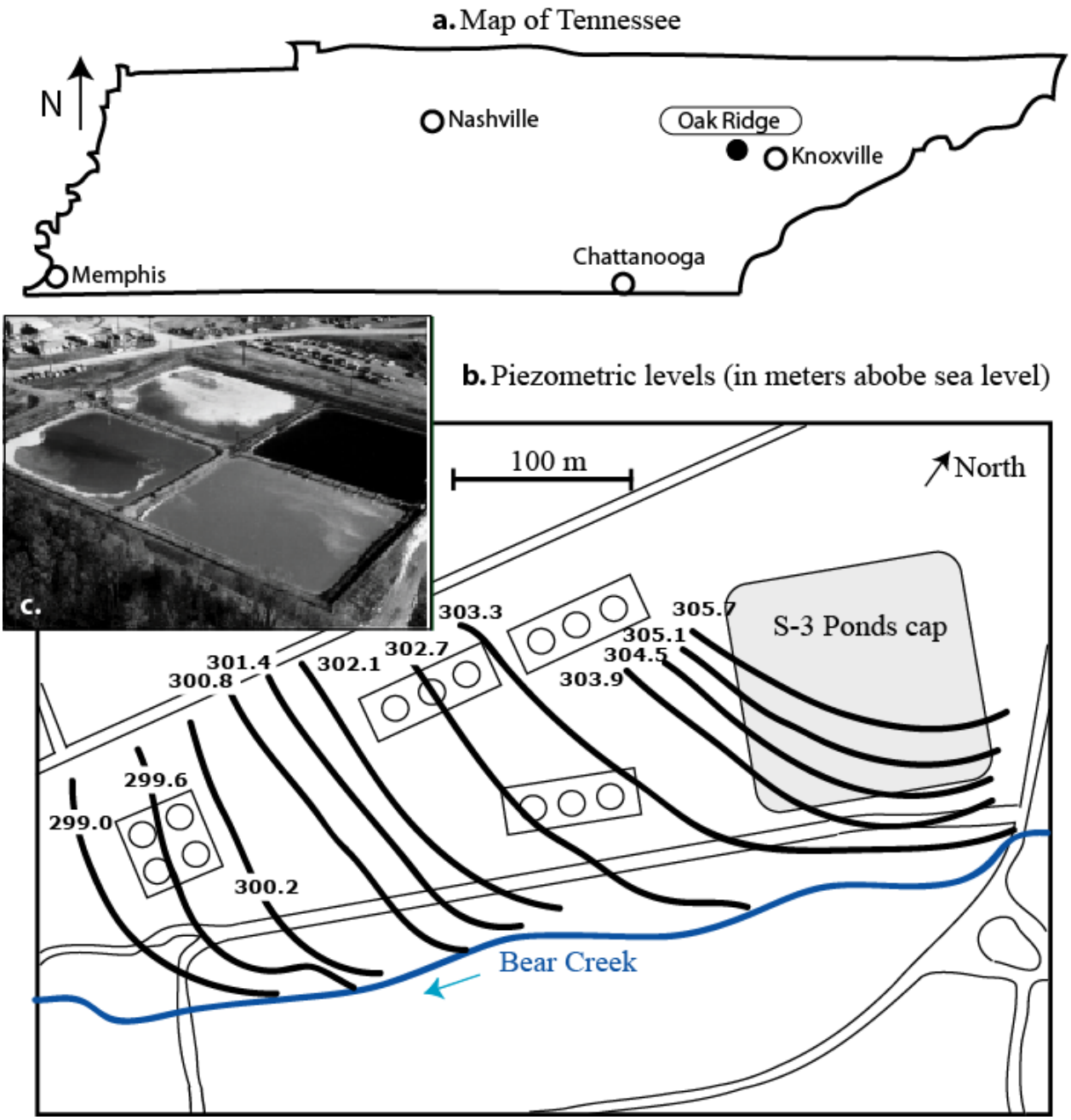

Figure 1. Localization of the test site. **a.** Position of Oak Ridge in Tennessee. **b.** Ground water elevation map around the S-3 ponds area in meters above sea level. The aquifers discharge to the Bear Creek River (modified from Watson et al., 2004). c. Picture taken from the West of the ponds when they were in activity and before they were filled and sealed with a five-layer cap and an asphalt parking lot was built on the top of them.

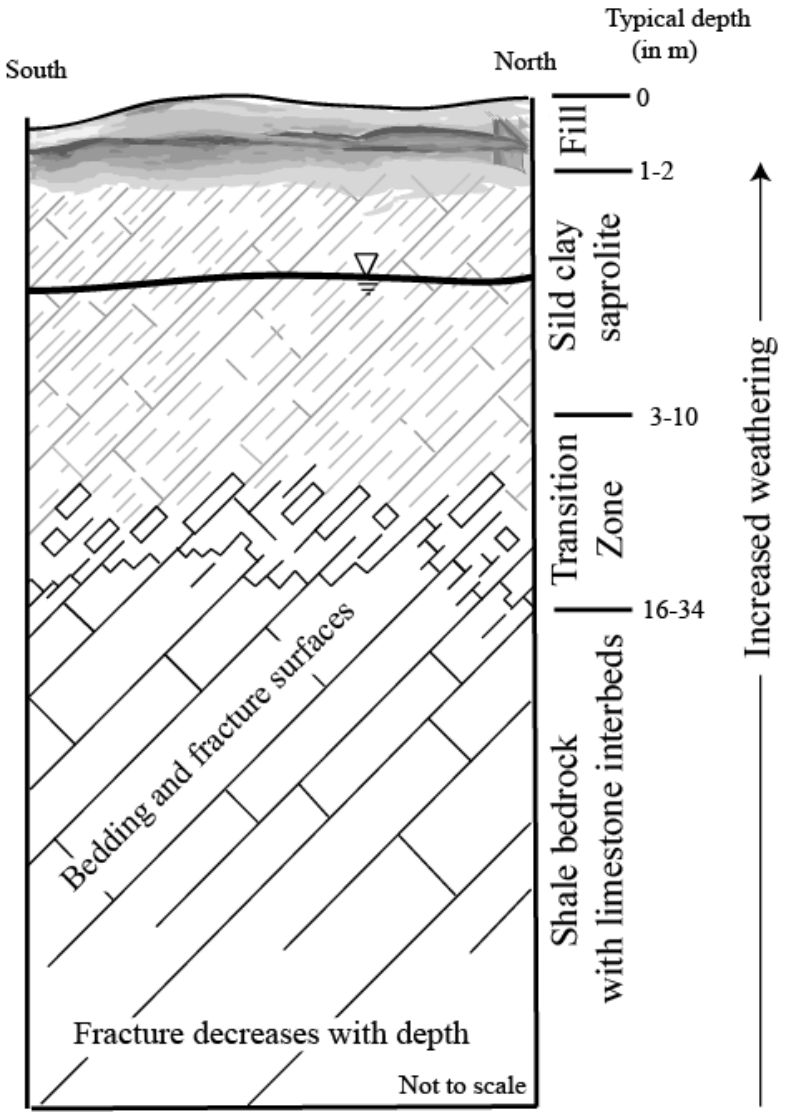

Figure 2. Sketch of a typical Oak Ridge FRC soil and bedrock profile showing the evolution of the density of fractures with depth. The transition zone between the saprolite and the parent bedrock is usually characterize by a permeability higher than in the saprolite itself. The transition between the parent bedrock and the saprolite can have a strong topography.

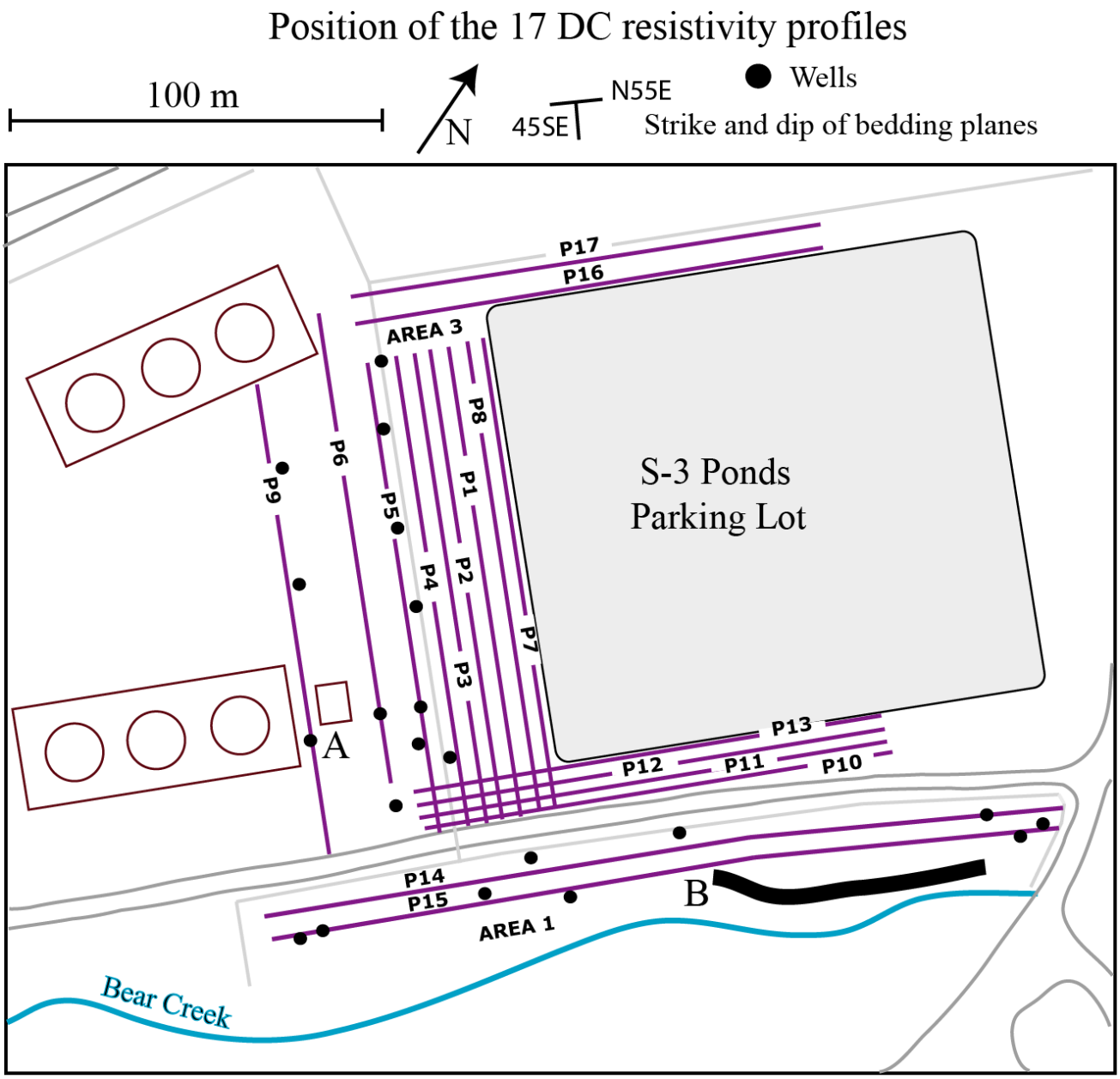

Figure 3. Position of the 17 DC-resistivity profiles used to investigate the position of the contaminant plumes. "A" represents a generator with cathodic protection generating spurious self-potential anomalies. "B" denotes a reactive barrier emplaced to protect Bear Creek. Only a subset of all the drilled wells is shown here.

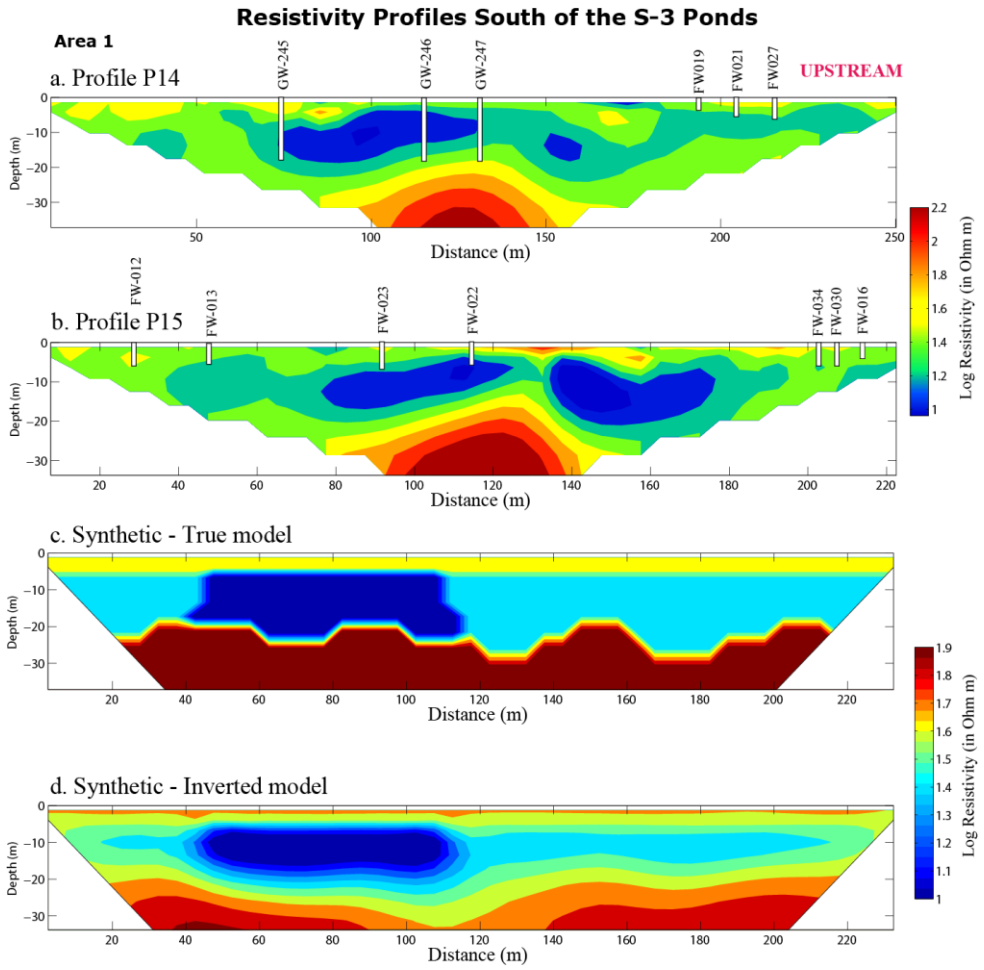

Figure 4. Examples of 2.5D resistivity inversion. **a. b.** Example of selected resistivity profiles South to the S-3 Ponds (Profiles P14 and P15, iteration 5, data RMR errors 5.8 and 6.2%, respectively). The main plumes (CP4) can be recognized. This plume breaks into two plumes CP4a and CP4b. Note the strong topography of the interface between the bedrock and the saprolitic aquifer. The vertical bars show the position of the wells. The position of the bedrock is in agreement with lithological information from several wells drilled in Area 1. **c. d.** Synthetic case study using a true model and its inversion (data RMS error 1.8%). All the profile inversions were performed with the code developed by Karaoulis et al. (2011a, b, see Appendix A for further details).

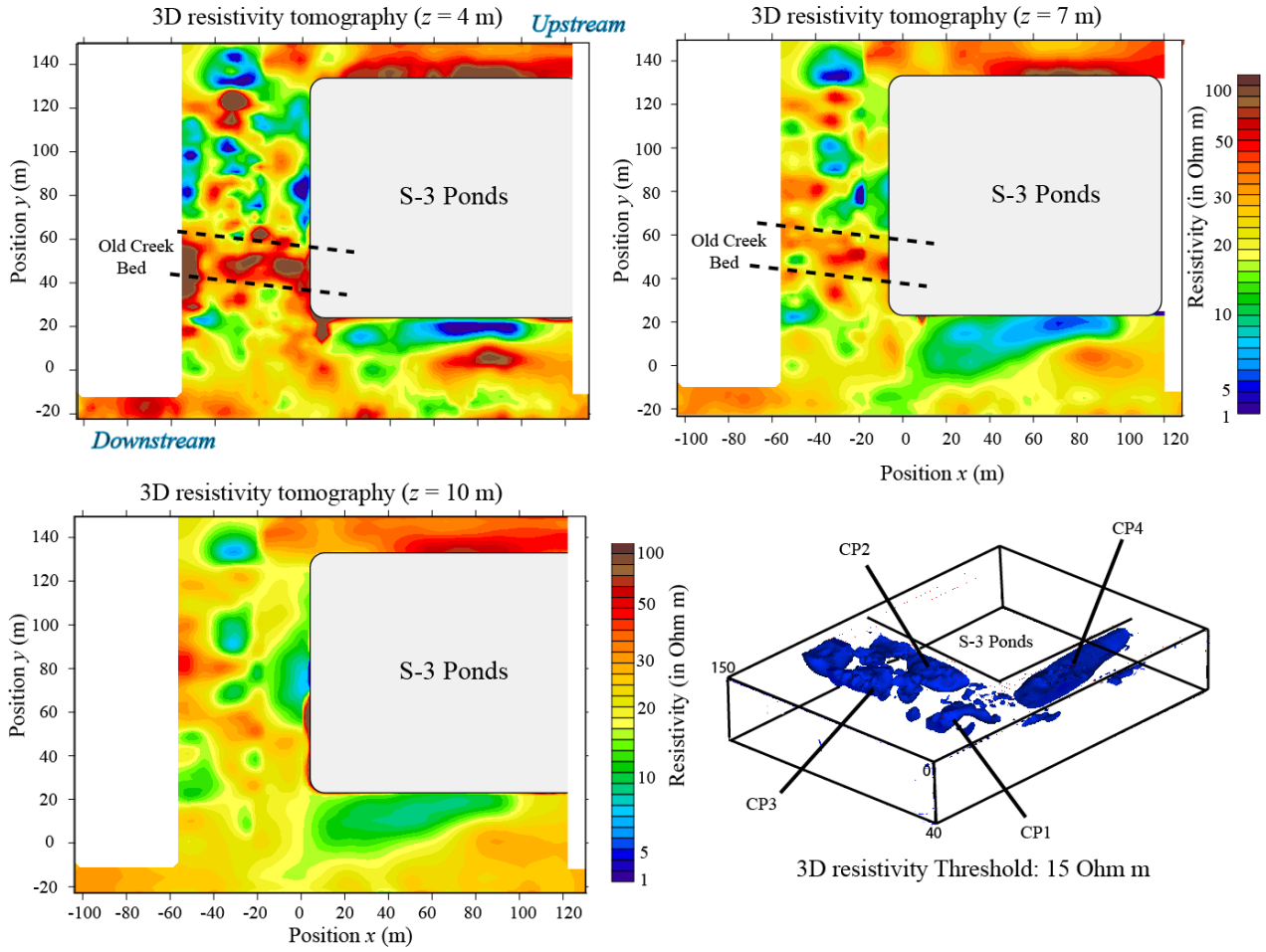

Figure 5. Result of the 3D resistivity tomography at three different depths (4, 7, and 10 m). The resistivity feature showing downstream may play the role of a natural barrier of permeability for the contaminant plume CP2. It corresponds to Old Creek Bed. We see that the upstream area is relatively resistive (> 50 ohm m).

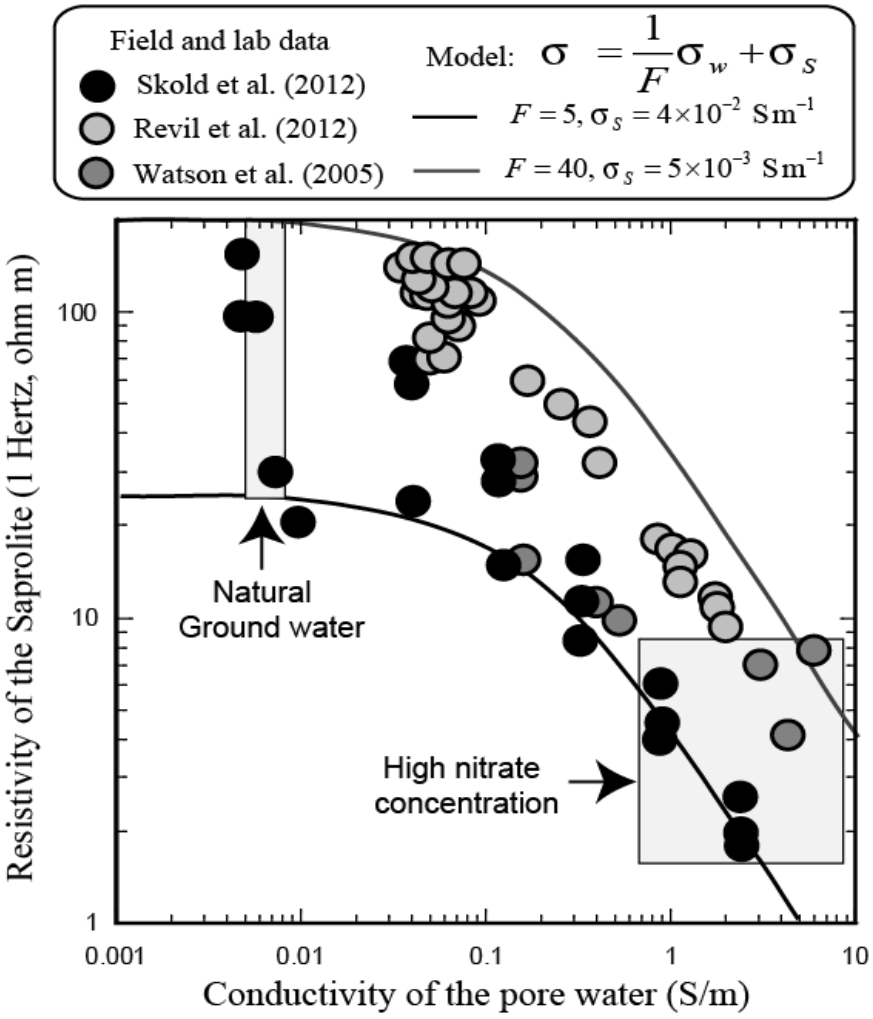

Figure 6. Resistivity of saprolitic aquifer. The data from Sold et al. (2012) corresponds to laboratory measurements with remolded core samples and NaCl solutions while the data by Revil et al. (2012) corresponds to an undisturbed core sample with in situ ground waters in a column experiment. The other data are coming from the field (cross plot of the resistivity from the tomograms and the pore water conductivity from the well data). At high pore water conductivity, the resistivity response is controlled by the value of the formation factor and the conductivity of the pore water. At low pore water conductivities, the resistivity is controlled by surface conductivity, which is controlled by the cation exchange capacity of the clay minerals. The two shaded boxes correspond to the range of value for the background (uncontamined) ground water (upper-left side) and for the heavily contaminated CP2 plume (lower-right side). They form the two end-members cases.

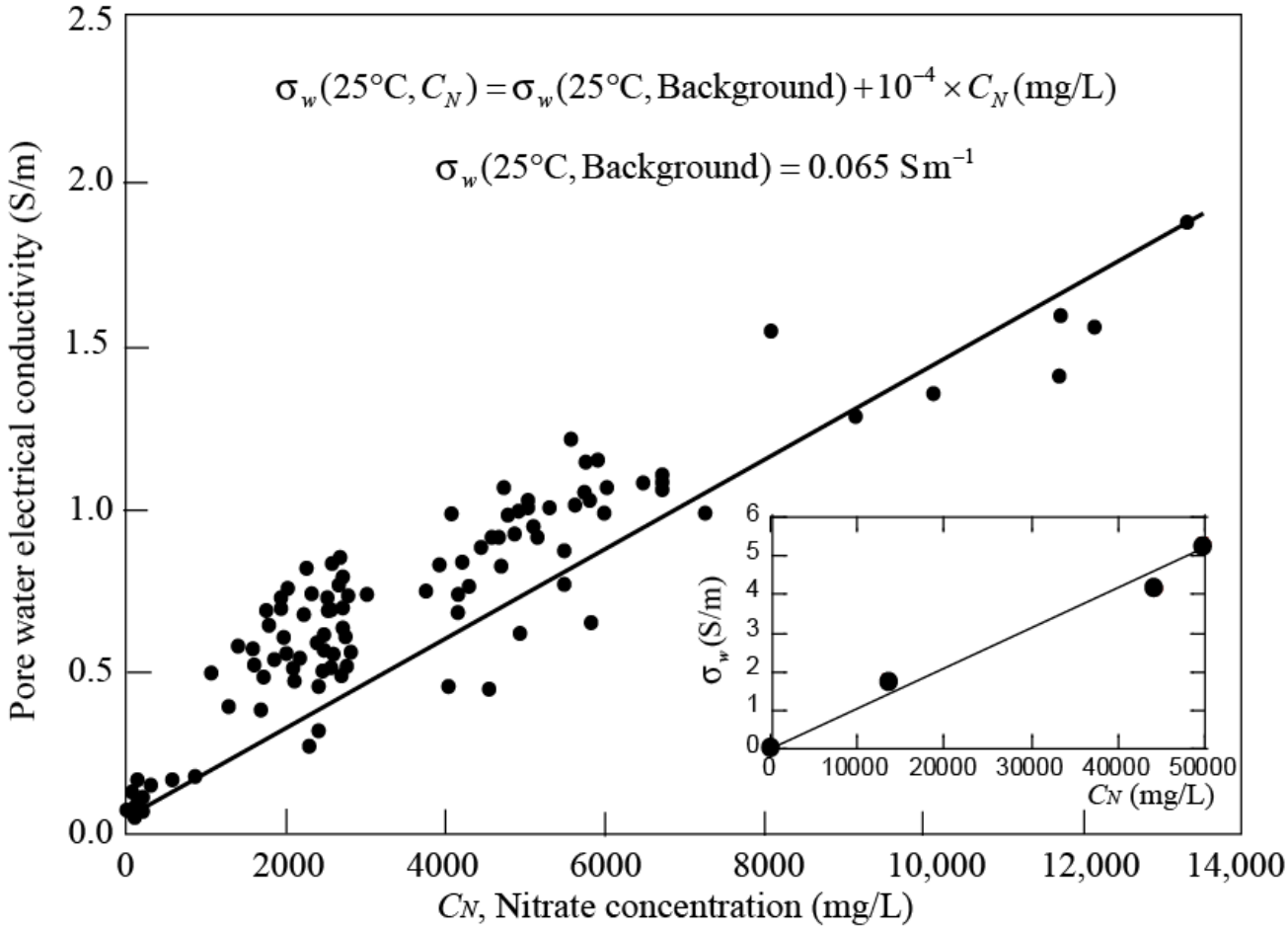

Figure 7. Relationship between the electrical conductivity of the pore water σ_w (in S m^{-1}) and the nitrate concentration C_N (in mg L^{-1}). This relationship respects the value of the background pore water in absence of nitrate in the background pore water (see Table 1). Insert: test of the same relationship for the very high nitrate concentrations found in plume CP2.

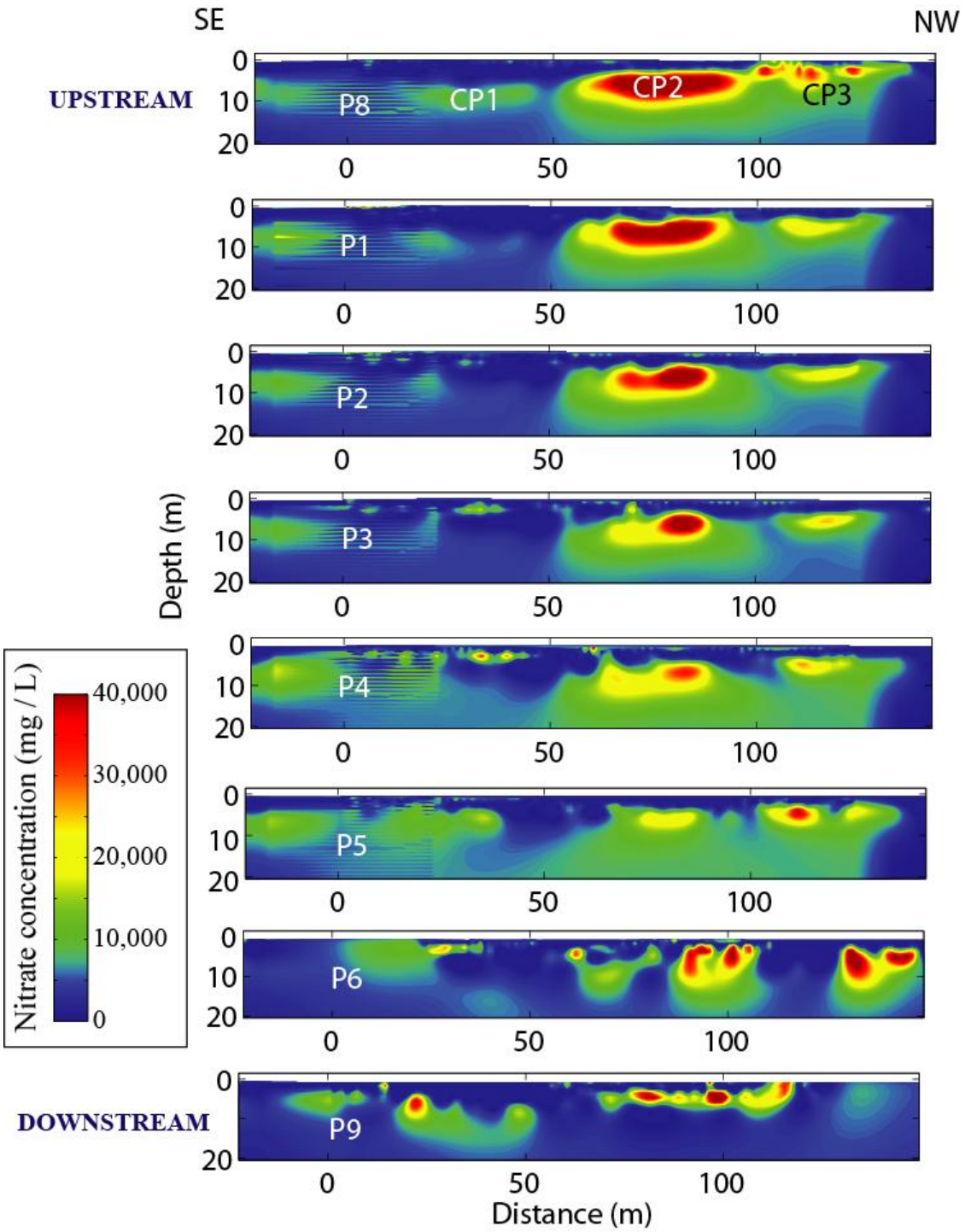

Figure 8. Nitrate concentration determined from the 3D resistivity inversion. Eastern part of the S-3 ponds. Profiles P6 and P9 are very noisy and there is a lot of uncertainty on these results. Noe that the contaminant follows a tube-type flow pattern.

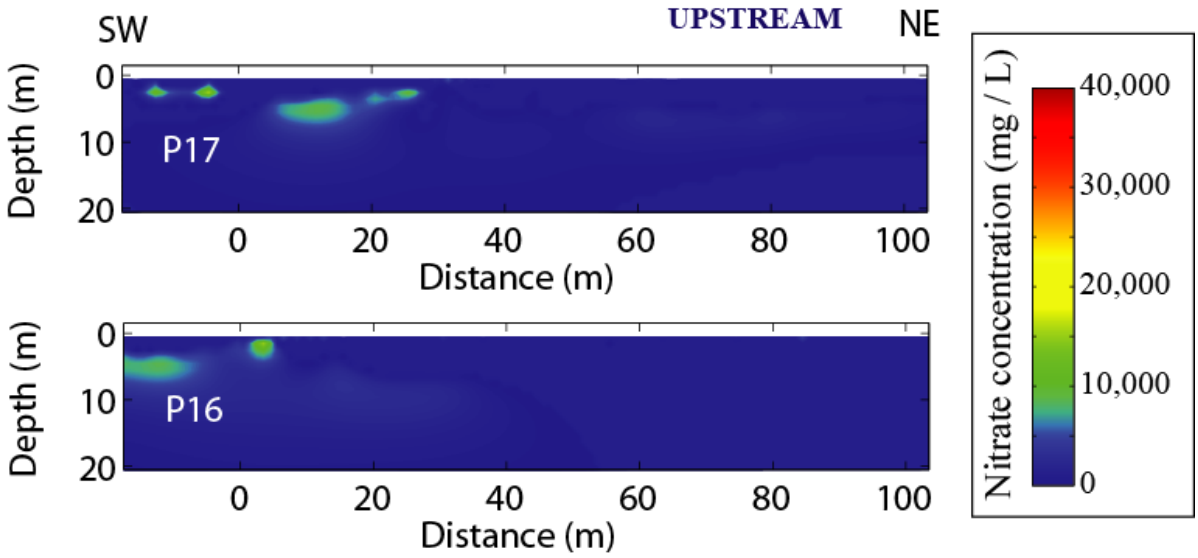

Figure 9. Nitrate concentration determined from the resistivity inversion of profiles P17 and P16 located in the Northern part of the S-3 ponds. These profiles do not indicate the presence of contaminant plumes with the exception of a small plume (CP5) located on the SW edge of the S-3 ponds.

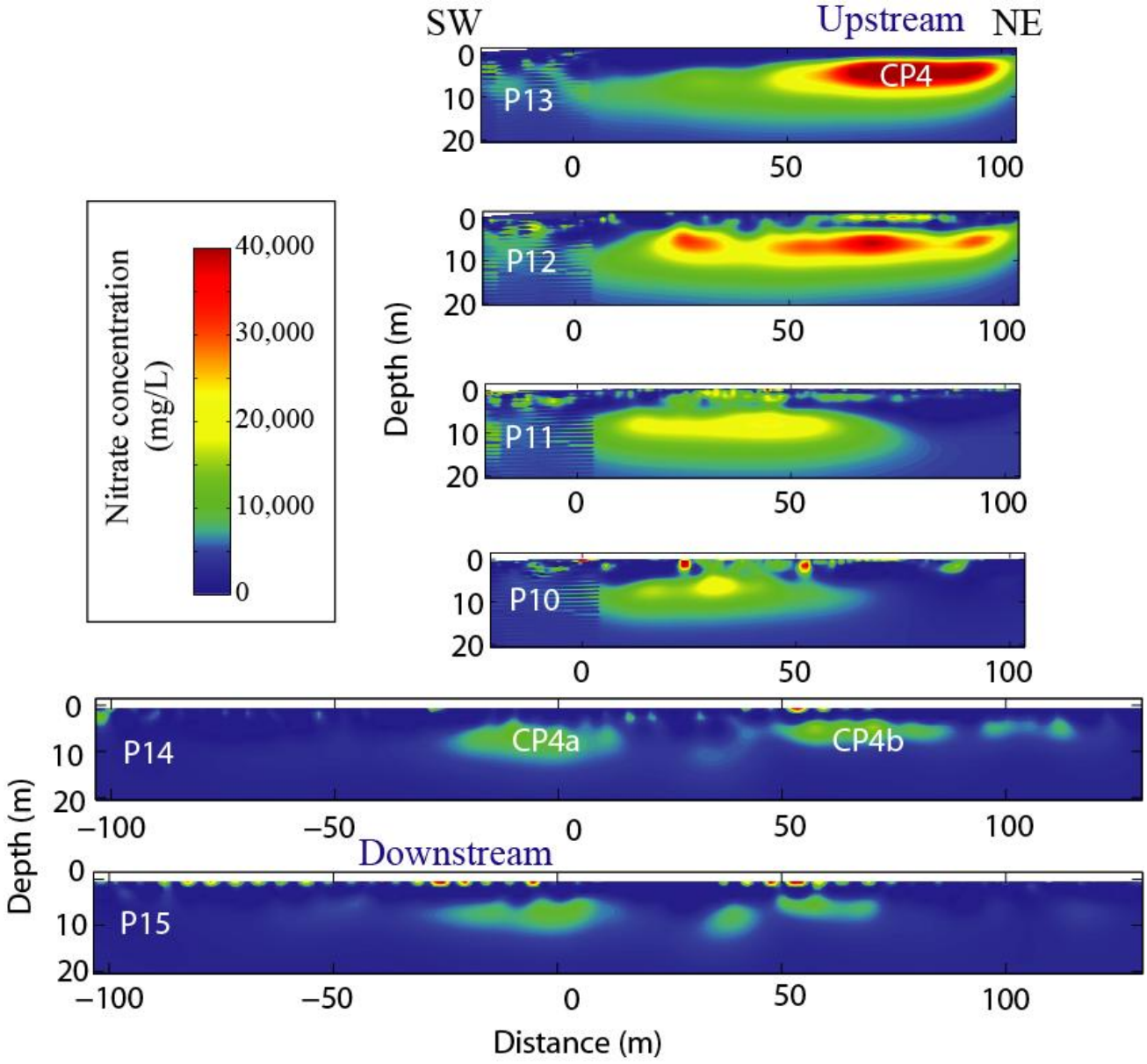

Figure 10. Determination of the nitrate concentration for the 3D resistivity inversion of the profiles located south to the S-3 ponds. Downstream, the main plume CP4 breaks into two plumes (CP4a and CP4b).

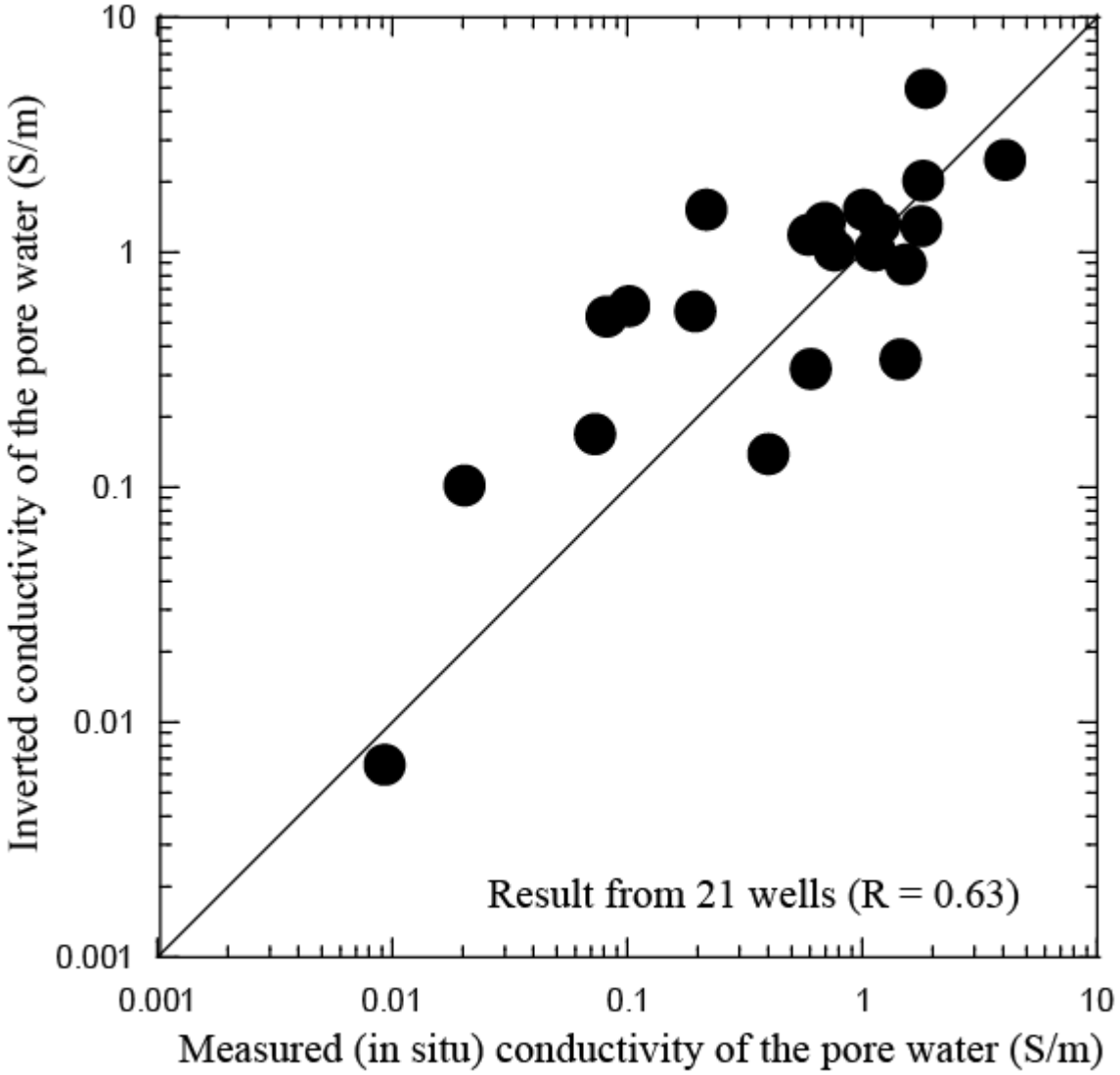

Figure 11. Comparison between the conductivity of the pore water determined from the tomograms and the in situ sampling of the pore water conductivity in 21 wells located around the former S-3 basins (see Figure 3).

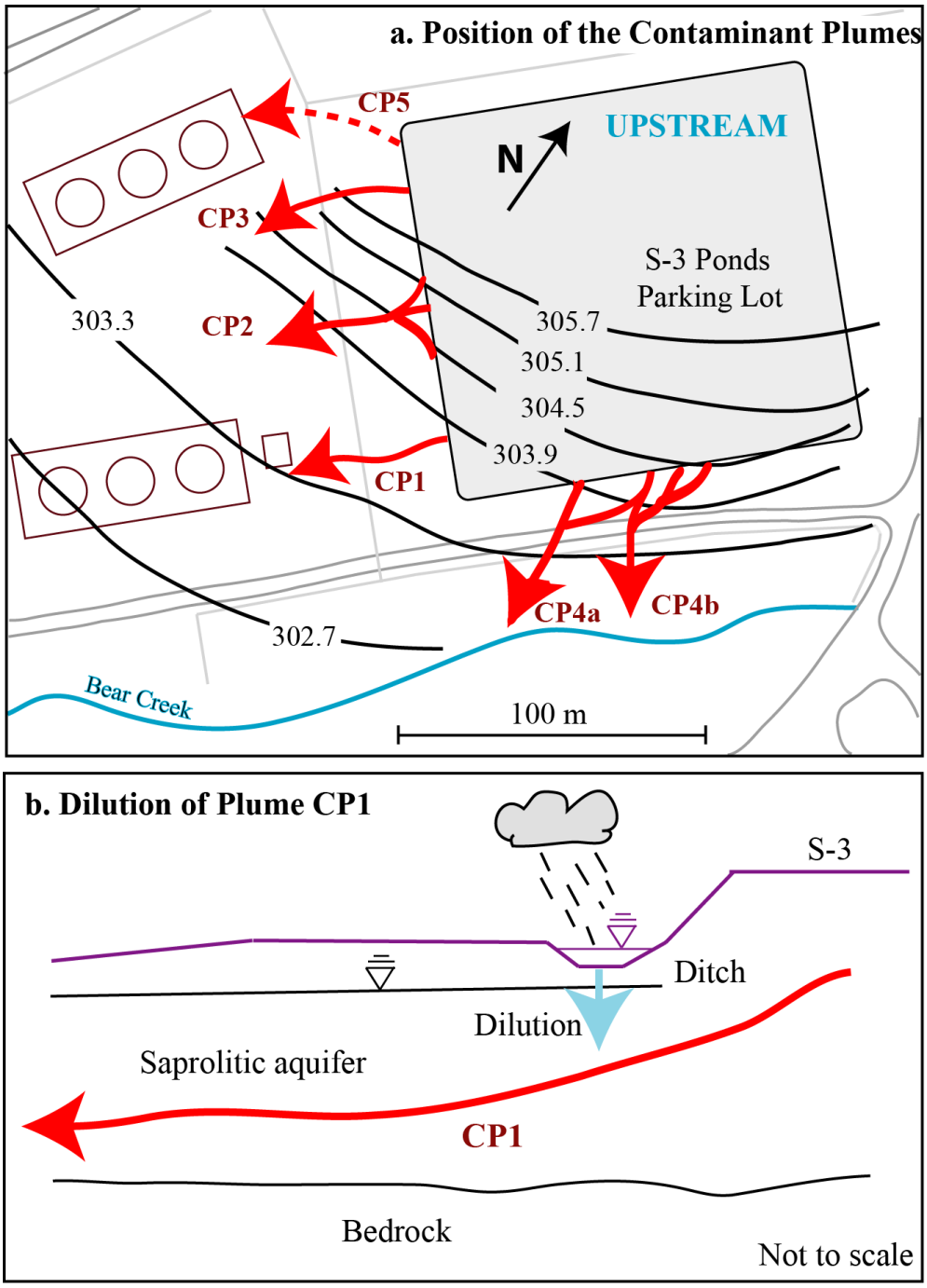

Figure 12. Geometry of the contaminant plumes. **a.** Horizontal position of the contaminant plumes downstream the S-3 pond. **b.** Contaminant plume CP2 breaks into two plumes, one descending along a fault zone into the bedrock. The ditch is also recharging the saprolitic aquifer and influence the nitrate concentration of the contaminant plume CP1.

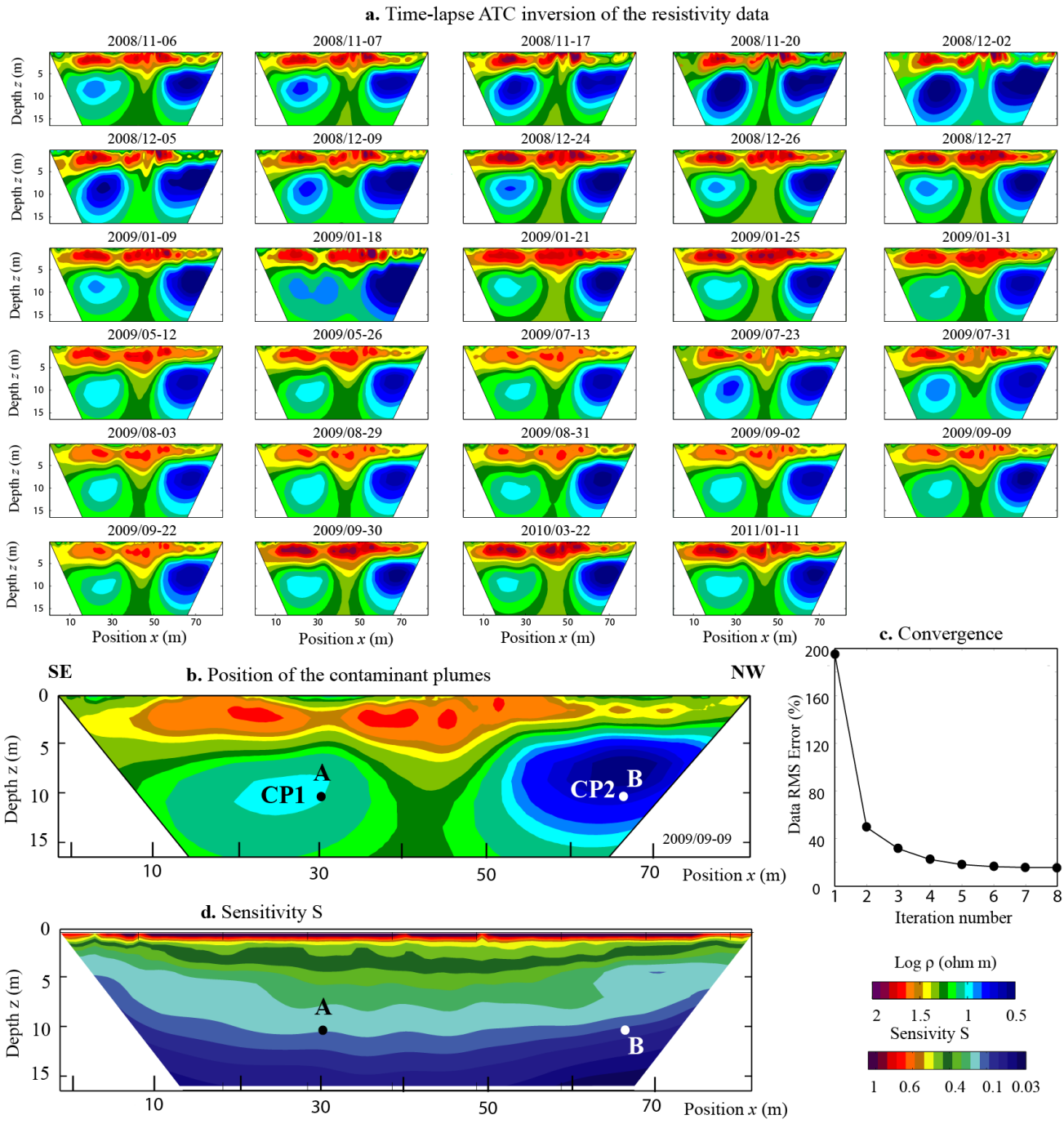

Figure 13. Time lapse tomography based on the Active Time Constrain (ATC) approach. **a.** Results of the time lapse inversion for the profile in Area 3. **b.** Analysis of a tomogram showing the position of the plumes CP1 and CP2. **c.** Data RMS Error as a function of the number of iterations for the time lapse 2.5D resistivity tomography. The algorithm converged after 7 iterations. **d.** Sensitivity map.

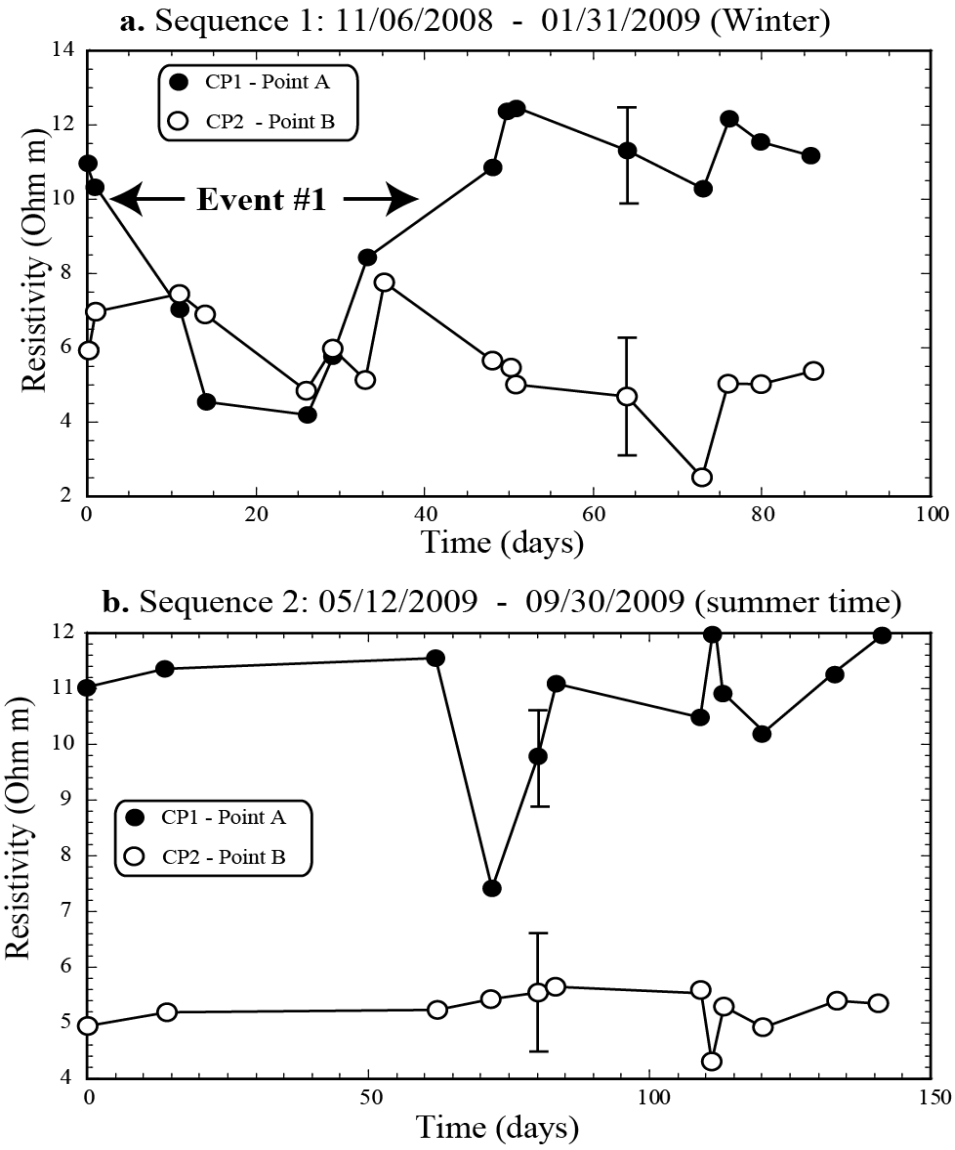

Figure 14. Evolution of the resistivity data for plumes CP1 and CP2. **a.** Winter time. **b.** Summer time. The uncertainty for the resistivity estimate is coming from a comparison between a synthetic test and the inversion of this synthetic test.

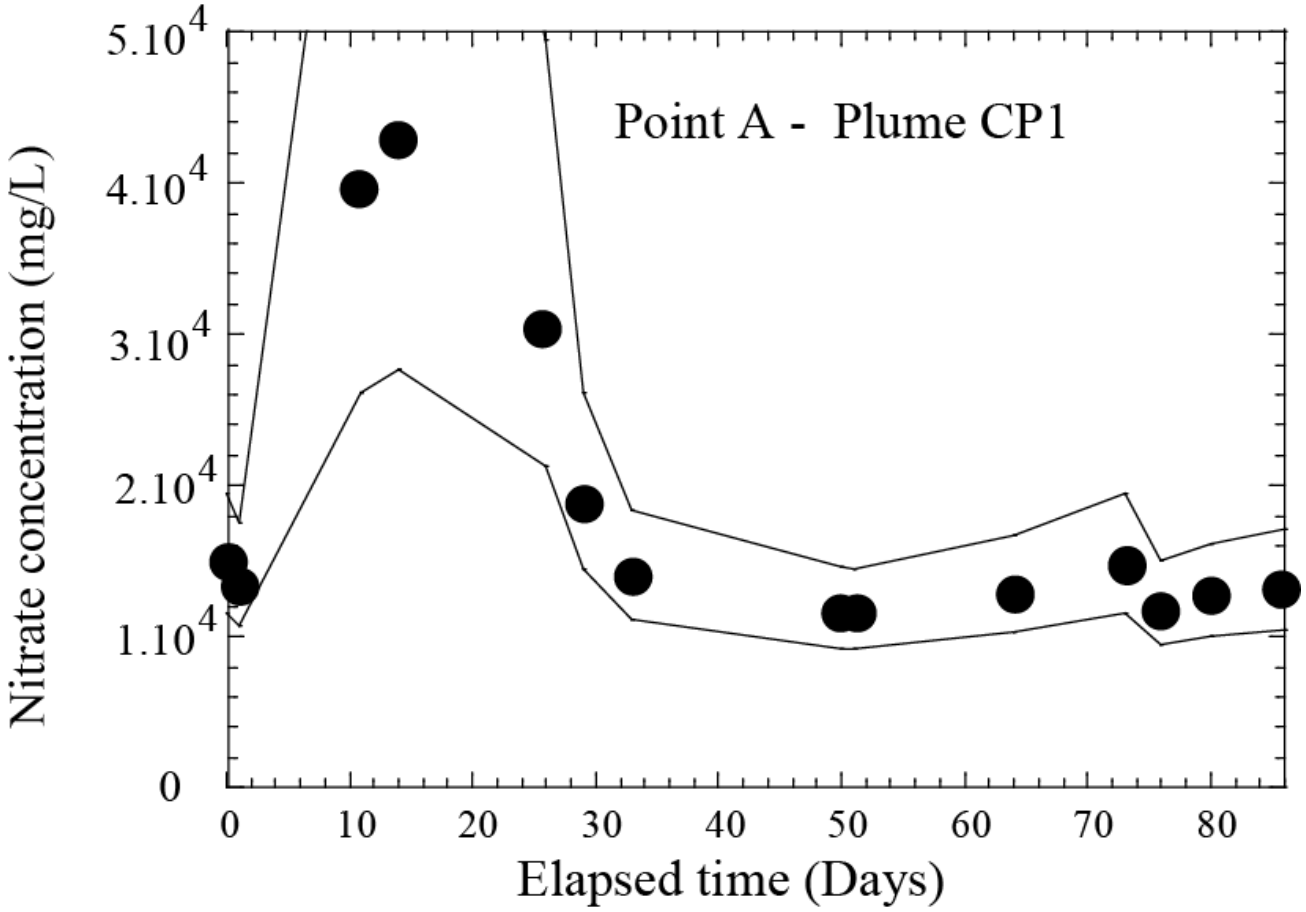

Figure 15. Evolution of the nitrate concentration in Plume CP1 during the winter 2008-2009. the nitrate concentration is determined from the evolution of the resistivity at point A (see Figures 13 and 14) and the transforms discuss in the main text to convert resistivity into nitrate concentration. The two plain lines correspond to the uncertainty (95% confidence interval).

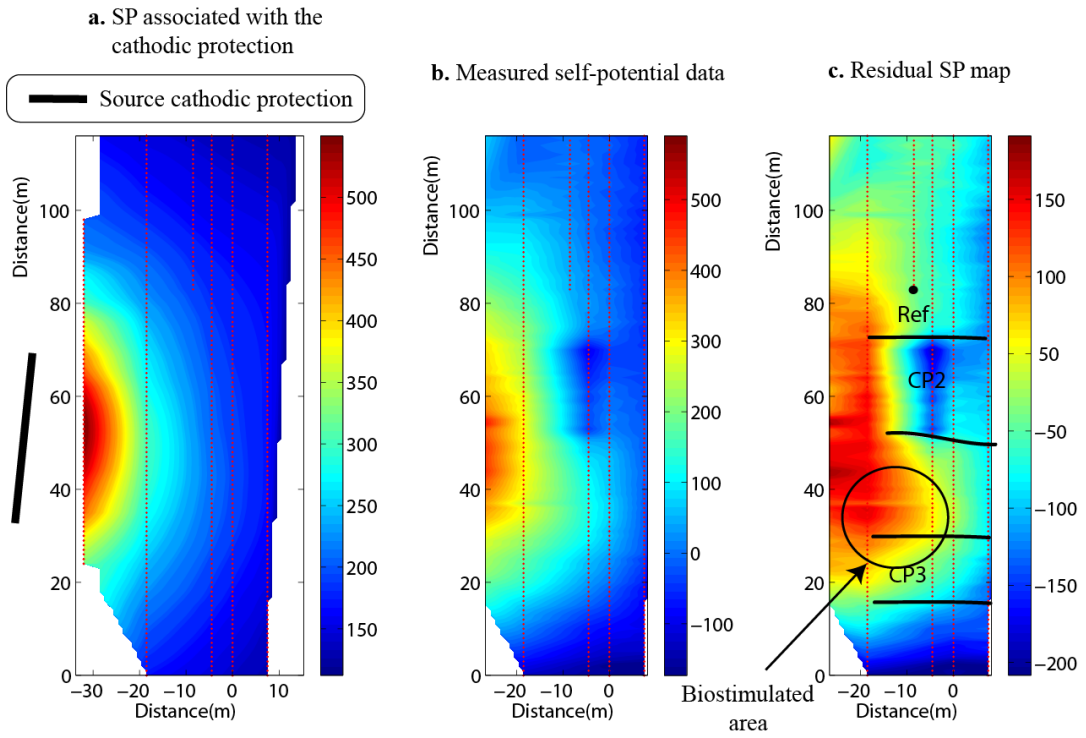

Figure 16. Self-potential map. **a.** There is a strong cathodic protection component to the measured self-potential data in Area 3 This figure shows the self-potential distribution from the inverted source position (the black segment) using the genetic algorithm and the 3D resistivity distribution from Figure 5. **b.** Measured self-potential data. **c.** Residual self-potential map obtained by substracting the contribution associated with the cathodic protection (Figure 16a) to the raw self-potential data (Figure 16b). The small dots correspond to the self-potential stations. Note the biostimulated area corresponds to an area characterized a positive anomaly.

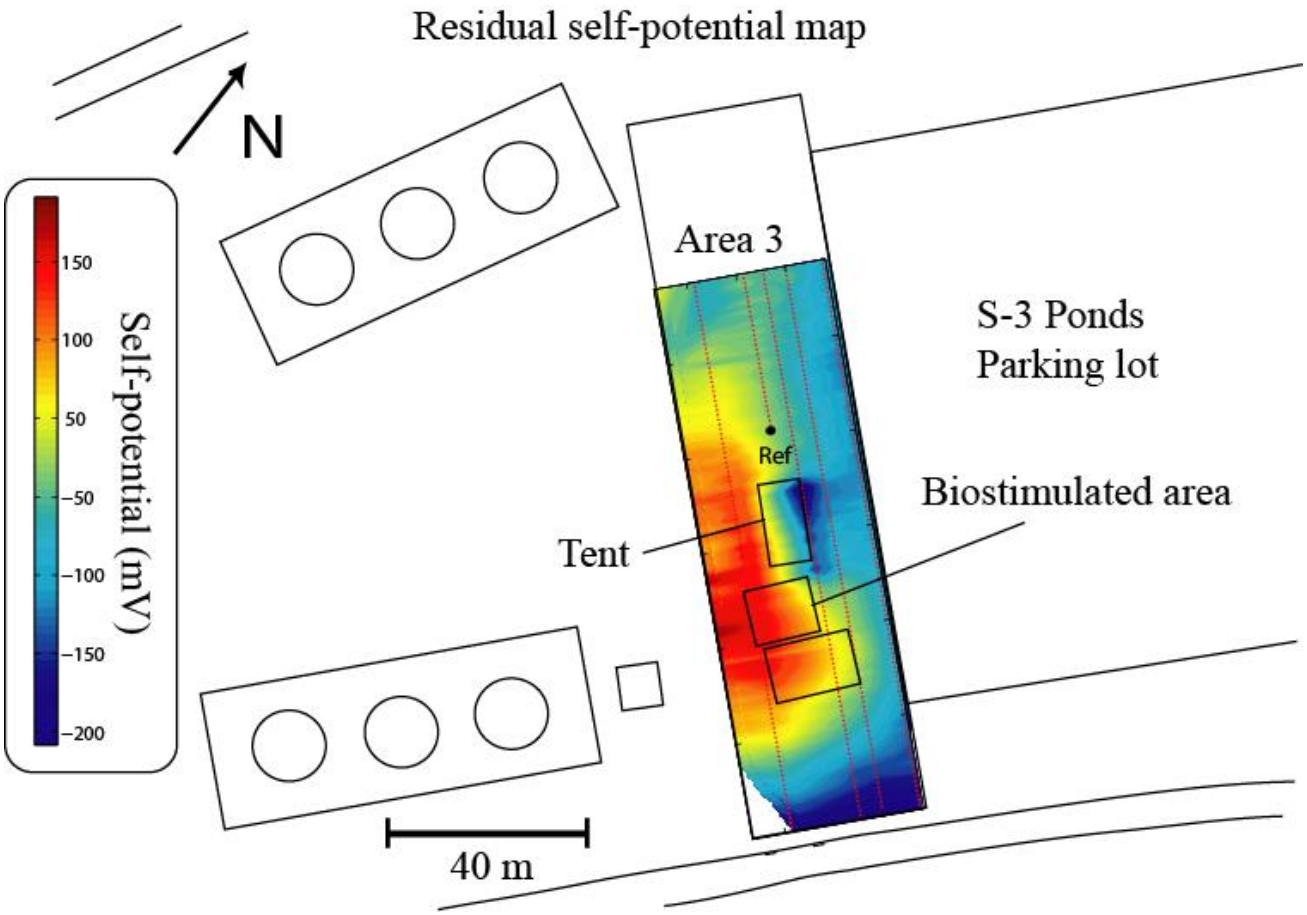

Figure 17. Residual self-potential map and position of the biostimulated area. The self-potential anomaly is on the order of 400 mV. It is negative in the oxidized area (characterized by a positive redox potential of about 200 mV) and is positive around the biostimulated area, which corresponds to negative values of the redox potential of about -250 mV.

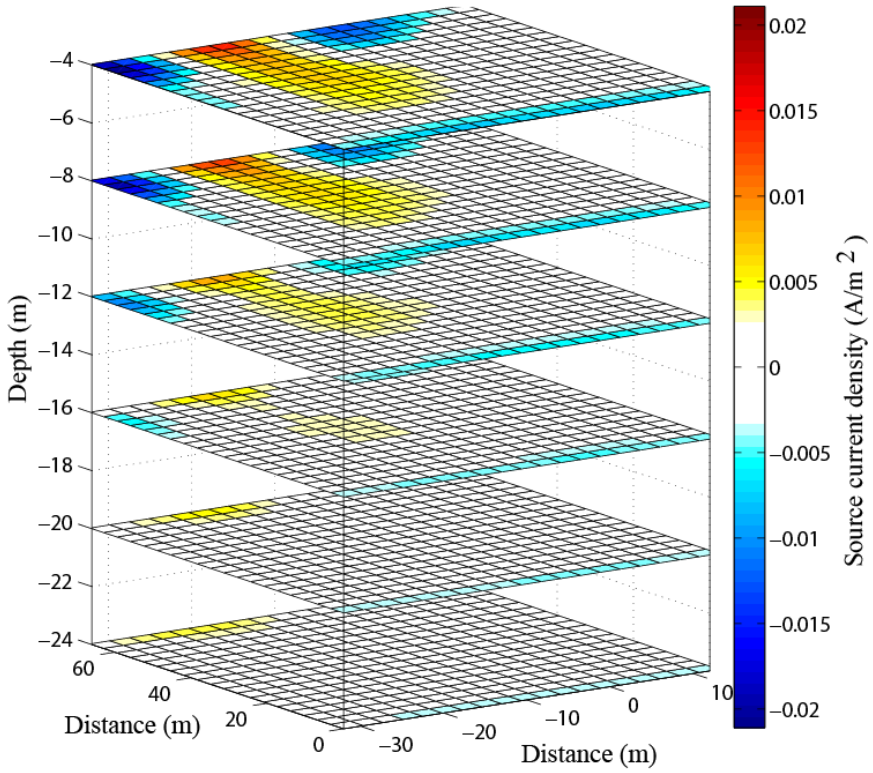

Figure 18. Self-potential tomogram showing the distribution of the source current density responsible for the observed residual self-potential anomaly at the ground surface (see Figure 17). The main current source are located between 4 and 8 m, inside the saprolitic aquifer at depths that are consistent with the biostimulated area.

Appendix C

Geochemical and geophysical responses during the infiltration of fresh water into the contaminated saprolite of the Oak Ridge Integrated Field Research Challenge site, Tennessee

A. Revil (1, 2), Y. Wu (3), M. Karaoulis (2), S. S. Hubbard (3), and J.D. Eppehimer (1)

(1) Colorado School of Mines, Department of Geophysics, Golden, 80401, CO, USA

(2) ISTerre, CNRS, UMR CNRS 5275, Université de Savoie, 73376 cedex, Le Bourget du Lac, France

(3) Lawrence Berkeley National Laboratory, 1 Cyclotron Road, MS 74R120, Berkeley, 94720, CA.

Running Head: Geochemical and geophysical monitoring

Corresponding author: André Revil arevil@mines.edu

Emails: ywu3@lbl.gov; arevil@mines.edu; sshubbard@lbl.gov; watsondb@ornl.gov; jeppehim@mymail.mines.edu; marios.karaoulis@gmail.com

Intended for publication in Water Resources Research

Abstract. At the Oak Ridge Integrated Field Research Challenge (IFRC) site, near Oak Ridge, Tennessee, the saprolitic aquifer was contaminated by past infiltration and leakage from the former S-3 disposal ponds between 1951 and 1983. The chemistry of the contaminant plume is also episodically impacted by fresh meteoritic water infiltrating vertically from a shallow variably saturated perched zone and the ditch surrounding the former S-3 ponds. We performed a column experiment to understand the geochemical and complex electrical conductivity signatures associated with such events. The changes in the pH and pore water conductivity are responsible for measurable changes in both the in-phase and quadrature conductivities of the saprolite. The pore water conductivity can be related to the nitrate concentration (the dominate ionic species in the plume) while the release of uranium is controlled by the pH. We developed a simple model to determine the pore water conductivity and pH from the recorded complex conductivity. This model is applied to time-lapse resistivity data at the IFRC site. Time-lapse inversion of resistivity data shows the occurrence of an infiltration event during the winter of 2008-2009 with a dilution of the pore water chemistry and an increase of the pH. A simple numerical simulation of the infiltration of fresh water into the unconfined contaminated aquifer is consistent with this scenario.

1. Introduction

The Oak Ridge Integrated Field Research Challenge (OR-IFRC) site is a DOE test site located near Oak Ridge, Tennessee. This site was established to understand the migration of various contaminants from the former S-3 disposal ponds (located in the Bear Creek Valley) into the surrounding saprolitic aquifer [*Watson et al.*, 2004]. The S-3 disposal ponds consisted of four ponds built in 1951. They received a yearly volume of 7.6 million liters of acidic (pH <2) liquid wastes consisting of nitric acid, uranium, technetium, cadmium, mercury, and chlorinated solvents for 32 years [*Shevenell et al.*, 1994]. The wastes were disposed of in liquid acid form so the contaminants could readily migrate away from the ponds and precipitate when encountering carbonate high pH buffered zones. As a result, there is a huge reservoir of contaminants in the saprolite and rock matrix beneath the ponds. In 1983, the ponds were drained and filled with fill materials. The disposal ponds were capped with a multilayer RCRA cap (including an asphalt cap) so there is presently minimal leaching from above. The meteoric water is also diverted into a ditch surrounding the former S3 basins. The primary mechanism of contaminant transport is therefore groundwater flow through the underlying contaminated materials.

Understanding contaminant transport from the former S-3 Ponds is a key component of the remediation program undertaken at Oak Ridge. One of the difficulties is that the properties of the saprolite are not well-understood in terms of transport and geophysical properties. The saprolite is the result of shale and limestone weathering and is rich in illite and smectite. The clay content and mineralogy play an important role in controlling the specific surface area and therefore interfacial chemistry and petrophysical properties like permeability and porosity [*McKay et al.*, 2000; *Watson*, 2004].

The relatively high amounts of clay minerals also plays a role, as discussed below, on the electrical resistivity. Electrical resistivity tomography can be used in turn to locate the position of the contaminant

plumes and monitor the changes in the concentration of the contaminants. Indeed, a number of recent geophysical studies [*Watson et al*., 2005; *Chen et al*., 2006, 2010; *Kowalsky et al*., 2011; *Gasperikova et al*., 2012; *Revil et al*., 2012a] have focused on determining the extent of the plumes associated with contaminant migration from the former S-3 disposal ponds as well as evaluating the potential for natural attenuation of these plumes. Recently, *Revil et al*. [2013a] have pointed out that the interpretation of resistivity data cannot be properly done without taking into account the surface conductivity associated with the presence of clay minerals in the saprolite. That said, the *Revil et al*. [2013a] study was conducted with samples from the uncontaminated background site keeping only the fine fraction of the saprolite and using a simple NaCl solution as the leachate to conduct the experiments. No electrical conductivity experiments has been performed to date on contaminated saprolite (which have experienced acidic solution for a long time) and with the natural pore waters found at the site in order to understand the interfacial (surface) electrical conductivity and quadrature conductivity and their relationship to the presence of the contaminants.

Another point to address is that the geochemistry of the contaminant plume is influenced by rainfalls and infiltration events of fresh water. The interaction between the fresh, oxygen-rich, water from the perched zone and the contaminated water influence the geochemistry and redox chemistry of the contaminant plume. There are episodic recharges to the regional water table and plume associated with rainfall infiltration. There is therefore a need to quantify spatially these geochemical changes using time-lapse geophysical monitoring in order to assess natural attenuation mechanisms and to select effective remediation techniques.

Spectral induced polarization (complex conductivity) is a non-intrusive geophysical method that can be used to image contaminant plumes (e.g., *Vanhala* [1997]; *Morgan et al.* [1999] and more recently *Deceuster and Kaufman* [2012] and *Flores Orozco et al.* [2012]), to determine permeability [*Slater and Lesmes*, 2002; *Revil and Florsch*, 2010], and to monitor interfacial electrochemistry at the pore water mineral interface [*Vaudelet et al*., 2011a, b]. Induced polarization has a long history of use in colloidal chemistry and geophysics studies and various petrophysical models have been developed over time to determine the relationship between the in-phase and quadrature conductivities and the texture of the material as well as the electrochemical properties of the mineral water interface [*Marshall and Madden*, 1959; *de Lima and Sharma*, 1992; *Grosse*, 2011]. Recent works have focused on the development of a new model based on the polarization of the Stern layer to describe spectral induced polarization of clayey materials with simple supporting electrolytes (e.g., NaCl or KCl) [*Revil*, 2012; *Revil et al.*, 2012b].

In the present study, we investigate how spectral induced polarization can be used in the laboratory to monitor changes in the pore water and interfacial chemistry in a complex porous material (the contaminated saprolite mentioned above) and with complex natural ground waters from the less contaminated shallow aquifer and underlying plume of highly contaminated groundwater. To establish the relationship between induced polarization and geochemistry needed to interpret field data, we developed a column experiment to simulate the type of infiltration occurring in the field. Both the saprolite core and the ground waters were sampled from the OR-IFRC research site. This approach is then used to interpret time lapse resistivity data (unfortunately complex conductivity data were not available) to monitor one of the main contaminant plumes

(the CP1 plume) during an infiltration event and to interpret these results in terms of change in the pore water chemistry.

2. Position of the Problem

The location of the OR-IFRC research site is shown in Figure 1a and 1b as well as the position of the former S-3 disposal ponds (Figure 1c) and the two wells used in our study (the shallow well FW116 and the deeper well FW130, see their positions in Figure 1d). An important point is that Well FW116 (about 6 m deep) is not in the perched zone. It is screened at the very top of the water table where water from the perched zone has percolated down and is therefore less contaminated than at greater depths. It represents there what we will called below the upper portion of the saprolitic aquifer.

The scientific question we address below is sketched in Figure 2. Right downstream the former S-3 disposal ponds, there are some intermittent mixings of fresh water with the contaminated ground water located in the saprolitic aquifer that originated from the heavily contaminated sediments located below the former S-3 Ponds (Figure 1d). The perched aquifer results mostly from transient infiltration of meteoritic waters from the ditch surrounding the former S3 ponds in the permeable fill covering the saprolitic aquifer.

The saprolite material used in the column experiment described below in Section 4 was cored from Well FW130 (Figure 1d) at a depth of ~15 m. This sample is therefore from the transition zone between the saprolite and the basement rock. This zone is usually considered to have an enhanced permeability with respect to the upper more clay-rich portion of the saprolite (Watson et al., 2004). As explained in Section 4 in more details, the two types of groundwater were collected from Well FW130 (heavily contaminated ground water sampled at a depth of ~15 m) and Well FW116 (fresh ground water from the less-contaminated upper portion of the saprolitic aquifer). The compositions of the two ground waters are reported in Table 1.

During the mixing of the freshwater and the contaminated ground water, two key parameters that should be monitored are the conductivity of the pore water and the pH. The conductivity of the water can be related to the nitrate concentration by (Figure 3):

$$\sigma_w(25°\text{C}, C_N) = \sigma_w(25°\text{C}, \text{Background}) + 1.4\times10^{-4} C_N(\text{mg/L}) . \quad (1)$$

To be consistent with the data reported in Table 1 for the upper portion of the aquifer, the background conductivity of the pore water is taken equal to 0.03 S m^{-1} at 25°C for the perched water. Indeed, the nitrate concentration in the perched aquifer is $C_N \approx 254.5$ mg L^{-1} (Table 1) and therefore Eq. (1) predicts that the conductivity of the upper portion of the aquifer is 0.07 S m^{-1} at 25°C in agreement with the measured value in Table 1.

Eq. (1) can be also used to predict the conductivity of the contaminated groundwater in Well FW130 ($C_N \approx 14{,}000$ mg L^{-1}). We obtain 2.07 S m^{-1} at 25°C. This is consistent with the measured value of 2.08 S m^{-1} at 25°C. Because we are considering pH values higher than 3.8 (see Table 1), the change in pH has a negligible effect upon the pore water conductivity.

The other critical parameter to monitor is the pH of the pore water solution. Indeed, the change in pH can be related to the change in uranium concentration (see Figure 4) according to the following empirical relationship,

$$[\mathrm{U}](\mathrm{mg/L}) = [\mathrm{U}](\mathrm{Background, mg/L}) + a\left\{[\mathrm{H}^+] - 10^{-6.4}\right\}, \quad (2)$$

where $[\mathrm{U}](\mathrm{mg/L})$ represents the uranium concentration in mg L^{-1}, $[\mathrm{U}](\mathrm{Background})$ denotes the background concentration in uranium in the perched aquifer (at pH 6.4), and $[\mathrm{H}^+]$ denotes the concentration of protons in Mol L^{-1}. The concentration in uranium is both controlled by the dilution and a source term depending on the pH, which controls the release of uranium from the mineral surface. The key of our analysis is therefore to connect the complex conductivity to these two parameters. For this, we decided to perform a column experiment simulating an infiltration experiment in the same conditions existing in the field. In Section 3, we first describe the measurements we performed on core samples with only the fine fraction of the material and a simple (NaCl) supporting electrolyte.

3. Properties of Saprolitic Core Samples

We summarize here experimental data performed recently in the laboratory by *Revil et al*. [2013a] and Revil et al. (unpublished study) on core samples from the background (uncontaminated) site at Oak Ridge using a simple supporting electrolyte (NaCl). The goal of this section is to help the reader to get familiarize with the state of knowledge we have on the complex conductivity of saprolite for which, so far, only the fine fraction of the material has been studied.

3.1. Theory

The complex conductivity σ^* of a porous material is written as,

$$\sigma^* = |\sigma| \exp(i\varphi) = \sigma' + i\sigma'', \quad (3)$$

where $|\sigma|$ denotes the amplitude of the conductivity (in S m^{-1}), φ the phase lag (usually expressed in mrad), σ' and σ'' denote the real (in phase) and imaginary (quadrature) components of the conductivity (both in S m^{-1}), and *i* denotes the pure imaginary number ($|\sigma| = \sqrt{\sigma'^2 + \sigma''^2}$ and $\varphi = \mathrm{atan}(\sigma''/\sigma')$). The existence of a phase lag between the current and the voltage is coming from the fact that according to non-equilibrium thermodynamics, the current density depends not only on the electrical field but also on the gradient of the chemical potential of ionic species (e.g., *Leroy et al*. [2008]). Low-frequency polarization is indeed always driven by an electrochemical potential and the existence of polarization length scales along which accumulation or depletion of charge carriers are observed (e.g., *Leroy et al*. [2008], *Revil and Florsch* [2010]). Such type of low-frequency polarization is responsible for a phase lag between the current and the voltage. The amplitude and phase lag are then rewritten as a complex conductivity.

Because the phase is small (smaller than 100 mrad in amplitude), the phase is given by,

$$\varphi \approx \sigma''/\sigma'. \tag{4}$$

using a first order Taylor expansion for small quadrature conductivity with respect to the in phase conductivity. From a physical standpoint, the in-phase conductivity represents the ability of the porous material to transmit electrical current (conduction) while the quadrature conductivity describes the ability of the porous material to store reversibly electrical charges (polarization) under the influence of an electrical field or a current density.

In the following, we will not consider explicitly the frequency dependence of the complex conductivity. Instead, we will take the values of the in-phase and quadrature conductivities at 1 Hz, which is (as shown later) an adequate frequency in probing the polarization of the material. In addition, this frequency is typical of the frequencies used in the field to record resistivity and time-domain induced polarization. According to the Stern layer polarization model developed by *Revil* [2012] (see also *Leroy et al*. [2008] and *Revil et al.* [2013a]), the complex conductivity can be written as,

$$\sigma^* = \frac{1}{F}\sigma_w + \sigma_S^*. \tag{5}$$

$$\sigma^* = \sigma_w\left(\frac{1}{F} + \mathrm{Du}^*\right). \tag{6}$$

where F denotes the formation factor (dimensionless), σ_w denotes the (real) electrical conductivity of the pore water (in S m^{-1}), σ_S^* denotes the complex-valued surface conductivity (components expressed in S m^{-1}), and $\mathrm{Du}^* \equiv \sigma_S^*/\sigma_w$ denotes the complex-valued Dukhin number (unitless, ratio of the complex surface conductivity divided by the pore water conductivity). The formation factor F is related to the connected porosity ϕ by the first Archie's law $F = \phi^{-m}$ with m denoting the cementation exponent [*Archie*, 1942]. According to the Stern layer polarization model, the complex surface conductivity and the complex Dukhin number are defined as,

$$\sigma_S^* = \frac{2}{3}\rho_g \mathrm{CEC}\left[\beta_{(+)}(1-f) - i\beta_{(+)}^S f\right]. \tag{7}$$

$$\mathrm{Du}^* = \frac{2}{3}\left(\frac{\rho_g \mathrm{CEC}}{\sigma_w}\right)\left[\beta_{(+)}(1-f) - i\beta_{(+)}^S f\right]. \tag{8}$$

where f denotes the fraction of counterions in the Stern layer (dimesnionless), ρ_g denotes the grain density (typically 2650 kg m^{-3}), $\beta_{(+)}$ denotes the mobility of the counterions in the diffuse layer (equal to the mobility of the same cations in the bulk pore water, $\beta_{(+)}(\mathrm{Na}^+, 25°\mathrm{C}) = 5.2\times10^{-8}$ m^{2}s^{-1}V^{-1}), and $\beta_{(+)}^S$ denotes the mobility of the counterions in the Stern layer ($\beta_{(+)}^S(25°\mathrm{C}, \mathrm{Na}^+) = 1.5 \times 10^{-10}$ m^{2}s^{-1}V^{-1}). According to *Revil* [2012], $f \approx 0.90$ for illite and smectite (the salinity dependence of f is discussed in Appendix A). The surface

conductivity and the Dukhin number are defined as the real part of the complex surface conductivity and the real part of the complex Dukhin number,

$$\sigma_S = \mathrm{Re}\left[\sigma_S^*\right], \tag{9}$$

$$\mathrm{Du} = \mathrm{Re}\left[\mathrm{Du}^*\right], \tag{10}$$

respectively.

The in phase conductivity normalized by the pore water conductivity and the phase obey therefore the following relationships,

$$\frac{\sigma}{\sigma_w} = \frac{1}{F} + \mathrm{Du}\,, \tag{11}$$

$$\varphi \approx -\frac{\frac{2}{3} F \beta_{(+)}^S f \rho_g \mathrm{CEC}}{\sigma_w + \frac{2}{3}\beta_{(+)} F (1-f)\rho_g \mathrm{CEC}}\,. \tag{12}$$

Following *Revil* [2012] and *Revil et al*. [2013a], this last equation for the phase can be also approximated by,

$$\varphi \approx -\frac{\beta_{(+)}^S \, f \, Q_V}{\sigma_w + \beta_{(+)}(1-f)\, Q_V}\,, \tag{13}$$

where the charge per unit volume density is related to the cation exchange capacity of the material by [*Thomas*, 1976],

$$Q_V \equiv \rho_g \left(\frac{1-\phi}{\phi}\right)\mathrm{CEC}\,. \tag{14}$$

In Appendix A, following the ideas of the Stern layer polarization model developed by *Revil* [2012], we show that the salinity dependence of the quadrature conductivity of the saprolite can be expressed by the following relationship,

$$\sigma'' \approx \sigma_M'' \left(\frac{C_f K_{\mathrm{Na}}}{1 + C_f K_{\mathrm{Na}}}\right), \tag{15}$$

where,

$$\sigma_M'' = -\frac{2}{3}\left(\rho_g \beta_{(+)}^S \Gamma_{\mathrm{S}}^0 f_M\right) S_{sp}\,. \tag{16}$$

The quantity σ_M'' denotes the maximum value of the quadrature conductivity reached at high pH and high salinity values and K_{Na} denotes the apparent sorption constant of Na^+ in the Stern layer of the clay minerals.

3.2. Comparison with Experimental Data

Figure 5 shows that Eqs. (11) and (13) provide a correct representation of the experimental data (conductivity and phase) obtained recently by *Revil et al*. [2013a]. The formation factor F is in the range 4 to 6 (porosity in the range 0.43-0.49), the cementation exponent is in the range 1.8 to 2.5, and the surface conductivity is in the range (70-400)$\times 10^{-4}$ S m^{-1}. We will see later in Section 4 that these values are in contrast with the values obtained on an undisturbed core sample with the contaminated ground water. Indeed, we will get a formation factor of 19.5 (at a porosity of 0.37), a cementation exponent of 2.95, and a surface conductivity of 55×10^{-4} S m^{-1}.

In addition to the complex conductivity measurements, we also performed cation exchange capacity (CEC) and specific surface area (using the BET method) measurements on 7 saprolite core samples from the background site of Oak Ridge. The measurements were performed with a barium chloride solution to displace the cations sorbed to the clay mineral surfaces (see protocol in *Sumner and Miller* [1996]). All the seven samples were analyzed in duplicates with relative standard deviation less than 17% (see Figure 6). The average measured CEC value of the samples range from 5.0 to 8.6 cmol kg^{-1} or $CEC_M = (4.8\text{-}8.3)\times 10^3$ C kg^{-1}. The specific surface area is S_{sp} = 19,000 m^2 kg^{-1} (measured on same samples from the background site). Taking $CEC_M = 6\times 10^3$ C kg^{-1}, the equivalent total charge per unit surface area is therefore $Q_S = CEC_M / S_{sp}$ = 0.32 C m^{-2} (two elementary charges per nm2 as predicted bv *Revil et al.* [1998]). The CEC range reported above together with $\beta^S_{(+)}$(25°C, Na$^+$) = 1.5 × 10^{-10} m^{2}s^{-1}V^{-1}, and f_M = 0.92 (high salinity asymptotic value) yields σ_M'' = - (1.1-1.9)$\times 10^{-3}$ S m^{-1} at high salinities in excellent agreement with the laboratory data shown in Figure 7 (see the high salinity asymptote, σ_M'' = - (1.5)$\times 10^{-3}$ S m^{-1}).

4. Column Experiment: Material and Methods

4.1. Materials

The saprolite core sample used for the flow-through experiment was collected from Area 3 of the Oak Ridge IFRC (Figure 1c) site at a depth of ~ 15 m below ground surface in October 2008 (Well FW130, see position in Figure 1d). The material at this depth represents the weathered (heavily contaminated) saprolite. This depth corresponds to the lower part of the saprolite aquifer, which is characterized by an enhanced permeability with respect to the upper part of the saprolitic aquifer [*McKay et al*., 2000]. The permeability and hydraulic conductivity values for the column were determined from the differential pressure transducer data and flow rate using Darcy's law. The value of the permeability is ~1.46×10^{-13} m^2 (145.8 mD, hydraulic conductivity at 1.39×10^{-6} m s^{-1}, 0.12 m/day). This value is consistent with literature data with a hydraulic conductivity given at 10^{-6} m s^{-1} for the saprolite by *McKay et al*. [2005].

The sample is also coming from an area corresponding to one of the preferential pathways (called CP1 in the nomenclature developed by *Revil et al.* [2013b]) for contaminant migration from the contaminated

sediments located below the former S-3 disposal ponds. The porosity of the weathered saprolite ranges from 0.30 to 0.50 [*Jardine et al*., 1988, *Jardine et al*., 1993a, b; *Wilson*, 1992] and the porosity of our core sample is 0.37 based on gravimetric measurements performed after the completion of the experiment. This porosity is consistent with the range reported by *Jardine et al*. [1988, 1993a,b]. Weathered saprolites are indeed characterized by a porosity in the range 0.30 to 0.50. The soil sample used in our experiment is actually very typical of what is described as fractured saprolite at the site. It is a mixture of fractured rock pieces and fines. Note that only fines were used for the laboratory measurements on the core samples described in Section 3. Therefore the column experiment described below is believed to be more representative of the field conditions.

The effective porosity of a rock or soil is defined as the fraction of the pore network dynamically connected by the flow lines. The effective porosity is usually expected to be much lower that the measured connected (gravimetric) porosity, especially in the transition zone. This will be discussed in more details below when we will provide an idea of the effective porosity for the saprolite core samples in Section 5.3 below. The core was caped and stored at 4°C until used for the experiment. The dimension of the core is ~ 4.3 cm in diameter and 30 cm in length, a scale that is believed to correspond to the representative elementary volume defined in the field in terms of size of the heterogeneities.

Two types of groundwater were collected for the column experiment. Heavily contaminated ground water was extracted from Well FW130 at a depth of ~15 m, same to the depth where the core used for the experiment was retrieved. The second ground water sample was collected from the upper portion of the saprolitic aquifer in Well FW116 (located 8 m to the east of FW130). Both waters were collected shortly before the start of the experiment and were kept at 4°C until they were used for the experiment. The first (contaminated) groundwater was used to saturate the soil core while the second water was used to simulate the infiltration of fresh water. The compositions of both ground waters are given in Table 1.

4.2. Experimental Setup

To minimize disturbances to the sediment pore structure and to preserve the hydraulic properties of the cylindrical core, the sample was used directly for the experiment. Because the sidewall of the core tubing was too thin, a polycarbonate slab was fabricated and glued to the core sleeve for electrode housing. End caps with ports for fluid delivery were installed as well (Figure 8). After the attachment of the polycarbonate slab, four ports were drilled at an interval of 7 cm for the setting up the array of Ag/AgCl electrodes. Inline pH sensors were used at both ends of the column to monitor pH changes over time and an inline conductivity meter was also installed at the effluent side of the column to monitor the fluid conductivity (Figure 8).

Because of the importance of CO_2 partial pressure (pCO_2) on pH and carbonate species, in-situ pCO_2 level at ~ 90 kPa at the weathered saprolite zone (~ 50 ft below the ground surface) was simulated. The influent fluid reservoir was saturated and bubbled with CO_2 at ~90 kPa and a back pressure regulator was installed at the effluent end to maintain the pCO_2 value within the column. A HPLC pump was used to deliver the fluids into the saprolite-filled vertical column.

After construction, the column was saturated with the groundwater extracted from FW130 to establish the baseline geochemical conditions. After stabilization of the baseline geochemistry, the relatively fresh water from well FW116 was injected into the column to simulate fresh water infiltration. Spectral induced polarization (SIP) data were collected automatically. Inline pH and conductivity data were collected as well on a daily basis. The injection of the perched water was continued for ~ 90 days with a total of ~ 16 pore volumes injected through the sample. The flow rate was about 5.5 days per pore volume (~ 1.2 ml/hour, based on a measured porosity of ~ 0.366). This flow rate is consistent with a relaxation of the measured resistivity over time with a characteristic time of 19 days. This characteristic time is in turn very comparable to the characteristic time observed in the field for infiltration events as discussed below in Section 6. Effluent pore water samples were collected with syringes after filtration through a 0.2 micron filter.

The evolution of the pH and conductivity of the effluent is shown in Figure 9a. If the pH of the effluent is plotted as a function of the electrical conductivity of the effluent, there are two phases that can be observed (Figure 9b). Phase I corresponds to a rapid change in both the pH and conductivity of the effluent. In this phase, the pH of the effluent is linearly proportional to the conductivity of the effluent (Figure 9c). In the second phase (Phase II), the pore water conductivity is roughly constant while the pH of the effluent still changes over time. We will see below that the existence of these two phases is useful to analyze the effect of the pore water conductivity and pH upon the quadrature conductivity of the saprolite during the flow-through experiment.

4.3. Acquisition of the Complex Conductivity

Spectral induced polarization measurements were collected with a National Instruments (NI) dynamic signal analyzer (DSA, NI4461) using electrodes placed along the length of the column (Figure 8). A preamplifier was used to boost the input impedance to 10^9 Ohm to minimize current leakage. Water column calibration and repeatability tests indicate that errors were < 0.5 mrads for the phase and 0.5% for resistivity at low frequencies (< 1 kHz). Each measurement was composed of a phase lag between the current and the voltage □ and a magnitude |□| recorded relative to a precision reference resistor for forty frequencies spaced at equal logarithmic intervals from 0.1 to 1 kHz.

Typical spectra taken during the course of the experiment are shown in Figure 10. The resistivity and in-phase conductivity do not depend strongly on the frequency. The phase and the quadrature conductivity show a plateau at low frequencies, then a decrease of their magnitude (~10 Hz) and finally an increase of their magnitude above 10 Hz. This behavior is quite typical of low-frequency polarization with the low frequency (< 10 Hz) behavior being associated with electrical double layer polarization while the high frequency behavior is dominated by the Maxwell-Wagner polarization. We will report below the data at 1 Hz, which provides a good estimate of the low-frequency polarization.

In Figure 11a, we report the resistivity and the phase (at 1 Hz) during the course of the experiment while in Figure 11b we show the evolution of the in phase and quadrature conductivities. From Figures 9 and 11b, the in-phase conductivity is mainly controlled by the pore water conductivity while the quadrature conductivity is controlled by both the pore water conductivity and the pH.

4.4. Geochemical Data Acquisition

During the experiment, effluent samples were collected on regular basis with syringes attached to the outlet of the backpressure regulator (Figure 8). A 0.2 micron filter was used for filtration during sample collection. One milliliter of each sample was acidified with hydrochloric acid for cation analysis using Inductively Coupled Plasma – Mass Spectrometry (ICP – MS). Another milliliter was preserved for major anion analysis using Ion Chromatography (IC).

5. Column Experiment: Interpretation

5.1. Geochemistry

The evolution of the effluent pH and conductivity is shown in Figure 9a. If the effluent pH is plotted as a function of the effluent conductivity, there are two phases that can be observed (Figure 9b). Phase I corresponds to a rapid change in both the pH and conductivity of the effluent. In this phase, the pH of the effluent is linearly proportional to the conductivity of the effluent (Figure 9c). In the second phase (Phase II), the pore water conductivity is roughly constant while the pH of the effluent still changes over time. We will see that the existence of these two temporal phases is useful to analyze the effect of the pore water conductivity and pH upon the quadrature conductivity of the saprolite during the flow-through experiment.

The concentration of the major cations and anions are shown in Figure 12 and 13, respectively. The concentration of the effluent for species *i* is given by,

$$C_i(L,t) = (C_i^{\infty} - C_i^0)\tilde{C}_i(L,t) + C_i^0 , \tag{17}$$

and the normalized concentration of the effluent $\tilde{C}_i(L,t)$ is obtained by solving the 1D dispersion advection equation [*Lindstrom et al*., 1967; *Shackelford*, 1991, 1995],

$$\tilde{C}_i(L,t) = \frac{1}{2}\left\{ \mathrm{erfc}\left(\frac{R_d - T}{2\sqrt{\frac{R_d T}{P_L}}} \right) + \exp\left(P_L\right)\mathrm{erfc}\left(\frac{R_d + T}{2\sqrt{\frac{R_d T}{P_L}}} \right) \right\}, \tag{18}$$

$$T = \frac{vt}{L},\ P_L = \frac{vL}{\bar{D}}, \tag{19}$$

$$\bar{D} = D + \alpha v. \tag{20}$$

where v denotes the average pore water velocity (m s^{-1}), t is time (in s), T denotes the number of pore volumes of flow (unitless), P_L the column Peclet number (unitless), L the length of the column (0.3 m), $\bar{D}$ combines the diffusion coefficient (in m^2 s^{-1}), D, and the dispersion coefficient ($D_v = \alpha v$, in m^2 s^{-1} where α denotes the longitudinal dispersivity expressed in m). When the transport is dominated by advection and dispersion, the Peclet number is given by $P_L = L/\alpha$. In Eq. (18), the function $\mathrm{erfc}(x)$ denotes the complementary error function of argument x defined by $\mathrm{erfc}(x) = 1 - \mathrm{erf}(x)$ where $\mathrm{erf}(x)$ denotes the error function defined by,

$$\mathrm{erf}(x) = \frac{2}{\sqrt{\pi}} \int_0^x \exp(-\xi^2) d\xi. \tag{20}$$

For non-reactive solutes the retardation factor R_d is equal to 1 and therefore we have,

$$\tilde{C}_i(L,t) = \frac{1}{2}\left\{ \mathrm{erfc}\left(\frac{1 - T}{2\sqrt{\frac{T}{P_L}}} \right) + \exp\left(P_L\right)\mathrm{erfc}\left(\frac{1 + T}{2\sqrt{\frac{T}{P_L}}} \right) \right\}. \tag{21}$$

Eqs. (18) or (21) are used to fit the column data for some of the major cations and nitrate (Figure 12). The data agree with a Peclet number P_L = 3.5±0.5. The retardation coefficient are determined for each cation and reported in Table 3. Assuming molecular diffusion can be neglected, the longitudinal dispersivity is given by α = 0.086 m. This value is in agreement with the low range of values reported by *Gwo et al*. [1995, 1996, 1998] (α in the range 0.08-0.27 m from modeled tracer field experiments).

5.2. Conceptual flow model

The breakthrough of various species from the geochemical data support the conceptual flow model established for the weathered saprolite at the Oak Ridge IFRC site: A mixed advective flow through macro- and meso- pores with diffusive transport through low permeability micro- pores in soil matrix (*Jardine et al*. [1988, 1993a,b]; *Reedy et al.* [1996]; *Moline et al.* [1997]; *Sanford and Solomon* [1998]; *Mayes et al*. [2003]). The different flow regions are interconnected with flow through fractures. Although the fractures contribute to only 5-10% of the total porosity, it could contain greater than 95% of the pore water flux (*Watson et al* [2004]) due to its high permeability.

Geochemical data (Figures 12 and 13) show rapid decrease of major ion species, e.g. Na^+, Ca^{2+}, and SO_4^{2-}, during the injection of the first pore volume of low ionic strength perched water, indicating the existence of fast flow paths through the soil column. These fast flow paths interconnect the multi-porosity regions which promoted mixing and diffusion transport with the fast flow paths. The combination of advection and diffusion is responsible for the quick breakthrough of major ion species during the injection of the first two pore volume of the perched groundwater. The observed peaks for a few species, e.g. K, Fe, Pb and Rb, occurred around one pore volume with prolonged tails, which are indications of surface desorption and diffusive transfer from micropores into the fracture porosity.

5.3. In Phase Conductivity

The evolution of the conductivity of the effluent over time can be described by,

$$\sigma_w(L,t) = \frac{\sigma_w^\infty - \sigma_w^0}{2}\left\{\operatorname{erfc}\left(\frac{R_d - T}{2\sqrt{\frac{R_d T}{P_L}}}\right) + \exp\left(P_L\right)\operatorname{erfc}\left(\frac{R_d + T}{2\sqrt{\frac{R_d T}{P_L}}}\right)\right\} + \sigma_w^0 . \qquad (22)$$

The evolution of the conductivity of the material is therefore given by,

$$\sigma' = \left(\frac{\sigma_w^\infty - \sigma_w^0}{2F}\right)\left\{\operatorname{erfc}\left(\frac{R_d - T}{2\sqrt{\frac{R_d T}{P_L}}}\right) + \exp\left(P_L\right)\operatorname{erfc}\left(\frac{R_d + T}{2\sqrt{\frac{R_d T}{P_L}}}\right)\right\} + \frac{\sigma_w^0}{F} + \sigma_S . \qquad (23)$$

The in-phase conductivity data are analyzed in Figure 14. Figure 14a, we show the in-phase conductivity and effluent water conductivity versus time. The relationship between the material conductivity and the pore water conductivity can be used to determine the formation factor, F = 19.5 (Table 1). As discussed by *Revil et al*. [1998], the inverse of the formation factor is exactly the effective porosity (ϕ_{eff} = 1/F). It follows that the effective porosity is given by ϕ_{eff} = 0.05, which is therefore significantly lower than the total connected porosity (ϕ=0.37). This result is in agreement with the modeling of tracer tests at both laboratory and field scales (see *Jardine et al*. [1988]; *Reedy et al*., [1996]). The formation factor and the porosity can be used to determine the cementation exponent using $m = -\ln F / \ln \phi$. We obtain m = 2.95 (Table 1), higher than the value reported for the fine fraction (m = 2.2±0.3) for the core samples discussed in Section 3.

The surface conductivity determined in Figures 14b and 14c is 55×10^{-4} S m^{-1}. This value is smaller than for the core samples used from the background site with only the fine portion and with a simple supporting electrolyte (NaCl). This result is logical with respect to the sorption of ionic species in the Stern

layer than are less mobile than sodium as discussed by *Vaudelet et al.* [2011a, b]. This shows that a careful consideration of the pore water chemistry is needed if we want to account for the impact of surface conductivity in interpreting electrical resistivity tomograms, a point that has been unfortunately neglected in many studies in hydrogeophysics.

5.4. Quadrature Conductivity

Figure 15 shows the influence of the pH upon the quadrature conductivity (pore water conductivity ~0.07 S m^{-1} at 25°C) in Phase II of the experiment (once the pore water conductivity has stabilized). We see clearly a control of the quadrature conductivity by the pH of the pore water solution according to,

$$\sigma''(\mathrm{pH}) = -2\times10^{-5}(\mathrm{pH}-1), \tag{24}$$

at a constant pore water conductivity. As the quadrature conductivity is controlled by the surface electrochemistry of the Stern layer, this shows the impact of the pH on the sorption of the counterions in the Stern layer (see discussion in Appendix A).

6. Application to Field Data

We apply our model to time-lapse resistivity data collected downstream, south of the former S-3 disposal pond during the period 11/06/2008 to 01/31/2009 (see position Figure 16a and *Kowalsky et al*., 2011, and *Gasperikova et al*., 2012 for further details). The direction of the two contaminants plumes CP1 and CP2 (intersecting the resistivity profile) is south west because of the strong anisotropy of the formation and the topography of the aquifer-substratum interface while the head gradient is from north to south. Fall 2008 was characterized by strong rain events (Figure 16b). As the result, the ditch surrounding the S-3 pond was partially filled with water in its southern portion and meteoritic water infiltrated the perched aquifer (see Figure 2). In this section, we analyze the time-lapse resistivity data collected during this period using a recently developed method, the Active Time Constrained approach (ATC, see Appendix B). This time-lapse inversion is used to see how the infiltration event of fresh water was recorded in the resistivity time-series and how the model described in Section 3 and validated in Section 4 above can be used to interpret these data.

6.1. Geophysical Dataset

A total of 15 snapshots of dipole dipole resistivity data were obtained donwstream the former S-3 Ponds on a portion of Profile P1 (see position Figures 1c and 1d). Each snapshot comprises 2568 measurements. The inversion of the data was performed by using the code developed by *Karaoulis et al.* [2011a, b] (see also *Kim et al*. [2009] for a discussion of the Active Time Constrained, ATC, approach used to invert the data). The approach we followed is explained in Appendix B. The results of the inversion are shown

in Figure 17a. Inversion converged after 7 iterations with a data RMS misfit of 15% (Figure 17b). The inverted tomograms show the position of both the CP1 plume (characterized by low nitrate and high uranium concentrations) and the CP2 plume (characterized by high nitrate and low uranium concentrations).

In Figure 18, we show the time series for points A and B located in plumes CP1 and CP2, respectively (see Figure 17a). According to the time lapse resistivity tomograms, the main change in resistivity occurs in the plume CP1, which means that the mixing between the infiltrated water and the original water from the CP1 plume occurs upstream (with respect to the position of the resistivity profile) between the source (the former S-3 disposal ponds) and the position of the resistivity profile. The time-lapse resistivity variations shown in Figure 17a seem to exclude a direct infiltration from the perched aquifer into the deeper portion of the saprolite (the transition zone). Indeed, a gradual infiltration should show a gradual change in the resistivity from the top to the deeper portions of the saprolite over time. Instead we see only changes in the plume CP1 at the depth of the transition zone. This may therefore indicates that the mixing between the fresh water and the contaminated water occurs upstream with respect to the psoition of the resistivity profile.

Before discussing a conceptual model of mixing of the fresh and contaminated waters, we point out that the results displayed by the resistivity tomograms agree with some available and limited in situ observations during this time period. Indeed, Figure 18a shows the dilution of the nitrate plume in Well FW120 during this period. Figure 19 shows that the dilution of the contaminant plume followed an exponential relationship as observed in our column experiment (see Figure 11a).

As mentioned above our model indicates that the mixing between the fresh and contaminated water occurs in between the position of the resistivity profile and the position of the former S-3 ponds. As shown in Figure 20, this area is the setting of the ditch surrounding the former S-3 basins. We think therefore that the ditch plays a major role in the infiltration of the meteoric water and its mixing with the CP1 plume. Indeed, as explained above, the south corner of the ditch surrounding the S-3 basins has the lowest altitudes and therefore is an area where water accumulates preferentially after storms and rainfalls. This may explain why there is some infiltration and mixing for the CP1 plume and not for the CP2 plume.

The conceptual model sketched in Figure 20 implies that the fresh water and the contaminated water mixed just below the ditch. The next question to address is how much fresh water mixed with the contaminated water. This question is addressed in the next section.

6.2. Mixing of End-Members below the Ditch

We want now to determine how much fresh water mixes with contaminated water in plume CP1. According to our resistivity model (transforming the resistivity into nitrate concentration using a correction for the surface conductivity), the nitrate concentration of the CP1 plume is 33,000 mg L^{-1} in absence of

mixing with the fresh water and 11,500 mg L^{-1} during steady state infiltration of the fresh water. The concentration of nitrate in the fresh aquifer is 0 mg L^{-1}. We can therefore compute how much water from the perched aquifer mixes with the contaminated water from the source of the CP1 plume. During mixing, the nitrate concentration in the mixed pore water $C(NO_3, mix)$ is given by,

$$C(NO_3, mix) = \chi C(NO_3, CP1), \quad (25)$$

where $C(NO_3, CP1)$ denotes the concentration in the CP1 plume in absence of infiltration from the ditch or the perched aquifer (33,000 mg L^{-1}). From Eq. (25), we have,

$$\chi \approx \frac{C(NO_3, mix)}{C(NO_3, CP1)} \approx 0.35. \quad (26)$$

Therefore during the steady state infiltration into the CP1 plume, the pore water is a mix of one third of the original pore water from the heavily contaminated sediment located beneath the former S-3 pond and two thirds of fresh water possibly infiltrating the aquifer from the ditch.

6.3. Proposed Model of Infiltration

With the conceptual model proposed in Figure 20 and the amount of mixing allowed by the infiltration of the fresh water and contaminated water, we can test our model with respect to the resistivity data to see if it is compatible with the properties of the aquifer. We use therefore exactly the type of 1D model used for the column experiment. Initially, contaminated water flows in the CP1 plume. At a certain time, this water is replaced by a mix of one third of the original pore water from the S-3 pond and two thirds of fresh water infiltrating from the ditch. We use Eq. (23) to fit the time-lapse resistivity data in the plume CP1 (located in the transition zone) using the velocity of the pore water determined from the head gradient in the aquifer (0.02) and the permeability of the aquifer (see value in Table 2). The data are fitted with a Peclet number of 2.3 (Figure 21a) pretty close to the one determined in the flow through experiment (3.5).

In Figure 21b, we predict the variation of the nitrate concentration versus time in plume CP1 showing the transition from 33,000 mg L^{-1} to about 11,000 mg L^{-1}. The addition of complex conductivity data (through frequency-domain or time-domain induced polarization measurements) could be used to assess also the variation of the pH of the pore water versus time during such an infiltration event.

7. Conclusions

In order to understand dilution of some of the contaminant plumes associated with the former S-3 disposal ponds at the Oak Ridge IFRC site (Tennessee), we performed a flow through experiment using

relatively fresh ground water from the upper portion of the saprolitic aquifer. The saprolite core sample was initially saturated with the contaminated ground water sampled in the heavily contaminated portion of the aquifer. The following results were obtained:

1. Our sample was collected from the transition zone between the saprolitic aquifer and the shale bedrock. This transition zone is characterized by a higher hydraulic conductivity with respect to the overlying saprolitic aquifer. The formation factor is on the order of 20 and the surface conductivity associated with the presence of clays is on the order of 55×10^{-4} S m^{-1}. The cementation exponent is very high, close to 3. This high value is consistent with a strong decoupling between the mobile (effective) porosity, which is in turn associated with the presence of cracks in our sample, and the immobile porosity associated with the matrix porosity.

2. At a constant pore water conductivity, the quadrature conductivity of the saprolite is dependent on the pH of the pore water. This dependence could be used to monitor, non-intrusively, changes in the pH of the pore water. At the Oak Ridge IFRC site, monitoring pH changes is very important because the pH controls the concentration of uranium in the ground water, which is released through changes in the electrochemistry between the pore water and the surface of the clay minerals. Our results suggest therefore that time-lapse induced polarization should be performed at this test site over time to analyze the electrical resistivity and the chargeability in terms of nitrate concentration and pH changes.

3. The decrease in the ionic strength of the pore water is responsible for the desorption of various metals from the mineral surface. This has a direct impact on reactive transport modeling of the geochemistry of the CP1 plume downstream the former S-3 disposal ponds. We have provided a new set of CEC and specific surface area measurements that can be used in reactive transport modeling codes.

4. Time-lapse resistivity tomography can be performed by incorporating directly in the cost function to minimize a time dependent term. We use the Active Time Constrained approach as an efficient way to filter out the effect of noise in the recorded dataset of apparent resistivities. This approach was used to invert a sequence of 15 snapshots showing the effect of an infiltration event upon the conductivity of the CP1 plume located at the south corner of the S-3 pond.

5. Based on the field dataset, we have determined that during infiltration events the pore water is a mix of one third of the original pore water from the contamination source(S-3 ponds) and two thirds of fresh water. We have shown that very likely this fresh water is mixing the contaminated water just at the south portion of the ditch surrounding the S-3 pond.

Acknowledgments. We thank the Environment Remediation Science Program (ERSP), U.S. Department of Energy (DOE, award DE-FG02-08ER64659) for funding. The authors appreciate the efforts of Davis Lesmes, the ERSP program manager. We thank Marcella Mueller for her help in getting the Oak Ridge data and samples, Jennifer Earles for the Water levels, Kevin Birdwell for the precipitation data from the ORNL Meteorological Program, and Magnus Skold for his help with the experimental data.

References

Archie, G.E. (1942), The electrical resistivity log as an aid in determining some reservoir characteristics, *Transactions of AIME*, 146, 54–62.

Avena, M. J., and C. P. De Pauli (1998), Proton adsorption and electrokinetics of an Argentinean Montmorillonite, *J. Colloid Interface Sci*., *202*, 195–204, doi: 10.1006/jcis.1998.5402.

Chen, J., S.S. Hubbard, V. Korneev, D. Gaines, G. Baker, and D. Watson (2010), Stochastic inversion of seismic refraction data for estimating watershed-scale aquifer geometry: development and application to a contaminated aquifer, *Water Resources Research*, 46, W11539, doi:10.1029/2009WR008715.

Chen, J., S.S. Hubbard, J. Peterson, K. Williams, M. Fienen, P. Jardine, and D. Watson (2006), Development of a joint hydrogeophysical inversion approach and application to a contaminated fractured aquifer, *Water Resources Research*, 42, W06425, doi:10.1029/2005WR004694.

Chittoori B., and A.J. Puppala (2011), Quantitative Estimation of Clay Mineralogy in Fine-Grained Soils, *J. Geotech. Geoenviron. Eng., 137(11)*, 997-1008, doi: 10.1061/(ASCE)GT.1943-5606.0000521.

Deceuster J., and O. Kaufman (2012), Improving the delineation of hydrocarbon-impacted soils and water through induced polarization (IP) tomographies: A field study at an industrial waste land, *Journal of Contaminant Hydrology*, 136-137, 25–42.

de Lima, O.A.L., and M.M. Sharma (1992), A generalized Maxwell–Wagner theory for membrane polarization in shaly sands, *Geophysics*, 57, 431–440.

Gasperikova E., S. S. Hubbard, D. B. Watson, G. S. Baker, J. E., Peterson, M. B. Kowalsky, M. Smith, and S. Brooks, 2012. Long-term electrical resistivity monitoring of recharge-induced contaminant plume behavior, Contaminant Hydrogeology, 142–143, 33-49.

Grosse, C. (2011), Extension of the classic thin double layer polarization theory of colloidal suspensions to include the stagnant layer conductivity, *J. Phys. Chem. B*., 115, 29, 8996-9004.

Gwo, J.P., P.M. Jardine, G.V. Wilson, and G.T. Yeh. (1995), A multiple-pore-region concept to modeling mass transfer in subsurface media, *J. Hydrol*., 164, 217-237.

Gwo, J.P., P.M. Jardine, G.V. Wilson, and G.T. Yeh (1996), Using a multiregion model to study the effects of advective and diffusive mass transfer on local physical nonequilibrium and solute mobility in a structured soil, *Water Resource. Res*., 32, 561-570.

Gwo, J.P., R. O'Brien, and P.M. Jardine (1998), Mass transfer in structured porous media: embedding mesoscale structure and microscale hydrodynamics in a two-region model, *J. Hydrol*., 208, 204-222.

Flores Orozco, A., A. Kemna, C. Oberdörster, L. Zschornack, C. Leven, P. Dietrich, and H. Weiss, Delineation of subsurface hydrocarbon contamination at a former hydrogenation plant using spectral induced polarization imaging, Journal of Contaminant Hydrology, 136–137, 131–144.

Jardine, P. M., G. V. Wilson, and R. J. Luxmoore (1988), Modeling the transport of inorganic ions through undisturbed soil columns from two contrasting watersheds, *Soil Science Society of America Journal*, 52, 1252- 1259.

Jardine, P. M., G. K. Jacobs, and G. V. Wilson (1993a), Unsaturated transport processes in undisturbed heterogeneous porous media. I. Inorganic Contaminants, *Soil Science Society of America Journal*, 57, 945-953.

Jardine, P. M., G. K. Jacobs, and J. D. O'Dell (1993b), Unsaturated transport processes in undisturbed heterogeneous porous media II. Co-Contaminants, *Soil Science Society of America Journal*, 57, 954-962.

Karaoulis, M.,. J.-H. Kim, and P.I. Tsourlos (2011a), 4D Active Time Constrained Inversion, *Journal of Applied Geophysics*, 73(1), 25-34.

Karaoulis M., A. Revil, D.D. Werkema, B. Minsley, W.F. Woodruff and A. Kemna (2011b), Time-lapse 3D inversion of complex conductivity data using an active time constrained (ATC) approach, *Geophysical Journal International,* 187, 237–251, doi: 10.1111/j.1365-246X.2011.05156.x.

Kim J.-H., M.J. Yi, S.G. Park, and J.G. Kim (2009), 4-D inversion of DC resistivity monitoring data acquired over a dynamically changing earth model, *Journal of Applied Geophysics*, 68, no. 4, 522-532.

Kowalsky, M. B., E. Gasperikova, S. Finsterle, D. Watson, G. Baker, and S. S. Hubbard (2011), Coupled modeling of hydrogeochemical and electrical resistivity data for exploring the impact of recharge on subsurface contamination, *Water Resources Research*, 47, W02509.

Leroy P., A. Revil, A. Kemna, P. Cosenza, and A. Ghorbani (2008), Spectral induced polarization of water-saturated packs of glass beads, *Journal of Colloid and Interface Science*, 321 (1), 103-117.

Lindstrom, F.T., R. Haque, V.H. Freed, and L Boersma (1967), Theory of the movement of some herbicides in soils: Linear diffusion and convection of chemicals in soils, *Env. Sci. and Tech*., 1, 7, 561-565.

Lipsicas, M. (1984), Molecular and surface interactions in clay intercalates, in *Physics and Chemistry of Porous Media*, edited by D. L. Johnson and P. N. Sen, pp. 191–202, Am. Inst. of Phys., College Park, Md.

Lockhart, N. C. (1980), Electrical properties and the surface characteristics and structure of clays, II, Kaolinite: A nonswelling clay, *J. Colloid Interface Sci*., *74*, 520–529.

Ma, C., and R. A. Eggleton (1999), Cation exchange capacity of kaolinite, *Clays Clay Miner*., *47*, 174– 180.

Mayes, M.A., P.M. Jardine, T.L. Mehlhorn, B.N. Bjornstad, J.L. Ladd, and J.M. Zachara (2003), Hydrologic processes controlling the transport of contaminants in humid region structured soils and semi-arid laminated sediments, *J. Hydrol.,* 275, 141-161.

Marshall, D.J., and T.R. Madden (1959), Induced polarization, a study of its causes, *Geophysics,* 24**,** 790–816.

Moline, G. R., R. Ketcham, and C. R. Knight (1997), Fracture-matrix exchange processes and their relationship to fracture characteristics, *EOS Trans. Am. Geophys. Union*, 78, 17, S138.

Morgan, F. D., F. Scira-Scappuzzo, W. Shi, W. Rodi, J. Sogade, Y. Vichabian, and D. Lesmes (1999), Induced polarization imaging of a jet fuel plume: Symposium on the Application of Geophysics to Engineering and Environmental Problems "SAGEEP", *Environmental and Engineering Geophysical Society, Proceedings*, 541–548.

McKay, L.D., W.E. Sanford, and J.M. Strong (2000), Field scale migration of colloidal tracers in a fractured shale saprolite, *Ground Water*, 38, no. 1, 139-147.

Patchett, J. G. (1975), An investigation of shale conductivity, *Society of Professional Well Logging Analysis 16th Logging Symposium*, Paper U, 41 p.

Reedy, O. C., P. M. Jardine, G. V. Wilson, and H. M. Selim (1996), Quantifying diffusive mass transfer of non-reactive solutes in columns of fractured saprolite using flow interruption, *Soil Sci. Soc. Am. J*., 60, 1376-1384.

Revil, A., L.M., Cathles, S., Losh, and J.A., Nunn (1998), Electrical conductivity in shaly sands with geophysical applications, *Journal of Geophysical Research*, 103(B10), 23,925-23,936.

Revil, A. and N. Florsch (2010), Determination of permeability from spectral induced polarization in granular media, *Geophysical Journal International*, 181, 1480-1498, doi: 10.1111/j.1365-246X.2010.04573.x.

Revil, A., K. Koch, and K. Holliger (2012b), Is it the grain size or the characteristic pore size that controls the induced polarization relaxation time of clean sands and sandstones? Water Resour. Res., 48, W05602, doi:10.1029/2011WR011561.

Revil, A., Skold M., S. S. Hubbard, Y. Wu, D. B. Watson, M. Karaoulis (2013a), Petrophysical properties of saprolite from the Oak Ridge Integrated Field Research Challenge site, Tennessee, in press in *Geophysics*.

Revil A., M. Skold, M. Karaoulis, M. Schmutz, S. S. Hubbard, T.L. Mehlhorn, and D. B. Watson (2013b), Hydrogeophysical investigations of the S-3 ponds contaminant plumes, Oak Ridge Integrated Field Research Challenge site, Tennessee, submitted to Geophysics.

Sanford, W. E., and D. K. Solomon (1998), Site characterization and containment assessment with dissolved gases, *ASCE Journal of Environmental Engineering*, 124, 6, 572-574.

Shackelford, C.D. (1991), Laboratory diffusion testing for waste disposal-A review, *Journal of Contaminant Hydrology,* 7, 177-217.

Shackelford, C.D. (1995), Cumulative mass approach for column testing, *Journal of Geotechnical Engineering*, 10, 696-703.

Shainberg, I., N. Alperovitch, and R. Keren (1988), Effect of magnesium on the hydraulic conductivity of Na-smectite-sand mixtures, *Clays Clay Miner*., *36*, 432– 438.

Shevenell, L.A., G.K. Moore, and R.B. Dreier (1994), Contaminant spread and flushing in fractured rocks near Oak Ridge, Tennessee, *GWMR*, 120-129.

Sinitsyn, V. A., S. U. Aja, D. A. Kulik, and S. A. Wood (2000), Acid-base surface chemistry and sorption of some lanthanides on K^+-saturated Marblehead illite. I. Results of an experimental investigation, *Geochim. Cosmochim. Acta*, *64*, 185– 194.

Slater, L., and D.P. Lesmes (2002), Electrical-hydraulic relationships observed for unconsolidated sediments, *Water Resources Res*., 38, 1213-1225.

Su, Q., Q. Feng, and Z. Shang (2000), Electrical impedance variation with water saturation in rock, *Geophysics*, *65*, 68– 75.

Sumner, M.E., and W.P. Miller (1996), *Cation Exchange Capacity and Exchange Coefficients*, In: Page, D.L. (ed.) Methods of soil analysis Part 3: Chemical Methods, Soil Science Society of America, Madison, WI.

Thomas, E. C. (1976), Determination of Qv from membrane potential measurements on shaly sands, *Trans., Am. Inst. Min., Metall., & Petr. Eng*., 261, Part I, 1087-1096.

Vaudelet P., A. Revil, M. Schmutz, M. Franceschi, and P. Bégassat (2011a), Induced polarization signature of the presence of copper in saturated sands, *Water Resources Research*, 47, W02526, doi:10.1029/2010WR009310.

Vaudelet P., A., Revil, M., Schmutz, M., Franceschi, and P. Bégassat (2011b), Changes in induced polarization associated with the sorption of sodium, lead, and zinc on silica sands, *Journal of Colloid and Interface Science*, 360, 739-752.

Watson, D.B., J.E. Kostka, M.W. Fields, and P.M. Jardine (2004), The Oak Ridge Field Research Center Conceptual Model, NABIR FRC Technical Report: NABIR FRC. http://public.ornl.gov/orifc/FRC-conceptual-model.pdf.

Watson, D.B., W.E. Doll, T.J. Gamey, J.R. Sheehan, and P. M. Jardine (2005), Plume and lithologic profiling with surface resistivity and seismic tomography, *Ground Water*, 43(2), 169-177.

Wilson, G. V., P. M. Jardine, and J. P. Gwo (1992), Modeling the hydraulic properties of a multi-region soil, *Soil Sci. Soc. Am. J*., 56, 1731-1737.

Zundel, J. P., and B. Siffert (1985), Mécanisme de rétention de l'octylbenzene sulfonate de sodium sur les minéraux argileux, in *Solid-Liquid Interactions in Porous Media*, pp. 447– 462, Technip, Paris.

Appendix A. Salinity Dependence of the Quadrature Conductivity

We propose here an alternative to the model reported by *Revil* [2012] and describing the salinity dependence of the partition coefficient *f*. We first start considering the sorption of sodium in the Stern layer of clays and the dissociation of protons according to,

$$>SH^0 \Leftrightarrow >S^- + H^+, \tag{A1}$$

$$>S^- + Na^+ \Leftrightarrow >S^-Na^+, \tag{A2}$$

where >S refers the surface sites attached to the crystalline framework, H^0 are protons (which are assumed to be immobile) while weakly sorbed Na^+ are considered to be mobile in the Stern layer. The equilibrium constants for these reactions are related to the concentrations of the different species by:

$$K_{Na} = \frac{\Gamma^0_{SNa}}{\Gamma^0_{S^-}\left[Na^+\right]^0}, \tag{A3}$$

$$K_H = \frac{\Gamma^0_{S^-}\left[H^+\right]^0}{\Gamma^0_{SH}}, \tag{A4}$$

(K_{Na} is not the same equilibrium constant as defined in *Revil* [2012]) and a conservation equation for the surface species:

$$\Gamma^0_S = \Gamma^0_{SNa} + \Gamma^0_{SH} + \Gamma^0_{S^-} + \Gamma^0_X, \tag{A5}$$

where Γ^0_S denotes the (known) total surface site density (including the charge associated with isomorphic substitutions in the crystalline framework), Γ^0_{SNa}, $\Gamma^0_{S^-}$, and Γ^0_{SH} represents the surface charge density of the sites $>S^-Na^+$, $>S^-$, and $>SH^0$ respectively, and Γ^0_X represents the number of equivalent sites corresponding to isomorphic substitutions (all expressed in sites m^{-2}). To simplify the notation, we write pH = $-\log_{10}[H^+]$ and $[Na^+] = C_f$ denotes the salinity. The resolution of the previous set of equations yields,

$$\Gamma^0_{SH} = \frac{\Gamma^0_S - \Gamma^0_X}{1 + \frac{K_H}{10^{-pH}}\left(1 + C_f K_{Na}\right)}, \tag{A6}$$

$$\Gamma^0_{S^-} = \frac{(\Gamma^0_S - \Gamma^0_X)K_H / 10^{-pH}}{1 + \frac{K_H}{10^{-pH}}\left(1 + C_f K_{Na}\right)}, \tag{A7}$$

$$\Gamma^0_{SNa} = \frac{(\Gamma^0_S - \Gamma^0_X)C_f K_{Na} K_H / 10^{-pH}}{1 + \frac{K_H}{10^{-pH}}\left(1 + C_f K_{Na}\right)}. \tag{A8}$$

All the charged sites that are not compensated in the Stern layer needs to be compensated in the diffuse layer. Therefore, the fraction of the counterions in the Stern layer is defined by the following sorption isotherm,

$$f = \frac{\Gamma^0_{\mathrm{SNa}}}{\Gamma^0_{\mathrm{SNa}} + \Gamma^0_{\mathrm{S^-}} + \Gamma^0_{\mathrm{X}}}. \tag{A9}$$

$$f = f_M \left\{ \frac{C_f K_{\mathrm{Na}}}{f_M (1 + C_f K_{\mathrm{Na}}) + (1 - f_M)\left[1 + C_f K_{\mathrm{Na}} + \dfrac{10^{-\mathrm{pH}}}{K_H}\right]} \right\}. \tag{A10}$$

$$f_M = 1 - \frac{\Gamma^0_{\mathrm{X}}}{\Gamma^0_S}. \tag{A11}$$

The value of f_M for kaolinite, illite, and smectite can be found in *Revil* [2012]. An average value is f_M = 0.90. At high pH values,

$$f \approx f_M \left(\frac{C_f K_{\mathrm{Na}}}{1 + C_f K_{\mathrm{Na}}} \right). \tag{A12}$$

We look now for the pH dependence of the CEC. The CEC is defined by,

$$\mathrm{CEC} = \frac{e}{f_M} (\Gamma^0_{\mathrm{SNa}} + \Gamma^0_{\mathrm{S^-}} + \Gamma^0_{\mathrm{X}}) S_{sp}. \tag{A13}$$

where S_{sp} correspond to the specific surface area (in $\mathrm{m^2\ kg^{-1}}$) and e the elementary charge. After some algebraic manipulations and simplification, we obtain,

$$\mathrm{CEC(pH)} = \mathrm{CEC}_M \left(1 - g(C_f, \mathrm{pH})\right). \tag{A14}$$

where $\mathrm{CEC}_M = e\Gamma^0_{\mathrm{S}} S_{sp}$ corresponds to the maximum CEC at value at high pH values and the funding g is defined by,

$$g(C_f, \mathrm{pH}) = \frac{f_M \left(\dfrac{10^{-\mathrm{pH}}}{K_{\mathrm{H}}} \right)}{1 + C_f K_{\mathrm{Na}} + \dfrac{10^{-\mathrm{pH}}}{K_{\mathrm{H}}}}. \tag{A15}$$

The quadrature conductivity is given by,

$$\sigma'' = -\frac{2}{3} \rho_g \beta^S_{(+)} f\ \mathrm{CEC}. \tag{A16}$$

where the product of f by the CEC is given by $f\,\mathrm{CEC}=e\Gamma^{0}_{\mathrm{SNa}}S_{sp}$ (the quadrature conductivity is controlled by the density of weakly sorbed sodium counterions in the Stern layer). After some algebraic manipulations we get,

$$\sigma'' = \sigma_M''\left(\frac{C_f K_{\mathrm{Na}} K_{\mathrm{H}}}{10^{-\mathrm{pH}} + K_{\mathrm{H}}\left(1 + C_f K_{\mathrm{Na}}\right)}\right), \tag{A18}$$

$$\sigma_M'' = -\frac{2}{3}\left(\rho_g \beta^{S}_{(+)} f_M e\Gamma^{0}_{\mathrm{S}}\right) S_{sp}\,. \tag{A19}$$

where σ_M'' denotes the quadrature conductivity reached at high salinity and pH. We will see that the pH dependence of the quadrature conductivity is pretty weak, which means that Eq. (A19) can be approximated by,

$$\sigma'' \approx \sigma_M''\left(\frac{C_f K_{\mathrm{Na}}}{1 + C_f K_{\mathrm{Na}}}\right), \tag{A18}$$

Appendix B: Time-Lapse Inversion of the Resistivity Data

The 4D model described by *Kim et al*. [2009] defines the subsurface as a combined space-time model, which encompasses all space models during the entire monitoring period. The entire monitoring data set is defined as a data vector in the space-time domain as well. Since both the data and the model are defined using space-time coordinates, the 4D-ATC algorithm is able to adopt regularization in both time and space to stabilize the inversion. The regularization in both space and time is efficient in reducing inversion artifacts associated with random noise in the data (i.e., temporally uncorrelated) and improve the stability of the inversion problem. *Karaoulis et al.* [2011a, b] modified the algorithm of *Kim et al*. [2009] and proposed a 4D active time constraint (4D-ATC) algorithm allowing time regularization to vary between different monitoring steps. While it keeps the basic merit of minimizing time-lapse inversion artifacts due to random noise in the data, it still allows relatively abrupt resistivity changes to occur in areas where there are significant indications from the data that such changes truly take place.

The objective function S to minimize is given by,

$$S = \boldsymbol{\Phi}_d + \lambda \boldsymbol{\Phi}_m + \alpha \boldsymbol{\Phi}_t, \tag{B1}$$

where $\boldsymbol{\Phi}_m$ and $\boldsymbol{\Phi}_t$, are the two regularization functions. The function $\boldsymbol{\Phi}_m$ is used to perform the regularization in space using smoothness (second order derivative) as regularizer while the function $\boldsymbol{\Phi}_t$, is used to perform regularization in time using flatness (first order derivative) as regularizer. The two parameters λ and α are the two regularizations terms that are present to balance the different contribution of the objective function. Regarding the space-domain smoothness constraint, a second-order differential operator is applied to the model perturbation vector. The time-domain trade-off parameter is expressed either as a constant value α ($\boldsymbol{A}$=α$\boldsymbol{I}$) or as a diagonal matrix $\boldsymbol{A}$ (*Karaoulis et al*. [2011a]), where it contains a series of Lagrange parameters. Minimizing the objective function, Eq. (B1), with respect to the model perturbation vector yields normal equations that can be found in *Karaoulis et al*. [2011a]. The error on the data was included in the inversion in the form of a covariance diagonal matrix.

Tables

Table 1. Composition of the ground water samples used for the experiment. Ground water sample F116 denotes the relatively fresh water in the upper (nearly uncontamined) portion of the aquifer. Sample FW130 refers to the deeper contaminated ground water. All units in mg L^{-1} unless specified. BDL: Below detection limit.

Parameter	FW116	FW130
pH	6.54	3.8
Fluid conductivity (S m^{-1})	0.067	2.08
Dissolved O_2	0.6	0.19
Ca	50.8	1429
Mg	5.8	231.5
Na	272.7	752
K	9.4	1133
SO_4	31.2	196.6
NO_3	254.5	14,335
Al	110.4	533.8
Mn	1.32	231.6
Fe	BDL	26.3
U	0.47	14.8
Sr	0.65	3

Table 2. Petrophysical properties of the saprolite.

Property	Parameter	Value
Porosity	ϕ	0.37±0.01
Permeability	k	1.5×10^{-13} m^2
Hydraulic conductivity	K	1.4×10^{-6} m s^{-1}
Surface area	S_{sp}	19,000 m^2 kg^{-1}
Cation exchange capacity	CEC	5000 C kg^{-1}
Formation factor	F	19.5
Cementation exponent	m	2.95
Longitudinal dispersivity	α_L	0.086 m

Table 3. Retardation coefficients for the cations.

Cation	Value
Na	1.7±0.1
Ca	1.8±0.2
U	1.8±0.3
Mn	1.5±0.3
Si	1.4±0.2

Figures

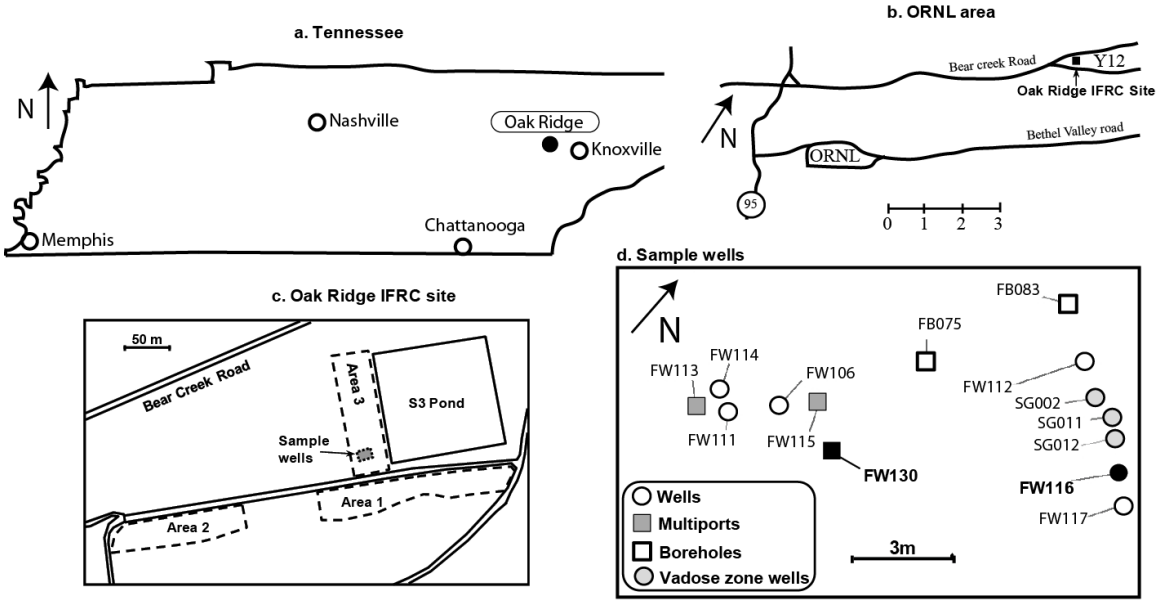

Figure 1. Position of the wells where the ground water was sampled. **a.** Location of Oak Ridge in Tennessee. **b.** Position of the Oak Ridge IFRC test site. **c.** Position of area 3 downstream the former S-3 disposal ponds. **d.** Position of the wells FW130 used to sample the contaminated ground water sampled at a depth of ~15 m and Well FW116 used to sample the fresh ground water from the shallow portion of the aquifer at a depth of ~ 2 m. SG012 is in the very shallow perched zone.

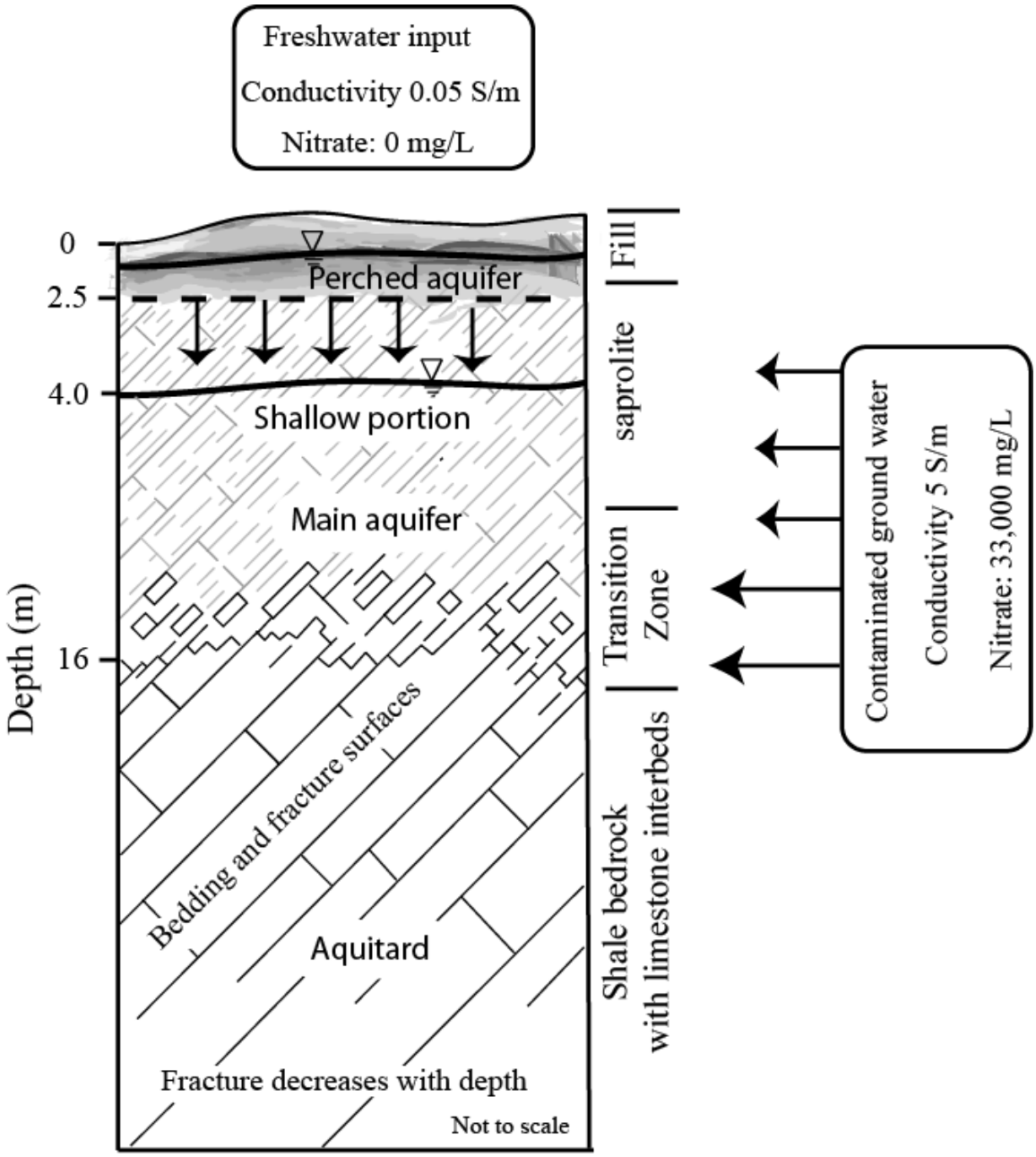

Figure 2. Position of the problem. Typical section of saprolite and parent rock at the Oak Ridge Integrated Field Research Challenge (IFRC) site. The transition zone at the bottom of the saprolitic aquifer is an area of higher permeability than the upper portion of the aquifer. Water infiltration can come either from the perched aquifer or from a ditch located in the vicinity of the S-3 pond. The shallow portion of the aquifer (sampled by the shallow Well F116) is influenced by the pervasive infiltration from the shallow aquifer.

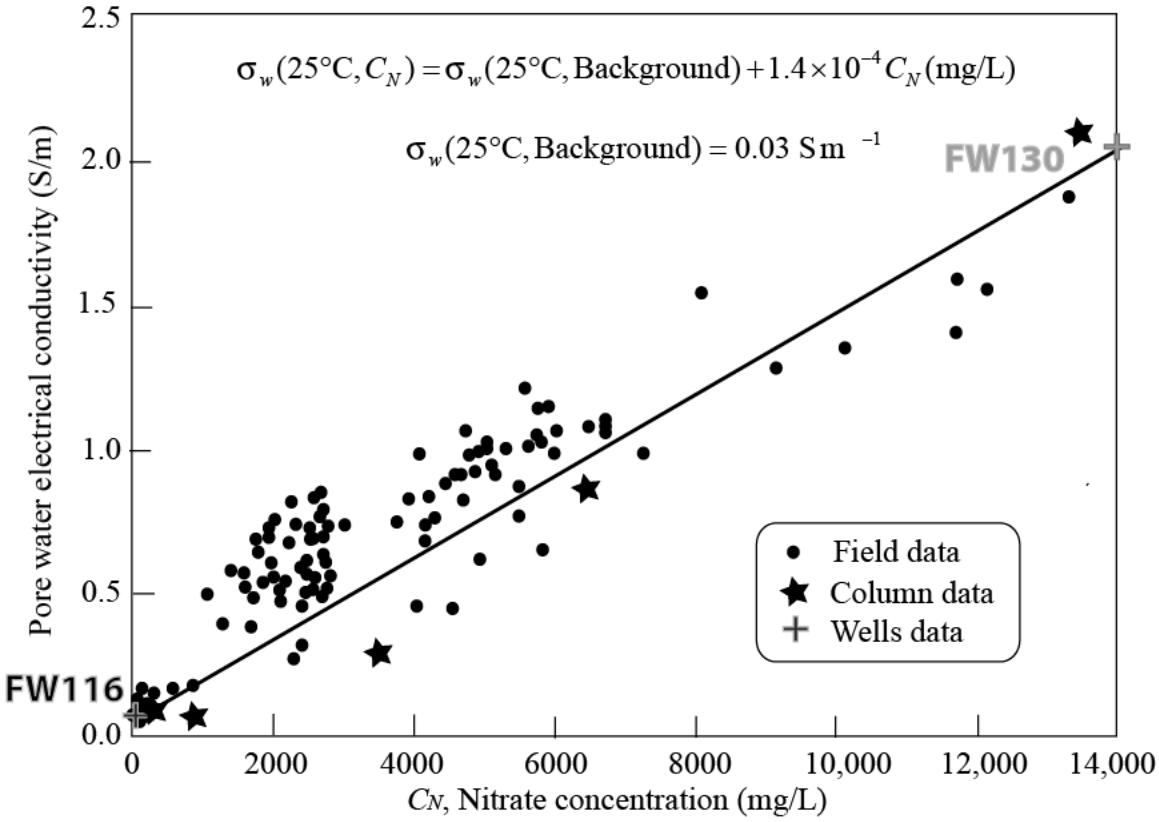

Figure 3. Relationship between the electrical conductivity of the pore water σ_w (in S m^{-1}) and the nitrate concentration C_N (in mg L^{-1}). This relationship respects the value of the conductivity and nitrate concentration in the perched and contaminated aquifers.

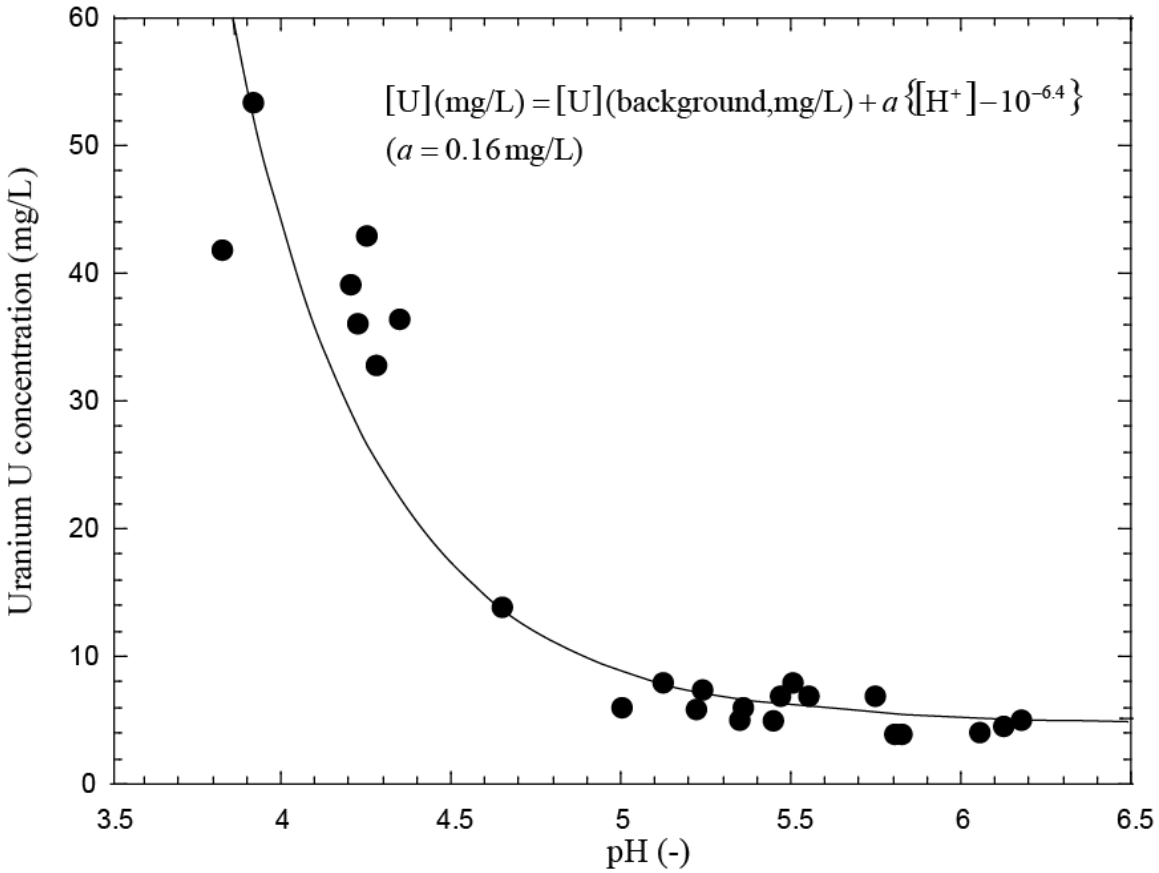

Figure 4. Relationship between the concentration of uranium and the pH of the pore water. This relationship respects the value of the pH and uranium concentration in the perched and contaminated aquifers.

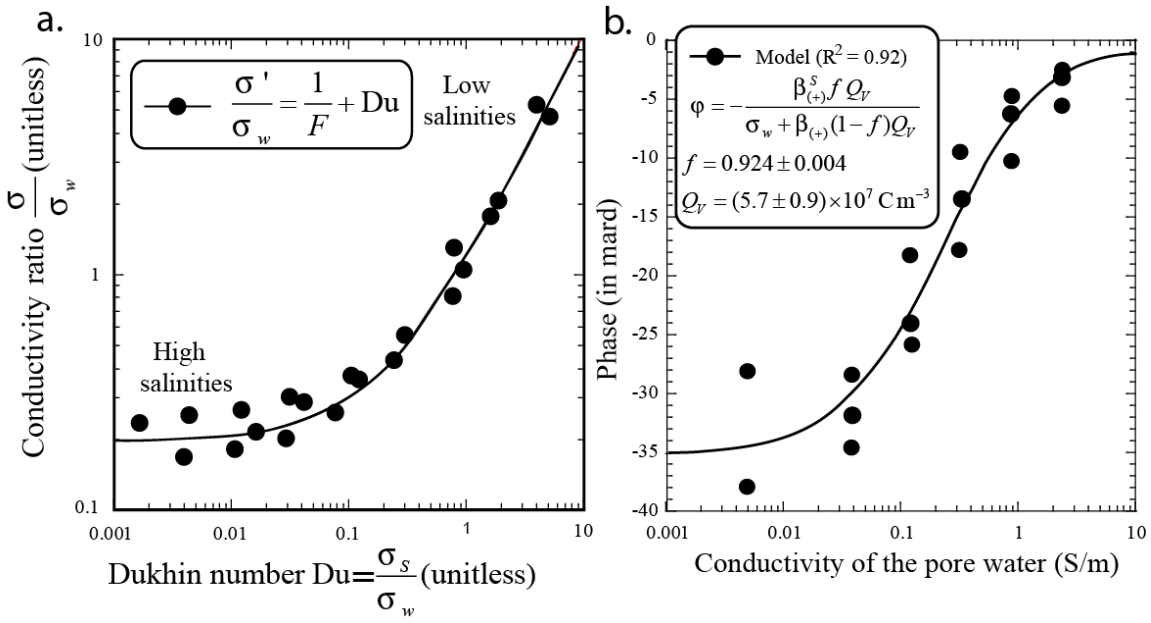

Figure 5. Complex conductivity properties of three core sample of saprolite from Oak Ridge saturated with NaCl solutions. **a.** Normalized conductivity versus the pore water conductivity for the three core samples investigated by *Revil et al*. [2013a]. (pH ~6). **b.** Phase as a function of the conductivity of the pore water for the three core samples investigated by *Revil et al*. [2013a]. The plain line corresponds to the best fit of the model with a constant partition coefficient *f*.

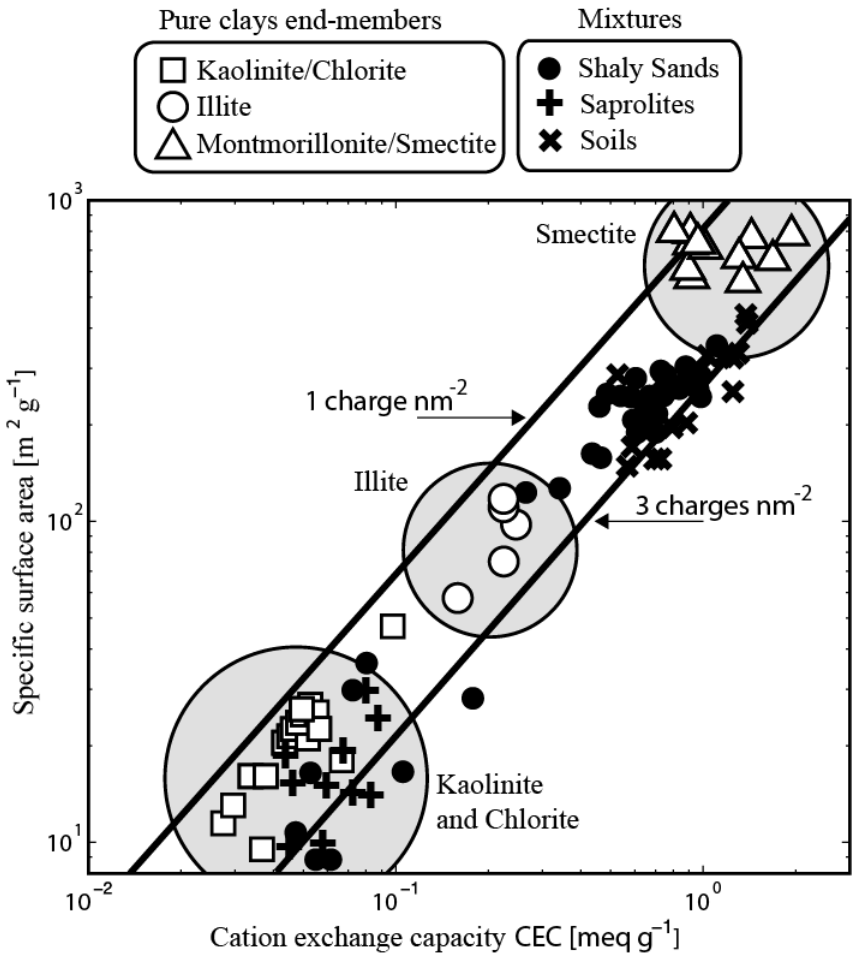

Figure 6. Specific surface area versus CEC (in meq g^{-1} with 1 meq g^{-1}=96,320 C kg^{-1} in SI units) for 18 saprolite core samples from the Oak Ridge background site. The two lines corresponds to 1 to 3 elementary charges per unit surface area. Data for the clay end-members are from: *Patchett* [1975], *Lipsicas* [1984], *Zundel and Siffert* [1985], *Lockhart* [1980], *Sinitsyn et al*. [2000], *Avena and De Pauli* [1998], *Shainberg et al*. [1988], *Su et al.* [2000], and *Ma and Eggleton* [1999]. the saprolite data are from Revil et al. (unpublished), and the soil data are from *Chittoori and Puppala* [2011].

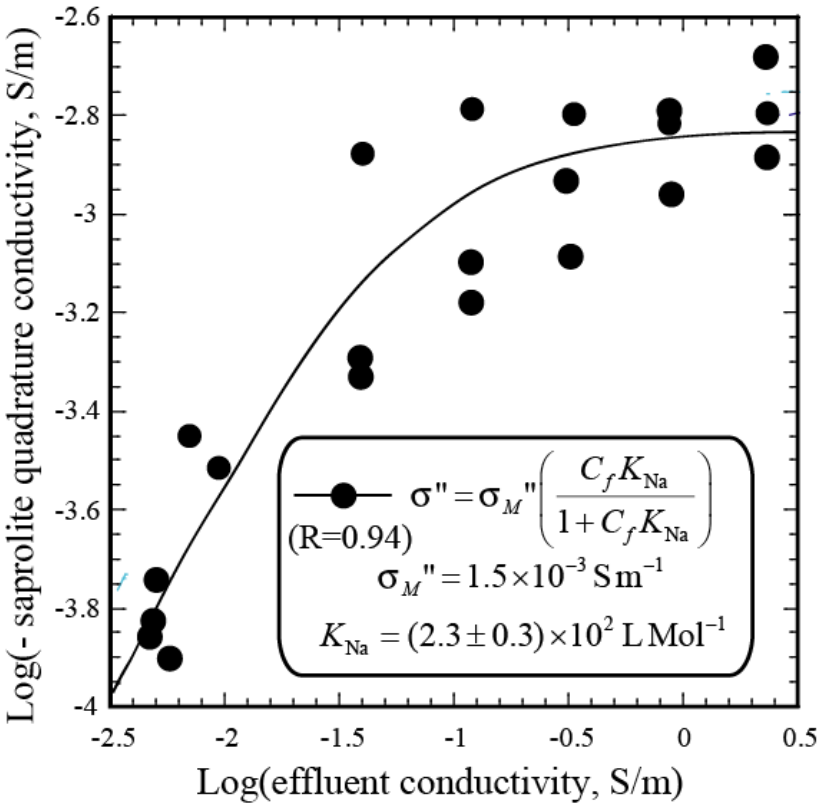

Figure 7. Dependence of the quadrature conductivity with the salinity (3 saprolite core samples, NaCl, pH ~ 5). The plain line corresponds to the prediction of the model with a Langmuir isotherm for the partition coefficient *f*.

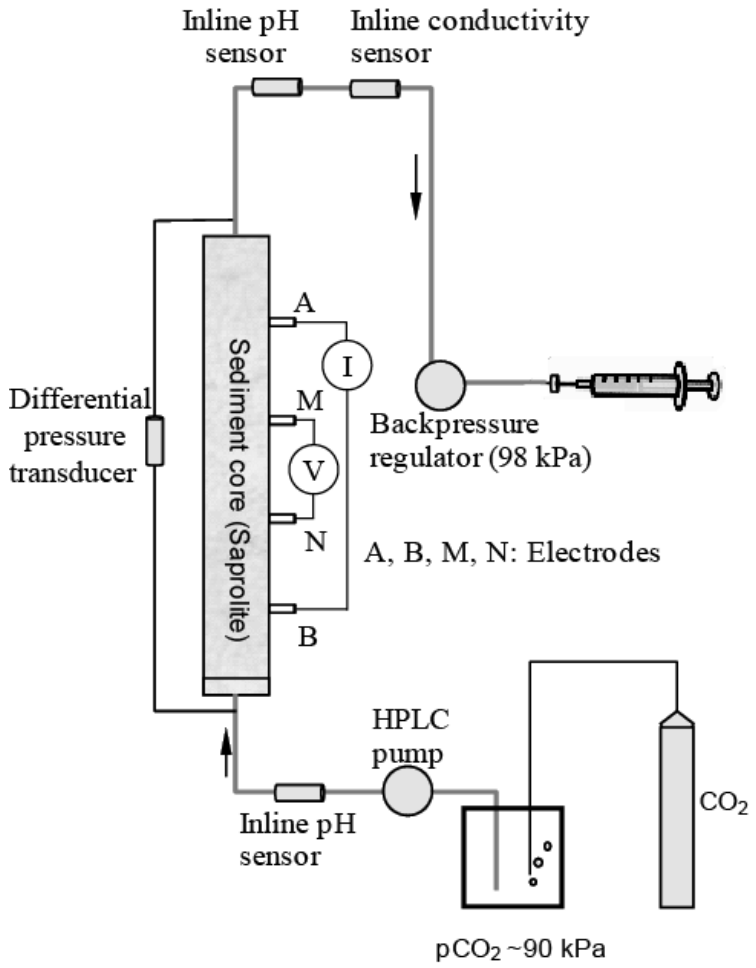

Figure 8. Sketch of the column experiment. The sediment core is made of the Oak Ridge saprolite from the transition zone shown in Figure 2. HPLC denotes the high Performance Liquid Chromatography pump. The sediment core from weathered saprolite zone (FWB130). GW from perched water table (Well #FW116) as infiltrating fluid. pCO_2 imposed at ~ 0.9 atm (90 kPa). Backpressure regulator is used to control pressure/prevent CO_2 outgazing in column. The differential pressure transducer is used to estimate the permeability. Inline pH and conductivity sensor. The flow rate corresponds to 7 days per pore volume (~1.2 ml/hour, ~200 ml pore volume). The syringe is used to sample the pore water for geochemical analysis. Complex resistivity measurements: AB current electrodes, MN voltage electrodes, V denotes the voltmeter while I denotes the current generator.

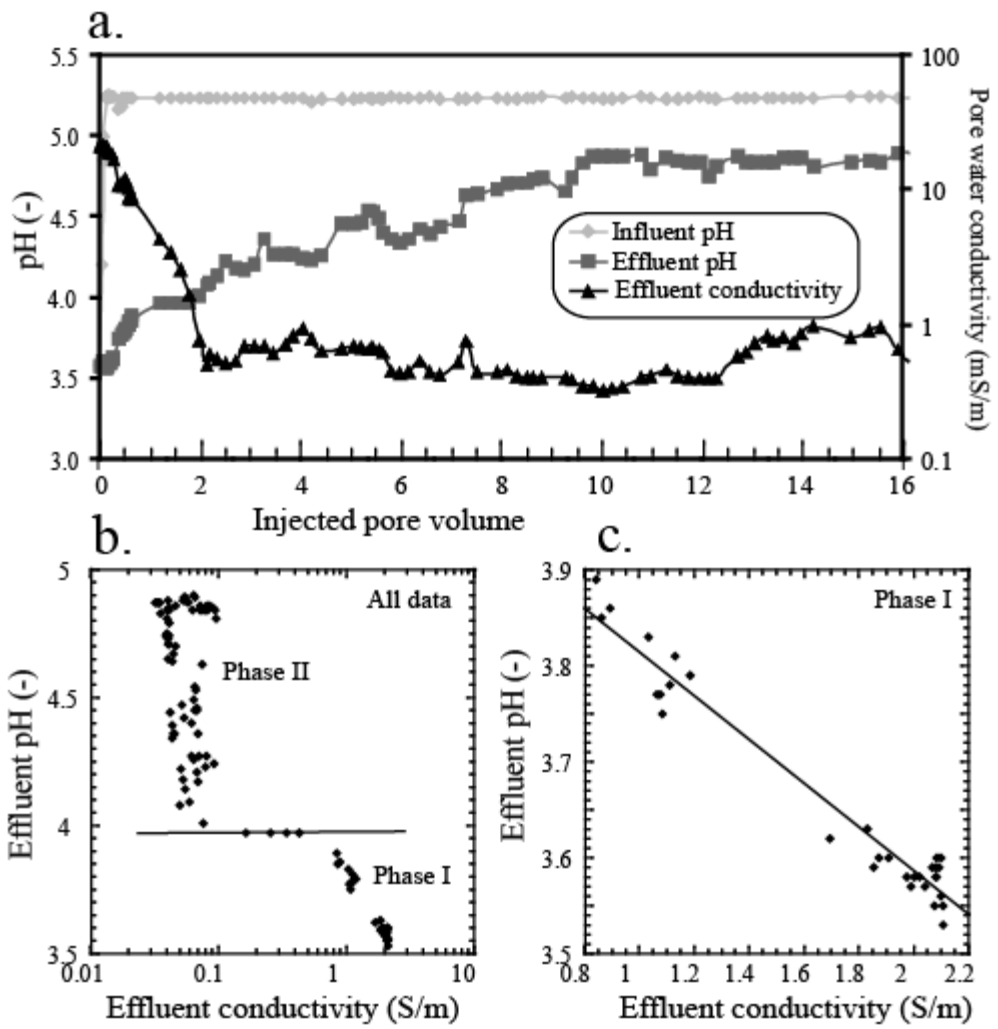

Figure 9. Evolution of the pore fluid properties during the course of the experiment. **a.** Changes of pH and conductivity during perched water infiltration. **b.** pH versus conductivity of the effluent showing two phases in the flow through experiment: Phase shows a linear dependence between the pH and the pore fluid conductivity while Phase II is characterized by a constant pore water conductivity and a slow change in the pH. **c.** pH versus conductivity of the effluent during Phase I.

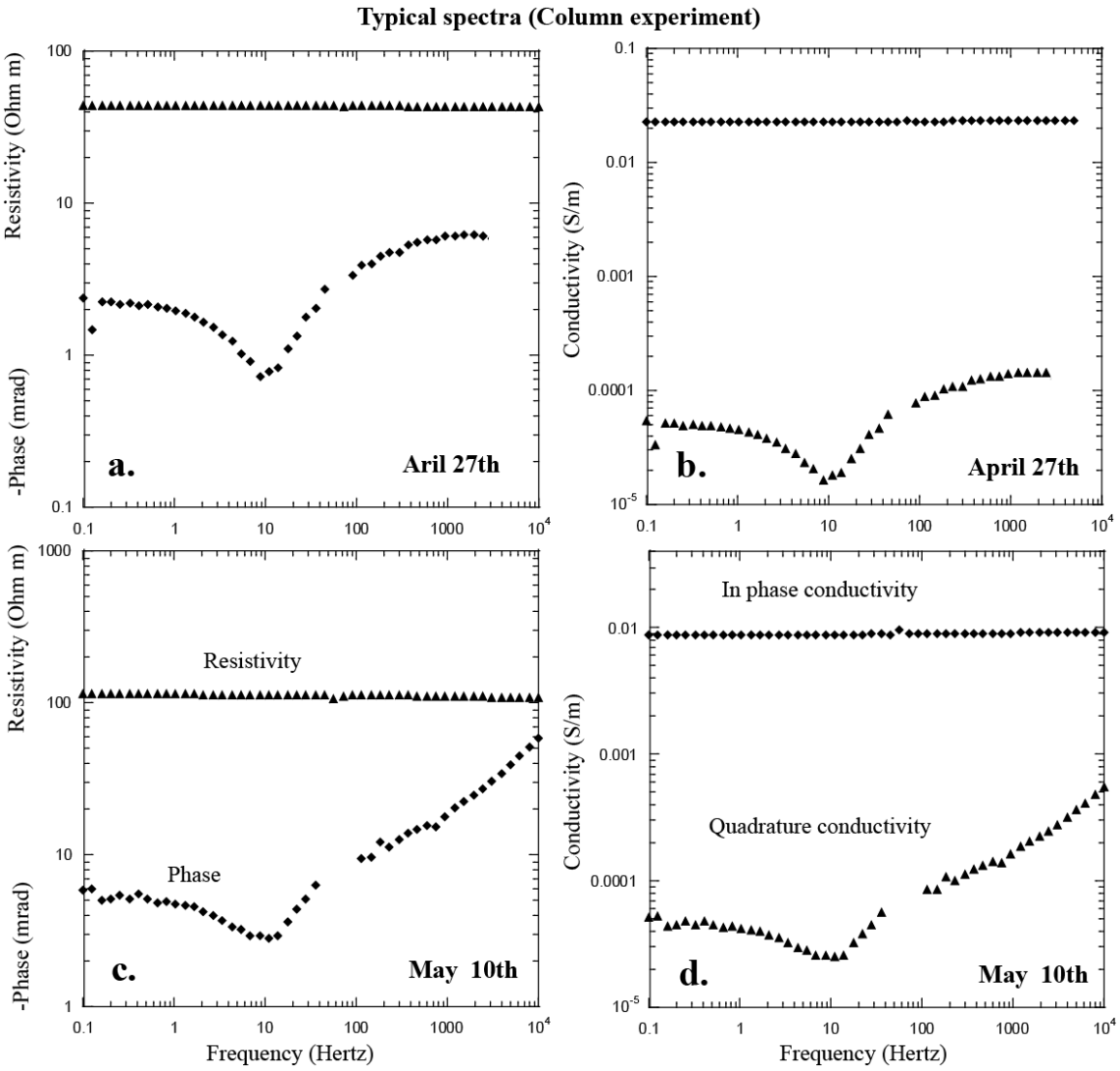

Figure 10. Typical conductivity spectra. The flow through experiment started April 10th. **a. b.** Complex conductivity on April 27th (17th day). **c. d.** May 10th (30th day). Note the increase of the resistivity from about 40 Ohm m to over 100 Ohm m and the increase of the magnitude of the phase from about -2.3 mrad at low frequencies to about -6 mrad.

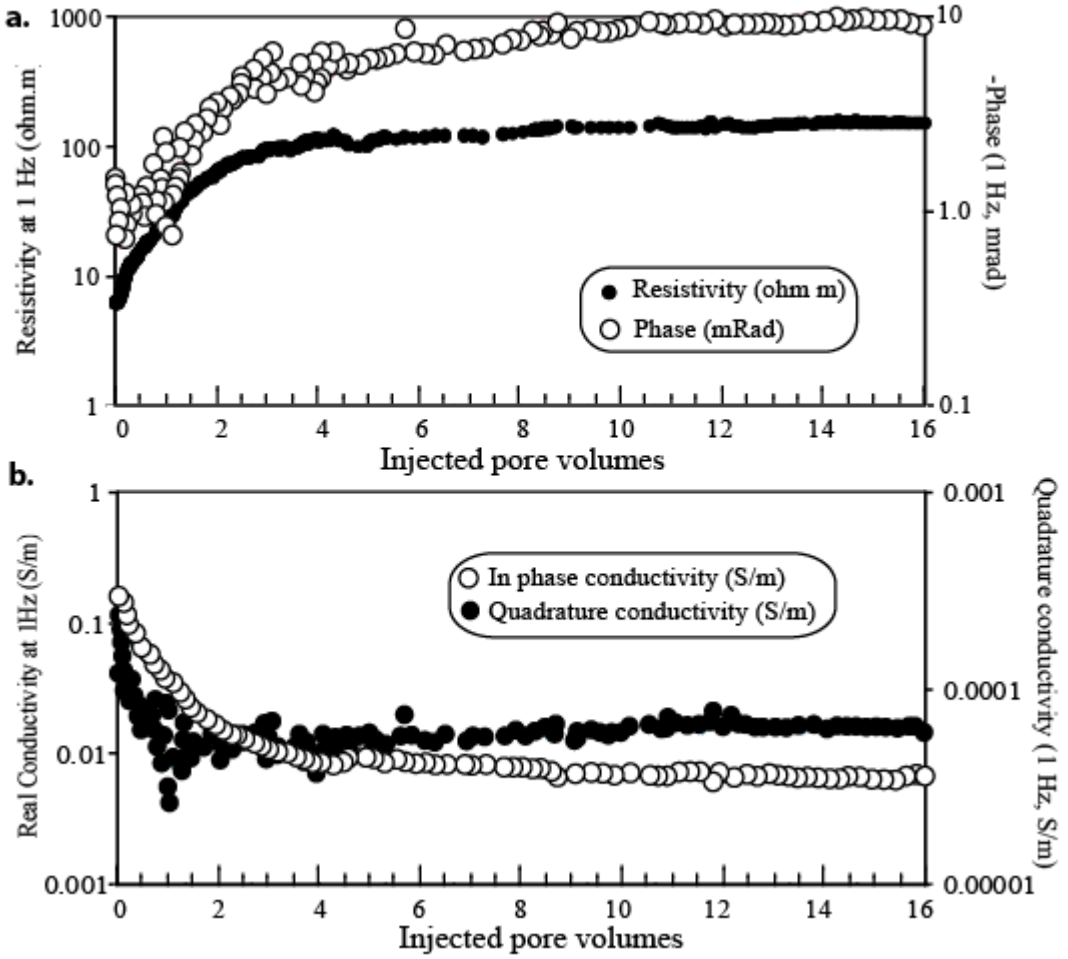

Figure 11. Complex conductivity during the flow through experiment. **a.** Changes of resistivity and phase at 1 Hz during fresh water infiltration sampled from the perched aquifer. **b.** Real and imaginary conductivity at 1Hz during fresh water infiltration sampled from the perched aquifer.

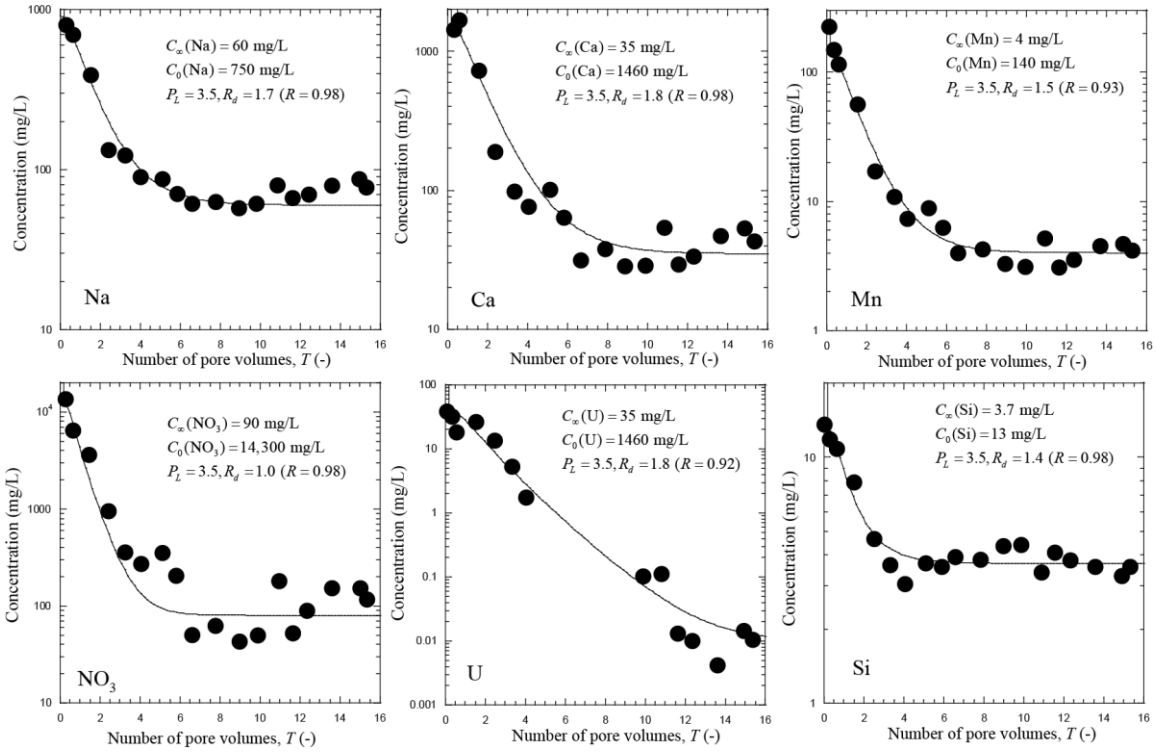

Figure 12. Breakthrough curve of some of the major cations and nitrate. The curves represent the model discussed in the main text and used to estimate the Peclet number and the retardation coefficient.

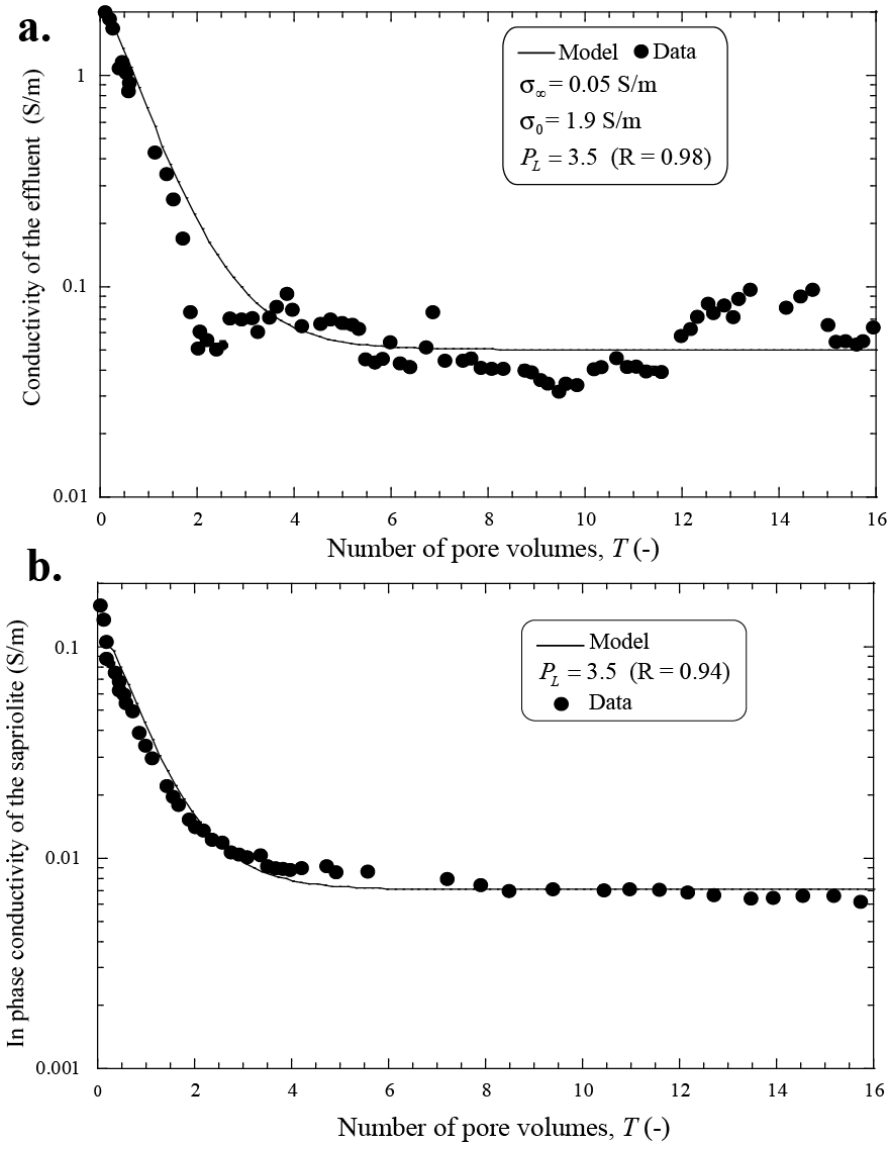

Figure 13. Conductivity versus time for the column experiment. **a.** Conductivity of the effluent versus the number of pore volumes *T*. The data are consistent with a Peclet number of 3.5 and a retardation coefficient of 1.0. **a.** Conductivity of the saprolite versus the number of pore volumes *T*. The data are consistent with a Peclet number of 3.5 and a retardation coefficient of 1.0, a formation factor of 19.5 and a surface conductivity of 5×10^{-3} S m^{-1}.

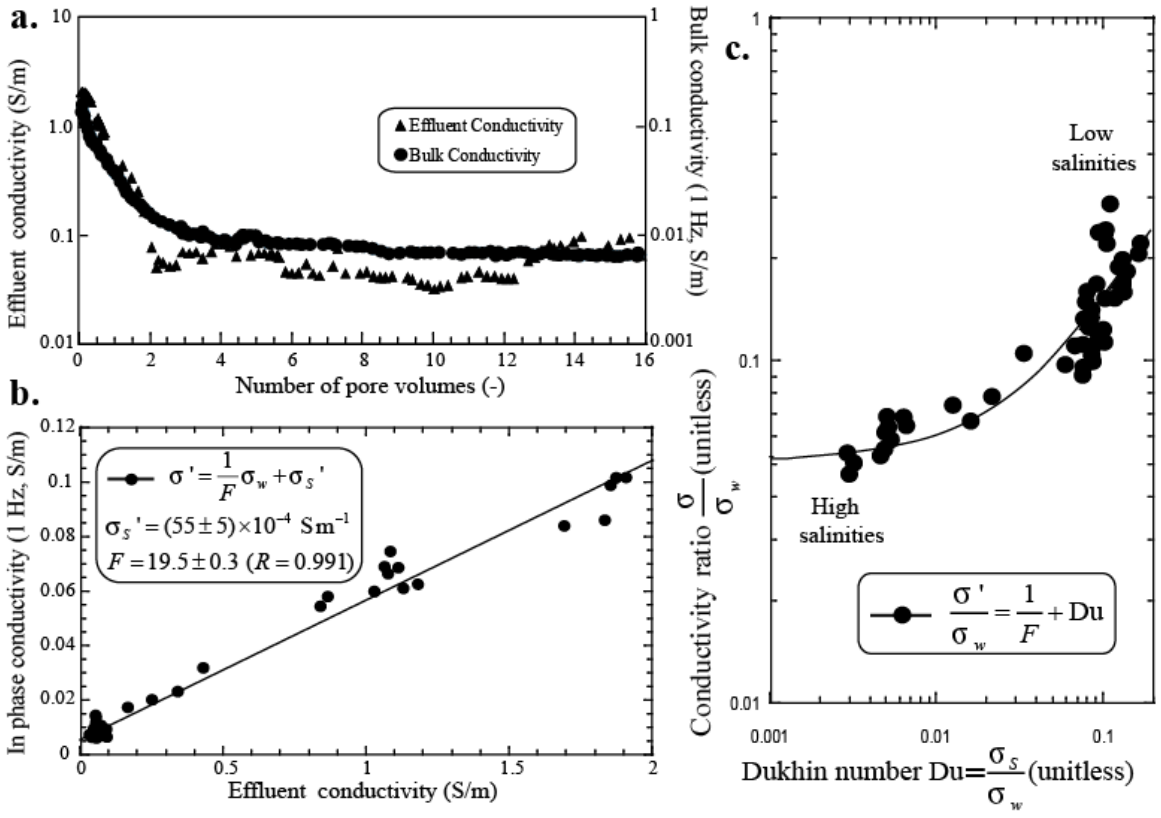

Figure 14. Changes of effluent and bulk conductivity during the experiment. **a.** Bulk and in-phase conductivity as a function of the number of pore volume of ground water from the perched aquifer flowing through the saprolite. **b.** In phase conductivity versus the effluent conductivity. The data are used to determine the surface conductivity and the formation factor at 1 Hz. **c.** Conductivity data plotted as a function of the Dukhin number. The data are showing that at the end of the experiment, the conductivity is dominated by the surface conductivity.

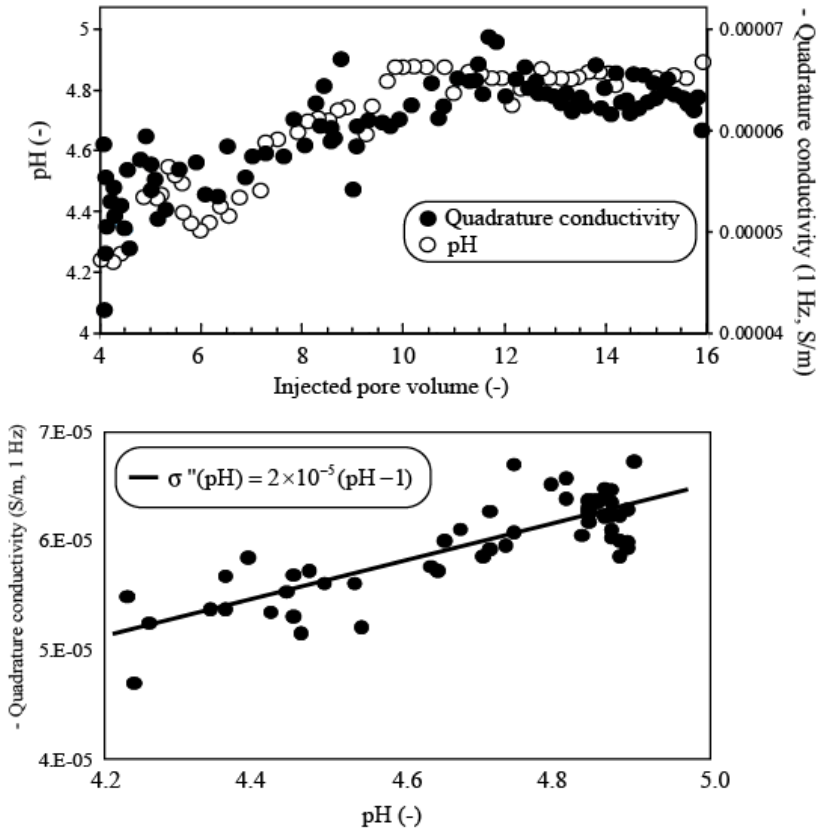

Figure 15. Influence of the pH upon the quadrature conductivity (pore water conductivity ~0.07 S m^{-1} at 25°C) in Phase II. **a.** Changes of pH and quadrature conductivity at 1 Hz during the infiltration of the fresh water from the perched aquifer. **b.** Correlation between pH and quadrature conductivity at 1 Hz during Phase II of the experiment.

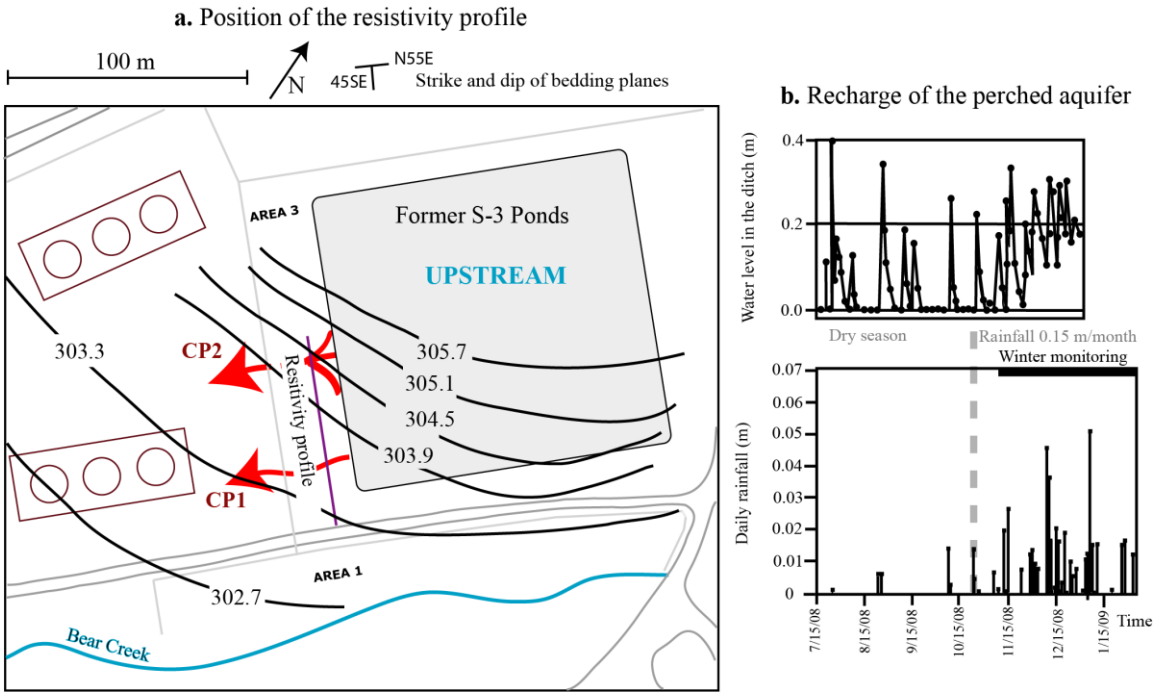

Figure 16. Position of the resistivity profile downstream the former S-3 disposal ponds. **a.** Sketch showing the position of the former disposal ponds, the piezometric lever in the saprolitic aquifer (in meters above sea level), and the position of the plumes CP1 and CP2. **b.** Water level in the ditch surround the former S-3 basins and daily rainfalls showing the recharge of the perched aquifer at the end of 2008. Note that the flow direction is controlled by the fractures along the bedding planes. So the flow is parallel to the bedding planes or strike.

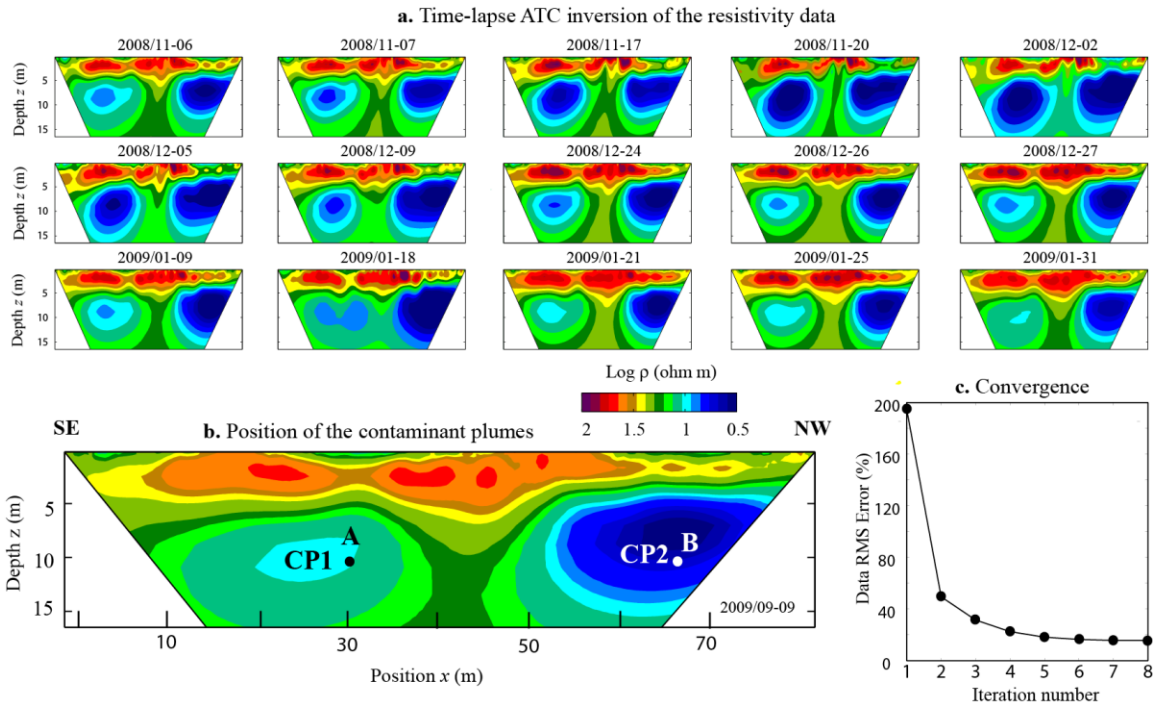

Figure 17. Time lapse tomography based on the Active Time Constrain (ATC) approach. **a.** Results of the time lapse inversion for a profile located in Area 3 (see Figure 1c). **b.** Analysis of a tomogram showing the position of the plumes CP1 and CP2. **c.** Data RMS Error versus the number of iterations (convergence is reached after 7 iterations).

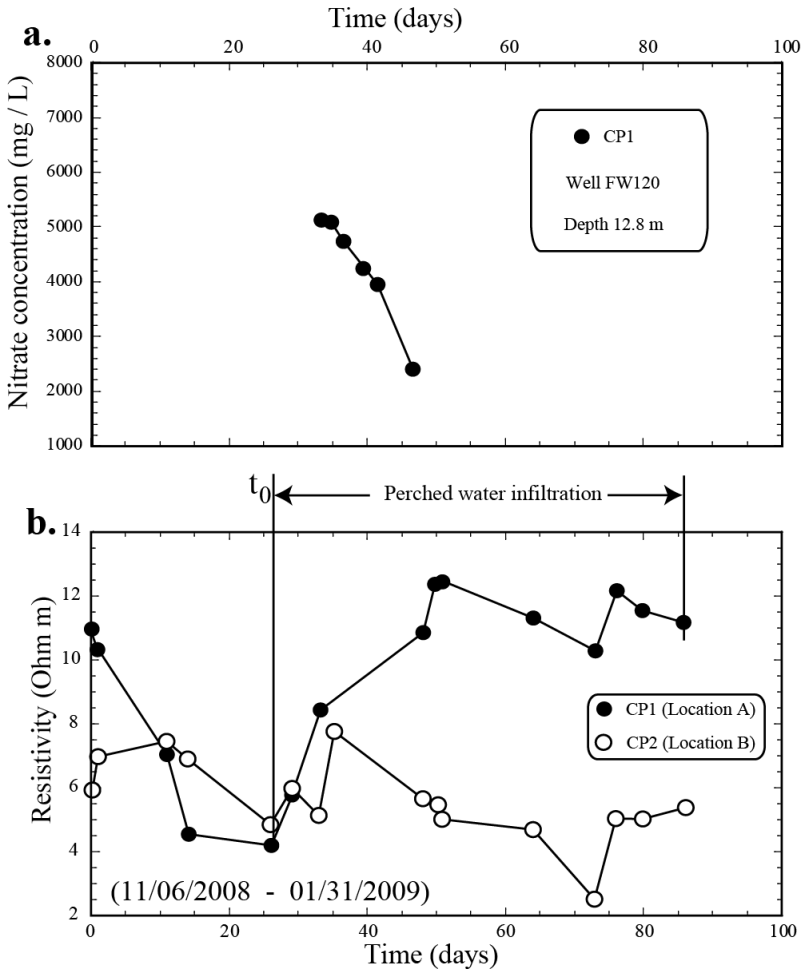

Figure 18. Change of the nitrate concentration and resistivity versus time. **a.** Change of nitrate concentration in Well FW120 at a depth of 13.2 m. **b.** Field data: Change of resistivity at points A and B (plumes CP1 and CP2) over time. In plume CP1, we see a consistent increase of the resistivity after Day 26 and corresponding therefore to a dilution of the CP1 plume by the infiltration of fresh water from the perched aquifer. Locations A and B are shown in Figure 17.

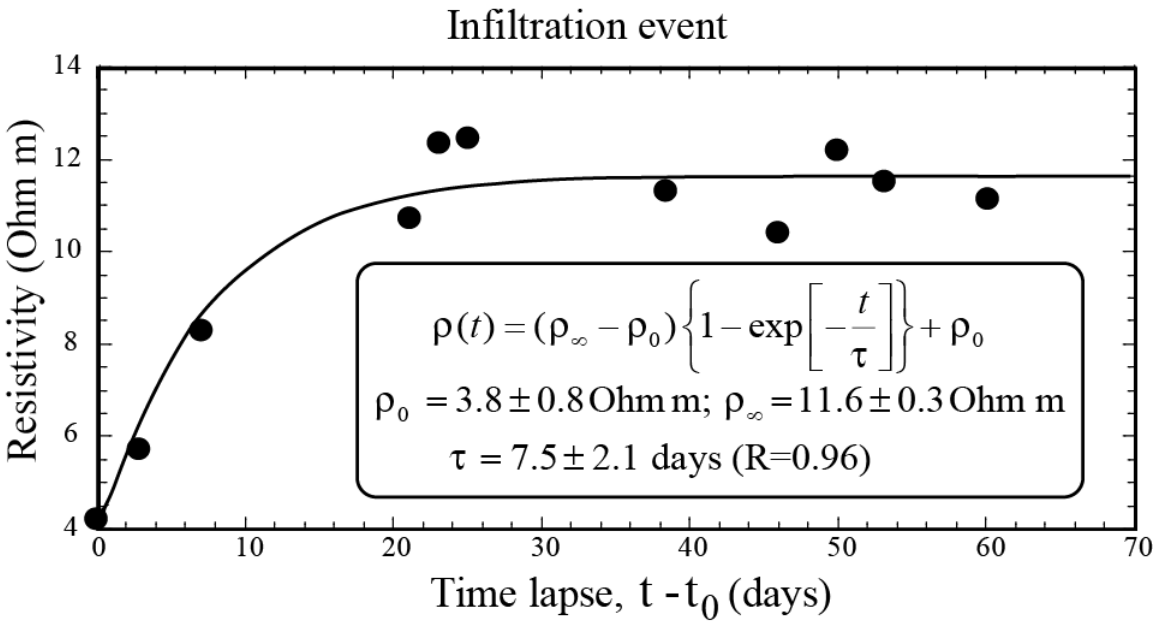

Figure 19. Field data: fit of an exponential relationship to the in situ resistivity data after Day 26. The relaxation time associated with the resistivity change is 7.5 days. This can be compared with a relaxation time of 19.4 days for the laboratory experiment, indicating that the timing of the laboratory column experiment is on the same magnitude as field changes.

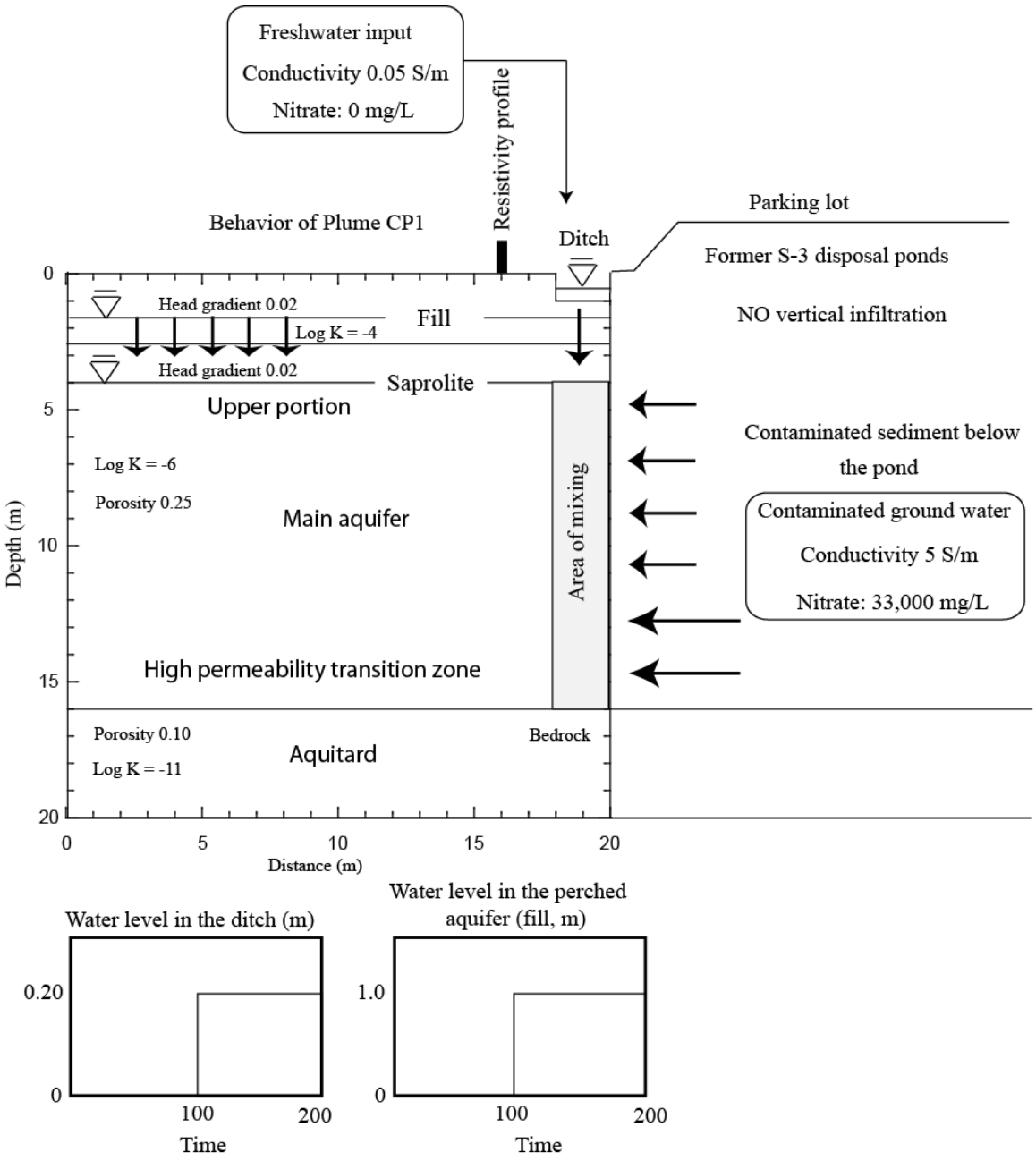

Figure 20. Conceptual model of infiltration in the plume CP1. The ponds are capped with a multilayer cap so there is minimal leaching from above. There is a huge reservoir of contaminants in the saprolite and rock matrix beneath the former disposal ponds and resulting from contamination between 1951 and 1983. The flow of groundwater through the underlying contaminated materials is responsible for the plumes found downstream in the strike direction. Possibly there is a mixing of this contaminated water with fresh water infiltrating the saprolite from the southern portion of the ditch.

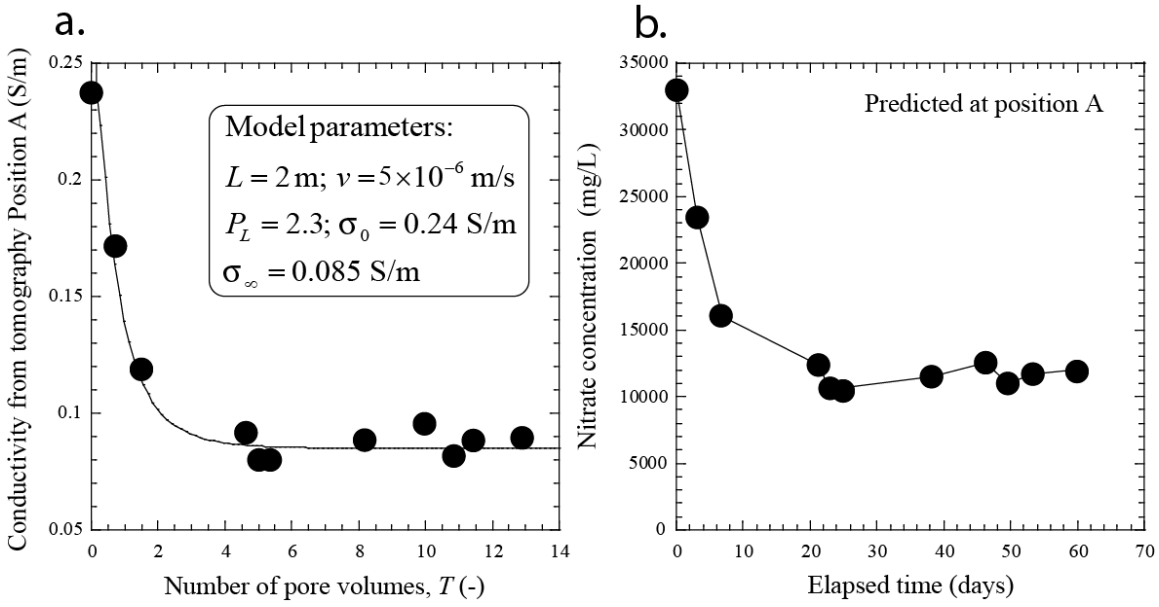

Figure 21. Analysis of the field data. **a.** Modeling of the conductivity data in terms of Peclet number, mean pore water velocity at a depth of 10 m (plume CP1, position A, see Figures 16 and 17). The conductivities σ_0 and σ_∞ denote the conductivity of the aquifer at the beginning and end of the infiltration event. We analysis is performed according to the conceptual model shown in Figure 20. **b.** Predicted evolution of the nitrate concentration during the infiltration event.

Appendix D

Low-frequency complex conductivity of sandy and clayey materials

A. Revil (1, 2), J.D. Eppehimer (1), M. Skold (1), M. Karaoulis (1),

L. Godinez (3), and M. Prasad (3)

(1) Colorado School of Mines, Department of Geophysics, Golden, 80401, CO, USA

(2) ISTerre, CNRS, UMR CNRS 5275, Université de Savoie, 73376 cedex, Le Bourget du Lac, France

(3) Lawrence Berkeley National Laboratory, 1 Cyclotron Road, MS 90R1116, Berkeley, 94720, CA.

(4) Oak Ridge National Laboratory, 1 Bethel Valley Road, MS 6038, Oak Ridge, 37831-6038, TN

Running Head: Low-frequency complex conductivity

Corresponding author: André Revil arevil@mines.edu

Emails: jeppehim@mymail.mines.edu; lgodinez@mymail.mines.edu; marios.karaoulis@gmail.com; mprasad@mines.edu; arevil@mines.edu; mskold@mines.edu;

Intended for publication in Journal of Colloid and Interface Science

Abstract. Low-frequency polarization of sands and sandstones seem to be dominated by the polarization of the Stern layer, the inner part of the electrical double layer coating the surface of the silica grains and clay particles. We investigate a simple model of Stern layer polarization combined with a simple complexation model of the surface of the grains immersed in a 1:1 electrolyte like NaCl. In isothermal conditions, the resulting model can be used to predict the complex conductivity of clayey materials as a function of the porosity, the cation exchange capacity of the clay fraction (alternatively the specific surface area of the material), and the salinity of the pore water. A new set of experimental data is presented. This dataset comprises low-frequency (1 mHz-45 kHz) complex conductivity measurements of saprolites and sandstones that are well-characterized in terms of their petrophysical properties (porosity, permeability, specific surface area or CEC, and pore size). This dataset, together with incorporating additional data from the literature, is used to test the Stern layer polarization model. We find an excellent agreement between the predictions of this model and this experimental dataset indicating that the new model can be used to predict the complex conductivity of natural clayey materials and clay-free silica sands.

Key-words: complexation; electrical conductivity; clay; low-frequency dielectric spectroscopy; quadrature conductivity; cation exchange capacity; specific surface area.

1. Introduction

From non-equilibrium thermodynamics, the current density of a porous material at rest (no deformation and no flow of the pore water allowed) can be written as the sum of the classical Ohm's law plus two source current densities, one associated with the gradient of the chemical potential of the charge carriers (diffusion current) and one with the pressure gradient (streaming current) [1-3]. These source current densities are responsible for a phase lag between the current and the electrical field for harmonic imposed current or electrical field [4-5]. The amplitude of the electrical conductivity and the phase can be used to define a complex electrical conductivity with an in-phase component characterizing electromigration and a quadrature component characterizing low-frequency polarization.

The understanding of the complex conductivity of dilute colloidal suspensions has been the subject of a high number of theoretical studies (e.g., [4, 6]). The "standard" model developed by Dukhin and Shilov [4, 7] is based on the polarization of the electrical diffuse layer. The standard model is , however, insufficient to reproduce the low-frequency polarization of colloidal suspensions [6]. It has been recognized back in the nineties that this deficiency could be explained by the polarization of the Stern layer and, since, a number of works have been devoted to understand the polarization of this layer [8-9].

Granular porous media are however not colloids because of their grain-to-grain contacts. As the grains are touching each other, there is an overlap of the diffuse layer in porous media from grain-to-grain. This overlapping may decrease the dipole moment associated iwth the polarization of the diffuse layer. The Stern layer remains however discontinuous. In a set of previous studies, Revil

and co-workers have argued that the polarization of the Stern layer may be the dominant polarization mechanism in sandy and clayey porous materials [5, 10-14].

In the present paper, following [12], we provide a simple polarization model of sands and clayey materials based on the polarization of the Stern layer neglecting completely the polarization of the diffuse layer. We also present a new set of experimental data on saprolites and sandstones. We see that the Stern layer polarization model seems to explain well these experimental data. It can be therefore used to develop time-lapse tomographic methods to visualize non-intrusively changes in the pore water chemistry and interfacial chemistry in granular media such as sands and clayey materials and using techniques developed in geophysical and medical imaging.

2. The Diffuse Layer "Standard" Polarization Model

2.1. Rationale

In this section, we provide the rationale of the standard model of Dukhin and Shilov [4-7] and its refinements. The standard model was developed to understand low frequency dielectric dispersion (α-polarization) of colloids. It based on the following assumptions: (1) a Gouy-Chapman diffuse layer surrounds insulating grains (spheres, rods, or ellipsoids can be considered) and the densities of the counterions and co-ions follow Bolzmann statistics and there are considered to be point charges, (2) the background electrolyte is a symmetric 1:1 electrolyte (e.g., NaCl), (3) the porous material is homogeneous and isotropic, (4) all the equations are linearized considering first-order perturbations only, (5) electroosmotic effects can be taken into accounts modifying the apparent mobility of the counterions and co-ions of the diffuse layer [15], (5) no Stern layer is considered (see Section 3 below).

The set of local coupled equations to upscale with proper microscopic and macroscopic boundary conditions are (1) the Nernt-Planck equation, (2) the Stokes equation (inertial effects are neglected so the flow is laminar) or alternatively the Navier-Stokes equation accounting for the inertial term, and (3) the local form of the Maxwell equations, which, for the problem of interest (< 50 kHz), can be taken in the quasi-magnetostatic approximation. The electrical field is considered to be harmonic and the field equations can be solved in the frequency domain or in the Laplace domain.

Modelling the low-frequency complex conductivity of granular media is a two-step process involving (1) the modelling of the dipole moment of a single grain (or type of grains) and (2) upscaling the solution for a water-saturated pack of grains or a colloidal suspension. The two operations are completely decoupled. Usually in colloidal chemistry, researchers used a consistent approximation rather than the differential effective medium theory because we they are dealing with dilute suspensions. The goal of the upscaling is to obtain an expression of the low-frequency complex conductivity σ^* (or alternatively the low-frequency dielectric constant) of the granular material defined as,

$$\sigma^* = |\sigma| \exp(i\varphi) = \sigma' + i\sigma''. \quad (1)$$

The term $|\sigma|$ denotes the amplitude of the electrical conductivity (in S m^{-1}) while φ describes the phase lag (usually reported in mrad) between the current and the electrical field. The terms σ' and σ'' denote the real (in phase) and imaginary (quadrature) components of the conductivity (both expressed in S m^{-1}) and i denotes the pure imaginary number. The relationships between the in-phase and quadrature conductivities and the amplitude and phase are given by $|\sigma| = \sqrt{\sigma'^2 + \sigma''^2}$ and $\varphi = \text{atan}(\sigma''/\sigma')$. Because the phase is small (smaller than 100 mrad in amplitude below 10 kHz), the phase is often approximated by $\varphi \approx \sigma''/\sigma'$.

There are many refinements of the standard model. For instance, Grosse [4] developed recently an extension of the standard model for non-symmetric electrolytes and Aranda-Rascón et al. [16] developed the theory to account for the finite size of the ions. Carrique et al. [17] developed a cell approach for concentrated colloids accounting for particle–particle interactions. They however claim that a dynamic Stern layer would be required to improve the theory. Pride [15] looked at the effect of electroosmosis on the frequency-dependent complex conductivity. For simple supporting 1:1 electrolytes, it was concluded in [18] that electroosmosis can be taken into account by considering an apparent mobility $B_{(\pm)}$ for cations (+) and anions(-) defined by

$$B_{(\pm)} = \beta_{(\pm)} + \frac{2\varepsilon_f k_b T}{\eta_f e}. \quad (2)$$

in the specific surface conductivity associated with the electrical diffuse layer. In Eq. (2), ε_f = (80×8.854) ×10^{-12} F m^{-1} denotes the dielectric constant of water, k_b denotes the Boltzmann constant (1.3807×10^{-23} J K^{-1}), T is the absolute temperature (in K), e denotes the elementary charge (1.6×10^{-19} C), η_f denotes the dynamic viscosity of the pore water (10^{-3} Pa s), and $\beta_{(+)}$ denotes the true mobility characterizing the electromigration of cations and anions in water (e.g., $\beta_{(+)}$(Na^+, 25°C) = 5.2×10^{-8} $m^2s^{-1}V^{-1}$). The last term of Eq. (2) is on the order of 0.4×10^{-8} $m^2s^{-1}V^{-1}$. This means that the apparent mobilities of the ions in the diffuse layer can be slightly higher than the true mobility of the same ions in water but the difference is very small and electroosmosis is not expected to play a big role.

2.2. Limitations

It was realized in the nineties that this standard model was unable to explain most experimental data even for dilute colloidal suspensions [6, 8]. The problems with the standard models are the following: (1) a complete analysis of the equations shows that the low-frequency response associated with the diffuse layer should be non-linear but harmonic distorsions are hardly observed at low frequencies for sandy and clayey materials, (2) there are many systems (like clays) in which an important fraction (>85%) of the countercharge is located in the Stern layer of sorbed counterions and not in the diffuse layer.

Zukoski and Saville [19, 20] and later Lyklema [9] introduced a dynamic Stern layer model that started to be used, in concert with the standard model, to describe low-frequency induced polarization of colloids [5, 21]. In the next section, we will give the rationale for a Stern layer polarization model and provide a simple, semi-empirical, way to describe low-frequency polarization of porous media.

3. A Simple Stern Layer Model

Our goal is to develop below a simple yet accurate model of the low-frequency complex conductivity of porous materials based on the polarization of the Stern layer. This model can be on connected to the interfacial electrochemistry of the mineral surface (complexation models). We first focus on providing the rationale for a Stern layer-based polarization model (Section 3.1), then we describe the maximum amplitude of low frequency polarization (Section 3.2), we couple the polarization model to a simple speciation model for clay minerals (Section 3.3), and finally we provide a simple frequency dependent polarization model (Section 3.4).

3.1. Rational for the Stern Layer Polarization Model

In silica sands and clays, the double layer coating the grains is composed of non-only a diffuse layer but also a Stern layer of sorbed counterions including inner-sphere and outer-sphere ligands. The existence of the Stern layer of weakly sorbed counterions is demonstrated by molecular dynamic simulations and corresponds to a condensation of the ions on the mineral surface breaking down the Boltzmann statistics [22, 23].

We consider an external electrical field varying with time as $\mathbf{E} = \mathbf{E}_0 \exp(i \square t)$. The conservation of ionic species along the mineral surface in the Stern layer is,

$$\frac{\partial \Gamma_{(+)}}{\partial t} = -\nabla_S \cdot \mathbf{j}_{(+)}, \tag{3}$$

where $\Gamma_{(+)}$ denotes the concentration of the weakly sorbed cations (in Mol m^{-2}) at the mineral surface (density of counterions per surface area), $\nabla_S \cdot$ denotes a surface divergence with respect to the curvilinear coordinates describing the mineral surface, and $\mathbf{j}_{(+)}$ is the flux density of the weakly sorbed cations along the mineral surface (in Mol s^{-1} m^{-1}). The electrostatic equations obeyed by the electrical field in the low-frequency limit of the Maxwell equations is,

$$\nabla \cdot \mathbf{E} = \frac{\rho}{\varepsilon}, \tag{4}$$

$$\nabla \times \mathbf{E} = 0, \tag{5}$$

where ε denotes the dielectric constant in the Stern layer and ρ is the volumetric charge density. Eq. (5) implies in turn that the electrical field can be derived from an electrostatic potential ψ which is distinct from the electrostatic potential of the electrical double layer φ. As shown in [15] and [18], the electroosmotic velocity is zero on the surface of the grains, so it should not be accounted for in the flux densities on the mineral surface. The flux of cations along the mineral surface is therefore given by the classical Nernst-Planck local equation,

$$\mathbf{j}_{(+)} = -\frac{\beta^S_{(+)}\Gamma_{(+)}}{\left|q_{(+)}\right|}\nabla_S\tilde{\mu}_{(+)}, \tag{6}$$

$$\mathbf{j}_{(+)} = --\frac{\beta^S_{(+)}\Gamma_{(+)}}{\left|q_{(+)}\right|}\nabla_S\left(q_{(+)}\psi + k_bT\ln\Gamma_{(+)}\right), \tag{7}$$

$$\mathbf{j}_{(+)} = -\frac{\beta^S_{(+)}}{\left|q_{(+)}\right|}\left(q_{(+)}\Gamma_{(+)}\nabla_S\psi + k_bT\nabla_S\Gamma_{(+)}\right), \tag{8}$$

where $\tilde{\mu}_{(+)}$ denotes the electrochemical potential of the waekly sorbed cations, ∇_S denotes a surface gradient along the mineral surface, $\beta^S_{(+)}$ denotes the (Stern layer) ionic mobility of the weakly sorbed cations, and $q_{(+)} = (\pm 1)z_{(+)}e$ is their charge ($z_{(+)}$ is the unsigned valence). The tangential mobility of the weakly sorbed counterions is confirmed by nuclear magnetic resonance (NMR) spectroscopy (e.g., [24] in the case of sodium on silica).

According to Eq. (6), the lateral transport of the counterions in the Stern layer by electromigration is coupled to diffusion. In other words, the flux density is controlled by the gradient of the electrochemical potential $\tilde{\mu}_{(+)}$ of the weakly sorbed cations in the Stern layer, which comprises an electrostatic term and a concentration gradient term (an activity gradient term for non-ideal solution). Combining Eqs (3) and (6) yields,

$$\frac{\partial\Gamma_{(+)}}{\partial t} = \frac{\beta^S_{(+)}}{\left|q_{(+)}\right|}\nabla_S\cdot\left(q_{(+)}\Gamma_{(+)}\nabla_S\psi + k_bT\nabla_S\Gamma_{(+)}\right). \tag{9}$$

Therefore both the concentration gradient and the imposed electrical field are locally tangential to the mineral surface. Note that the electrical field resulting from the electrical double layer is normal to the mineral surface and therefore the two electrical field are normal to each other. Concentration gradients and the electrical field provide the driving forces for the migration of the counterions along the Stern layer. The first boundary condition results from the continuity of the tangential component of the electrical field at the interface between the Stern layer and the diffuse layer. The second boundary condition results from the fact that the surface of the grain is insulating and therefore impervious to the transport of the counterions. For spherical grains, Gauss's law states [25],

$$-\varepsilon \frac{\partial \psi}{\partial r}\Bigg)_{r=d/2} = Q_0 + Q_\beta \,, \tag{10}$$

where Q_0 is the mineral surface charge density (C m^{-3}) and Q_β is the charge density of the Stern layer (C m^{-3}), r is the radial distance from the center of the spherical grain of diameter d. These equations can be solved analytically [5] or numerically [25]. *Rosen et al*. [25] considered in their model the possible exchange of counterions between the Stern layer and the diffuse layer.

The Stern layer model would involve predictions: 91) a strong control of the polarization response by the cation exchange capacity or alternatively the specific surface area of the material, (2) a reduced mobility for the electromigration of the counterions, and (3) a reduced diffusivity for the relaxation time (rather than the mutual diffusion coefficient used in the standard model). We will discuss in the next section, a model to capture the magnitude of the Stern layer polarization.

3.2. Expression for the Complex Conductivity

According to the Stern layer polarization model developed by Revil and co-workers [5, 13, 14, 26], the complex conductivity of a granular material can be written as,

$$\sigma^* = \frac{1}{F}\sigma_w + \sigma_S^* . \tag{11}$$

$$\sigma^* = \sigma_w \left(\frac{1}{F} + \mathrm{Du}^* \right). \tag{12}$$

where F denotes the formation factor (dimensionless), σ_w denotes the (real) electrical conductivity of the pore water (in S m^{-1}), σ_S^* denotes the complex-valued surface conductivity (in S m^{-1}), and $\mathrm{Du}^* \equiv \sigma_S^*/\sigma_w$ denotes the complex-valued Dukhin number (unitless). The electrical formation factor F is related to the connected porosity ϕ by Archie's law $F = \phi^{-m}$, m denotes the cementation exponent [27]. A physical explanation of the formation factor in terms of pore space topology is given in Appendix A.

As mentioned above, the electrical double layer comprises the Stern layer of weakly sorbed counterions (outer sphere complexes) and the diffuse layer (see Figure 1). According to the Stern layer polarization model, the complex surface conductivity and the complex Dukhin number are given by [12],

$$\sigma_S^* = \frac{2}{3}\rho_g \mathrm{CEC}\left[B_{(+)}(1-f) - i\beta_{(+)}^S f \right], \tag{13}$$

$$\mathrm{Du}^* = \frac{2}{3}\left(\frac{\rho_g \mathrm{CEC}}{\sigma_w} \right)\left[B_{(+)}(1-f) - i\beta_{(+)}^S f \right]. \tag{14}$$

where f denotes the fraction of counterions in the Stern layer (dimensionless), ρ_g denotes the grain density (typically 2650 kg m^{-3}), $B_{(+)} \approx \beta_{(+)}$ denotes the apparent mobility of the counterions in the diffuse layer (see Section 2 above) and $\beta_{(+)}^S$ denotes the mobility of the counterions in the Stern

layer. For clay minerals, Revil [12] found recently $\beta_{(+)}^{S}$ (25°C, Na^+) = 1.5 × 10^{-10} $m^2s^{-1}V^{-1}$ while for silica $\beta_{(+)}^{S}$ (Na^+, 25°C) ≈ 5.2×10^{-8} $m^2s^{-1}V^{-1}$ (these values will be discussed further below in Section 5.2). The salinity dependence of the partition coefficient *f* is discussed in Section 3.3 below.

The surface conductivity and the Dukhin (dimensionless) number are defined as the real part of the complex surface conductivity and the real part of the complex Dukhin number,

$$\sigma_S = \mathrm{Re}\left[\sigma_S^*\right], \tag{15}$$

$$\mathrm{Du} = \mathrm{Re}\left[\mathrm{Du}^*\right], \tag{16}$$

respectively.

The in phase conductivity normalized by the pore water conductivity and the phase obey therefore the following relationships,

$$\frac{\sigma'}{\sigma_w} = \frac{1}{F} + \mathrm{Du}\,, \tag{17}$$

$$\varphi \approx -\frac{\frac{2}{3}F\beta_{(+)}^{S} f \rho_g \mathrm{CEC}}{\sigma_w + \frac{2}{3}B_{(+)}F(1-f)\rho_g \mathrm{CEC}}, \tag{18}$$

respectively. Following [12] and [14], Eq. (18) for the phase lag can be also approximated by,

$$\varphi \approx -\frac{\beta_{(+)}^{S} f Q_V}{\sigma_w + B_{(+)}(1-f)Q_V}, \tag{19}$$

To go from Eq. (18) to Eq. (19), we use the following relationship $F \approx (3/2)(1-\phi)/\phi$ (see [10]). The total charge per unit volume (total excess charge density) is related to the cation exchange capacity (charge per unit mass of grains) of the material by,

$$Q_V \equiv \rho_g \left(\frac{1-\phi}{\phi}\right)\mathrm{CEC}\,. \tag{20}$$

In the next section, we describe how the partition coefficient depends on the salinity.

3.3. Influence of Surface Chemistry

We propose here a simple model to describe the salinity dependence of the partition coefficient *f*. We consider the sorption of sodium in the Stern layer of clays and the dissociation of protons,

$$>SH^0 \Leftrightarrow >S^- + H^+, \tag{21}$$

$$>S^- + Na^+ \Leftrightarrow >S^-Na^+, \tag{22}$$

where >S refers the surface (amphoteric) sites attached to the crystalline framework, H^0 are (immobile) protons while the weakly sorbed Na^+ are considered to be mobile in the Stern layer. The equilibrium constants for the reactions (21) and (22) are given by,

$$K_{Na} = \frac{\Gamma^0_{SNa}}{\Gamma^0_{S^-}\left[Na^+\right]^0}, \tag{23}$$

$$K_H = \frac{\Gamma^0_{S^-}\left[H^+\right]^0}{\Gamma^0_{SH}}. \tag{24}$$

The conservation equation for the surface species is given by,

$$\Gamma^0_S = \Gamma^0_{SNa} + \Gamma^0_{SH} + \Gamma^0_{S^-} + \Gamma^0_X, \tag{25}$$

where Γ^0_S denotes the total surface site density (including the charge associated with isomorphic substitutions in the crystalline framework), Γ^0_{SNa}, $\Gamma^0_{S^-}$, and Γ^0_{SH} represents the surface charge density of the sites $>S^-Na^+$, $>S^-$, and $>SH^0$ respectively, and Γ^0_X represents the number of equivalent sites corresponding to isomorphic substitutions (all expressed in sites m^{-2}). To simplify the notations, we write pH = $-\log_{10}$ $[H^+]$ while $[Na^+] = C_f$ denotes the salinity of the pore water solution. The resolution of the previous set of equations, Eqs. (23) to (25), is straightforward and yields,

$$\Gamma^0_{SH} = \frac{\Gamma^0_S - \Gamma^0_X}{1 + \frac{K_H}{10^{-pH}}\left(1 + C_f K_{Na}\right)}, \tag{26}$$

$$\Gamma^0_{S^-} = \frac{(\Gamma^0_S - \Gamma^0_X)K_H / 10^{-pH}}{1 + \frac{K_H}{10^{-pH}}\left(1 + C_f K_{Na}\right)}, \tag{27}$$

$$\Gamma^0_{SNa} = \frac{(\Gamma^0_S - \Gamma^0_X)C_f K_{Na} K_H / 10^{-pH}}{1 + \frac{K_H}{10^{-pH}}\left(1 + C_f K_{Na}\right)}. \tag{28}$$

All the charged sites that are not compensated in the Stern layer needs to be compensated in the diffuse layer. Therefore, the fraction of the counterions in the Stern layer is defined by the following equation,

$$f = \frac{\Gamma^0_{\mathrm{SNa}}}{\Gamma^0_{\mathrm{SNa}} + \Gamma^0_{\mathrm{S^-}} + \Gamma^0_{\mathrm{X}}}\,. \tag{29}$$

$$f = f_M \left\{ \frac{C_f K_{\mathrm{Na}}}{f_M (1 + C_f K_{\mathrm{Na}}) + (1 - f_M)\left[1 + C_f K_{\mathrm{Na}} + \dfrac{10^{-\mathrm{pH}}}{K_H}\right]} \right\}, \tag{30}$$

where f_M denotes the highest value of f reached at high salinities,

$$f_M = \lim_{C_f >> 1/K_{\mathrm{Na}}} f = 1 - \frac{\Gamma^0_{\mathrm{X}}}{\Gamma^0_S}\,. \tag{31}$$

The value of f_M is about 0.99 for kaolinite, 0.90 for illite, and 0.85 for smectite (see [12]). At high pH values (typically near-neutral pH or higher),

$$f \approx f_M \left(\frac{C_f K_{\mathrm{Na}}}{1 + C_f K_{\mathrm{Na}}} \right). \tag{32}$$

We look now for the pH dependence of the CEC. The CEC is defined by,

$$\mathrm{CEC} = \frac{e}{f_M} (\Gamma^0_{\mathrm{SNa}} + \Gamma^0_{\mathrm{S^-}} + \Gamma^0_{\mathrm{X}}) S_{sp}\,. \tag{33}$$

where S_{sp} correspond to the specific surface area (in $\mathrm{m^2\ kg^{-1}}$) and e the elementary charge. After some algebraic manipulations and simplification, we obtain,

$$\mathrm{CEC}(\mathrm{pH}, C_f) = \left(\frac{K_H + C_f K_{\mathrm{Na}} K_H}{K_H + C_f K_{\mathrm{Na}} K_H + 10^{-\mathrm{pH}}} \right) \mathrm{CEC}_M\,. \tag{34}$$

$$\mathrm{CEC}_M = e \Gamma^0_{\mathrm{S}} S_{sp}\,. \tag{35}$$

where CEC_M corresponds to the maximum CEC at value at high pH values.

From Eqs. (1), (11), and (13), the quadrature conductivity is given by,

$$\sigma'' = -\frac{2}{3} \rho_g \beta^S_{(+)} f\ \mathrm{CEC}\,, \tag{36}$$

where the product of f by the CEC is given by $f\,\mathrm{CEC}=e\Gamma^0_{\mathrm{SNa}}S_{sp}$ (the quadrature conductivity is controlled by the density of weakly sorbed sodium counterions in the Stern layer). Starting with Eqs. (30) and (34) to (36), we obtain,

$$\sigma'' = \sigma_M''\left(\frac{C_f K_{\mathrm{Na}} K_{\mathrm{H}}}{10^{-\mathrm{pH}} + K_{\mathrm{H}}\left(1 + C_f K_{\mathrm{Na}}\right)}\right), \tag{37}$$

$$\sigma_M'' = -\frac{2}{3}\left(\rho_g \beta^S_{(+)} f_M e\Gamma^0_{\mathrm{S}}\right) S_{sp}\,. \tag{38}$$

where σ_M'' denotes the quadrature conductivity reached at high salinity and high pH. At high pH values, Eq. (37) can be approximated by

$$\sigma'' \approx \sigma_M''\left(\frac{C_f K_{\mathrm{Na}}}{1 + C_f K_{\mathrm{Na}}}\right). \tag{39}$$

Equation (39) offers a simple expression to compute the salinity dependence of the quadrature conductivity.

3.4. Influence of frequency

In the previous model, we have not accounted for the frequency dependence of the complex conductivity. Low-frequency induced polarization is classically described in terms of a Cole-Cole distribution given by (e.g., [10, 28]),

$$\sigma^* = \sigma_\infty\left[1 - \frac{M}{1 + \left(i\omega\tau_{CC}\right)^c}\right], \tag{40}$$

$$M = \frac{\sigma_\infty - \sigma_0}{\sigma_\infty}\,, \tag{41}$$

where M ($0<M<1$) denotes chargeability (dimensionless but usually expressed in mV V^{-1} when the measurements are obtained in the time-domain, σ_0 denotes the DC (Direct Current) electrical conductivity (ω=0), σ_∞ the high frequency electrical conductivity ($\omega >> 1/\tau_{\mathrm{CC}}$), τ_{CC} denotes the Cole Cole time constant, c denotes the Cole Cole exponent for the complex conductivity. Expressions for σ_0 and σ_∞ that are compatible with the ones described above in Section 3.1 are provided in Appendix B. The case c = 1/2 corresponds to the Warburg impedance model, which corresponds in turn to have the Stern layer behaving as a leaking capacitance because of the sorption/desorption of counterions.

The in phase and quadrature components of Eq. (40) are given by,

$$\sigma' = \sigma_\infty - \frac{1}{2} M_n \left\{ 1 - \frac{\sinh\left[c \ln(\omega\tau) \right]}{\cosh\left[c \ln(\omega\tau) \right] + \cos\left[\frac{\pi}{2}(1-c) \right]} \right\}, \tag{42}$$

$$\sigma'' = -\frac{1}{2} \left\{ \frac{M_n \cos\left[\frac{\pi}{2}(1-c) \right]}{\cosh\left[c \ln(\omega\tau) \right] + \sin\left[\frac{\pi}{2}(1-c) \right]} \right\}. \tag{43}$$

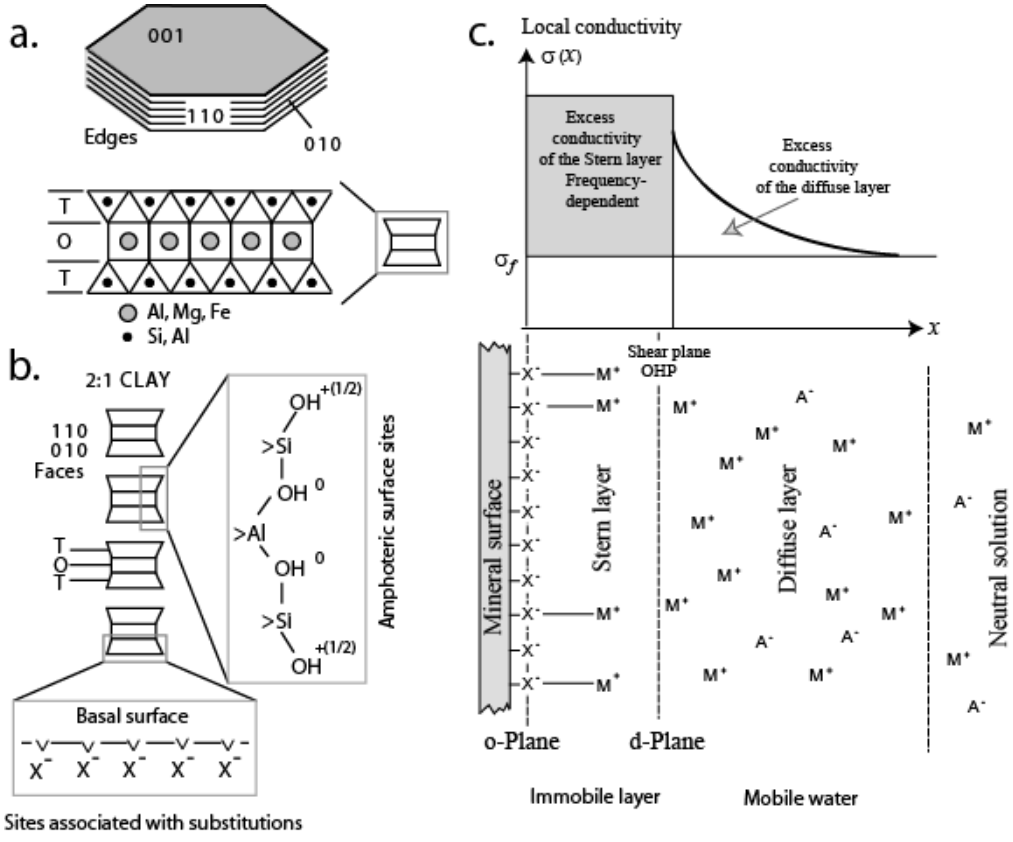

Figure 1. Double layer associated with clay minerals. **a.** TOT structure of clay minerals (T stands for the tetrahedral layer, O stands for the Octohedral layer). **b.** The charge on the surface of the clay minerals depends on the amphoteric sites located on the edges of the clay crystals and negative sites associated with isomorphic substitutions in the crystalline framework of the clay minerals in the T- and O-layers. These isomorphic substitutions are responsible for the charge on the surface of the basal planes. **c.** The mineral charge is compensated by counterions (M^+) and coions (A^-) forming a double layer. This double layer comprises a layer of sorbed counterions (the Stern layer) and a diffuse layer.

where $M_n = M\sigma_\infty = \sigma_\infty - \sigma_0$ denotes the normalized chargeability of the material. Eqs. (42) and (43) can be used to invert complex conductivity spectra in terms of the four Cole Cole parameters: $\rho_0 = 1/\sigma_0$, M, c, and τ_{CC}. The normalized chargeability is actually equal to the quadrature conductivity given by Eq. (39) at the peak frequency.

The angular frequency of the phase peak is given by

$$\omega_{\text{peak}} = \left(\frac{\sigma_\infty}{\sigma_0}\right)^{1/2c} \frac{1}{\tau_{CC}} = \left(\frac{1}{1-M}\right)^{1/2c} \frac{1}{\tau_{CC}} . \tag{44}$$

If $M << 1$, then $\omega_{\text{peak}} \approx 1/\tau_{CC}$.

For clean sands, The Cole Cole relaxation time was found to be controlled by the mean pore size of the material Λ according to [13]

$$\tau_{CC} = \frac{\Lambda^2}{2D_{(+)}^S}, \tag{45}$$

where $D_{(+)}^S$ denotes the diffusion coefficient of the counterions in the Stern layer (see Section 5.2 below).

4. Experimental Data

In order to test further the Stern polarization model on natural porous media, we developed a new database of well characterized sandstones and saprolites. This data base comprise 17 samples divided into two sets of materials: 11 unconsolidated saprolitic core samples and 6 weakly consolidated sandstones (including a mudstone).

4.1. Core Samples

Six samples were collected from the Great Divide Basin (Wyoming). Five samples are grain supported sandstones with angular to subrounded grains (Figure 2). Sample S439 is a mudstone (Figure 2f). The pore size distributions of these materials were determined form mercury intrusion (Figure 3).

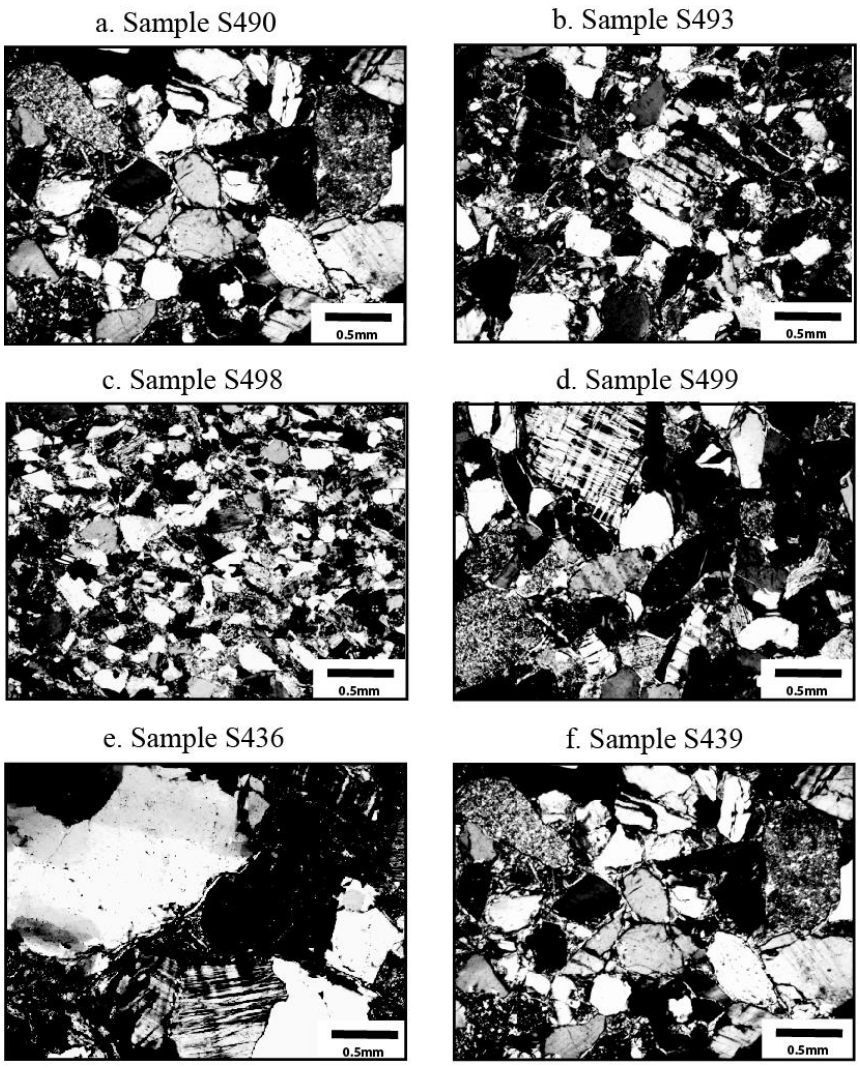

Figure 2. Thin section photomicrographs of the six samples. **a.** Medium to very coarse, poorly sorted, arkosic sandstone. **b.** Very fine to medium, moderately sorted, subarkosic sandstone. **c.** Very fine to medium, moderately to well sorted, subarkosic sandstone. **d.** Fine to very coarse, poorly sorted, arkosic sandstone. **e.** Poorly sorted sandy conglomerate. **f.** Clay with silt and very fine sand (mudstone).

Eleven saprolite samples were taken from the Oak Ridge National Laboratory (Tennessee). The saprolite results from the weathering of Middle Cambrian interbedded shale, siltstone, and limestone forming the parent rock material [29]. The sand and silt fractions (in weight) are grossly 50% and 30%, respectively, and the clay fraction is about 20% [30-33]. The clay is mainly illite with some mixed-layer illite-smectite clay minerals. The petrophysical properties of all the samples are reported in Tables 1 and 2.

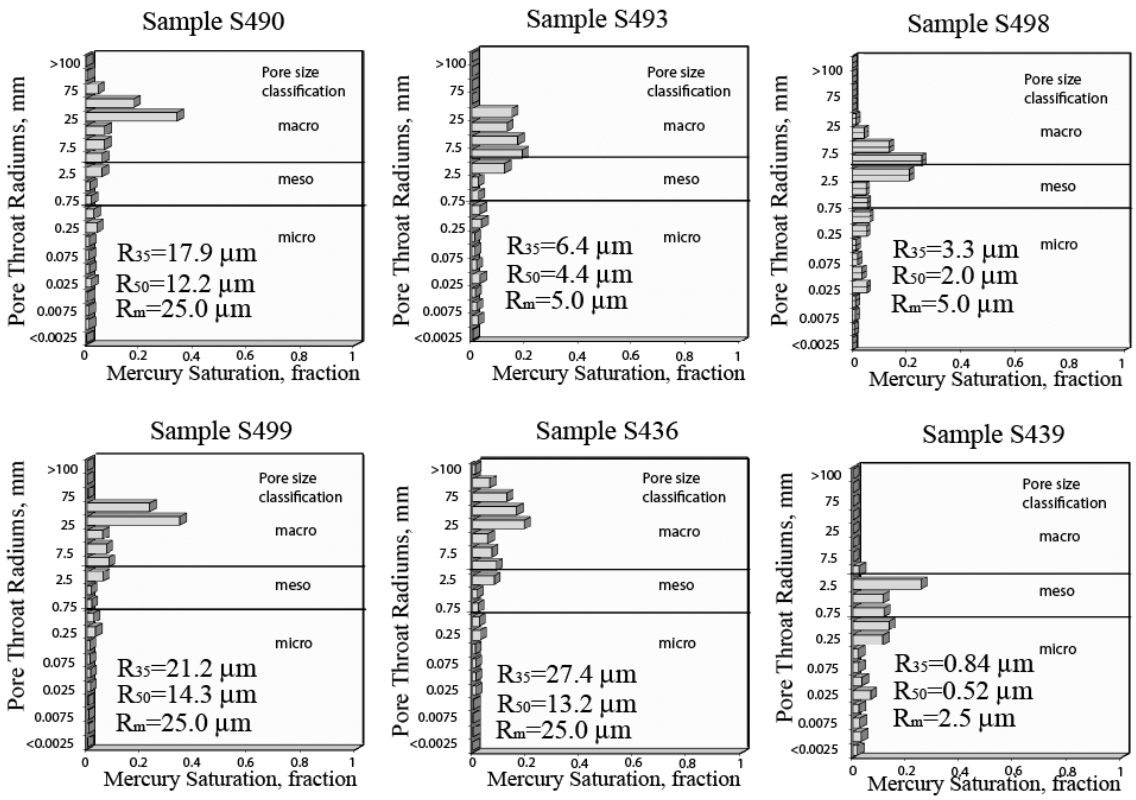

Figure 3. Pore size distribution from mercury intrusion experiments. We have also indicated the median values of the pore size distributions R_{50} and the modal pore throat size R_m. The mudstone corresponds to the core sample with the smallest pore sizes.

4.2. Measurement of the Complex Conductivity

Complex conductivity measurements were performed using four electrodes. The complex impedance Z^* (in ohm) is defined as

$$Z^*(\omega) = \frac{U}{I} = \left|Z^*(\omega)\right| e^{i\varphi(\omega)}, \tag{46}$$

where U is the measured voltage difference between two electrodes M and N, I denotes the magnitude of the current injected/retrieved at electrodes A and B, and $\left|Z^*(\omega)\right|$ and $\varphi(\omega)$ denote the amplitude and the phase of the complex impedance, respectively. The complex resistivity $\rho^* = 1/\sigma^*$ (in ohm m) is related to Z^* by a geometrical factor K (in m): $\rho^*(\omega) = KZ^*(\omega)$. This geometrical factor K takes into account the position and dimensions of the electrodes and the insulating boundary conditions on the sample holder.

The electrical measurements were taken using a ZEL-SIP04-V02 impedance meter (Figure 4a, see [34] for details on this apparatus and [35] for benchmark tests). Spectral induced polarization spectra were recorded at 25 frequencies from 1 mHz to 45 kHz, with repeatability checked by

running samples twice, or running a limited frequency range several times. The accuracy of the instrument is ~0.1-0.3 mrad at frequencies below 1 kHz.

For the 5 sandstones and the mudstone, the following fluids were used to saturate the samples: (1) natural site groundwater (conductivity at 25°C, 0.048±0.013 S m^{-1}) and (2) the following NaCl solutions at 1 mM (measured conductivity 0.033 S m^{-1}), 10 mM (0.204 S m^{-1}), 30 mM (0.328 S m^{-1}), and 100 mM (1.125 S m^{-1}).

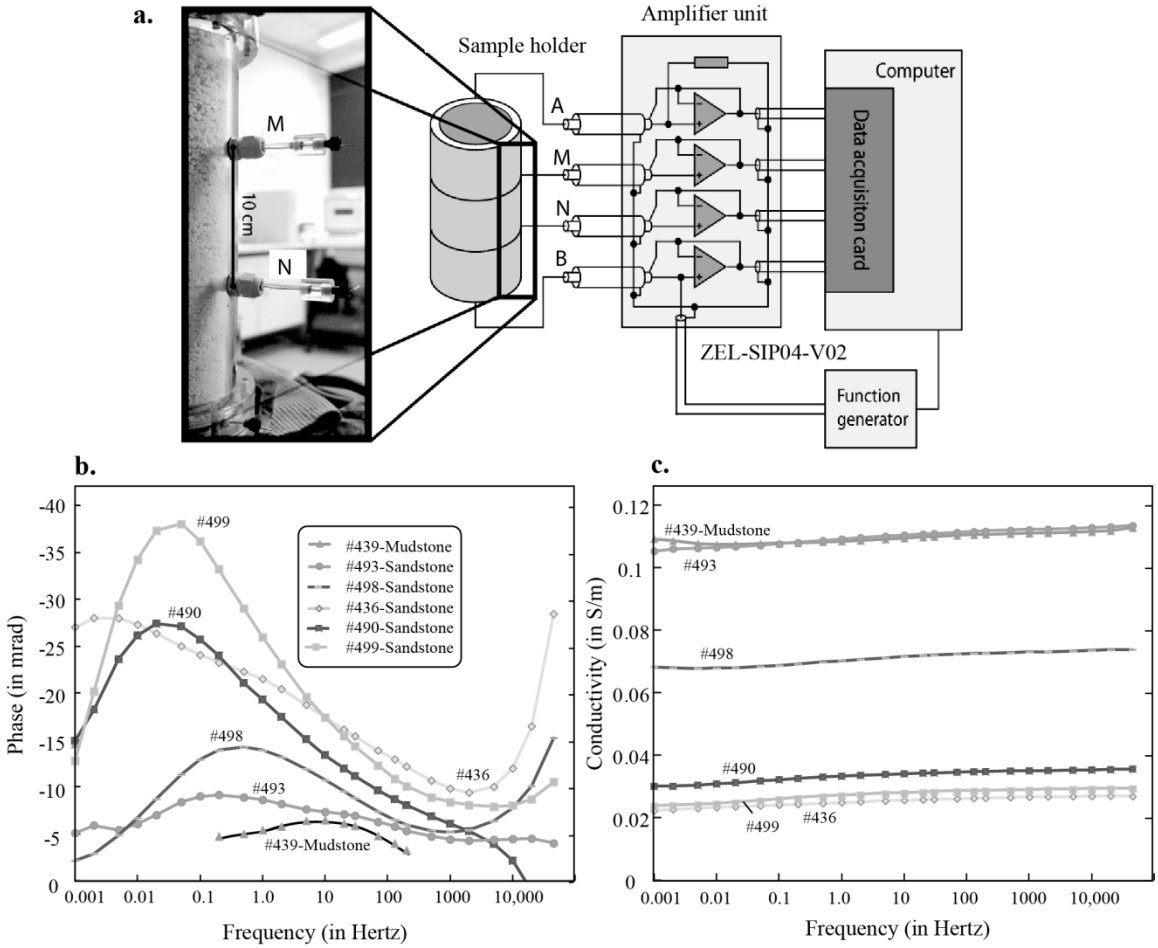

Figure 4. Raw in situ pore water conductivity data. **a**. Sketch of the high-sensitivity impedance meter used to collect the SIP measurements (ZEL-SIP04-V02). Adapted from [34] and [35]. The measurements were collected using a Wenner-type array: A and B correspond to the current electrodes while M and N correspond to the potential electrodes. **b.** Measured phase versus frequency for the six samples saturated with native groundwater (for typical site groundwater quality see Table 2). **c.** Electrical conductivity versus frequency for the six samples saturated with the native groundwater (see Table 2, conductivity at room temperature: 0.048±0.013 S m^{-1}).

Ag-AgCl electrodes were used for both injection and potential electrodes. Most electrode arrays were circumferential with some being axially arranged. The spectra for the sandstone/mudstone samples saturated with the ground water (see composition in Table 3) are shown in Figures 4b and 4c. The spectra obtained for Samples S439 and S436, at different salinities, are shown in Figure 5. Saturation of the samples was done with a vacuum chamber.

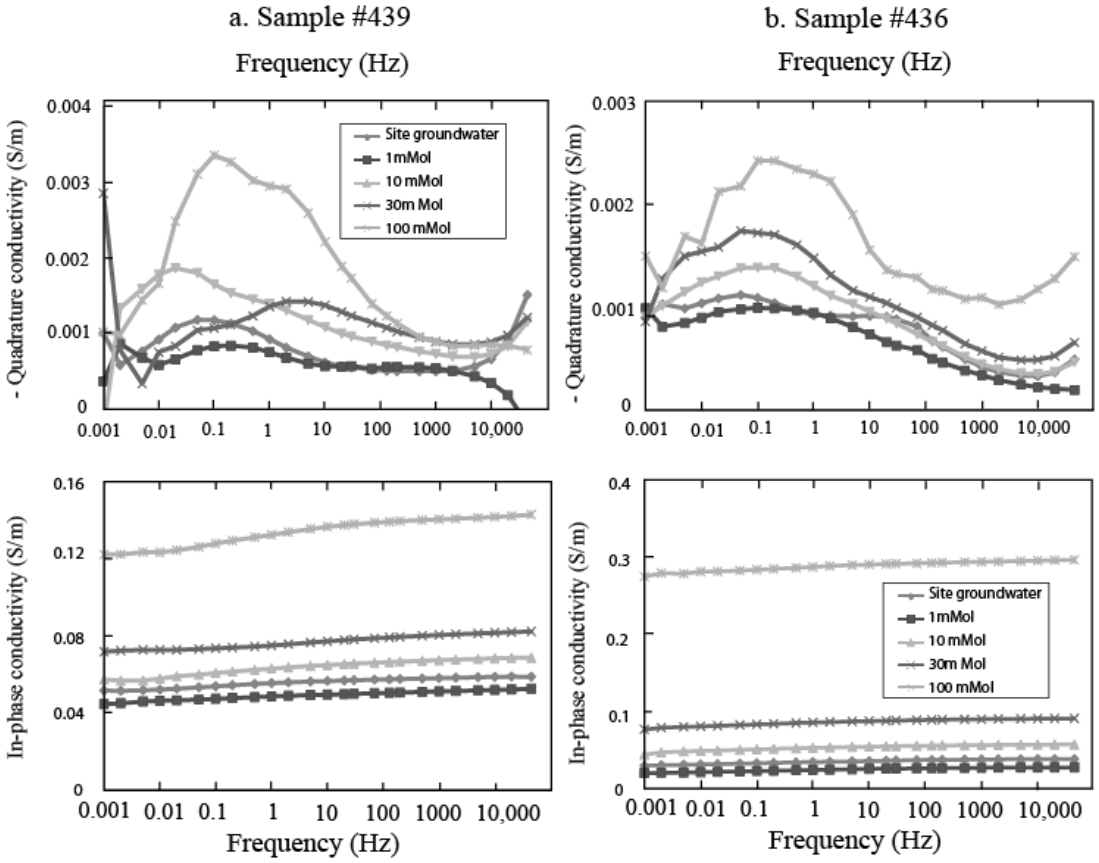

Figure 5. Example of spectra for samples S439 (mudstone) and S436 (sandy conglomerate). These data show a well-defined peak frequency in the quadrature conductivity.

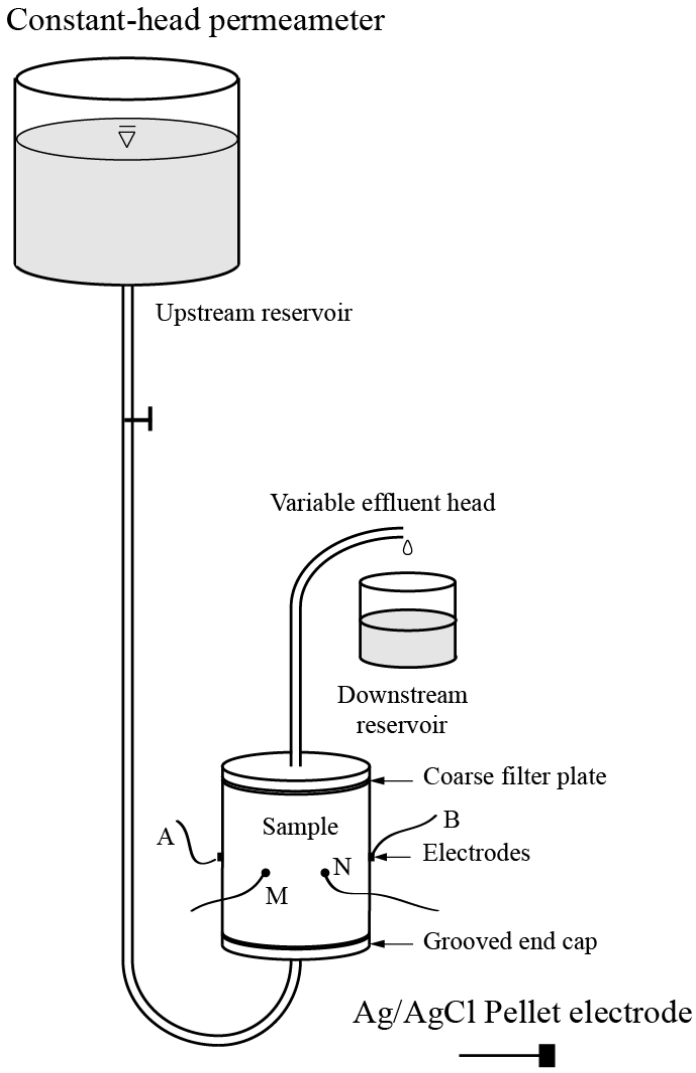

Figure 6. Sketch of the equipment used for the permeability and electrical measurements. Constant head permeameter. The non-polarizing Ag/AgCl electrodes for the measurement of the complex conductivity are organized in a Wenner array (A and B are the current electrodes, M and N are the potential electrodes). The electrodes ABMN are located in the middle of the sample holder (see comparison with the sample holder shown in Figure 4). We use the same impedance meter as shown in Figure 4 (ZEL-SIP04-V02).

For the saprolite core samples, we used the permeameter shown in Figure 6. The reported pore water conductivity is the conductivity of the effluent once equilibrium has been reached at a given salinity with a NaCl solution. The complex conductivity of samples S14, S20, S18, S5, S10, S12, and S7 were measured with salinities at 10 mM, 30 mM, and 100 mM (NaCl) while the Samples S9, S16, and S22 were measured at the following salinities natural ground water (see Table 2, typical conductivity of the effluent comprised between 0.0064 and 0.0072 S m^{-1}), 3 mM (typical conductivity of the effluent 0.0390 S m^{-1}), 10 mM (typical conductivity of the effluent 0.12 S m^{-1}), 30 mM (typical conductivity of the effluent 0.32 S m^{-1}), 100 mM (typical conductivity of the effluent 0.90 S m^{-1}), and 300 mM (typical conductivity of the effluent 2.54 S m^{-1}) (NaCl solutions) plus using

the ground water described in Table 2. We use the same impedance meter (ZEL-SIP04-V02) and we investigated the same frequency range than above for the sandstones and the mudstone. Some of the spectra are displayed in Figure 7.

4.3. Determination of the Permeability

For the sandstones and the mudstone, the permeability was determined from the mercury intrusion experiments using the Swanson approach [36]. The validity of this approach was checked on two samples for which the permeability was measured by a flow-through experiment. For instance for Sample S498, we obtain a Klinkenberg-corrected air permeability of 78 mD versus an estimated permeability of 87 mD using the Swanson approach. For Sample S493, we obtain a Klinkenberg-corrected air permeability of 25 mD versus an estimated permeability of 27 mD using the Swanson approach.

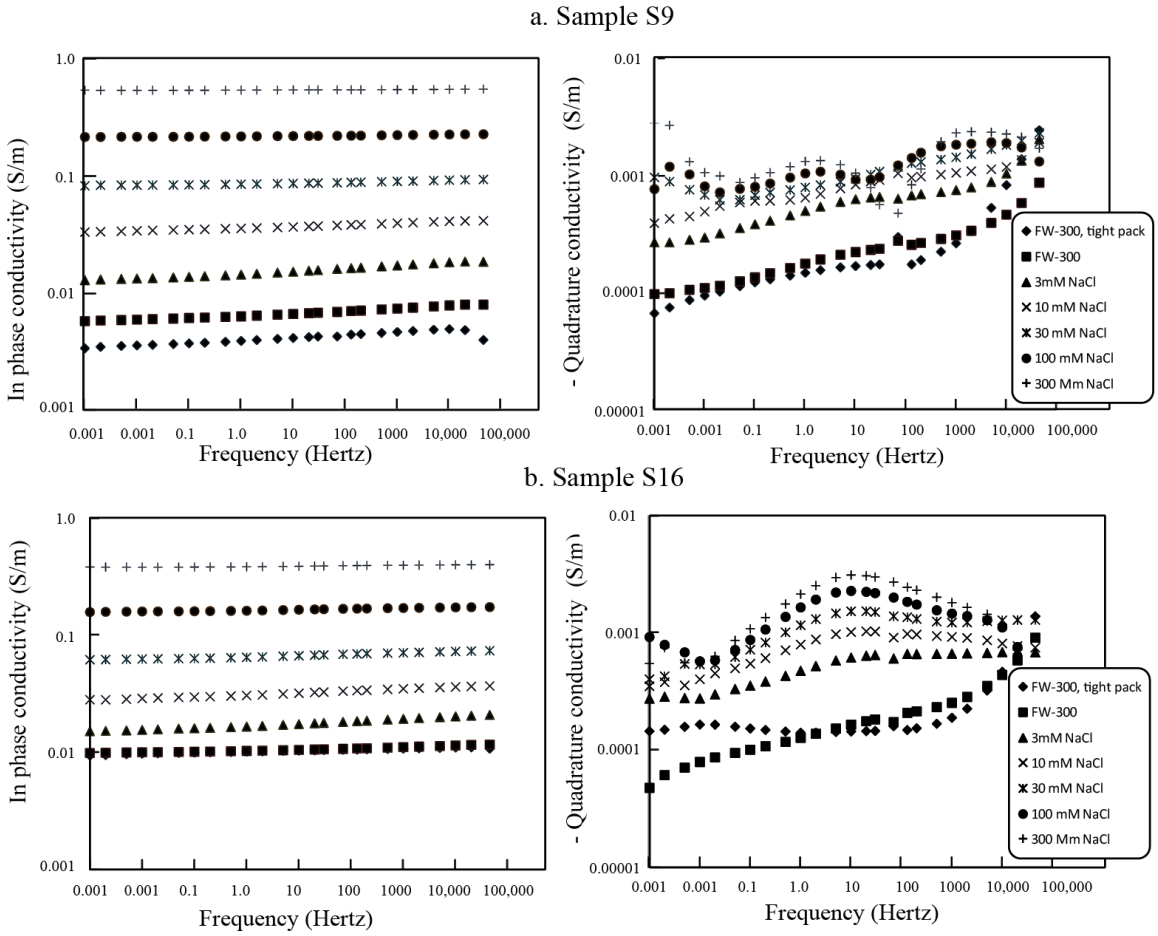

Figure 7. In-phase and quadrature conductivities at different pore water salinities. pH values in the range 5-6. For sample S16, we observe that the quadrature conductivity peaks at the same frequency whatever the salinity of the NaCl solution.

For the saprolite core samples, the permeability was directly estimated using the permeameter shown in Figure 7 using flow-through experiments with the pore water. The permeability was measured at each salinity and we found no dependence of the permeability on the salinity (potential swelling/shrinking effects associated with the presence of smectites could have been expected). All the data are reported in Table 1.

4.4. Measurement of the CEC and Specific Surface Area

In addition to the complex conductivity measurements, we also performed cation exchange capacity (CEC) and specific surface area (using the BET method) measurements. The CEC measurements were performed on 7 saprolite core samples using a barium chloride solution to displace the cations sorbed to the clays (see protocol in [37]). All the seven samples were analyzed in duplicates with relative standard deviation less than 17%. The average measured CEC value of the samples range from 5.0 to 8.6 cmol kg^{-1} or $CEC_M = (4.8\text{-}8.3)\times10^3$ C kg^{-1} (see measurements in Table 2).

Specific surface area measurements were performed with the BET method using nitrogen as the adsorbent gas. Measurements were collected using a surface area analyzer (Micromeritics ASAP 2020). The surface area of pores of the core samples was calculated using the Brunauer, Emmett, and Teller (BET)-theory [38-39]. The specific surface area measurements are reported in Table 2 for all the core samples.

In Figure 8, we plot the specific surface area measurements of the seven saprolite core samples versus their cation exchange capacity. The ratio of the CEC by the specific surface area defines the equivalent charge per unit surface area: $Q_S = CEC_M / S_{sp}$ which is approximately equal to 0.32 C m^{-2} (two elementary charges per nm^2, [40]). In Figure 8, our measurements are shown to be consistent with a broad range of literature data indicating a surface charge density comprised between 1 to 3 elementary charges per nm^2 for clay minerals [41-49].

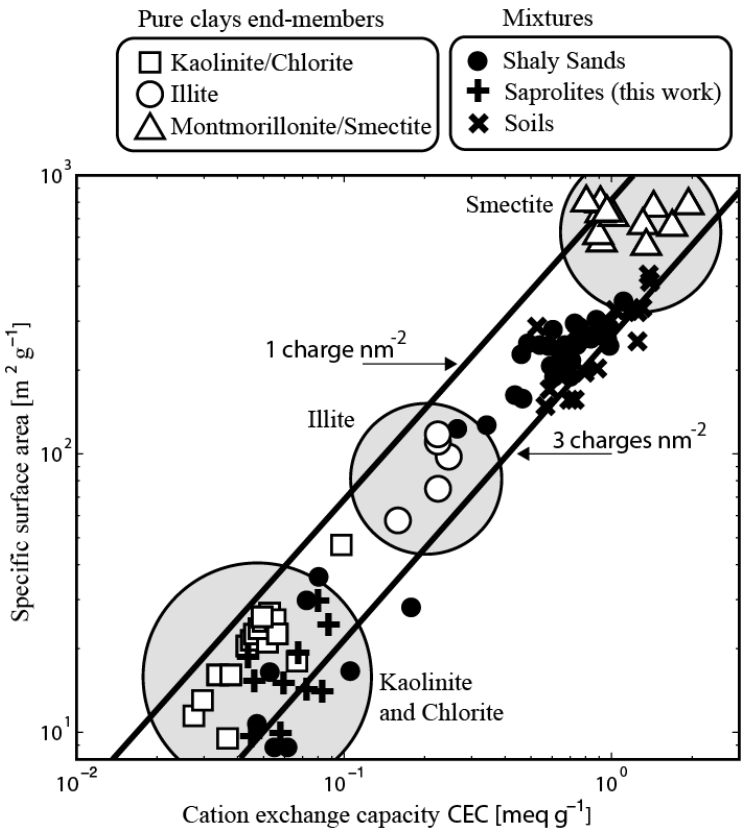

Figure 8. Specific surface area versus CEC (in meq g^{-1} with 1 meq g^{-1}=96,320 C kg^{-1} in SI units) for 18 saprolite core samples from the Oak Ridge background site. The two lines corresponds to 1 to 3 elementary charges per unit surface area. Data for the clay end-members are from: [41] to [48]. The soil data are from [49].

5. Theory versus Experimental Data

In this section, we compare the model discussed in Section 3 with the experimental data described in Section 4. The following aspects of the model are tested: dependence of the complex conductivity on the salinity, specific surface area, cation exchange capacity, and pore size.

5.1. Dependence on the Dukhin Number

From Eqs. (12) and (16), the in phase conductivity can be written as,

$$\sigma' = \sigma_w \left(\frac{1}{F} + \mathrm{Du} \right). \tag{47}$$

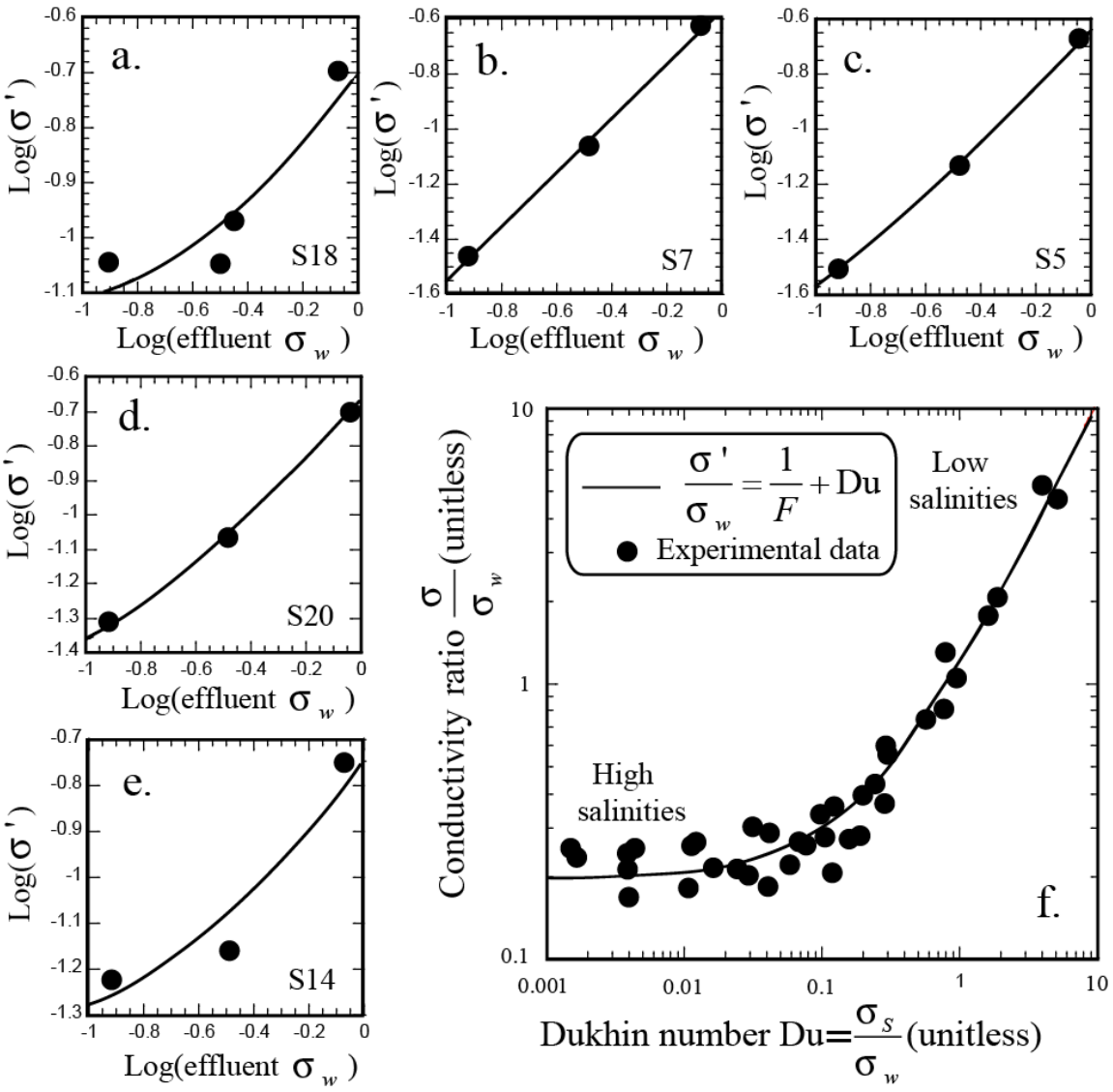

Figure 9. Normalized conductivity versus the Dukhin number for all the saprolite core samples (pH ~5-6,) having the same range of formation factors 5.1±1.0 (see Table 2). The measurements are reported at 1 Hz.

Therefore the normalized conductivity (σ'/σ_w) depends only on the unitless Dukhin number Du and the formation factor *F*. In Figure 9, we plot the normalized conductivity versus the Dukhin number for three saprolite core samples having the same formation factor. All the data falls along the trend predicted by Eq. (47) showing that a linear conductivity model provides a correct representation of the electrical conductivity at different pore water conductivities.

5.2. Dependence on the Specific Surface Area

According to Eq. (38), the plateau of the quadrature conductivity is also a measure of the specific surface area (in kg m^{-2}) of the porous material. From Eq. (38), we have,

$$\sigma'' = -aS_{Sp}\,, \tag{48}$$

$$a = \frac{2}{3}\beta_{(+)}^{S} f \rho_g Q_S\,. \tag{49}$$

where Q_S denotes the charge density of the mineral surface (0.32 C m^{-2}, see Section 4.4 above) and ρ_g denotes the mass density of the grains (solid phase). The mobility of the counterions in the Stern layer is vastly different for silica and aluminosilicates i.e. clay minerals [12-13], and such different property materials should therefore yield two distinct master curves with very different values of the coefficient a.

For clayey sands, taking $\beta_{(+)}^{S}(Na^+)$ = 1.5 × 10^{-10} $m^2s^{-1}V^{-1}$ at 25°C, f = 0.90, Q_S = 0.32 C m^{-2}, ρ_g = 2650 kg m^{-3}, we can write $\sigma'' \approx -a\,S_{Sp}$ with a = 7.6×10^{-8} S kg m^{-3} [12]. For the clean sands and sandstones, if we use $\beta_{(+)}(Na^+)$=5.2×10^{-8} $m^2s^{-1}V^{-1}$, f = 0.50, Q_S = 0.64 C m^{-2}, ρ_g = 2650 kg m^{-3}, we obtain a = 2.9×10^{-5} S kg m^{-3} [13]. For the clean sands and sandstones, the specific surface areas were calculated from the median grain diameters, (d_{50}) using S_{Sp} = 6 / (ρ_g d_{50}) where ρ_g = 2650 kg m^{-3} denotes the density of the silica grains.

In Figure 10, we plot the quadrature conductivity versus the specific surface area of the core samples investigated in the present study together with additional data from the literature. The datasets split into two distinct linear trends: one for clean sands and one for clayey materials. This indicates that the mobilities of the counterions in the Stern layer of silicates and alumino-silicates are very different from each other.

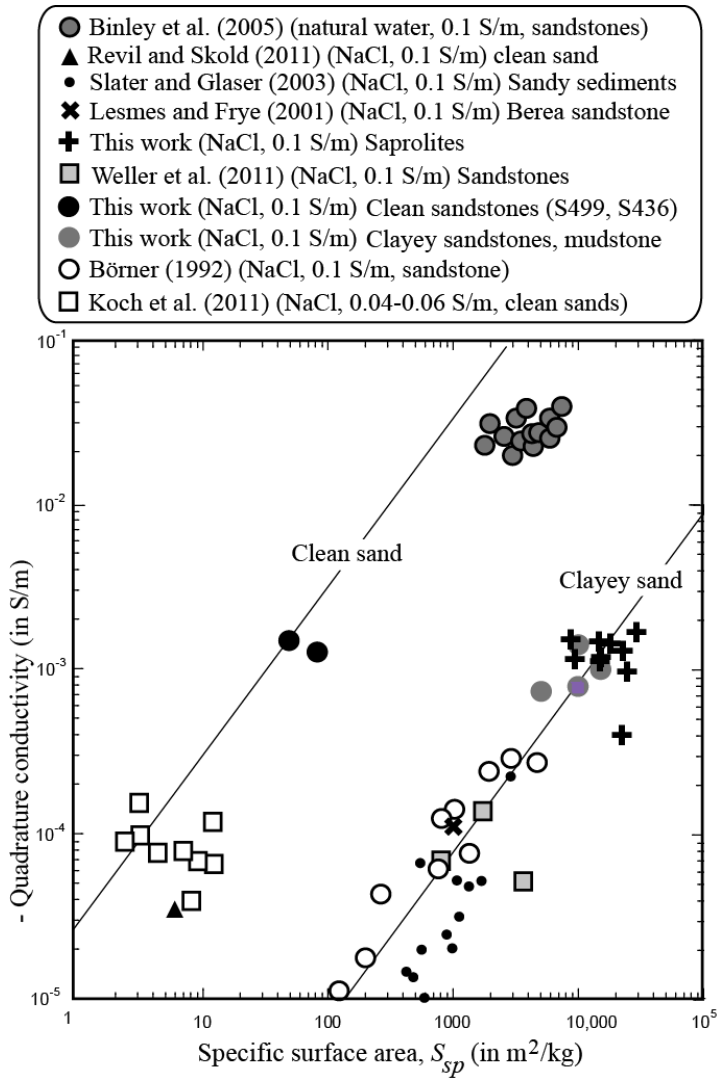

Figure 10. Influence of the specific surface area S_{Sp} upon the quadrature conductivity. Trend determined for clayey sands from the model developed by Revil [12] at 0.1 S m^{-1} NaCl. For the data from [13] and [55-59], the measurements are reported at 10 Hertz. For the data from Binley et al.[60] (Eggborough and Hatfield sandstones), they are reported at 1.4 Hz.

5.3. Dependence on the Salinity

In Figures 11 and 12, we test the dependence of the phase and quadrature conductivity on the pore water conductivity. In Figure 10, we test Eq. (19) together with the data on the saprolite core samples using $\beta^S_{(+)}(Na^+) = 1.5 \times 10^{-10}$ m^{2}s^{-1}V^{-1} and $B_{(+)}(Na^+)=5.6\times10^{-8}$ m^{2}s^{-1}V^{-1} at 25°C (see Section 2 above). The data are fitted with a constant value of the partition coefficient $f = 0.92$ and a charge per unit volume of 5.7×10^7 C m^3 as determined in Figure 11. The partition coefficient is consistent with the presence of illite in the pore space while the charge per unit pore volume is consistent with Eq. (20). Indeed, taking a grain density of ρ_n of 2650 kg m^{-3}, a cation exchange capacity CEC of 6 cmol kg^{-1} (see Table 2), and a porosity of □ = 0.40 (Table 1), we obtain Q_V = 2.3×10^7 C m^{-3}.

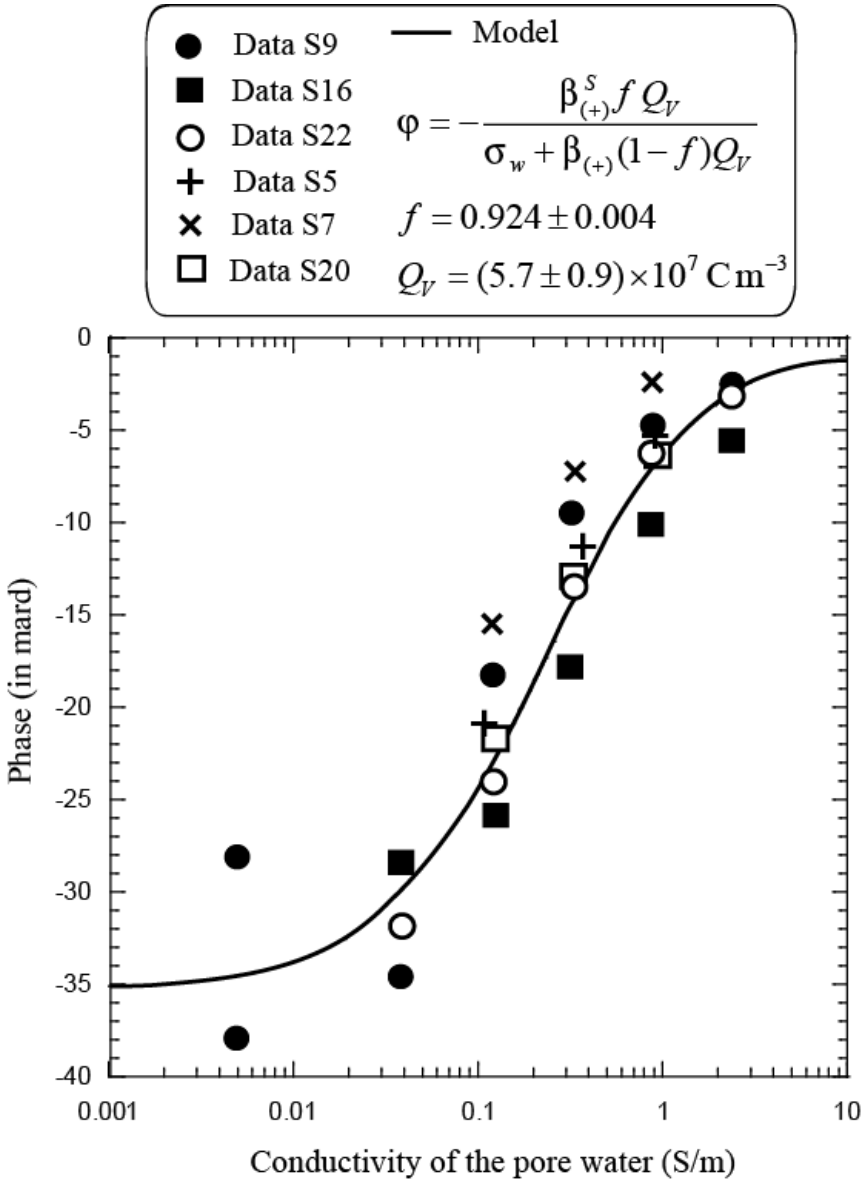

Figure 11. Determination of the partition coefficient *f* (fraction of the counterions in the Stern layer) and total volumetric charge density Q_V using the phase lag data plotted as a function of the conductivity of the pore water (at 1 Hertz, NaCl). The plain line corresponds to the best fit of the model using a constant value of the partition coefficient.

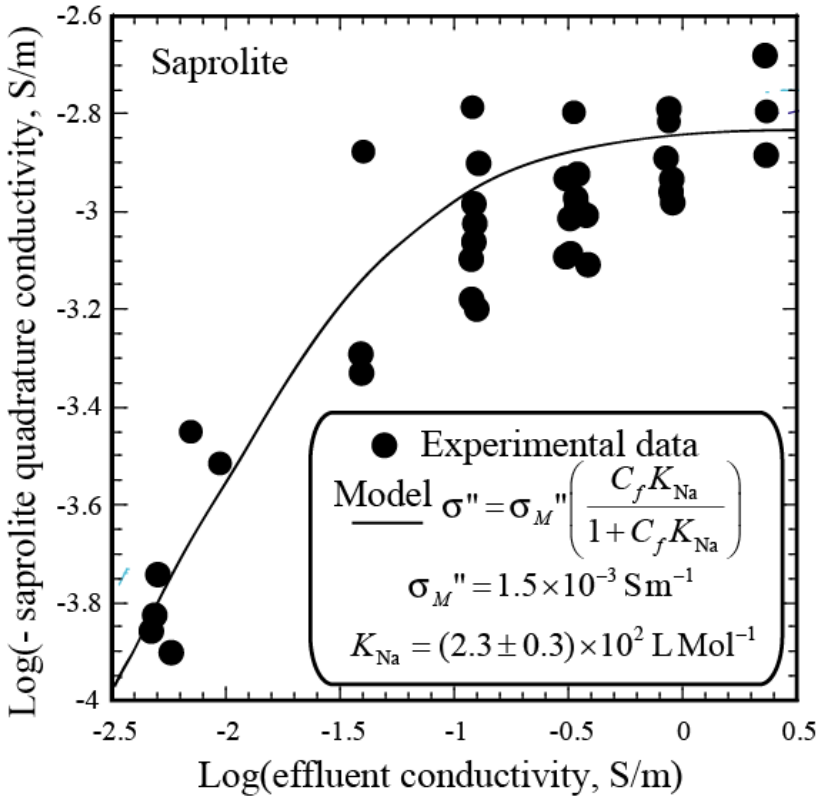

Figure 12. Dependence of the quadrature conductivity with the salinity (all the saprolite core samples, NaCl, pH ~ 5-6). The plain line corresponds to the prediction of the model. Note that the quadrature conductivity data reach a plateau at high salinities.

In Figure 12, we test the prediction of Eq. (39) regarding the salinity dependence of the quadrature conductivity with the pore water conductivity. Eq. (39) is able to represent all the saprolite data fairly well. Using Taking $CEC_M = 6 \times 10^3$ C kg^{-1} (see Table 2), $\beta_{(+)}^{S}(25°C, Na^+) = 1.5 \times 10^{-10}$ m^{2}s^{-1}V^{-1} (see Section 5.2. above), and $f_M = 0.92$ (high salinity asymptotic value) yields σ_M'' = - (1.1-1.9)×10^{-3} S m^{-1} at high salinities in excellent agreement with the laboratory data shown in Figure 12 (see the high salinity asymptote for which σ_M'' = - (1.5)×10^{-3} S m^{-1}).

5.4. Dependence on Frequency

We develop a methodology to invert the Cole Cole parameters using the genetic algorithm. We first determined the initial values of the Cole Cole parameters with the use of two existing deterministic algorithms from [50] and [51]. An extensive series of tests of these two algorithms showed that there were not able to converge property in fitting our data (not shown here). That said, if we used these algorithms to get a set of values for the Cole-Cole parameters, which are then used as starting parameters for the genetic algorithm, we obtain an excellent fit of the data (Figure 13). The genetic algorithm we used is based on the built-in MATLAB Global Optimization Toolbox.

In Figure 14a, we show that the Cole Cole time constant inverted from the genetic algorithm seems independent on the salinity of the pore water solution. This is consistent with our model as the diffusion coefficient of the counterions in the Stern layer is expected to have only a weak dependence on the salinity. We have performed a similar analysis for the Cole Cole exponent (Figure 14b) and we found also that the Cole Cole exponent *c* is independent on the salinity of the pore water.

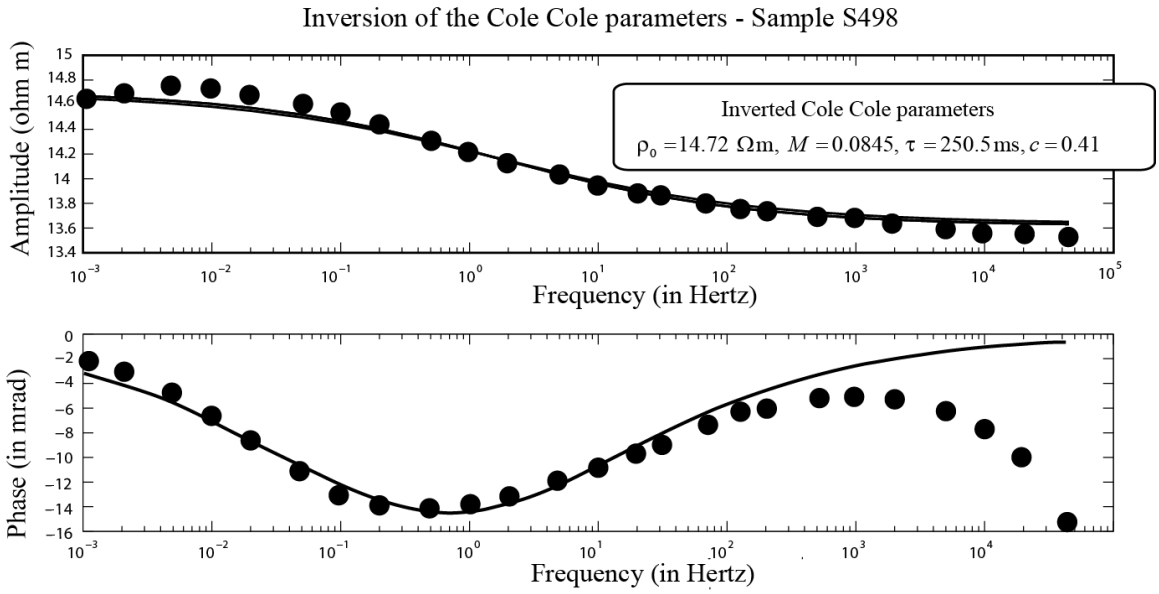

Figure 13. Inversion of the Cole Cole parameters using the genetic algorithm. Example for Sample S498. The filled circles correspond to the measurements for the amplitude of the resistivity and the phase. Above 100 Hz, the measurements are not considered very reliable and so we did not try to match the data above 1 kHz.

5.5. Dependence on the Pore Size

We are now in the position to determine the relationship between the Cole Cole time constant and the pore size. If we look at Figure 3, we see that Samples S490, S499, and S436 are characterized by the biggest pores (median in the range 12-14 □m). Their spectra peaks at low frequencies (0.05-0.1 Hz, see Figure 4). At the opposite, Sample S439 is characterized by narrow pores (median 0.5 □m) and a its phase peaks at high frequencies (10 Hz).

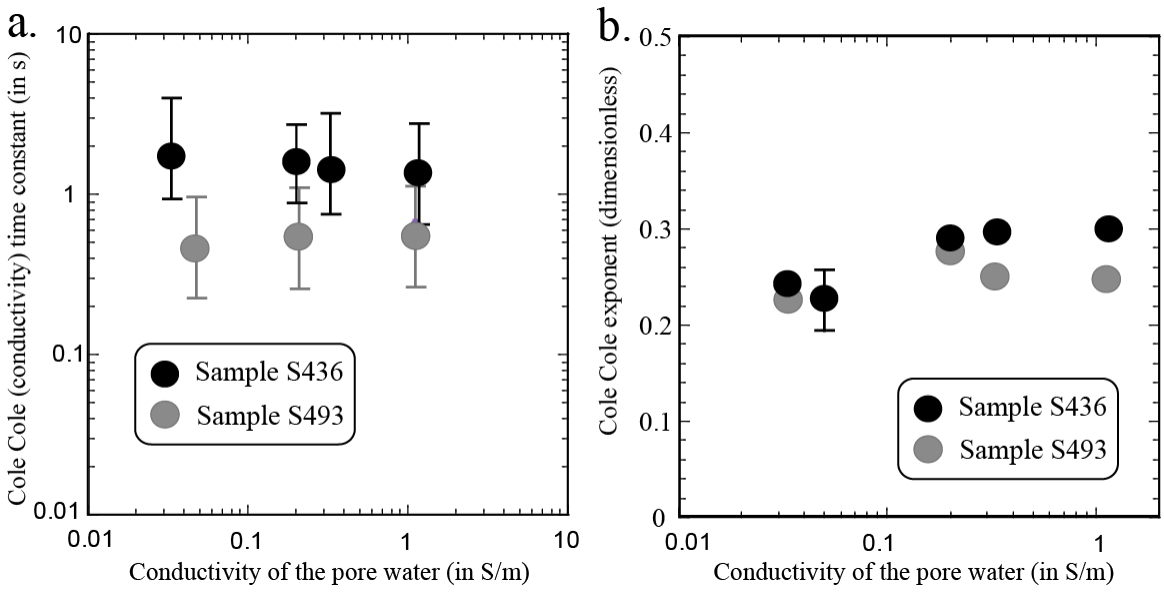

Figure 14. Variation of the Cole-Cole time constant and the Cole Cole exponent for two sandstone core samples as a function of the pore water conductivity. **a.** The Cole Cole time constants were determined from the spectra using the genetic algorithm as explained in the main text. The samples are chosen to represent the full range of grain sizes (sample S436 is the coarsest oxidized sandstone, sample S493 is a reduced medium to fine grained silty sandstone). The trends shown by the data are inside the error bars of the inverted Cole Cole time constant. **b.** The Cole Cole exponent versus the pore water conductivity for the same samples. The error bar is typical of the Cole Cole exponent estimates.

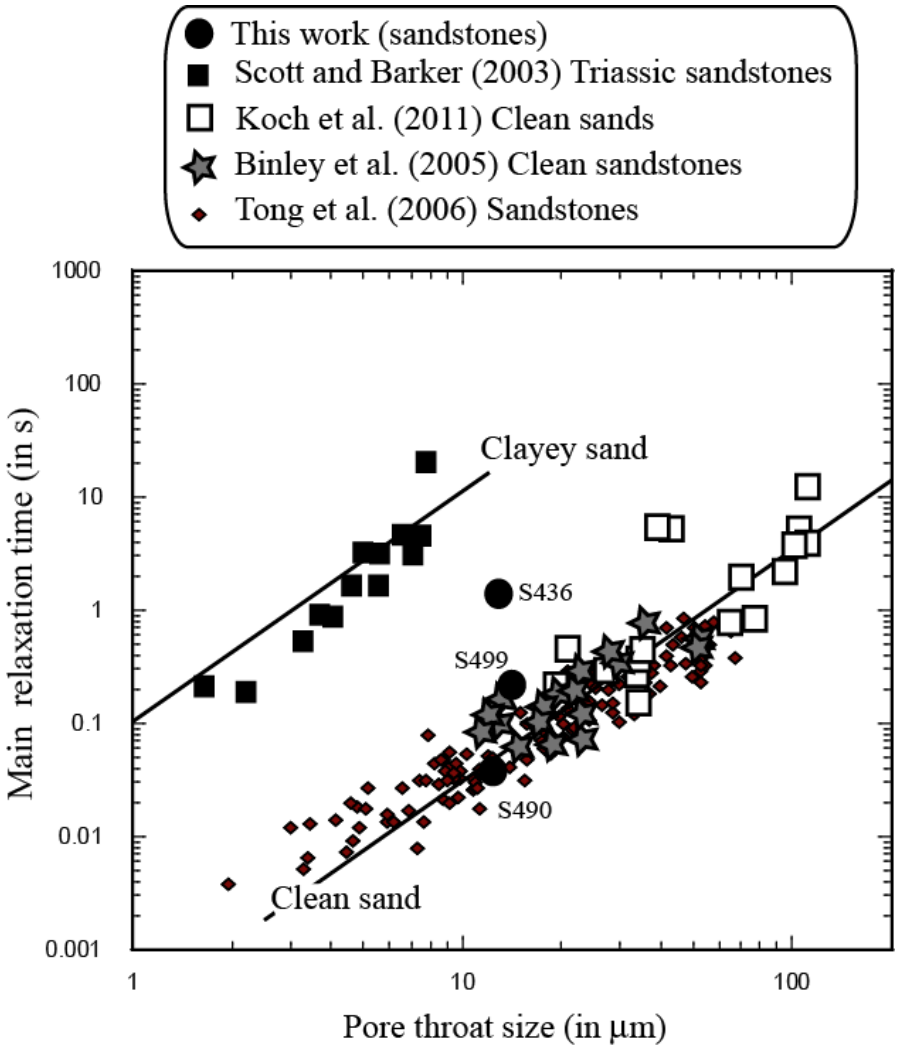

Figure 16. Main relaxation time τ_0 versus the pore size Λ. The pore size data from this study are median values obtained from mercury injection data or permeability data. For the data from [55], the pore size is determined from the median grain size and the formation factor using the relationship developed by Revil and Florsch [10]. The mean pore size is either determined from mercury intrusion porosimetry (Binley et al. [60]) or from permeability for the data of Tong et al. [63]). The plain lines correspond to the prediction of the model.

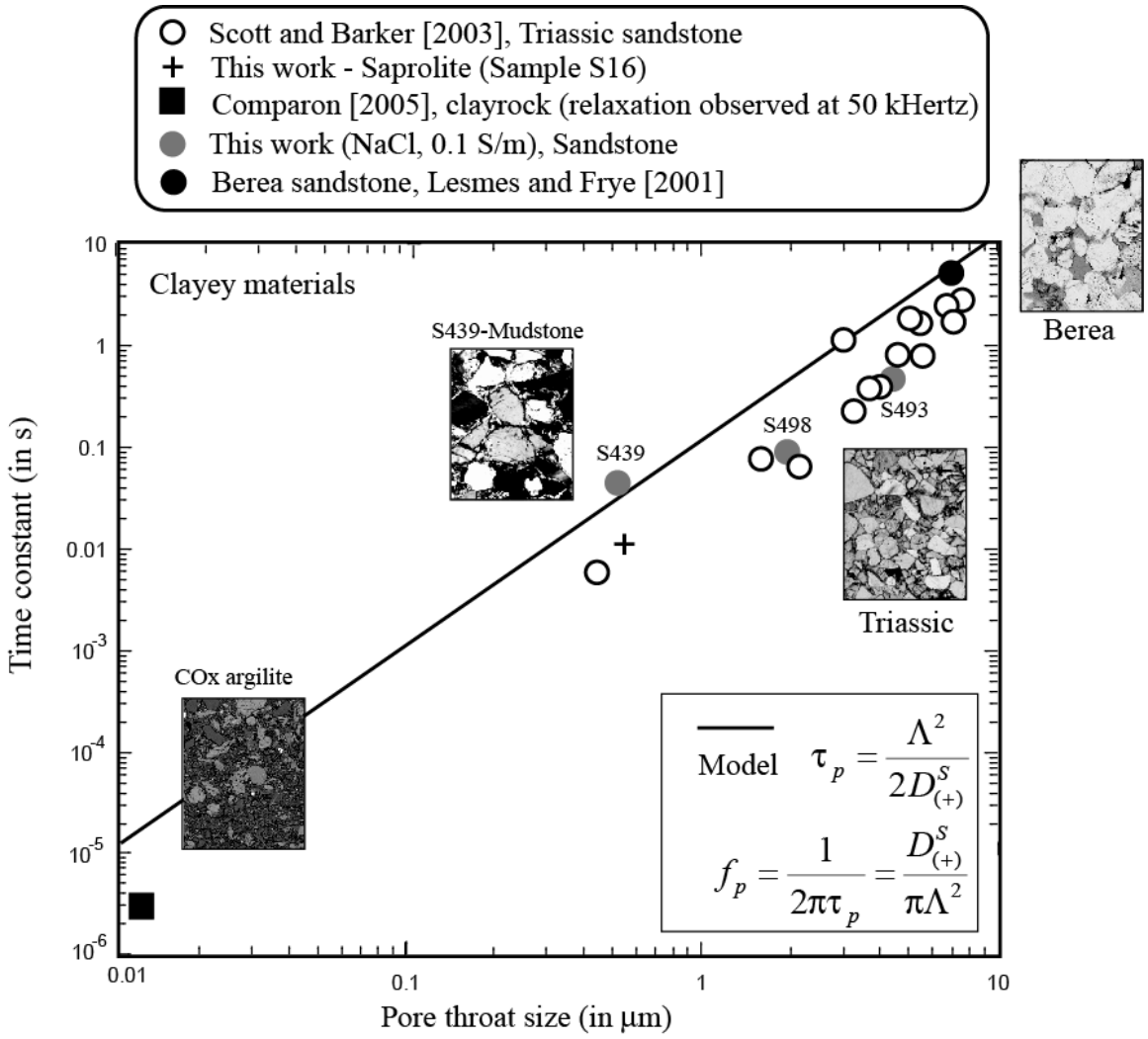

Figure 15. Relationship between the low-frequency time constant and the mean size of the pore throat for clayey materials. The size of the thin section images is 1 mm in *x*. COx stands for Callovo-Oxfordian. The plain line corresponds to the prediction of the model. Data from [59] and [61-62].

In Figures 15 and 16, we plot the Cole Cole time constant versus the pore size of the material, either determine from the permeability or from mercury intrusion experiments. In the first case, the permeability is related to the mean pore size by,

$$k = \frac{\Lambda^2}{8F}. \tag{50}$$

where F denotes the formation factor discussed in Appendix A. Katz and Thompson [52] developed a relationship between the permeability and a percolation length scale R_c that can be determined from mercury data: $k_S = R_c^{\,2}/(226F)$. A comparison between this equation and Eq. (50) yields $R_c \approx 5.3\,\Lambda$.

We found, here again, that the data for clean sands and clayey materials split into two distinct linear trends. This observation is gain consistent with a mobility of the counterions of the Stern layer of clays two orders of magnitude smaller for clays than on the surface of silica. The diffusion coefficient entering into the expression of the Cole Cole time constant is indeed related to the mobility of the counterions in the Stern layer, $\beta^S_{(+)}$, by the Nernst-Einstein relationship,

$$D^S_{(+)} = \frac{k_b T}{|q_{(+)}|}\beta^S_{(+)}, \tag{51}$$

where $|q_{(+)}|$ is the absolute value of the charge of the counterions in the Stern layer. A value of $\beta^S_{(+)}$ (Na^+, 25°C) = 1.5 × 10^{-10} $m^2s^{-1}V^{-1}$ (Section 5.3) yields $D^S_{(+)}$(Na^+, 25°C) = 3.8 × 10^{-12} m^2s^{-1} for clays. This value is used to compute the trends for clayey materials shown in Figures 15 and 16. For the clean sands and sandstones, we use the value of the mobility of the cations in water, which leads to a diffusion coefficient of $D^S_{(+)}$(Na^+, 25°C) = 1.32 × 10^{-9} m^2s^{-1}.

Another point worth discussion is the relationship between the value of the Cole Cole exponent *c* and the broadness of the distribution of the pore sizes (see Figure 3). Samples S490 and S499 have a relatively high value of *c* (0.4-0.5) and are characterized by narrow peaks in the pore size distribution (Figure 3). At the opposite, Samples S493 and S439 have low value of *c* (flatter spectra) and are also characterized by broader distributions of their pore sizes. So the value of *c* could be associated to the broadness of the pore size distribution with values close to 0 for very broad pore size distributions and close to 0.5 for very narrow pore size distributions.

In Table 4, we report the value of the Cole Cole exponent *c*, the value of the cementation exponent *m*, and the broadness of the pore size distribution. We see that the Cole Cole exponent is always comprised between 0.5 (in this case the Cole Cole model is equal to a Warburg impedance model) to values smaller than 0.10 (very flat spectra). The cementation exponent *m* is always larger or equal to unity (Appendix A).

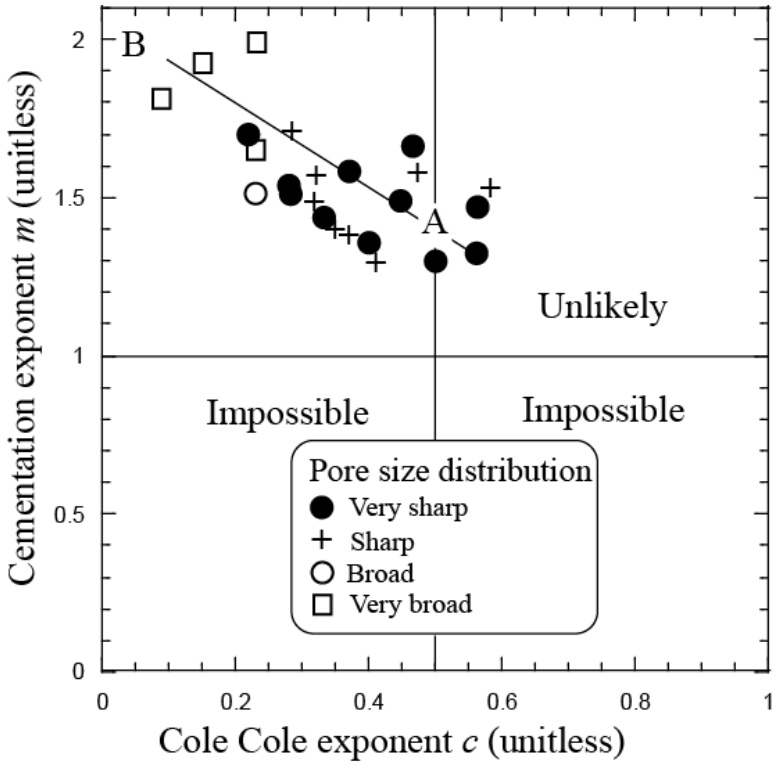

Figure 17. Cementation exponent *m* versus the Cole Cole exponent *c*. There are two extreme end-regions denoted as A and B. Domain A is typical of well-sorted clean sands while domain B is typical of clay-rich materials. The plain line denotes the trend between *m* and *c*.

We plot these data in Figure 17 using a rough marker of the grain size distribution (very sharp, sharp, broad, and very broad). Domain A is characterized by very narrow pore size distributuons and cementation exponent close to 1.5, which is the theoretical value according to the differential effective medium theory for a pack of spherical grains. The value of the Cole Cole exponent for this domain is the one corresponding to a Warburg impedance. This is typically the domain corresponding to clean well-sorted sands. Domain B is characterized by complex microgeometry, broad pore size distributions, the presence of clays. For this domain, the Cole Cole exponent reaches small values consistent with the broad pore size distributions and m reaches a value close to 2 characterizing a complex pore space topology. This implies that the exponent *c* is a measure of the pore size distribution and that for a pore distribution defined by the delta function, the frequency dependent model is the Warburg model. This also implies that the Debye decomposition used in various disciplines (colloidal chemistry and geophysics for instance) to determine the distribution of relaxation times is not correct (it would imply indeed that if all the pores are the same, the Cole Cole exponent should be equal to 1, which translates to a Debye model). In other words, complex conductivity spectra should be deconvoluted by a Warburg model to obtain the pore size distribution. Such pore size distribution could be compared to the T2 relaxation time distributions from Nuclear Magnetic resonance (NMR) spectra. We let this point for a future work.

5.6. Dependence on the CEC

As explained in Section 4.4, the CEC and the specific surface area are related to each other by $Q_S = \mathrm{CEC}_M / S_{sp}$ where the surface charge density Q_S is about 0.32 C m^{-2}. Using this relationship in Eq. (36), we obtain,

$$\sigma'' = -b\,\mathrm{CEC}_M\,, \tag{52}$$

$$b = \frac{a}{Q_S} = \frac{2}{3}\beta^S_{(+)} f \rho_g\,. \tag{53}$$

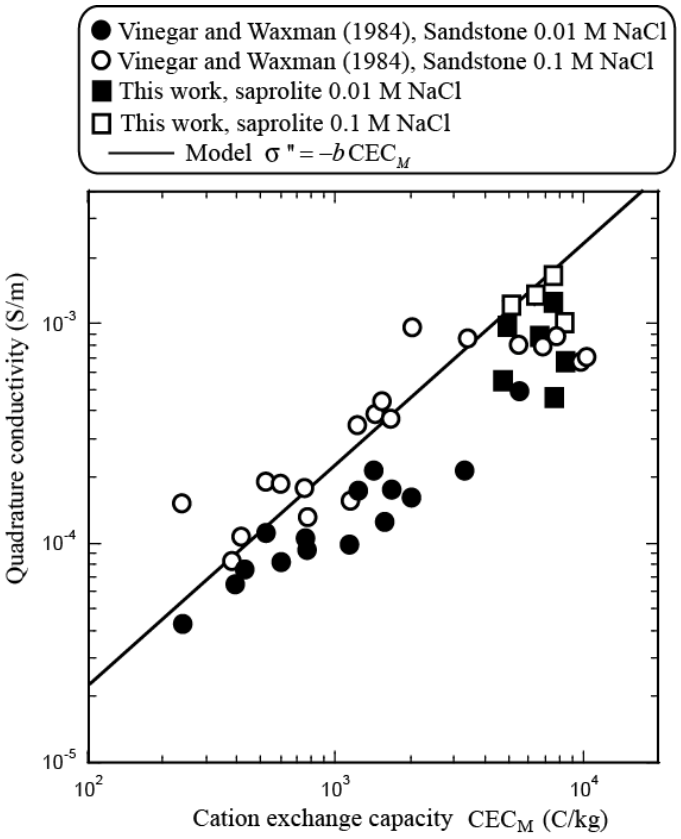

Figure 18. Quadrature conductivity versus the cation exchange capacity at different salinities (0.01 and 0.1 M NaCl). The line represents the prediction of our model as discussed in the main text. The data shows clearly the effect of salinity on the quadrature conductivity.

For clayey sands, taking $a = 7.6\times10^{-8}$ S kg m^{-3}, we obtain $b = 2.38\times10^{-7}$ S kg C^{-1} m^{-1}. The prediction of Eq. (52) with $b = 2.38\times10^{-7}$ S kg C^{-1} m^{-1} is shown in Figure 18 with both the experimental data of [53] and those of the present work. There is a fair agreement between the model and the data.

6. Conclusions

We have reached the following conclusions.

(1) We have developed a simple polarization model accounting for the dependence of the in-phase and quadrature conductivities on the porosity, cation exchange capacity (or specific surface area of the material), and salinity of the pore water for simple supporting electrolytes like NaCl in isothermal conditions. This model is coupled with a very simple complexation model on the surface of the minerals. This model is used to define the salinity dependence of the partition coefficient of the counterions between the Stern and diffuse layers.

(2) The quadrature conductivity of sands and sandstones seems to be controlled by the polarization of the Stern layer. The mobility of the counterions in the Stern layer of silica sands is two orders of magnitude higher than the mobility of the counterions in the Stern layer of clay minerals. This is confirmed through the inversion of the Cole Cole time constant as the diffusion coefficient entering this time constant can be related as well to the mobility of the counterions in the Stern layer.

(3) The salinity dependence of the in-phase and quadrature conductivity are very well-explained by our model. The quadrature component is controlled by the salinity dependence of the partition coefficient for the counterions between the Stern and diffuse layers.

(4) The frequency dependence of the complex conductivity is usually well described by a Cole Cole model with a Cole Cole exponent comprised between 0.5 (for very narrow pore size distribution) to values smaller than 0.10 for very broad pore size distributions. Both the Cole Cole exponent and the Cole Cole time constant are independent on the salinity of the pore water solutions for simple supporting electrolytes like NaCl.

Molecular dynamics simulations could be performed to see how to explain the mobility of the counterions in the Stern layer and to simulate the dynamic Stern layer in order to better understand low-frequency induced polarization in sandy and clayey materials. Such simulations could be also sued to coupled diffuse and Stern layer polarizations.

Acknowledgments. We thank the Environment Remediation Science Program (ERSP), U.S. Department of Energy (DOE, award DE-FG02-08ER646659) for funding. We thank Sophie Hancock for her help with the experimental data with the sandstones. We deeply thank Egon Zimmermann for the construction of the ZEL-SIP04-V02 impedance meter.

References

[1] L. Onsager, Physical Review 37 (1931) 405-426.
[2] I. Prigogine, Etude Thermodynamique des Phénomènes Irréversibles, Desoer, Liège, Belgium, 1947.
[3] A. Revil, N. Linde, J. Coll. Interf. Sci. 302 (2006) 682-694.
[4] C. Grosse, J. Phys. Chem. B. 115 (29) (2011) 8996-9004.
[5] P. Leroy P., A. Revil, A. Kemna, P. Cosenza, A. Ghorbani, Journal of Colloid and Interface Science, 321 (1) (2008) 103-117.
[6] I.A. Razilov, S.S. Dukhin, Colloid Journal, 57(3) (1995) 364-371 (translated from Kolloidnyi Zhurnal 57(3) (1995) 391-399).
[7] S.S. Dukhin, V. N. Shilov, Dielectric phenomena and the double layer in disperse systems and polyelectrolytes, Wiley, New York (1974).
[8] L.A. Rosen, D.A., Saville, Langmuir 7 (1991) 36-42.
[9] J. Lyklema, Edited by A.V. Delgado, Surfactant Science Series, 106 (2002) 87-97, 991 pp.
[10] A. Revil, N. Florsch, Geophys. J. Int. 181 (2010) 1480-1498, doi: 10.1111/j.1365-246X.2010.04573.x.
[11] M. Schmutz, A. Revil, P. Vaudelet, M. Batzle, P. Femenía Viñao, D. D. Werkema, Geophys. J. Int. 183 (2010) 211–224, doi: 10.1111/j.1365-246X.2010.04751.x.
[12] A. Revil, Water Resour. Res. 48 (2012) W02517, doi:10.1029/2011WR011260.
[13] A. Revil, K. Koch, K. Holliger, Water Resour. Res. 48 (2012) W05602, doi:10.1029/2011WR011561.
[14] A. Revil, M. Skold, S. S. Hubbard, Y. Wu, D. B. Watson, M. Karaoulis, in press in Geophysics (2013).
[15] S. Pride Phys. Rev. B 50 (21) (1994) 15678-15696.
[16] M.J. Aranda-Rascón, C. Grosse, J.J. López-García, J. Horno, Journal of Colloid and Interface Science 336 (2009) 857–864.
[17] F. Carrique, F. J. Arroyo, M. L. Jiménez, A. V. Delgado, Journal of Chemical Physics 118 (4) (2003) 1945.
[18] A. Revil, A., P.W.J. Glover, Physical Review B. 55 (3) (1997) 1757-1773.
[19] C.F. Zukoski, D.A. Saville, Journal of Colloid and Interface Science 114 (1) (1986) 32-44.
[20] C.F. Zukoski, D.A. Saville, Journal of Colloid and Interface Science 114 (1) (1986) 45-53.
[21] R. Barchini, D.A. Saville, Journal of Colloid and Interface Science, 173 (1995) 86-91.
[22] M. Wang, J. Liu, and S. Chen, Molecular Simulation 33(15) (2007) 1273-1277.
[23] C. Tournassat, Y. Chapron, P. Leroy, M. Bizi, F. Boulahya, Journal of Colloid and Interface Science 339 (2) (2009) 533-541.
[24] S. Carroll, R. S. Maxwell, W. Bourcer, S. Martin, S. Hulsey, Geochimica et Cosmochimica Acta 66 (6) (2002) 913-926.
[25] L.A. Rosen J. C. Baygents, D. A. Saville, J. Chem. Phys., 98 (5) (1993) 4183-4194.
[26] A. Revil, in press in Water Resources Research (2013).
[27] G.E. Archie, Transactions of AIME 146 (1942) 54–62.
[28] K.S. Cole, R.H. Cole, Journal of Chemical Physics 9 (1941) 341-351.
[29] D.B. Watson, J.E. Kostka, M.W. Fields, P.M. Jardine, NABIR FRC Technical Report: NABIR FRC. http://public.ornl.gov/orifc/FRC-conceptual-model.pdf (2004).
[30] P. M. Jardine, G. V. Wilson, R. J. Luxmoore, Soil Science Society of America Journal 52 (1988) 1252- 1259.

[31] P. M. Jardine, G. K. Jacobs, G. V. Wilson, Soil Science Society of America Journal 57 (1993) 945-953.
[32] P. M. Jardine, G. K. Jacobs, J. D. O'Dell, Soil Science Society of America Journal 57 (1993) 954-962.
[33] Y.J. Kim, J.W. Moon, Y. Roh, S. C. Brooks, Environmental Geology 58 (2009) 1301–1307.
[34] E. Zimmermann, A. Kemna, J. Berwix, W. Glaas, H.M. Münch, J.A. Huisman, Measurement Science and Technology 19 (2008) doi:10.1088/0957-0233/19/10/105603.
[35] A. Revil A., M. Skold, Geophysical Journal International 187 (2011) 813–824, doi: 10.1111/j.1365-246X.2011.05181.x.
[36] B.F. Swanson, Journal of Petroleum Technology 33 (1981) 2498-2504.
[37] M.E. Sumner, W.P. Miller, Cation Exchange Capacity and Exchange Coefficients, In: Page, D.L. (ed.) Methods of soil analysis Part 3: Chemical Methods, Soil Science Society of America, Madison, WI (1996).
[38] K.S.W. Sing, Pure and Applied Chemistry 57 (4) (1985) 603-619.
[39] S. Brunauer, P.H. Emmett, E. Teller, Journal of the American Chemical Society 60 (1938) 309–319.
[40] A. Revil, L.M., Cathles, S., Losh, J.A., Nunn, Electrical conductivity in shaly sands with geophysical applications, J. Geophys. Res., 103(B10) (1998) 23,925-23,936.
[41] J. G. Patchett, Society of Professional Well Logging Analysis 16th Logging Symposium, Paper U, 41 p. (1975).
[42] M. Lipsicas, Physics and Chemistry of Porous Media, edited by D. L. Johnson and P. N. Sen, pp. 191–202, Am. Inst. of Phys., College Park, Md. (1984).
[43] J.P. Zundel, B. Siffert, in Solid-Liquid Interactions in Porous Media, pp. 447– 462, Technip, Paris (1985).
[44] N. C. Lockhart, J. Colloid Interface Sci. 74 (1980) 520–529. V. A. Sinitsyn, S. U. Aja, D. A. Kulik, S. A. Wood, Geochim. Cosmochim. Acta 64 (2000) 185– 194.
[45] M. J. Avena, C. P. De Pauli, J. Colloid Interface Sci. 202 (1998) 195–204, doi: 10.1006/jcis.1998.5402.
[46] I. Shainberg, N. Alperovitch, R. Keren, Clays Clay Miner. 36 (1988) 432– 438.
[47] Q. Su, Q. Feng, Z. Shang, Geophysics 65 (2000) 68– 75.
[48] C. Ma, R. A. Eggleton, Clays Clay Miner. 47 (1999) 174– 180.
[49] B. Chittoori, A.J. Puppala, J. Geotech. Geoenviron. Eng. 137 (11) (2011) 997-1008.
[50] A. Kemna, Tomographic inversion of complex resistivity-theory and application, Ph.D Dissertation, Ruhr-University of Bochum, Germany, 196 pp. (2000).
[51] J. Xiang, D. Cheng, F.S. Schlindwein, N.B. Jones, On the adequacy of identified Cole–Cole models, Computers & Geosciences 29 (2003) 647–654.
[52] A.J. Katz, A.H. Thompson, J. Geophys. Res. 92 (1987), 599-607.
[53] H.J. Vinegar, M.H. Waxman, Geophysics 49 (1984) 1267-1287.
[54] P. Vaudelet, A. Revil, M. Schmutz, M. Franceschi, P. Bégassat, Water Resour Res. 47 (2011) W02526, doi:10.1029/2010WR009310.
[55] K. Koch, A. Kemna, J. Irving, K. Holliger, Hydrology and Earth System Science 15 (2011) 1785-1794, doi: 10.5194/hess-15-1785-2011.
[56] L.D. Slater, D.R. Glaser, Geophysics 68 (5) (2003) 1547-1558.
[57] A. Weller, K. Breede, L. Slater, S. Nordsiek, Geophysics 75 (6) (2011) F315-F327.
[58] F.D. Börner, Proc Third European Core Analysis Symposium, Paris, 359-386 (1992).
[59] D. P. Lesmes, K.M. Frye, J. Geophys. Res. 106(B3) (2001) 4079-4090.

[60] A. Binley, L.D. Slater, M. Fukes, G. Cassiani, Water Resour Res. 41, W12417 (2005).
[61] J. Scott, R. Barker, Geophys. Res. Lett., 30 (9) (2003) 1450.
[62] L. Comparon, Etude expérimentale des propriétés électriques et diélectriques des matérieux argileux consolidés, PhD Thesis, Institut de Physique du Globe de Paris 400 pp. (2005)
[63] M. Tong, L. Li, W. Wang, Y. Jiang, Geophysics 71 (2006) N33–N40.
[64] D.L. Johnson, T.J. Plona, H. Kojima, Physics and Chemistry of Porous Media II (1986) edited by R. Jayanth, J. Banavar, and K. W. Winkler, 243–277, AIP, New York.
[65] M. Avellaneda, S. Torquato, Physics of Fluids A 3 (1991) 2529–2540.
[66] A. Revil, L.M. Cathles III, Water Resources Research 35 (1999) 651-662.

Appendix A. Physical Description of the Formation Factor

The formation factor is defined by the electrical conductivity problem of a porous material when surface conductivity by be neglected. From Eq. (8), we have indeed,

$$\lim_{\mathrm{Du}=0}\left(\frac{\sigma'}{\sigma_w}\right)=\frac{1}{F}. \tag{A1}$$

In a porous material with insulating grains, the following canonical boundary value problem for the normalized electrical potential Γ for a cylindrical representative elementary volume of porous material of length L

$$\nabla^2\Gamma=0 \text{ in } V_p \tag{A2}$$

$$\hat{n}\cdot\nabla\Gamma=0 \text{ on } S \tag{A3}$$

$$\Gamma=\begin{cases} L \text{ at } z=L \\ 0 \text{ at } z=0 \end{cases} \text{ on } S \tag{A4}$$

where $\hat{n}$ is the unit vector normal to the pore water/mineral interface S and V_p denote the pore volume [64]. The formation factor F is obtained by summing up the Joule dissipation of energy [64-65]). this yields,

$$\frac{1}{F}=\frac{1}{V}\int_{V_p}|\nabla\Gamma|^2\,dV_p\,, \tag{A5}$$

where V is the total volume of the considered representative elementary volume. From Eq. (B5), $1/F$ can be regarded as an effective porosity [66], which is only a fraction of the total connected porosity $\phi=V_p/V$. This implies in turn,

$$\frac{1}{F}\le\phi \text{ and } F\equiv\phi^{-m}\Rightarrow m\ge 1. \tag{A6}$$

Appendix B. Low and High Frequency Conductivity

The main assumption made in our analysis is that the grains are touching each other so the diffuse layer is continuous but not the Stern layer [12]. Under this assumption, we expect that the Direct Current (DC) conductivity and the high-frequency conductivity are given by,

$$\sigma_0 = \frac{1}{F}\left[\sigma_w + \beta_{(+)}(1-f)Q_V\right], \tag{B1}$$

$$\sigma_\infty = \frac{1}{F}\left\{\sigma_w + \left[\beta_{(+)}(1-f) + \beta^S_{(+)} f\right]Q_V\right\}. \tag{B2}$$

These equations can be demonstrated through a volume averaging approach (Revil, 2013). The normalized chargeability $M_n = M\sigma_\infty = \sigma_\infty - \sigma_0$ is therefore, using Eq. (20), the normalized chargeability is given as,

$$M_n = \left(\frac{1}{F}\right)\left(\frac{1-\phi}{\phi}\right)\rho_g \beta^S_{(+)} f \,\mathrm{CEC}, \tag{B3}$$

$$M_n \approx \left(\frac{2}{3}\right)\rho_g \beta^S_{(+)} f \,\mathrm{CEC}, \tag{B4}$$

which is also the same equation obtained for the quadrature conductivity (see Eq. 36). To go from Eq. (B3) to (B4), we have used the approximations (see [10]),

$$F - 1 \approx F, \tag{B5}$$

$$F \approx 1 + \frac{3}{2}\left(\frac{\phi}{1-\phi}\right). \tag{B6}$$

Tables

Table 1. Description of the core samples in terms of petrology, porosity, permeability, and grain mass density. When the grain density is not directly measured, it is assumed equal to the grain density of silica (2650 kg m^{-3}).

Sample	Type	Porosity (-)	Permeability (mD)	Density grains (kg m^{-3})
S499	Coarse sandstone	0.265	1103	2596
S498	Medium sandstone	0.206	35.9	2635
S490	Coarse sandstone	0.233	635	2602
S493	Medium silty sandstone	0.232	115	2619
S439	Mudstone	0.208	2.62	2613
S436	Coarse sandstone	0.306	1623	2619
S9	Saprolite	0.48	16	-
S16	Saprolite	0.49	5.0	-
S22	Saprolite	0.43	7.7	-
S14	Saprolite	0.39	54.1	-
S20	Saprolite	0.33	10.2	-
S18	Saprolite	0.36	54.0	-
S5	Saprolite	0.45	21.4	-
S10	Saprolite	-	-	-
S12	Saprolite	0.37	29.7	-
S7	Saprolite	0.48	326	-

Table 2. Petrophysical Properties of the core samples. S_{Sp} (in m^2/g) denotes the specific surface area determined by the BET method, F (-) denotes the intrinsic formation factor determined from the conductivity measurements performed at different pore water salinities, and σ_S' (in S m^{-1}) denotes the surface conductivity from the same data.

Sample	Specific surface area (m^2 kg^{-1})	CEC (cmol kg^{-1})	Formation factor (-)	Surface conductivity (10^{-4} S m^{-1})	Quadrature conductivity (S m^{-1}) (1)
S499	48.6	-	5.6±0.4	3.3±0.7	-4×10^{-3}
S498	5,020	-	9.0±0.8	390±90	-1.6×10^{-3}
S490	10,100	-	12.1±0.4	400±130	-1.5×10^{-3}
S493	10,100	-	18.3±0.4	570±90	-2.5×10^{-3}
S439	15,200	-	13.3±0.7	290±90	-1.5×10^{-3}
S436	88	-	4.0±0.3	-	-2×10^{-3}
S9	14,957	-	4.1±0.3	39±6	-1.1×10^{-3}
S16	9,261	-	5.9±0.1	95±2	-1.7×10^{-3}
S22	18,174	-	4.4±0.5	376±34	-1.6×10^{-3}
S14	14,834	5.24±0.86	7.1±2.5	386±157	-1.2×10^{-3}
S20	9.329	5.19±0.84	5.1±0.2	237±23	-1.2×10^{-3}
S18	13,659	7.86±0.42	7.3±2.6	633±169	-1.6×10^{-3}
S5	24,321	8.57±0.18	4.4±0.3	39±32	-1.0×10^{-3}
S10	29,091	7.95±0.08	4.1±0.8	-	-1.7×10^{-3}
S12	18,353	6.85±0.01	5.1±0.2	148±15	-1.3×10^{-3}
S7	17,102	4.96±0.87	3.7±0.3	14±13	-4.0×10^{-4}

(1) 1 Hz or at the peak frequency. Pore water conductivity (NaCl): about 0.1 S m^{-1}.

Table 3. Typical composition of the natural groundwater (GW) for the sandstones and saprolites used to perform some of measurements. TDS: Total Dissolved Solids.

Parameter	Units	Sandstone	Saprolite
TDS	mg L^{-1}	318	433
Conductivity	□S cm^{-1}	479	64
pH	-	8.1	7.5
Alkalinity	mg L^{-1}	109	175
Na^{+}	mg L^{-1}	30.6	2.7
K^{+}	mg L^{-1}	3.9	2.0
Ca^{2+}	mg/L	65.0	26
Mg^{2+}	mg L^{-1}	3.1	5.0
Cl^{-}	mg L^{-1}	6.0	3.5
HCO_3^{-}	mg L^{-1}	123	220
SO_4^{2-}	mg L^{-1}	132	90

Table 4. Relationship between the sharpness of the pore size distribution and the value of the Cole Cole exponent *c*.

Sample	Reference	Sharpness	*c*	*m*
S499	This work	Sharp	0.41	1.30
S498	This work	Sharp	0.37	1.39
S490	This work	Sharp	0.28	1.71
S493	This work	Very broad	0.23	1.99
S439	This work	Very broad	0.23	1.65
S436	This work	Broad	0.23	1.50
S9	This work	Very broad	0.15	1.92
S22	This work	Very broad	0.09	1.81
A1	[53]	Very sharp	0.56	1.32
F36	[54]	Sharp	0.47	1.59
F32	[54]	Sharp	0.58	1.54
WQ1	[54]	Sharp	0.32	1.56
SP1	[54]	Very sharp	0.57	1.48
SP2	[54]	Very sharp	0.32	1.49
SP3	[54]	Very sharp	0.47	1.65
SP4	[54]	Very sharp	0.37	1.58
SP5	[54]	Very sharp	0.33	1.54
SP6	[54]	Very sharp	0.22	1.70
F36-C	[54]	Sharp	0.32	1.48
F32-C	[54]	Sharp	0.35	1.40
WQ1-C	[54]	Sharp	0.44	1.59
SP1-C	[54]	Very sharp	0.50	1.30
SP2-C	[54]	Very sharp	0.40	1.35
SP3-C	[54]	Very sharp	0.45	1.49
SP4-C	[54]	Very sharp	0.28	1.54
SP5-C	[54]	Very sharp	0.33	1.44
SP6-C	[54]	Very sharp	0.28	1.53